The Role of the Cosmic Web in the Structural and Dynamical Evolution of Dark Matter Subhaloes

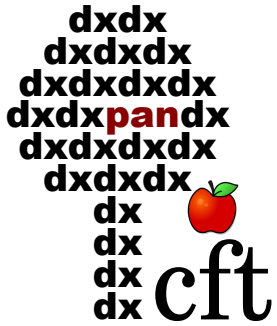

Author: Feven Markos Hunde
Supervisors: dr. hab. Wojciech A. Hellwing, prof. CFT PAN
dr. hab. Maciej A. Bilicki, prof. CFT PAN

Center for Theoretical Physics
Polish Academy of Sciences

Thesis submitted in partial fulfilment of the requirements for the degree of Doctor of Philosophy in Physics

2026

Dedicated to my parents
Bezunesh and Markos

Abstract

The standard Lambda cold dark matter (ΛCDM) cosmological paradigm predicts that structure formation proceeds hierarchically, assembling the large-scale cosmic web. High-resolution computer simulations suggest that evolution of dark matter (DM) haloes is closely linked to this network of nodes, filaments, walls, and voids. Rather than serving as a passive backdrop, the cosmic web may exert an active dynamical influence on the structures residing within it. This dissertation explores how the cosmic web environment of the host DM halo is associated with the abundance, internal structure, and evolutionary history of its subhalo populations at present (redshift $z = 0$) and past (higher redshifts), and examines how these dependencies may propagate into the substructure boost factor of possible DM annihilation signatures.

Using COLOR N-body simulation and the `CaCTus` cosmic web classification framework, we analyze cumulative subhalo populations hosted by fixed-mass haloes residing in distinct cosmic web environments to help isolate environmental effects from simple halo mass scaling. Our results suggest that the cosmic web environment of the host imprints a systematic signal on its subhalo populations independently of the host mass. Subhaloes hosted by filament haloes tend to be 5 to 30% more abundant than the cosmic mean, while those hosted by void haloes show deficits of up to 50% at the high-mass end of the subhalo mass function. The total subhalo mass fraction varies by 2 to 20% between environments. Furthermore, subhaloes hosted by filament haloes appear 5 to 9% more concentrated than those hosted by void haloes, a trend most pronounced in the lowest-mass host systems.

For models where DM annihilates into gamma rays, we extend this analysis to the substructure boost factor of predicted DM annihilation. Since the annihilation rate scales with the square of the local density, environmental shifts in the properties of subhaloes hosted by haloes in different environments may alter the boost factor. By incorporating our environment-dependent host concentrations, subhalo mass functions, and internal density profiles into two semi-analytic frameworks, we find tentative indications that subhaloes hosted by void haloes exhibit boost factor suppressions of about 30% relative to the cosmic average, while those hosted by filament haloes display a mass-dependent transition, ranging from suppressions of $\sim$15% at low host masses to enhancements of $\sim$12% at high host masses. We also derive an empirical fitting prescription for this environment-conditioned boost factor as a potential basis for future implementation.

We investigate the physical origin of these signatures by tracing subhalo histories through cosmic time using merger trees. We compare subhalo populations across different environments at their present-day values and at their peak state, defined as the state in which they attain maximum mass or velocity in their merger history. Our results are consistent with a two-stage evolutionary picture. Part of the environmental dependence may be already established before the subhaloes fall into their host, which is also reflected in their peak properties. Afterward, subsequent evolution within the host further modifies these dependencies through environment-dependent tidal processing. Structural ratios suggest that the mass at the outskirts of subhaloes is substantially depleted, dropping to 25% to 60% of its peak value by the present day. Conversely, the inner structural potential appears more resilient, with the maximum circular velocity retaining 70% to 90% of its peak amplitude.

Tracing earlier time (simulation snapshots) suggests that this environmental ordering builds up progressively during major assembly phases. At redshift $z = 2.0$, the subhalo mass function shows an emerging differentiation for subhaloes hosted by proto-filament haloes, while the relation between maximum circular velocity and its corresponding radius exhibits a 30% to 40% environmental variation. These trends may be relevant for semi-empirical galaxy–halo modelling, as they are broadly consistent with the relative robustness of velocity-based proxies such as peak subhalo velocity compared to present-day bound mass, and may provide useful simulation-based baselines for future studies of environmental satellite evolution, lensing-related substructure statistics, and galaxy assembly bias.

The results of this thesis suggest that neglecting the cosmic web environment of the host halo when modelling subhalo statistics and DM annihilation signals at $z = 0$ and at higher redshifts may introduce systematic biases on the order of tens of percent. This indicates that the large-scale environment of the host warrants consideration as a potentially important component in future investigations of satellite galaxy populations, substructure demographics across cosmic time, gravitational lensing sensitivities, and indirect DM detection predictions.

Streszczenie

Standardowy model kosmologiczny ΛCDM (Lambda Cold Dark Matter) przewiduje, że tworzenie się struktur przebiega hierarchicznie, prowadząc do powstania wielkoskalowej sieci kosmicznej. Symulacje komputerowe o wysokiej rozdzielczości sugerują, że ewolucja hal ciemnej materii (DM) jest ściśle powiązana z tą siecią węzłów, włókien, ścian i pustych przestrzeni. Sieć kosmiczna nie pełni jedynie roli biernego tła, lecz może wywierać aktywny wpływ dynamiczny na struktury znajdujące się w jej obrębie. Niniejsza rozprawa bada, w jaki sposób środowisko sieci kosmicznej otaczające halo ciemnej materii jest powiązane z liczebnością, strukturą wewnętrzną i historią ewolucji populacji subhalo w teraźniejszości (przesunięcie ku czerwieni $z = 0$) i przeszłości (wyższe przesunięcia ku czerwieni), a także analizuje, w jaki sposób zależności te mogą przekładać się na współczynnik wzmocnienia podstruktury (*boost factor*) potencjalnych sygnatur anihilacji ciemnej materii.

Wykorzystując symulację N-ciałową COLOR oraz system klasyfikacji sieci kosmicznej `CaCTus`, analizuję zbiorcze populacje subhalo znajdujące się w halach o stałej masie, położonych w różnych środowiskach sieci kosmicznej, aby oddzielić wpływ środowiska od prostego skalowania masy hal. Moje wyniki sugerują, że środowisko sieci kosmicznej gospodarza wywiera systematyczny wpływ na populacje subhalo niezależnie od masy gospodarza. Subhalo znajdujące się w halach we włóknach są zazwyczaj o 5 do 30% liczniejsze niż średnia kosmiczna, podczas gdy te znajdujące się w halach w pustkach wykazują deficyt sięgający nawet 50% w górnej części rozkładu mas subhalo. Całkowity udział masowy subhalo waha się od 2 do 20% w zależności od środowiska. Ponadto subhalo znajdujące się w halach we włóknach wydają się być o 5 do 9% bardziej skoncentrowane niż te znajdujące się w halach w pustkach, co jest najbardziej widoczne w systemach o najniższej masie.

W przypadku modeli, w których ciemna materia anihiluje z wytworzeniem promieniowania gamma, rozszerzamy tę analizę na współczynnik wzmocnienia przewidywanej anihilacji ciemnej materii w podstrukturach. Ponieważ tempo anihilacji jest proporcjonalne do kwadratu lokalnej gęstości, zmiany właściwości subhalo znajdujących się w halach w różnych środowiskach mogą wpływać na współczynnik wzmocnienia. Uwzględnienie zależnych od środowiska koncentracji hal macierzystych, funkcji masy subhalo oraz profili gęstości wewnętrznej w dwóch modelach półanalitycznych, prowadzi do konkluzji, że subhalo znajdujące się w halach w pustkach wykazują osłabienie współczynnika wzmocnienia o około 30% w stosunku do średniej kosmicznej, podczas gdy te znajdujące się w halach we włóknach wykazują

zależne od masy przejście, od osłabienia o ∼15% przy niskich masach gospodarza do wzmocnienia o ∼12% przy wysokich masach gospodarza. Rozprawa zawiera również empiryczny wzór na dopasowanie tego współczynnika wzmocnienia uwarunkowanego środowiskiem jako potencjalną podstawę do przyszłego wdrożenia.

Praca bada fizyczne pochodzenie tych sygnatur, śledząc historię subhalo w czasie kosmicznym za pomocą drzew połączeń. Porównuję populacje subhalo w różnych środowiskach, zarówno w ich obecnym stanie, jak i w stanie szczytowym, zdefiniowanym jako moment, w którym osiągają one maksymalną masę lub prędkość w swojej historii połączeń. Moje wyniki są zgodne z dwuetapowym obrazem ewolucji. Część zależności środowiskowych może być już ustalona, zanim subhalo zostaną wchłonięte przez swojego gospodarza, co znajduje również odzwierciedlenie w ich właściwościach szczytowych. Następnie dalsza ewolucja w obrębie gospodarza dodatkowo modyfikuje te zależności poprzez zależne od środowiska procesy pływowe. Współczynniki strukturalne sugerują, że masa na obrzeżach subhalo uległa znacznemu zmniejszeniu, spadając do 25–60% wartości szczytowej w dniu dzisiejszym. Z drugiej strony, potencjał strukturalny w środku wydaje się bardziej odporny, a maksymalna prędkość kołowa zachowuje 70–90% swojej amplitudy szczytowej.

Analiza wcześniejszych etapów (migawki symulacji) sugeruje, że porządkowanie środowiskowe narasta stopniowo podczas głównych faz formowania się struktur. Przy przesunięciu ku czerwieni $z = 2$ funkcja masy subhalo wykazuje zróżnicowanie w przypadku subhalo znajdujących się w halach w proto-włóknach, podczas gdy zależność między maksymalną prędkością kołową a odpowiadającym jej promieniem wykazuje 30–40-procentową zmienność środowiskową. Trendy te mogą mieć znaczenie dla półempirycznego modelowania galaktyk i hal, ponieważ są one zasadniczo zgodne ze wskaźnikami opartymi na prędkości, takimi jak szczytowa prędkość subhalo w porównaniu z obecną masą związaną, i mogą stanowić użyteczne punkty odniesienia oparte na symulacjach dla przyszłych badań ewolucji satelitów środowiskowych, statystyk podstruktury związanych z soczewkowaniem oraz tendencji w tworzeniu się galaktyk.

Wyniki niniejszej pracy wskazują, że pominięcie wpływu kosmicznej sieci otaczającej halo macierzyste podczas modelowania statystyk subhalo oraz sygnałów anihilacji ciemnej materii przy $z = 0$ i wyższych przesunięciach ku czerwieni może powodować systematyczne odchylenia rzędu kilkudziesięciu procent. Wskazuje to, że należy uwzględniać otoczenie gospodarza w skali makro jako potencjalnie ważny element w przyszłych badaniach populacji galaktyk satelitarnych, demografii podstruktury w czasie kosmicznym, czułości soczewkowania grawitacyjnego oraz prognoz dotyczących pośredniego wykrywania ciemnej materii.

Acknowledgements

As I reach the completion of this doctoral thesis, I am filled with a deep sense of humility and gratitude. It has been said that it takes a village to make me who I am today.

I would like to express my sincere gratitude to my supervisors, **Prof. Wojciech A. Hellwing and Prof. Maciej Bilicki**. Without your support and encouragement, I could never have finished this work. Thank you for your patience and for encouraging me to grow as a thinker. The hours we spent discussing ideas and exploring new directions have been invaluable, shaping my curiosity and my love for discovery. I am sincerely thankful for your trust and for challenging me to reach beyond what I thought possible.

I am very grateful to **Prof. Amare Abebe** for the important discussions we had and the clarity provided during difficult moments, and to **Prof. Satya Gontcho A. Gontcho**, my Supernova Foundation mentor, for your encouragement and the great talks we had, which always gave me more confidence in my work.

A warm thanks goes to all my office mates, **Suhani, Pawel, Anjitha, Gursharanjit, and Julius**, for the great time we spent together. Your companionship made this research journey feel less like work and more like a shared adventure. I also want to thank **Mariana, Oliver, Krishna, Priyanka, Maria Luiza, and Szymon** for all the advice and encouragement you provided.

I also wish to thank the unique collection of family and those who have walked alongside me in different seasons, including **Bekele, Wube, Mengistu, Sintayehu, Alemayehu, the late Dr. Mamo, Tadele, Natnael, Flora, Henok, and Mekedes**. Your kindness, laughter, and advice have carried me through challenges and reminded me of the beauty in human connection.

To my **parents**, your sacrifices and steadfast belief in me have carried me through every distance. Even when miles separated us, your prayers and quiet care were constant sources of strength and reassurance. To my siblings **Endashaw, Mihret, Amanuel, and Biruk**, you are my heartbeat and my greatest source of courage. Your laughter and unwavering faith in me reminded me that I was never alone, no matter how far I travelled. I am thankful to my grandparents, uncles, aunts, and cousins for being the roots that keep me grounded. In particular, the care and warm presence of **Zewdie, Markos, Zenebech, Dinknesh, Genet, and Temesgen** reached me even from afar, making this journey feel infinitely richer.

I am grateful to **CTP PAS** for the invaluable support and the administration for making the academic journey smoother. I acknowledge with gratitude the financial support from **NAWA, the Warsaw4PhD doctoral school, and CTP PAS**.

A special thank you goes to **Thebooks.pl** bookstore for offering a sanctuary amid deadlines, providing a place to pause, reflect, and simply breathe.

Above all, I offer my deepest praise and thanks to YHWH, whose grace and strength have sustained me through every single step of this journey.

To my entire village, thank you very much for your support and encouragement.

Declaration

The research presented in this thesis was carried out between 2021 and 2026 during my doctoral studies under the supervision of Prof. Wojciech A. Hellwing and Prof. Maciej A. Bilicki at the Center for Theoretical Physics of the Polish Academy of Sciences in Warsaw, Poland. No part of this thesis has been submitted previously for any other degree. The thesis includes the following co-authored works:

- Feven Markos Hunde, Oliver Newton, Wojciech A. Hellwing, Maciej Bilicki, and Krishna Naidoo
  Caught in the Cosmic Web: Environmental Effects on Subhalo Abundance and Internal Density Profiles
  A&A, 700, A65 (2025)
  https://doi.org/10.1051/0004-6361/202452246
  I am the first author of this publication. In the process of this article preparation, I led the numerical analysis using the COLOR simulation data, including the computation of environment-dependent subhalo proxies. I was responsible for assigning haloes to cosmic web environments using the density field classifications from the `CaCTus` algorithm, constructing the environment-conditioned ingredient ratios, and producing the figures and data visualisations, with the exception of Figure 1. I also led the physical interpretation of the results and wrote the majority of the manuscript.
- Feven Markos Hunde, Wojciech A. Hellwing, and Maciej Bilicki
  Caught in the Cosmic Web: Environmental Impacts on Halo Substructure Boosts to Dark Matter Annihilation Signals
  Under review by Physical Review D
  https://doi.org/10.48550/arXiv.2604.26072
  I am the first author of this publication. In the process of this article preparation, I led the numerical analysis of the COLOR simulation data and the adaptation of semi-analytic boost frameworks to incorporate environment-dependent parameters and propagate them into the boost factor calculations. I handled the assignment of haloes to cosmic web environments using the `CaCTus` algorithm, generated all figures and data visualisations, and wrote the majority of the manuscript.

Contents

List of Figures

List of Tables

List of Abbreviations

2LPT	Second-order Lagrangian Perturbation Theory
ΛCDM	Lambda Cold Dark Matter
AHF	AMIGA Halo Finder
AMR	Adaptive Mesh Refinement
BBN	Big Bang Nucleosynthesis
CDM	Cold Dark Matter
CIC	Cloud-in-Cell
CMB	Cosmic Microwave Background
COCO	COpernicus COmplexio
COLOR	COpernicus complexio LOw Resolution
CSHMF	Cumulative Subhalo Mass Function
CSHVF	Cumulative Subhalo Velocity Function
DM	Dark Matter
FDM	Fuzzy Dark Matter
FFT	Fast Fourier Transform
FLRW	Friedmann–Lemaître–Robertson–Walker
FoF	Friends-of-Friends
GR	General Relativity
LHC	Large Hadron Collider
MAH	Mass Accretion History
NFW	Navarro–Frenk–White
PM	Particle-Mesh
SIDM	Self-Interacting Dark Matter
SO	Spherical Overdensity
TBTF	Too-Big-To-Fail
TSC	Triangular Shaped Cloud
WDM	Warm Dark Matter
WHIM	Warm-Hot Intergalactic Medium
WIMP	Weakly Interacting Massive Particle
WMAP	Wilkinson Microwave Anisotropy Probe

Useful Definitions and Units

Symbol	Definition or convention used in this thesis
H_0	Present-day Hubble constant, written as $H_0 = 100\,h\,\mathrm{km\,s^{-1}\,Mpc^{-1}}$.
h	Dimensionless Hubble parameter. Lengths and masses are often quoted in h^{-1}Mpc, h^{-1}kpc, or $h^{-1}M_\odot$.
z	Cosmological redshift, related to the scale factor by $a = 1/(1+z)$ for $a(z=0) = 1$.
M_{200}	Host halo mass enclosed within R_{200}, where the mean enclosed density is $200\rho_{\mathrm{crit}}(z)$.
R_{200}	Radius enclosing M_{200}. It is used as the operational host-halo boundary.
V_{200}	Circular velocity at R_{200}, $V_{200} = \sqrt{GM_{200}/R_{200}}$.
M_{sub}	Present-day bound mass of a subhalo as identified by SUBFIND.
V_{max}	Maximum value of the circular velocity curve, $V_{\mathrm{max}} = \max\sqrt{GM(<r)/r}$.
R_{max}	Radius at which V_{max} is reached. The V_{max}–R_{max} relation is used as a structural proxy.
M_{peak}	Maximum bound mass reached by a subhalo over its resolved merger-tree history.
V_{peak}	Maximum value of V_{max} reached by a subhalo over its resolved merger-tree history.
μ	Reduced subhalo mass, $\mu = M_{\mathrm{sub}}/M_{200}$.
ν	Reduced subhalo velocity, $\nu = V_{\mathrm{max}}/V_{200}$.
CSHMF	Cumulative subhalo mass function, usually written as $N(>\mu)$.
CSHVF	Cumulative subhalo velocity function, usually written as $N(>\nu)$.
f_{sub}	Fraction of host-halo mass bound in resolved subhaloes.
$B(M)$	Substructure boost factor for dark matter annihilation luminosity.

Chapter 1

Introduction

"Look deep into nature, and then you will understand everything better." — Albert Einstein

Modern cosmology is defined by a persistent tension. We rely on a mathematical model that works with high precision, yet we cannot directly see the very components that drive its evolution. This ΛCDM paradigm grew out of Einstein's general theory of relativity and the subsequent discovery that the Universe is an expanding system that began in a hot and dense state [9]. What started as theoretical speculation has since transformed into a data-driven science. Today, this allows us to trace cosmic history from its first fractions of a second down to the complex architectures we observe in the present day [4].

The model works because it matches independent data sets with remarkable consistency, from the abundance of light elements created in the early Universe to the temperature patterns etched into the Cosmic Microwave Background (CMB) [10]. However, this agreement comes at a price. We must accept that approximately 95% of the cosmic composition consists of dark energy and dark matter (DM) [11, 12]. These components remain hidden from our telescopes and are known only through their gravitational influence. Within this framework, structure grows hierarchically as small objects merge to form larger ones [13]. To make this vast system manageable, we rely on the cosmological principle and assume that on the largest scales the Universe is homogeneous and isotropic.

Under these conditions, gravity acts on tiny initial density variations to build the cosmic web [14]. This network of nodes, filaments, walls, and voids defines the environment for every galaxy and the gravitationally bound DM structures in which they reside. While we have a strong grasp of how this web grows on large-scales where gravity is weak, the transition to smaller and denser regions creates a much more

complex, non-linear problem. This is where the internal properties of DM haloes and their substructures become critical to our understanding of the dark sector [15].

The primary objective of this thesis is to investigate how the large-scale environment influences the properties and abundance of DM halo substructures. We focus on this relationship to explore how these environmental effects may impact potential signals from DM annihilation. This central theme provides the motivation for the following chapters, which lay out the necessary foundation for the study. Chapter 1 introduces the theoretical basis of ΛCDM and the physics of structure formation. Chapter 2 then describes the numerical methods employed to model these systems, including N-body techniques and the morphological frameworks used to classify the cosmic web. Together, these chapters set the stage for the specific investigations and findings presented in Chapters 3 and beyond.

1.1 The cosmological model

1.1.1 Friedmann-Lemaître-Robertson-Walker metric

By adopting the cosmological principle as a foundational starting point, it becomes possible to construct models of the Universe where large-scale uniformity is preserved. This framework portrays the Universe as a continuously expanding entity with matter governed by the principles of General Relativity (GR) as formulated by Albert Einstein. In this environment, objects in free fall travel along geodesics in a four-dimensional manifold. The curvature of this spacetime is determined by the distribution of energy and momentum and may remain nonzero even in the absence of matter. This geometric structure leads to the relative acceleration of nearby trajectories, which is interpreted as gravitational effects in the Newtonian limit. The field equations of GR establish a connection between the distribution of matter and the curvature of spacetime. These equations are formulated under the assumptions of coordinate invariance and their correspondence to Newtonian gravity under weak-field conditions.

The Einstein Field Equations, in four-dimensional tensor form (with indices μ and ν running over the four dimensions of time and space), can be written as:

$$G_{\mu\nu} \equiv R_{\mu\nu} - \frac{1}{2} g_{\mu\nu} R + g_{\mu\nu}\Lambda = \frac{8\pi G}{c^4} T_{\mu\nu} \tag{1.1}$$

Here, G is the gravitational constant and c is the speed of light. $R_{\mu\nu}$ and R are the Ricci tensor and Ricci scalar, respectively, derived from the Riemann curvature tensor. Λ is the cosmological constant, $g_{\mu\nu}$ is the metric tensor, and $T_{\mu\nu}$ is the energy-momentum

tensor. The left-hand side of Eq. (1.1) represents the curvature of spacetime, while the right-hand side describes its contents in terms of mass-energy.

One of the earliest approaches to modelling an expanding Universe with a homogeneous and isotropic distribution of matter and energy is based on the Friedmann-Lemaître-Robertson-Walker (FLRW) metric. This metric provides a form of the spacetime line element consistent with these symmetries. When this metric is substituted into the Einstein Field Equations, one obtains solutions describing the dynamics of the expanding Universe. In spherical coordinates, the FLRW metric is expressed as:

$$ds^2 = g_{\mu\nu}dx^\mu dx^\nu = -c^2dt^2 + a^2(t)\left[\frac{dr^2}{1-kr^2} + r^2(d\theta^2 + \sin^2\theta d\phi^2)\right], \tag{1.2}$$

where $a(t)$ is the scale factor describing the expansion of space, defined to be unity at present ($a(t_0) = 1$). The parameter k can take values of +1, 0, or -1, corresponding to a closed, flat, or open Universe. c is the speed of light, and (r, θ, ϕ) are comoving coordinates, which remain fixed with respect to the expanding space. For convenience, spatial positions can be expressed in comoving coordinates $\vec{x}$ that expand along with the Universe. The physical position $\vec{r}$ is then related to $\vec{x}$ through

$$\vec{r}(t) = a(t)\vec{x}. \tag{1.3}$$

Differentiating this relation with respect to time relates physical velocities to the scale factor. To characterise the change in the scale factor and its relation to the energy content, it is useful to introduce the Hubble parameter, defined as the fractional rate of change of the scale factor:

$$H(t) \equiv \frac{\dot{a}(t)}{a(t)}. \tag{1.4}$$

Its present-day value is referred to as the Hubble constant, $H_0 = H(t_0)$, and $t_0 \sim H_0^{-1}$ provides an approximate estimate of the age of the Universe. Quantities that depend on H_0 are usually expressed by using the dimensionless parameter:

$$h = \frac{H_0}{100\,\mathrm{km\,s^{-1}\,Mpc^{-1}}} \tag{1.5}$$

1.1.2 The Friedmann equations

The evolution of the scale factor $a(t)$ is determined by the energy content of the Universe, as described by the energy-momentum tensor $T_{\mu\nu}$. For a homogeneous and

isotropic Universe filled with a perfect fluid of energy density ρ^2 and pressure p, the Einstein field equations reduce to the Friedmann equations, which govern how the expansion rate depends on the energy density and pressure of the cosmic components [16]. Using the FLRW metric and assuming a perfect fluid description of cosmic matter, these equations can be expressed as

$$\left(\frac{\dot{a}}{a}\right)^2 = \frac{8\pi G}{3}\rho - \frac{kc^2}{a^2} + \frac{\Lambda c^2}{3} \tag{1.6}$$

$$\frac{\ddot{a}}{a} = -\frac{4\pi G}{3}\left(\rho + 3\frac{p}{c^2}\right) + \frac{\Lambda c^2}{3} \tag{1.7}$$

These equations describe how the scale factor $a(t)$ evolves over cosmic time depending on the dominant component of the Universe. In the radiation-dominated era, the scale factor grows as $a(t) \propto t^{1/2}$. During the matter-dominated epoch, $a(t) \propto t^{2/3}$. As the Universe transitions into a dark energy-dominated phase, it begins to undergo accelerated expansion. An exponential expansion ($a(t) \propto e^{Ht}$) represents the asymptotic behaviour of a Λ-dominated Universe, whereas the current epoch is characterised by a competition between matter and dark energy, marking the onset of this acceleration.

Differentiating the first Friedmann equation, Eq. (1.6), with respect to time and applying energy-momentum conservation gives the evolution of the energy density:

$$3\frac{\dot{a}}{a}\left(\rho + \frac{p}{c^2}\right) + \dot{\rho} = 0, \tag{1.8}$$

where $w = p/\rho c^2$ is the equation of state parameter. Integrating this relation gives the scaling of each component with the scale factor:

$$\rho \propto a^{-3(1+w)}, \tag{1.9}$$

with $\rho_m \propto a^{-3}$ for matter ($w_m = 0$), $\rho_r \propto a^{-4}$ for radiation ($w_r = 1/3$), and $\rho_\Lambda =$ constant for cosmological constant ($w_\Lambda = -1$).

Substituting the total energy density $\rho(a) = \rho_m(a) + \rho_r(a) + \rho_\Lambda$ into Eq. (1.6), it is convenient to rewrite the expansion rate in terms of fractional density parameters. To this end, the critical density is defined as:

$$\rho_{\text{crit}}(t) = \frac{3H^2(t)}{8\pi G}. \tag{1.10}$$

The fractional density parameters are defined as the ratio of each energy density component to the critical density,

$$\Omega_i(t) \equiv \frac{\rho_i(t)}{\rho_{\rm crit}(t)}. \tag{1.11}$$

Using the fractional density parameters at the present epoch ($a(t_0) = 1$), the first Friedmann equation can be written as:

$$H^2(a) = H_0^2 \left[\Omega_{r,0} a^{-4} + \Omega_{m,0} a^{-3} + \Omega_{k,0} a^{-2} + \Omega_{\Lambda,0}\right], \tag{1.12}$$

where $\Omega_{r,0}$, $\Omega_{m,0}$, $\Omega_{k,0}$, and $\Omega_{\Lambda,0}$ denote the present-day density parameters for radiation, matter, curvature, and the cosmological constant, respectively. These parameters satisfy

$$1 = \Omega_{r,0} + \Omega_{m,0} + \Omega_{k,0} + \Omega_{\Lambda,0}. \tag{1.13}$$

Redshift

Observed by comoving observers, a photon emitted by a distant galaxy at cosmic time $t_{\rm em}$ experiences an increase in its wavelength as it propagates through the expanding Universe [17, 18]. In observational cosmology, redshift quantifies this stretching, shifting photon wavelengths toward longer wavelengths of the electromagnetic spectrum. The wavelength measured by an observer today, when the scale factor is $a_0 = 1$, is related to the emitted wavelength by:

$$1 + z = \frac{\lambda_{\rm obs}}{\lambda_{\rm em}} = \frac{a(t_{\rm obs})}{a(t_{\rm em})}, \tag{1.14}$$

where $\lambda_{\rm em}$ and $\lambda_{\rm obs}$ denote the emitted and observed wavelengths, respectively, and z is the cosmological redshift. This expression directly connects the observed photon wavelength to the expansion history of the Universe through the scale factor $a(t)$. Using this relation, the expansion rate of the Universe can be expressed in terms of the Hubble parameter as a function of redshift:

$$\frac{H^2(z)}{H_0^2} = \Omega_{m,0}(1+z)^3 + \Omega_{r,0}(1+z)^4 + \Omega_{\Lambda,0} + \Omega_{k,0}(1+z)^2, \tag{1.15}$$

Recent cosmological observations, including measurements of the CMB by the Planck Collaboration, provide precise constraints on these parameters. The best-fit values are $\Omega_{m,0} = 0.315 \pm 0.007$, $\Omega_{r,0} \lesssim 10^{-4}$, $\Omega_{k,0} = 0.001 \pm 0.002$, and $\Omega_{\Lambda,0} =$

0.685 ± 0.007 [4]. These results indicate a Universe that is spatially flat and dominated by dark energy, commonly adopted in modern cosmological simulations.

1.1.3 A brief history of the Universe

The expansion of the Universe is driven by the evolving energy density of its components, where the overall evolution is reflected in the changing scale factor $a(t)$. This history began with the Big Bang approximately 13.8 billion years ago. At its inception, the Universe was extremely hot and dense, allowing for the production of fundamental particles. During Big Bang nucleosynthesis, these particles combined to form protons and neutrons, leading to the creation of light elements such as hydrogen, helium, and trace amounts of lithium, which provided the building blocks for subsequent cosmic structures.

The standard Big Bang model faces challenges, including the horizon and flatness problems, which suggest a high degree of fine-tuning for observed homogeneity and spatial flatness. Cosmic inflation, introduced by Guth in 1981, addresses these issues by proposing a brief period of exponential expansion beginning approximately 10^{-36} seconds after the Big Bang [19]. This phase smoothed out initial inhomogeneities and generated quantum fluctuations that seeded the density perturbations observed in the Cosmic Microwave Background (CMB).

Approximately 380,000 years after the Big Bang, the recombination epoch marked a major thermodynamic transition. As temperatures dropped to $T \sim 3000$K, protons and electrons combined to form neutral hydrogen, rendering the Universe transparent and allowing photons to travel freely as the CMB relic radiation observed today [20]. Following this, the gravitational amplification of density perturbations initiated the collapse of matter during the cosmic dark ages. DM haloes grew hierarchically to serve as the underlying framework for the assembly of galaxies, galaxy clusters, and large-scale structures [13, 21].

Table 1.1: Proportions of the three primary components of the ΛCDM model [4].

Component	**Mass-Energy Proportion (%)**
Baryons	4.9
Cold dark matter	26.8
Dark energy	68.3

The evolution of the Universe is divided into three primary eras defined by the dominant energy component. In the radiation-dominated era, the energy density evolves as $\rho_r \propto a^{-4}$ and the scale factor follows $a(t) \propto t^{1/2}$. During the matter-dominated era, the energy density is described by $\rho_m \propto a^{-3}$ with the scale factor evolving as $a(t) \propto t^{2/3}$. In the current Λ-dominated era, the energy density is constant, and the scale factor grows exponentially as $a(t) \propto \exp(H_0 t)$, which underscores the transition through distinct phases governed by the dominant energy components at different times.

The ΛCDM model stands as the prevailing cosmological paradigm, successfully integrating the Big Bang theory, cosmic inflation, and GR to describe the evolution of our Universe. Its strongest empirical validation emerges from precision measurements of the CMB [4, 22, 23]. This framework fundamentally consists of three primary components: cold dark matter (CDM), comprising non-relativistic particles that interact mainly through gravitational forces; dark energy, represented by the cosmological constant Λ and responsible for the observed late-time cosmic acceleration; and baryonic matter, which forms all visible structures in the Universe. Current measurements from [4] indicate that the total energy density of the Universe is dominated by dark energy, which contributes approximately 68.3%, while CDM accounts for about 26.8% and baryonic matter comprises less than 5%.

1.2 Structure formation

One of the primary objectives of cosmology is to comprehend the structure of the Universe on its largest scales. In particular, in the current model of cosmic structure formation, all observed structures trace their origins back to primordial seed fluctuations. These initial conditions are imprinted in the temperature fluctuations of the CMB, which encode information about the density field at the time of recombination. The subsequent evolution of these fluctuations is governed by gravitational instability, leading to the growth of structures over cosmic time [24].

1.2.1 The gravitational instability theory

The gravitational instability paradigm [24] provides the conceptual foundation for modern structure formation theory. In this picture, the nearly homogeneous early Universe contains small primordial density perturbations that grow under their own gravity while the background expands. Over cosmic time, this gravitational amplification transforms tiny fluctuations into the highly structured cosmic web observed today.

The inhomogeneous matter distribution is described by the density contrast

$$\delta(\mathbf{x}, t) = \frac{\rho(\mathbf{x}, t) - \bar{\rho}(t)}{\bar{\rho}(t)}, \tag{1.16}$$

which measures local departures from the mean matter density $\bar{\rho}(t)$. After matter–radiation equality, and on scales well below the Hubble radius, the dominant matter component can be treated as a pressureless fluid in comoving coordinates. The evolution of structures for a perfect fluid under gravity in the Newtonian limit is described by the continuity, Euler, and Poisson equations [24]:

$$\frac{\partial \delta}{\partial t} + \frac{1}{a}\nabla \cdot \Big[(1+\delta)\mathbf{v}\Big] = 0, \tag{1.17}$$

$$\frac{\partial \mathbf{v}}{\partial t} + \frac{1}{a}(\mathbf{v}\cdot\nabla)\mathbf{v} + H\mathbf{v} = -\frac{1}{a}\nabla\Phi, \tag{1.18}$$

$$\nabla^2\Phi = 4\pi G\bar{\rho}a^2\delta. \tag{1.19}$$

where $\mathbf{v}$ is the peculiar velocity of the fluid, Φ is the Newtonian gravitational potential perturbation, and G is the gravitational constant. These equations make explicit the competition between gravitational attraction and cosmological expansion. The Hubble term acts as a friction term, damping peculiar velocities, which are the velocities of fluid elements relative to the cosmological expansion or, equivalently, to the cosmological rest frame of fundamental observers. Meanwhile, the Poisson equation couples density fluctuations to the gravitational potential that drives gravitational collapse.

DM is essential in this process. Because it is non-relativistic and effectively collisionless after decoupling, CDM can start responding gravitationally before recombination; however, the growth of sub-horizon matter perturbations is strongly suppressed during radiation domination and becomes efficient only after matter-radiation equality. In contrast, before recombination, baryons are tightly coupled to photons and supported by radiation pressure. They therefore cannot collapse efficiently on sub-horizon scales. After recombination, baryons rapidly fall into the gravitational potential wells already seeded by DM. The growth of structure is thus driven primarily by DM, with baryons tracing the evolving DM distribution.

The growth of perturbations is nevertheless regulated by the competition between gravity and pressure support. Early work by Jeans [25] demonstrated that density fluctuations can only collapse if self-gravity overcomes the restoring effects of internal pressure gradients. This introduces a characteristic critical scale, known as the Jeans length, below which perturbations remain pressure-supported and gravitational

collapse is suppressed. The Jeans length is given by

$$\lambda_J = c_s \left(\frac{\pi}{G\rho} \right)^{1/2}, \tag{1.20}$$

where c_s is a sound speed. The associated Jeans mass, corresponding to the mass enclosed within a sphere of radius $\lambda_J/2$, is

$$M_J = \frac{4\pi}{3} \rho \left(\frac{1}{2} \lambda_J \right)^3. \tag{1.21}$$

Perturbations with masses below M_J remain stabilised against collapse by pressure forces, whereas more massive perturbations are gravitationally unstable and can grow over time.

1.2.2 The linear regime

When the density contrast is small ($\delta \ll 1$), the evolution of structure is governed by the competition between gravitational collapse and the expansion of the background Universe. In this regime, linear perturbation theory provides an analytically tractable description of structure growth [24]. By decomposing the spatial density field $\delta(\mathbf{x}, t)$ into Fourier modes $\delta(\mathbf{k}, t)$, the governing fluid equations (1.17)-(1.19) can be linearised.

Assuming pressureless matter ($P \approx 0$), this formalism yields a single second-order differential equation for the growth of perturbations,

$$\ddot{\delta} + 2\frac{\dot{a}}{a}\dot{\delta} - 4\pi G\bar{\rho}\delta = 0, \tag{1.22}$$

where the second term represents the friction due to cosmic expansion. As a linear second-order equation, the general solution is expressed as a linear combination of two independent modes: a growing mode $D_+(t)$ and a decaying mode $D_-(t)$. At the late times relevant for large-scale structure, the decaying mode becomes negligible, allowing the evolution of the density field to be described by decoupling its spatial and temporal components:

$$\delta(\mathbf{x}, t) = D_+(t)\delta(\mathbf{x}, t_0). \tag{1.23}$$

In this regime, where interactions between matter particles are neglected, the matter distribution at any given time is simply the initial distribution scaled by the growth factor $D_+(t)$. The statistical properties of these fluctuations are captured by the matter power spectrum $P(k, t)$. This is related to the primordial power spectrum

$P_0(k)$ generated during inflation via:

$$P(k,t) = P_0(k)T^2(k)D_+^2(t), \tag{1.24}$$

where the transfer function $T(k)$ is defined as

$$T(k) \equiv \frac{\delta(k,t)}{\delta_0(k)D_+(t)}, \tag{1.25}$$

such that it encodes the scale-dependent suppression or enhancement of perturbations relative to the primordial spectrum.

1.2.3 The nonlinear regime

As the amplitude of perturbations approaches unity, non-linear effects become unavoidable. Mode coupling, shell crossing, and eventual virialisation lead to the formation of gravitationally bound haloes. The fully non-linear dynamics are governed by the Vlasov–Poisson system and are studied using cosmological N-body simulations, which successfully reproduce the emergence of the filamentary cosmic web and the statistical properties of DM haloes [1].

Linear perturbation theory provides a robust framework to describe the early growth of density fluctuations. However, as the overdensities grow, the self-gravitational forces become significant, leading to the breakdown of the linear approximation. This transition marks the epoch when structures such as galaxies, galaxy clusters, and the large-scale filaments of the cosmic web begin to form. Understanding this evolution is necessary for accurately modelling the present-day distribution of matter and for interpreting observational surveys. Several analytic and semi-analytic approaches have been developed to bridge the gap between linear theory and fully non-linear numerical N-body simulations.

1.2.3.1 The Zel'dovich approximation

The Zel'dovich approximation, introduced by Yakov Zel'dovich, is the foundational first-order scheme within Lagrangian perturbation theory and remains a significant analytic approach for modelling the early quasi-linear evolution of cosmic structure [26]. The key concept is that the trajectory of each fluid element is tracked from its initial Lagrangian position in the unperturbed density field. This approach provides a natural extension of linear theory by describing the motion of particles based on the initial gravitational displacement field. This framework offers a clear physical picture

of gravitational collapse and the subsequent formation of the first non-linear structures [24, 27].

In the Lagrangian framework, each fluid element is labelled by its initial coordinate $\mathbf{q}$. The proper Eulerian position $\mathbf{r}(t)$ is given by:

$$\mathbf{r}(t) = a(t)\Big[\mathbf{q} + \mathbf{\Psi}(\mathbf{q}, t)\Big], \tag{1.26}$$

where $\mathbf{\Psi}(\mathbf{q}, t) = D(t)\mathbf{s}(\mathbf{q})$ denotes the comoving displacement field. The peculiar velocity simplifies to $\mathbf{v}_{\rm pec}(t) = a(t)\partial\mathbf{\Psi}/\partial t$. The density field follows from the conservation of mass:

$$1 + \delta = \frac{\rho}{\bar{\rho}} = \left|\frac{\partial \mathbf{r}}{\partial \mathbf{q}}\right|^{-1}. \tag{1.27}$$

In this approximation, the density contrast is expressed as:

$$\delta(\vec{\mathbf{x}}, t) = \frac{1}{\prod_{i=1}^{3}\left(1 - D(t)\lambda_i(\mathbf{q})\right)} - 1, \tag{1.28}$$

where λ_i are the eigenvalues of the initial deformation tensor. This demonstrates how anisotropic collapse naturally produces sheet-like 'pancakes', filaments, and nodes. While it breaks down at shell-crossing when the mapping ceases to be single-valued, it remains the standard method for generating initial conditions for N-body simulations [28].

1.2.3.2 Spherical Collapse model

The spherical collapse model describes the evolution of a perfectly symmetric overdense region in an expanding background [29]. Relying on Birkhoff's theorem, the region evolves as an independent closed sub-Universe. For an Einstein-de Sitter Universe, defined as a flat cosmology dominated entirely by matter with $\Omega_m = 1$, the radius $r(t)$ and time t are given by

$$r(\theta) = A\Big(1 - \cos\theta\Big), \tag{1.29}$$

$$t(\theta) = B\Big(\theta - \sin\theta\Big). \tag{1.30}$$

Here, $\theta \in [0, 2\pi]$ is the development angle that serves as a parametric time variable representing the phase of the collapse. The constants are defined as $A = \frac{GM}{2|E|}$ and $B = \frac{GM}{(2|E|)^{3/2}}$ where M is the mass and E is the energy of the shell.

This solution shows that the shell begins its expansion at $r = 0$ with $t = 0$ and $\theta = 0$. Setting $dr/dt = 0$, the shell reaches its maximum radius at the turnaround

time $t_{\rm ta} = \pi B$, corresponding to $\theta = \pi$. Beyond turnaround, the shell recollapses and formally returns to $r = 0$ at the collapse time $t_{\rm col} = 2\pi B = 2t_{\rm ta}$, when $\theta = 2\pi$. In the idealised spherical top-hat model, this collapse to a point of infinite density arises from perfect symmetry and the absence of pressure support or velocity dispersion. In a collisionless system, this singular state is not physically realised. Instead, shell crossing and phase mixing drive violent relaxation, leading to virial equilibrium before formal collapse is reached. In the Einstein-de Sitter case, this corresponds to a characteristic virial radius of approximately half the turnaround radius, $r_{\rm vir} \approx r_{\rm ta}/2$ [24]. Within this framework, the spherical collapse model yields two key quantitative predictions. The critical linear overdensity at the epoch of formal collapse is $\delta_c \approx 1.686$, a value that is only weakly dependent on cosmology and is widely used as a collapse threshold in analytic structure formation models. The mean interior overdensity at virialisation, relative to the critical density of the Universe at that time, is $\Delta_{\rm vir} \simeq 178$ in the Einstein-de Sitter model [24].

These thresholds underpin the hierarchical bottom-up scenario of ΛCDM, where small-scale fluctuations collapse first to form the lowest-mass DM structures [30]. The assembly history is a consequence of the initial Gaussian density fluctuations established during inflation and constrained by the CMB [4]. The differential growth rate ensures that smaller perturbations cross δ_c earlier than larger ones. This is quantified by the halo mass function and excursion set theory [31, 32], which relates the linear density field to the number density of haloes, successfully modelling the abundance of systems across cosmic time.

1.3 The Cosmic Web

The large-scale distribution of galaxies is not a stochastic arrangement but a sophisticated, interconnected scaffold known as the cosmic web [14]. This network represents the most prominent manifestation of non-linear structure formation in the Universe, bridging the gap between the primordial, Gaussian density fluctuations observed in the CMB and the highly non-linear, virialised clusters of the present epoch. On scales ranging from a few to over a hundred megaparsecs, the cosmic web fills the observable volume with a hierarchical, foam-like architecture defined by its four morphological constituents: nodes, filaments, walls, and voids [33, 34]. Fig. 1.1 provides a visual illustration of the large-scale structure as represented in DM-only Millennium simulation [1].

The emergence of this structure is fundamentally driven by the anisotropic nature of gravitational collapse. According to the Zel'dovich approximation, the initial tidal shear and velocity fields dictate a sequential collapse along the principal axes of the

deformation tensor [26]. Formally, this is described by the eigenvalues $\lambda_1, \lambda_2, \lambda_3$ of the gravitational tidal tensor. It is important to note, that the physical interpretation of these eigenvalues depends sensitively on the precise formulation adopted, whether one works with the tidal tensor itself, the velocity-shear tensor, or a density-field Hessian. Different sign conventions and threshold criteria apply [see, e.g., 7, 8]. The eigenvalue discussion presented here is therefore intended to provide an intuitive geometric picture of anisotropic collapse rather than to serve as a strict operational basis for environmental classification. Within this picture, the number of axes along which matter undergoes net contraction increases monotonically as structures evolve from the linear to the non-linear regime. Collapse along a single principal axis produces flattened sheet-like walls. Subsequent contraction along a second axis generates elongated filaments. The final collapse along the third axis leads to the formation of compact virialised nodes. This hierarchical sequence, from expanding voids through walls and filaments to dense cluster nodes, describes the large-scale dynamical flow of matter that constitutes the cosmic web and establishes the environmental history experienced by galaxies residing within each of its constituent structures.

Nodes

Nodes represent the most dynamically advanced and gravitationally bound components of the cosmic web, forming at the intersections of multiple filaments where matter has undergone a near-spherical, three-dimensional collapse. Mathematically, these regions correspond to local volumes where all three eigenvalues of the tidal tensor are positive, indicating compression along all principal axes [7]. These regions host the most massive virialised structures in the Universe, primarily large-scale DM concentrations that act as the potential wells for galaxy clusters [14]. These clusters often exceed $10^{14} M_\odot$ and are the most recently collapsed objects in the cosmic hierarchy. Prominent local examples of such virialised nodes include the Coma, Virgo, and Perseus clusters, which were first highlighted as central components of the cosmic network in early mapping surveys [35].

Node environments are dynamically dense and strongly processed: baryonic matter is shock-heated to X-ray-emitting temperatures (10^7-10^8 K) and forms the intracluster medium in a state of near-hydrostatic equilibrium [36]. Within these massive gravitationally bound systems, a significant population of smaller satellite structures exists. These represent DM concentrations that have been accreted along filaments. Because these nodes are virialised, galaxies are accelerated by the deep gravitational potential and reach high velocity dispersions as they orbit within the gravitational well of the cluster. Consequently, galaxies within these satellite structures undergo

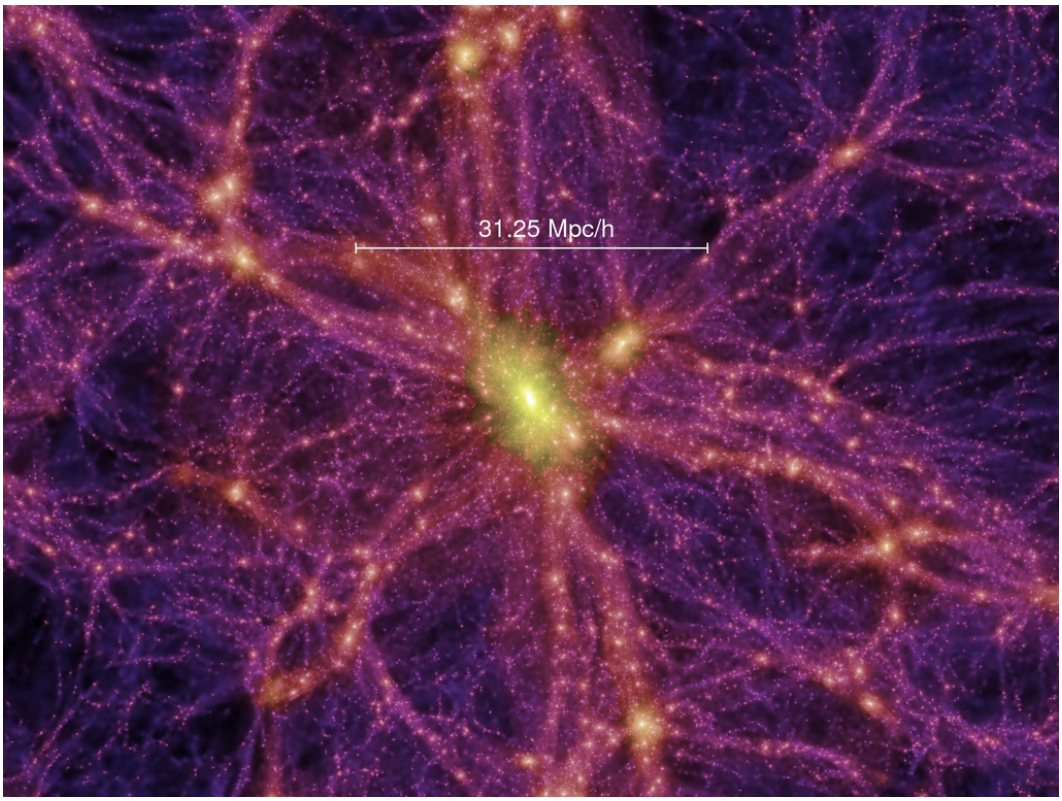

Figure 1.1: Dark matter cosmic web structure from the Millennium Simulation [1], showing a $15h^{-1}$Mpc thick slice of the density field at $z = 0$. *Image credit: https://wwwmpa.mpa-garching.mpg.de/galform/virgo/millennium.*

intense environmental preprocessing [37, 38]. Mechanisms such as ram-pressure stripping and tidal disruption lead to the rapid quenching of star formation [29]. When combined with frequent gravitational interactions and mergers, these processes provide the necessary dynamical transformations to convert star-forming spirals into the red and quiescent ellipticals that dominate cluster cores, driving the observed morphology-density relation [39, 40].

Filaments

Filaments are elongated, tube-like structures that connect nodes and act as preferential channels for matter accretion within the cosmic web. They represent regions that have collapsed along two principal axes while remaining extended along the third, typically identified by two positive eigenvalues in the tidal deformation tensor. While filaments occupy only approximately 6% of the cosmic volume, they are estimated to contain roughly half of the total mass of the Universe [41]. These

structures act as cosmic highways, channelling matter and DM haloes into the deeper potential wells of the nodes. As smaller haloes migrate along these filaments, they often merge to form the central haloes of clusters or survive as part of the satellite population.

Filaments are of particular interest in the context of the missing baryon problem, which describes the observed deficit of baryonic matter in the local Universe compared to the abundances predicted by early-universe cosmology. Hydrodynamical simulations suggest that a significant fraction of these baryons reside within filaments in the form of the Warm-Hot Intergalactic Medium [42, 43]. This diffuse plasma exists at temperatures between 10^5 and 10^7 K and remains difficult to observe directly due to its low density. In the hierarchical model of structure formation, filaments serve as the fundamental reservoirs from which nodes accrete their mass. The continuous inflow of gas and smaller systems along these structures creates a unique intermediate environment where the local density is significantly higher than the cosmic mean but remains below the virialised density of cluster cores [44–46]. This environment facilitates a complex interplay of evolutionary mechanisms, where galaxies may undergo preprocessing through star formation suppression and morphological transformation or experience cosmic web enhancement via the accretion of multiphase filamentary gas [47–49].

Walls

Walls or sheets are flattened two-dimensional structures that enclose the large underdense regions of the Universe. They are the result of gravitational collapse along only a single principal axis corresponding to one positive eigenvalue in the tidal deformation tensor. This makes them dynamically the youngest overdense structures in the cosmic web. Within the framework of the Zel'dovich approximation, walls represent the first non-linear structures to form through the fragmentation of primordial pancakes [26]. While visually less prominent than filaments due to their lower galaxy densities, walls can form immense configurations on the largest scales, such as the BOSS Great Wall and the Sloan Great Wall [50–52].

Walls are characterised by highly anisotropic velocity fields and primarily host low-mass DM haloes. These structures serve as the interface between the expanding voids and the collapsing filamentary network, acting as the primary membranes that prevent the total merger of underdense regions [41]. Because environmental processing is minimal in these regions compared to clusters or filaments, walls provide a pristine laboratory for studying galaxy evolution within DM haloes that have not yet been subjected to violent mergers or cluster-scale tidal forces [53]. They represent the

final stage of large-scale gravitational collapse before matter is channelled into the filamentary network, making them crucial for understanding the transition of galaxies from the field into the high-density web [46, 54].

Voids

Voids are the largest and most underdense components of the cosmic web, representing regions of three-dimensional expansion. Mathematically, these regions are defined by three negative eigenvalues of the tidal deformation tensor, indicating that matter is flowing away from the centre along all axes. These regions occupy the vast majority of the cosmic volume, with estimates ranging from 60% to 80% while containing only about 10% to 20% of the total mass [41]. Voids expand faster than the background Universe due to the self-depletion of matter, leading to a characteristic density contrast of $\delta < -0.8$ [55, 56].

From a cosmological perspective, voids are clean laboratories because they are minimally contaminated by non-linear baryonic physics. The DM haloes found within voids are typically isolated and low-mass, having experienced minimal tidal interference. These void haloes host pristine star-forming galaxies that provide a unique sample for testing the baseline of galaxy evolution models [57, 58]. Furthermore, the shapes and abundance of voids are direct reflections of dark energy and DM parameters, offering unique opportunities to test modified gravity theories and the properties of the cosmological constant Λ [59, 60].

1.4 Dark matter

Over the past century, a robust body of evidence derived from astrophysical and cosmological observations has established that the luminous, baryonic matter constitutes only a minority fraction ($\sim 15\%$) of the total matter content of the Universe. The existence of an unseen mass component, DM, is an inescapable requirement to reconcile gravitational theory (GR) with observation across all spatial scales. This necessity dates back to Fritz Zwicky's 1933 dynamical measurements of galaxy velocities in the Coma cluster, where he applied the virial theorem to demonstrate the need for unseen mass [61].

This finding was subsequently corroborated and strengthened by multiple independent lines of evidence. These include the flat rotation curves of spiral galaxies [62]; the precise quantification of gravitational lensing effects in both strong and weak regimes [63]; and the study of colliding galaxy clusters, such as the Bullet Cluster, which reveal a spatial separation between the dominant gravitating mass component (inferred

from lensing) and the hot X-ray emitting baryonic gas [64]. These systems provide some of the most direct astrophysical constraints on the non-baryonic nature of DM and place strong limits on possible self-interaction cross-sections, although they do not in themselves uniquely determine the microphysical properties of DM. The combined evidence from the CMB and large-scale structure analysis confirms that DM accounts for approximately 85% of the total matter density of the Universe, $\Omega_{\rm DM}h^2 \approx 0.12$.

1.4.1 The nature of dark matter

Within the context of the ΛCDM model, DM must satisfy several stringent particle and cosmological properties. It must be non-baryonic, a constraint confirmed by the precise consistency between Big Bang Nucleosynthesis (BBN) predictions and the observed light element abundances, which tightly limit the total density of ordinary matter to $\Omega_b h^2 \approx 0.022$ [65]. Secondly, DM must be electrically neutral, consistent with its inability to interact electromagnetically.

Critically, the success of the hierarchical structure formation model requires that DM be CDM, meaning that its constituent particles were non-relativistic ($v \ll c$) during the critical epoch of structure formation ($z \sim 1000$). This cold property suppresses the particle free-streaming length of DM particles. It preserves density fluctuations down to sub-galactic scales essential for the bottom-up assembly of structures. As a reference framework for structure formation, CDM is effectively collisionless, in the sense that DM particles interact negligibly with one another except through gravity. Any possible non-gravitational self-interactions are therefore constrained observationally, and are typically expressed as an upper bound on the self-interaction cross-section per unit DM particle mass, σ/m_χ, where m_χ denotes the DM particle mass:

$$\frac{\sigma}{m_\chi} \lesssim 1 \text{ cm}^2\text{g}^{-1}. \tag{1.31}$$

Furthermore, CDM is stable on cosmological timescales, allowing structures to persist once formed. The hypothetical canonical particle candidate for CDM remains the Weakly Interacting Massive Particle (WIMP), a stable particle with mass typically in the GeV to TeV range, whose interaction strength is mediated by the weak nuclear force and gravity [66]. While its thermal relic density from the early Universe elegantly yields the observed DM density today via the classic "WIMP miracle", this minimal paradigm faces increasing experimental pressure. In the absence of definitive signals across collider, direct or indirect detection channels, attention has shifted toward more general frameworks, including non-minimal dark sectors, loop-suppressed interactions, and scenarios extending to sub-GeV to multi-TeV mass scales [67, 68].

1.4.2 Dark matter searches

The minimal interaction cross-section of DM presents a profound experimental challenge necessitating a multi-pronged search strategy spanning particle colliders, deep underground laboratories and astronomical observations. Searches focus on three distinct experimental approaches.

Direct detection

Direct detection experiments aim to measure the minute kinetic energy transferred to an atomic nucleus or electron from an elastic scattering or conversion interaction with a galactic DM particle [69, 70]. Observations of nearby stellar velocities indicate that the solar neighbourhood resides in a DM background with a local mass density in the range of $\rho_\chi \approx 0.3 - 0.5$ GeV/cm^3 moving at virial speeds of $v \approx 10^{-3}c$ [71–74]. Because the expected interaction rate is extremely low, these detectors are located in deep underground laboratories like Gran Sasso or SNOLAB to mitigate cosmic ray backgrounds. Early efforts by collaborations such as CDMS, XENON10 and DAMA established the initial boundaries of the WIMP parameter space, including the controversial annual modulation signal attributed to the Earth's motion through the DM halo [75, 76]. State-of-the-art experiments like XENONnT and LUX-ZEPLIN (LZ) now use dual-phase Time Projection Chambers to push the sensitivity limits for spin-independent scattering cross-sections to unprecedented levels [77].

Indirect detection

Indirect detection searches focus on identifying stable high-energy Standard Model particles created as byproducts when DM particles self-annihilate or decay in high-density regions of the cosmos [78, 79]. These products include gamma rays, anti-protons, positrons and neutrinos, which are measured by space based instruments like the Fermi Large Area Telescope and AMS-02 or ground based telescopes like IceCube, H.E.S.S. and MAGIC [80–83]. The predicted flux of these annihilation products depends on both the particle physics properties and the cosmological distribution of DM in astrophysical targets. In particular, because the annihilation rate scales with the square of the local DM density, ρ^2, small-scale inhomogeneities and unresolved substructure within haloes can significantly enhance the expected signal compared to that of a smooth halo. This enhancement is commonly referred to as a substructure boost factor and reflects the contribution of dense subhaloes and clumps to the total annihilation luminosity [84–88]. Distinguishing this subtle DM signal from

intense astrophysical backgrounds requires detailed modelling of foreground cosmic ray sources and the hierarchical structural properties of the DM distribution [89, 90].

Collider searches

Collider searches primarily conducted at the LHC aim to produce DM particles in high energy proton proton collisions, providing a complementary probe that avoids the kinematic barriers faced by terrestrial detectors at low masses [91]. Because DM particles escape without interacting with the detector, they leave a signature of missing transverse energy (E_T^{miss}) representing a momentum imbalance perpendicular to the beam axis. These searches rely on the production of a visible Standard Model partner, such as a jet or photon, to provide a measurable recoil in what are known as monojet or monophoton signatures [92]. To interpret these results, researchers employ both UV-complete theories like Supersymmetry and simplified models that focus on a limited set of essential interaction ingredients [93, 94]. This approach allows for a broad characterisation of DM candidates, including exotic signals like long lived particles and lepton jets, ensuring a comprehensive exploration of the dark sector.

1.4.3 Dark matter haloes

DM haloes are the fundamental self-gravitating structures that emerge from the non-linear growth of primordial density fluctuations. In the ΛCDM paradigm, every observed galaxy resides within a DM halo whose gravitational potential well regulates gas accretion and star formation and satellite dynamics. Halo formation begins after a density perturbation grows sufficiently large ($\delta \approx 1$) and enters the non-linear regime. This process is often modelled through the spherical collapse approximation, which follows the evolution of a spherical overdensity in an expanding universe. As the perturbation decouples from the Hubble flow it reaches a maximum turnaround radius before undergoing gravitational collapse. Linear theory predicts that regions with a linearly extrapolated density field of $\delta \geq \delta_c = 1.69$ have undergone this collapse. Application of the virial theorem shows that these systems eventually reach dynamical equilibrium or virialisation at a mean overdensity Δ_{vir}. In the spherical collapse approximation, virialisation occurs when the system reaches dynamical equilibrium, typically characterised by a mean overdensity of order $\Delta_{\text{vir}} \approx 200$ relative to the critical density. The corresponding virial mass and radius are defined through

$$M_{\text{vir}} = \frac{4\pi}{3}\Delta_{\text{vir}}\rho_{\text{crit}}(z)R_{\text{vir}}^3. \tag{1.32}$$

The abundance of these haloes is described statistically by the Press-Schechter mass function, which relates the number density of haloes to the initial Gaussian density field. This was later expanded into the Extended Press-Schechter theory using excursion set formalism to describe the conditional mass function. This provides the mathematical framework for Monte Carlo algorithms that generate halo mass accretion histories, which show that halo growth proceeds hierarchically. This hierarchical growth can be visualised using merger trees, which trace the formation history of haloes through successive accretion and merger events. A schematic of this process is shown in Fig. 1.2, illustrating that halo growth proceeds through the hierarchical assembly of smaller progenitor systems. These progenitors may persist as bound substructures within the host halo over cosmological timescales.

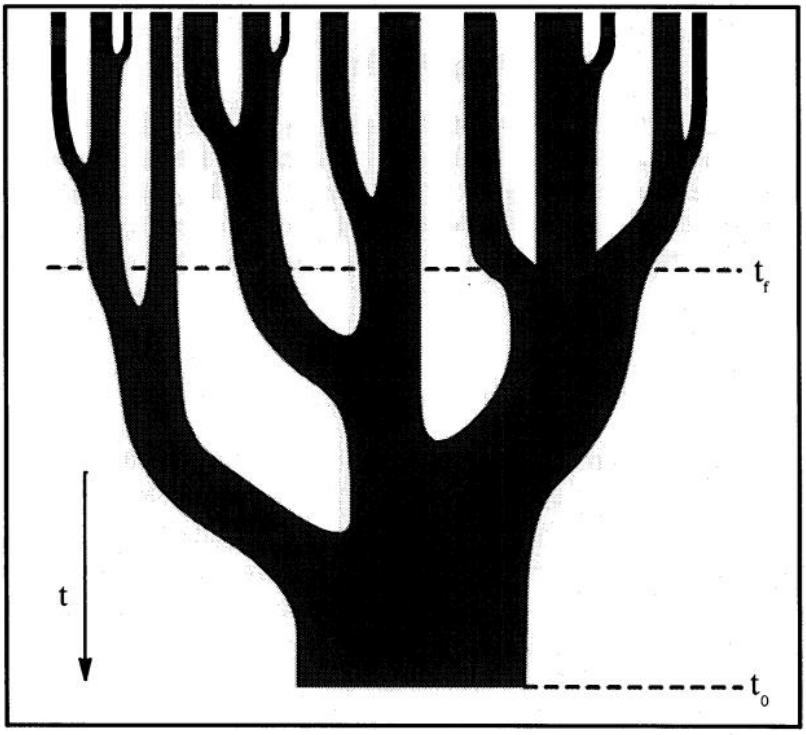

Figure 1.2: Schematic merger tree illustrating hierarchical halo assembly through successive mergers and accretion events, adapted from [2].

Cosmological N-body simulations have revealed that relaxed haloes exhibit nearly universal internal density profiles over many orders of magnitude in mass. The Navarro–Frenk–White (NFW) profile [15] is the most well known description of this structure and is given by

$$\rho_{\rm NFW}(r) = \frac{\rho_s}{\left(\frac{r}{r_s}\right)\left(1+\frac{r}{r_s}\right)^2}, \tag{1.33}$$

where r_s is a characteristic scale radius and ρ_s a corresponding density scale. Although the Einasto profile was first used to describe star counts in the Milky Way [95], it has since been argued to be a better description of cosmological profiles than the NFW form [96–98]. The Einasto profile allows for a continuously varying logarithmic slope

$$\rho_{\rm Einasto}(r) = \rho_s \exp\left[-\frac{2}{\alpha}\left(\left(\frac{r}{r_s}\right)^{\alpha} - 1\right)\right], \tag{1.34}$$

where $\alpha \sim$ 0.16-0.3 controls the curvature. Unlike the NFW profile, the Einasto profile does not have a strict central power-law cusp but instead exhibits a gradually steepening inner slope. A key structural parameter is the concentration

$$c \equiv \frac{R_{\rm vir}}{r_s}, \tag{1.35}$$

which encodes information about the halo assembly history. Lower mass haloes are typically more concentrated because they collapse earlier when the mean cosmic density is higher.

Overall halo growth is an anisotropic process where early rapid accretion phases are dominated by mergers and violent relaxation [14, 99]. Mergers are classified as minor or major based on the mass ratio of the two merging systems where a mass ratio of 1 : 3 or 1 : 4 is often used as a boundary [100]. In minor mergers, a smaller system falls into a larger host and evolves mainly through dynamical friction and tidal stripping [101, 102]. Dynamical friction occurs as the subhalo travels through the background particles of the host and creates a wake that causes the orbit to decay toward the centre [103]. Tidal stripping occurs because the subhalo exists in a non-uniform potential, which removes material from the subhalo and incorporates it into the host [104]. Eventually, the smaller system may become completely disrupted. In comparison, major mergers involve haloes of similar sizes, so both merging systems are significantly disrupted and undergo strong non-linear relaxation [105]. Major mergers are primary determinants of halo 3D shape, which is typically triaxial rather than spherical [106].

Halo mass assembly is strongly influenced by anisotropic accretion along filaments [14]. This directional inflow provides the physical link between halo growth and the surrounding large-scale structure, implying that halo properties such as spin, shape, and assembly history are expected to be environmentally dependent. In particular, the filamentary nature of mass accretion naturally introduces a preferred direction in the local tidal field, making halo angular momentum and orientation sensitive to

the geometry of the cosmic web. A substantial body of numerical work based on gravity-only simulations has confirmed this connection. Halo properties including abundance, formation time, concentration, and internal structure are found to vary systematically with the surrounding density field, reflecting the imprint of anisotropic mass accretion within the cosmic web [107–110]. In particular, haloes in filamentary and node like environments tend to assemble earlier and exhibit higher concentrations than those in underdense regions. In addition, coherent alignments between halo spin and the local tidal field indicate a coupling between halo dynamics and cosmic web geometry [7, 111, 112]. These trends become increasingly strong toward lower mass haloes, reflecting the growing importance of the environment on small scales.

1.4.4 Halo substructures

A fundamental prediction of hierarchical structure formation in a CDM Universe is that virialised haloes are not smooth objects but contain a wealth of bound substructure [30, 113]. This follows directly from the bottom-up nature of gravitational collapse in CDM cosmologies, where small-scale perturbations collapse first and are subsequently incorporated into progressively larger systems through mergers and accretion [31]. As a result, every massive halo is expected to possess a population of self-bound remnants of its formation history, commonly referred to as subhaloes.

In this picture, when a smaller halo crosses the virial radius of a more massive system, it ceases to evolve as an isolated object and becomes a subhalo embedded in the host potential. Its subsequent evolution is governed by tidal forces, dynamical friction, and repeated impulsive heating during pericentric passages [101, 102]. Despite strong environmental effects, the dense inner regions of many infalling haloes survive, leading to a long lived population of bound substructures [104, 114].

This hierarchical picture is strongly supported by high-resolution N-body simulations such as *Via Lactea*, *Aquarius*, *ELVIS*, *COCO*, *Millennium*, and *Cosmogrid* [1, 6, 84, 115–118]. These simulations consistently show that CDM haloes exhibit self similar substructure across a wide dynamic range. The subhalo hierarchy extends from the host virial mass down to a fundamental cutoff scale set by the microphysical properties of the DM particle. For thermal WIMP candidates, the smallest scale of structure is determined by kinetic decoupling and free-streaming effects. This leads to a cutoff in the matter power spectrum corresponding to a minimum halo mass typically in the range 10^{-12} to $10^{-4} M_{\odot}$, depending on the particle physics model and the kinetic decoupling temperature [119]. Below this scale, perturbations are erased, suppressing further halo formation.

The resulting subhalo population is well described by a nearly scale-invariant mass function,

$$\frac{dN}{dm} = Am^{\alpha}, \tag{1.36}$$

with α found to lie in the range -1.8 to -2.0, as measured in simulations across halo masses and cosmological environments. The condition $\alpha > -2$ implies that the total mass in substructure is dominated by the most massive subhaloes, while the number count is dominated by low-mass objects. Typically, 5% to 15% of a host halo's virial mass is bound in resolved substructure, although this fraction increases in cluster-sized haloes due to their later formation time and reduced cumulative tidal processing [120, 121].

The internal structure and evolution of subhaloes are shaped by several competing dynamical processes. Tidal stripping removes material beyond the tidal radius,

$$r_t \approx R \left(\frac{m}{3M(< R)} \right)^{1/3}, \tag{1.37}$$

where R is the distance from the host centre and $M(< R)$ is the enclosed host mass. This process gradually truncates the outer density profile and reduces the bound mass, while leaving the central regions relatively intact due to their high phase-space density. In addition to stripping, subhaloes are subject to tidal shocking during rapid variations of the host gravitational field, particularly at pericentre, which can heat and further disrupt loosely bound material.

More massive subhaloes experience dynamical friction, arising from the gravitational wake induced in the background DM distribution. This leads to orbital decay and eventual merger with the central halo. Together, these processes produce a strong radial dependence in the surviving subhalo population, with older subhaloes preferentially residing in the inner regions and recently accreted systems dominating the outskirts. From a statistical perspective, subhaloes are therefore not uniformly distributed but exhibit both mass and spatial biases determined by their accretion history and dynamical evolution.

One of the most important implications of substructure is its impact on indirect DM detection. For annihilating DM, the expected signal scales as ρ^2, so dense subhaloes can enhance the luminosity relative to a smooth host halo [122, 123]. This enhancement is usually described by a substructure boost factor. Decaying DM follows a different scaling, proportional to ρ, and is therefore much less sensitive to unresolved clumpiness. The total annihilation luminosity of a halo can be written as

$$L_{\rm total} = L_{\rm smooth} + \int_{m_{\rm min}}^{M} \frac{dN}{dm} L_{\rm sh}(m) dm, \tag{1.38}$$

where $L_{\rm sh}(m)$ depends sensitively on the internal concentration and density profile of each subhalo. The resulting boost factor,

$$1 + \mathcal{B}(M) = \frac{L_{\rm total}}{L_{\rm smooth}}, \tag{1.39}$$

is therefore highly sensitive to the unresolved low-mass structure and the extrapolation of the concentration–mass relation. Depending on these assumptions, predicted boost factors for Milky-Way-sized haloes range from order unity to values exceeding on the order of 100 [85, 86, 123, 124].

1.4.4.1 Small-scale challenges of ΛCDM

Despite the success of CDM on large-scales, several persistent challenges exist at sub-galactic scales. Cosmological DM-only simulations have been very successful in predicting the observable structures on scales $>$ 1 Mpc in an expanding Universe that is dominated by a cosmological constant at late times. On scales concerning the low-mass end of the galaxy population, however, the ΛCDM model has historically faced claims of tension with observations. It is important to note that several of these challenges have been substantially alleviated or effectively resolved by more realistic modelling, and they should not be regarded as equally open failures of the framework. These discrepancies serve as a primary motivation for the high-resolution modelling of subhalo dynamics [125, 126]. The most relevant challenges are the *missing satellites problem* [127–129], the *cusp-core tension* [130, 131], and the *too-big-to-fail problem* [132].

The missing satellite problem

The Missing Satellites problem highlights the apparent mismatch between the large number of low-mass subhaloes predicted by high-resolution ΛCDM simulations and the smaller population of observed dwarf galaxies in the Milky Way system [129, 133]. Simulations predict a subhalo mass function that continues as a steep power law toward the low masses [84, 134]. This historical challenge is now largely considered as alleviated within the ΛCDM framework. Successively deeper observational surveys have revealed a growing population of ultra-faint satellite galaxies, and corrections for survey incompleteness, limited sky coverage, and surface-brightness selection effects bring the observed satellite count into substantially better agreement with predictions

[135]. Rather than indicating a fundamental failure of the ΛCDM model, this discrepancy is generally interpreted as a consequence of galaxy formation inefficiency in low-mass haloes. Star formation is strongly suppressed in shallow potential wells due to baryonic feedback processes. In particular, photoheating during cosmic reionization limits gas accretion into low-mass systems. In addition, inefficient gas cooling below the atomic cooling threshold at $M_{\rm vir} \sim 10^8$-$10^9 M_\odot$ further reduces the likelihood of star formation [136]. As a result, a large fraction of low-mass subhaloes are expected to remain entirely dark and host no observable stellar component. Reframed in terms of the galaxy-halo occupation relation and realistic stellar-to-halo mass assignments, the satellite number counts predicted by ΛCDM are consistent with observations, making this a problem of galaxy formation physics rather than a structural failure of the DM model.

The too-big-to-fail problem

The too-big-to-fail problem refers to the finding that the most massive subhaloes of simulated Milky Way-sized systems, identified in DM-only runs such as Aquarius and Via Lactea II, are systematically denser in their inner regions than inferred from the stellar kinematics of the classical dwarf spheroidal satellites [132, 137]. Because these massive subhaloes should be too large to have their star formation entirely suppressed by reionisation, they were expected to host luminous galaxies, yet no kinematic counterparts were observed [84, 115]. The problem was subsequently identified not only in the Milky Way but also in Andromeda and among isolated field dwarfs in the Local Group [138]. However, the severity of this tension has been substantially reduced once baryonic physics is included self-consistently. Hydrodynamical simulations demonstrate that supernova feedback, tidal stripping of infalling satellites, and the response of the DM halo to baryonic mass loss can significantly lower the central densities of massive subhaloes, bringing their predicted kinematics into much closer agreement with observations [139]. Additional uncertainty in the total mass of the Milky Way halo also affects the expected number and density of massive subhaloes, further relaxing the original tension. The too-big-to-fail problem is therefore not regarded as a robust failure of ΛCDM when baryonic effects and observational uncertainties are treated consistently, though questions about the diversity and normalisation of dwarf-galaxy inner density profiles in a broader context remain relevant.

The cusp-core problem

The cusp-core problem refers to the discrepancy between the steep inner density profiles predicted in collisionless CDM simulations, which generically follow $\rho \propto r^{-1}$ at small radii [15, 140], and the approximately constant-density cores inferred from dwarf galaxy rotation curves and stellar kinematics [141]. Such cuspy profiles arise as a generic outcome of hierarchical collapse and violent relaxation in numerical simulations, whereas observationally motivated mass models for low-mass galaxies often favour shallower inner slopes. A closely related and arguably more challenging aspect is the *diversity problem*: observed rotation curves of galaxies with similar halo masses span a wide range of inner profile shapes, from steeply rising to nearly solid-body, a variety that standard ΛCDM simulations struggle to reproduce [142]. While baryonic processes, including supernova-driven gas outflows, repeated cycles of gas inflow and expulsion, and early suppression of star formation through reionisation, can reduce central densities in gas-rich, actively star-forming dwarfs, these mechanisms appear insufficient in gas-poor dwarf spheroidals where star formation has long ceased [143]. The cusp-core tension and the associated diversity of inner profiles therefore remain the most active and unresolved small-scale challenge to the ΛCDM framework, motivating both more detailed baryonic modelling and investigation of alternative DM models, including self-interacting and fuzzy DM, that modify halo structure on small scales.

1.4.4.2 Alternative Dark Matter Paradigms

Warm Dark Matter (WDM) introduces a non-negligible thermal velocity dispersion, leading to free-streaming that suppresses structure formation below a characteristic mass scale. Unlike CDM, where power exists down to Earth-mass scales, WDM particles decouple while still relativistic, erasing small-scale density perturbations. This results in a sharp cutoff in the matter power spectrum at a half-mode mass scale, which can alleviate the abundance of low-mass subhaloes, subject to observational constraints. Current Lyman-α forest constraints require thermal relic masses of $m_\chi \gtrsim 3.5$ to 5.3 keV [144, 145], pushing the suppression scale to increasingly smaller masses.

Self-Interacting Dark Matter (SIDM) introduces elastic scattering between DM particles with cross sections $\sigma/m \sim 0.1$ to 10 cm^2/g, enabling energy exchange in high-density regions. In the dense centres of haloes, frequent collisions facilitate heat transfer from the hotter outer regions to the cooler core. This thermalisation process lowers the central density and naturally produces cored density profiles, offering a potential solution to the cusp-core and too-big-to-fail problems without requiring extreme baryonic feedback [146, 147].

Fuzzy Dark Matter (FDM), composed of ultra-light bosons with masses of $m \sim 10^{-22}$ eV, generates a macroscopic quantum pressure that suppresses small-scale structure. At these mass scales, the de Broglie wavelength of the particle becomes comparable to kiloparsec scales, preventing collapse into structures smaller than the wavelength. This wave-like nature leads to stable, solitonic cores embedded in extended haloes, providing a distinct signature from the NFW profiles of CDM and effectively smoothing out the central density field [148, 149].

Ultimately, the abundance, internal structure, and survival of subhaloes provide a sensitive probe of both the microphysical properties of DM and the interplay between dark and baryonic physics. Disentangling these effects remains one of the central challenges in modern cosmology, and the detailed study of subhalo populations offers a direct observational window into the physics of the dark sector [150].

1.5 An Overview of This Thesis

This section provides an overview of the structure of the thesis and the main content of each chapter.

This thesis is guided by three central research questions: (i) Does the cosmic web environment systematically affect subhalo abundance and internal structural properties at fixed host halo mass? (ii) Do these environmental dependencies propagate into predictions for substructure-induced signals such as DM annihilation boost factors? (iii) Are the observed environmental trends primarily imprinted at the time of infall, or do they emerge predominantly through subsequent dynamical evolution within the host halo?

The analysis presented in this thesis is based on numerical simulations combined with the application of morphological classification algorithms. This allows us to study how the large-scale environment, composed of nodes, filaments, walls, and voids influences the distribution and internal properties of DM subhaloes.

The methodological foundation of the thesis is the classification of halo and subhalo populations by their cosmic web environment within high-resolution cosmological simulations. This part is discussed in Chapter 2. Cosmological simulations are the primary tools used to understand the non-linear regime of structure formation. While the general properties of DM haloes are well documented, the relationship between a halo and its cosmic web environment requires sophisticated numerical treatments. Chapter 2 provides an overview of the methods used to quantify these environmental effects. This includes a description of the COpernicus COmplexio LOw Resolution (COLOR) simulation, which provides the high-resolution data necessary for the study of subgalactic structures. This chapter also details the implementation of the `CaCTus`

algorithm, an adaptation of the NEXUS+ framework used to segment the cosmic web and define the tidal environments used throughout the analysis.

The second objective is the quantification of the dependence of subhalo populations and DM annihilation signals on the hosting environment. This part is discussed in Chapters 3, 4, and 5. Advancements in cosmological simulations demonstrate that DM halo properties have an intricate relationship with their assembly histories and the environments that host them. Such dependencies can introduce systematic effects in the interpretation of subhalo statistics, satellite populations, and indirect-detection predictions, and should therefore be quantified before substructure models are used as environment-independent inputs. This analysis is essential for understanding environmental differences in the assembly of DM systems and their consequences for indirect-detection signals.

Chapter 3 is based on a published peer-reviewed article, while Chapter 4 is based on a manuscript currently under peer review. Both works are co-authored and were developed within collaborative projects. A detailed description of my individual contributions to these works is provided in Sections 3.2 and 4.2, respectively.

In Chapter 3, the focus is on identifying environmental effects on subhalo abundance and internal density profiles. Using data from the high-resolution COLOR simulation, the study investigates how the placement of a host halo within the cosmic web affects its sub-galactic population. The research examines variations in the subhalo mass function and internal kinematic properties across different environmental classifications. This analysis seeks to determine if host location in the large-scale cosmic web introduces systematic shifts in internal subhalo properties and population statistics, which are crucial for the unbiased interpretation of observations related to satellite galaxies.

Building on these foundations, Chapter 4 investigates the environmental impact on subhalo boosts to DM annihilation signals. This part of the work extends standard semi-analytic frameworks by incorporating environment-dependent variables for host halo concentrations, subhalo mass functions, and internal subhalo properties. The primary goal is to develop an environment-aware prescription for subhalo boosts that can be employed in indirect detection forecasts and related halo population modelling applications.

In Chapter 5, the role of the environment in shaping subhalo properties is extended beyond the present-day analysis presented in Chapters 3 and 4. In particular, this chapter investigates whether the environmental trends observed at $z = 0$ are already established prior to infall, arise during the process of accretion into the host halo, or develop later through tidal evolution and survival bias within the host environment. By tracking the evolution of subhaloes across simulation snapshots, the study reconstructs their past trajectories and properties from infall to the present day. This enables a

quantitative assessment of environmental pre-processing in the cosmic web and clarifies the origin of the observed present-day environmental dependencies in substructure populations.

Finally, Chapter 6 summarises the research findings regarding the role of the environment in structure formation. This concluding chapter discusses the implications of the results within the broader context of the ΛCDM paradigm and outlines avenues for future work with a focus on the application of environmental data to the next generation of cosmological surveys.

The analysis presented in this thesis is based on collisionless cosmological N-body simulations combined with cosmic web classification methods. As such, it does not include baryonic physics, detailed galaxy-formation modelling, or direct treatment of observational gamma-ray data, and it does not aim to derive particle-physics constraints on DM models. Its contribution is instead to quantify how subhalo populations depend on their large-scale environment within the ΛCDM framework, and to demonstrate how these environment-conditioned properties propagate into theoretical predictions for substructure-related observables.

Chapter 2

Methodology and Simulation Data

"Everything is physics and math." – Katherine Johnson

2.1 Numerical Cosmology

The rapid technological progress and the growth of computational resources over the past decades have played a central role in shaping modern cosmology and our understanding of structure formation in the Universe. In particular, early numerical experiments were instrumental in establishing the standard model; they demonstrated that baryonic matter alone cannot account for the observed large-scale structure, effectively solidifying the case for CDM. High-resolution simulations now allow researchers to model cosmic evolution across a wide range of scales, providing a primary tool to test the predictions of the ΛCDM framework.

These numerical approaches are indispensable because gravitational clustering is a scale-dependent process. While linear theory accurately describes the evolution of large-scale perturbations even at late times, clustering becomes highly non-linear on smaller scales as structures grow. This transition renders purely analytical treatments inadequate for describing the formation and complex internal dynamics of bound objects, such as haloes and subhaloes, which require fully non-linear numerical modelling.

Since DM dominates the mass content responsible for gravitational collapse, simulations that follow only its gravitational evolution already reproduce the main statistical properties of large-scale structure, including the cosmic web, halo mass function, and clustering patterns. This provides a robust first-order description of structure formation, grounded in the physical assumption that DM is collisionless and electrically neutral, meaning gravity is the only interaction of cosmological relevance.

The earliest simulations, such as those by [151] and [113], pioneered this gravity-only approach and demonstrated that the evolution of collisionless matter can successfully generate filamentary and clustered structures that closely resemble the observed Universe.

This chapter provides an overview of the numerical methods and data products commonly used in cosmological studies. It is important to emphasise that the simulations, halo catalogues, and cosmic web classifications analysed in this work were not generated as part of this thesis; rather, they were provided as pre-existing data products. Consequently, the focus of this work is on the analysis and physical interpretation of these datasets, rather than on their numerical generation. In Section 2.1.1, we discuss the general application of N-body simulations and introduce the specific characteristics of the *COpernicus Complexio LOw Resolution* simulation from which our data are derived. Section 2.1.3 describes the algorithmic techniques used in the field to identify DM haloes and their constituent subhaloes, as implemented in the catalogues adopted for this study. Finally, Section 2.2 presents the segmentation methodologies used to classify the cosmic web, focusing on the `CaCTus` framework employed to generate the web environments studied throughout this thesis.

2.1.1 N-body Simulations

Numerical cosmology provides the essential framework for probing structure evolution through the direct analysis of matter dynamics in a discretised form. In this approach, DM haloes are studied using numerical N-body simulations, in which a representative volume of the Universe is modelled by coarsely sampling its continuous phase-space distribution with N discrete mass elements. These "particles" act as numerical macro-particles that represent coarse-grained elements of the underlying DM fluid rather than individual physical particles. While the linear approximation for density evolution remains valid during the early stages of gravitational instability, it fails once fluctuations enter the non-linear regime. At this stage, different fluctuation modes become coupled, rendering analytical solutions unfeasible [152]. N-body simulations are therefore required to solve the gravitational equations of motion for these tracer particles, providing a numerical bridge between the primordial initial conditions and the complex cosmic web observed at low redshift [153].

The mathematical foundation of collisionless cosmological simulations rests upon the Vlasov–Poisson system [154]. For CDM, the evolution is described by the Vlasov equation, which governs the phase-space distribution function in six dimensions. This is coupled to the Poisson equation (Eq. 1.19), which determines the gravitational potential sourced by density fluctuations.

To model this evolution within an expanding background, the equations of motion are solved in a finite, periodic simulation volume using comoving coordinates $\mathbf{x}$. Periodic boundary conditions are adopted to mimic an effectively infinite Universe within a finite computational domain, ensuring statistical homogeneity while avoiding artificial edge effects associated with finite boundaries. In this framework, each particle interacts not only with others within the simulation box but also with their periodic images, providing a consistent representation of large-scale gravitational fields.

The resulting equation of motion includes the effect of cosmic expansion through a Hubble drag term,

$$\ddot{\mathbf{x}} + 2\frac{\dot{a}}{a}\dot{\mathbf{x}} = -\frac{1}{a^2}\nabla\Phi, \tag{2.1}$$

where Φ is the same Newtonian gravitational potential perturbation in comoving coordinates introduced in Eq. 1.19, sourced by density fluctuations $\delta = (\rho - \bar{\rho})/\bar{\rho}$. This form can be obtained from the Euler equation (Eq. 1.18) in the fluid limit, or equivalently from the characteristics of the collisionless Vlasov equation expressed in comoving coordinates. The additional term proportional to $\dot{a}/a$ encapsulates the effect of cosmological expansion, acting as a friction term that damps peculiar velocities.

The N-body approach approximates the continuous phase-space distribution by sampling it with discrete tracer particles. This collisionless fluid approximation remains valid because DM is effectively collisionless, with negligible non-gravitational interaction cross-sections, such that its dynamics on cosmological scales are governed entirely by gravity.

For this thesis, we use DM-only simulations in which baryonic processes are not included. This approximation is commonly adopted in studies of structure formation. In this regime, the dominant role of DM allows the gravitational assembly of the cosmic web to be isolated and studied in a controlled manner [155]. It should nevertheless be noted that baryonic physics can modify the internal structure and survival of subhaloes. This includes effects on tidal stripping, density profiles, and structural parameters such as $V_{\rm max}$ and $R_{\rm max}$, which in turn can impact predictions for annihilation boost factors. As a result, all conclusions in this thesis should be interpreted within gravity-only framework. The inclusion of baryonic feedback represents an important extension beyond the scope of the present work.

In this context, gravitational collapse leads to the emergence of bound haloes and a nested hierarchy of substructure driven by successive accretion events and mergers, reflecting the bottom-up nature of structure formation.

Through gravitational collapse and hierarchical merging, DM-only simulations show that haloes develop approximately universal density profiles and contain a rich population of substructure in the form of subhaloes [88]. These subhaloes are

remnants of earlier generations of haloes that survive tidal interactions within their host environment, retaining dense inner regions that can persist over cosmological timescales [156].

Modern N-body codes calculate these interactions using techniques designed for both speed and accuracy. Mesh-based methods, such as the Particle-Mesh (PM) technique [151, 157], sample the density field onto a grid to solve the Poisson equation via Fast Fourier Transforms (FFTs). Mass is deposited onto the computational grid using assignment schemes such as Cloud-in-Cell (CIC) or Triangular Shaped Cloud (TSC) [28, 151, 157], which smooth the density field on scales comparable to the grid spacing and thereby reduce discreteness effects. This procedure introduces an effective suppression of force resolution at scales comparable to the grid spacing, effectively smoothing gravitational forces at high spatial frequencies and helping to prevent numerical divergences [158]. To improve force resolution beyond the grid scale, these methods are often supplemented with hierarchical tree algorithms [159] or Adaptive Mesh Refinement (AMR), which combine long-range force estimates with locally refined calculations [160].

The accuracy of the resulting cosmic structures depends sensitively on the choice of initial conditions, since any inaccuracies at early times propagate non-linearly during gravitational evolution and can affect halo formation and clustering statistics at late times. In cosmological N-body simulations, initial conditions are typically generated by constructing a Gaussian random field consistent with the ΛCDM matter power spectrum at a sufficiently high starting redshift, with $z \sim 100$ being a typical choice in the literature, where density perturbations remain within the linear regime. This choice ensures that perturbative approaches such as second-order Lagrangian Perturbation Theory (2LPT) can be applied reliably, producing accurate initial displacements while minimising transient numerical effects. The specific initial condition setup used in this thesis is described in Section 2.1.2.

Particles are typically displaced from a uniform glass-like or grid distribution. While the Zel'dovich approximation provides a first-order Lagrangian mapping between the initial density field and particle displacements, 2LPT captures higher-order contributions to the growing mode of structure formation [161]. This reduces transients associated with the finite starting redshift and improves the fidelity of the initial displacement field, ensuring that the simulated volume reproduces the statistical properties of the early linear Universe prior to the onset of non-linear gravitational collapse.

In the following section, we describe the specific simulation suite used in this thesis and the algorithmic techniques used to identify the resulting DM structures.

2.1.2 The COpernicus COmplexio LOw Resolution Simulation

The COpernicus COmplexio (COCO) project is a high-resolution, DM-only N-body simulation suite carried out by the Virgo Consortium within the ΛCDM paradigm [6, 162]. It consists of a high-resolution zoom-in region embedded within a large parent cosmological volume known as the COpernicus COmplexio LOw Resolution (COLOR) simulation. By embedding high particle and force resolution within a representative cosmological environment, this configuration allows for the study of structure formation down to galactic and sub-galactic scales. The numerical and cosmological specifications of the COLOR volume are summarised in Table 2.1. The cosmological parameters are consistent with the seven-year results of the Wilkinson Microwave Anisotropy Probe (WMAP-7) mission [5].

Table 2.1: Numerical specifications and cosmological parameters adopted in the COLOR simulation [5, 6].

Parameter	COLOR
Box size [h^{-1} Mpc]	70.4
Number of particles, N_p	$\sim 4.2 \times 10^9$
Particle mass, m_p [$h^{-1}M_\odot$]	6.19×10^6
Softening length, ϵ_h	1 h^{-1} kpc
Ω_m	0.272
Ω_Λ	0.728
Ω_b	0.04455
h	0.704
σ_8	0.81
n_s	0.967

COLOR traces 1620^3 particles (approximately 4.25 billion) in a periodic box of side length $70.4h^{-1}$Mpc, evolved from $z = 127$ to $z = 0$ using a modified version of the GADGET-3 code [159, 163]. Each particle carries a mass of $m_p = 6.19 \times 10^6 h^{-1}\mathrm{M}_\odot$, and the gravitational softening length is set to $\epsilon_h = 1h^{-1}$kpc. Initial conditions were generated using phase information drawn from the publicly available Gaussian white-noise field Panphasia [164]. The large periodic volume ensures a statistically representative sample of haloes spanning the full range of cosmic web environments,

from voids to nodes, providing the cosmological framework within which the halo populations analysed in this thesis are embedded.

We choose the COLOR volume over the higher-resolution zoom-in region because an environment-dependent analysis requires a large, statistically robust sample. Investigating subhalo populations across the cosmic web demands a high volume of host haloes in every environment type. This is especially true for voids; although they occupy most of the cosmic volume, they are severely underrepresented in small simulation boxes. A zoom-in region offers superior mass and force resolution, but its limited cosmological volume cannot yield adequate statistics across all web environments simultaneously. In contrast, the larger COLOR volume provides a rich and diverse population of haloes across filaments, walls, and voids alike. Therefore, we prioritise sample size and environmental completeness over higher per-particle resolution. We accept this resolution trade-off as a necessary and justified compromise to achieve the statistical goals of this thesis.

2.1.3 Halo and subhalo identification

Identifying DM haloes and their constituent substructures within cosmological N-body simulations requires numerical techniques capable of distinguishing stable, gravitationally bound systems from the surrounding cosmic web [165, 166]. The most widely adopted approach for defining primary haloes is the Friends-of-Friends (FoF) algorithm [113]. This method links particles together if their spatial separation is smaller than a predefined linking length, typically chosen as 0.2 times the mean interparticle distance. While FoF captures large-scale overdensities efficiently, it lacks an internal mechanism to verify gravitational binding. This limitation leads to bridging issues where two separate, dynamically independent haloes are incorrectly joined into a single object by a thin chain of particles, a problem occurring frequently during major mergers [167].

To establish halo boundaries more rigorously, virial-related quantities such as M_{200} and R_{200} are used, defining the halo as the region where the average density is 200 times the critical density of the Universe [168]. This convention is widely adopted as an operational approximation to the virialised region, motivated by the spherical collapse model, which predicts a virial overdensity of $\Delta \simeq 178$ for an Einstein–de Sitter cosmology. In ΛCDM, the exact virial overdensity is cosmology-dependent, so the $\Delta = 200$ definition serves as a convenient and consistent reference rather than a unique physical boundary.

FoF haloes and spherical overdensity (R_{200}) haloes are therefore not identical objects since FoF defines a connectivity-based structure that may be non-spherical, whereas

R_{200} enforces a spherical definition around a density peak. In practice, FoF groups are used as initial candidates from which spherical overdensity properties are then computed.

Once these main haloes are established, subhalo extraction is necessary to identify the smaller density peaks surviving within the host environment. In this thesis, we employ the SUBFIND algorithm [169] for this purpose. SUBFIND identifies candidate substructures as locally overdense regions within a parent FoF group. While FoF boundaries can be problematic, they provide a necessary spatial search domain that ensures the algorithm captures substructures across the full distribution of DM, including those outside the idealised R_{200} radius.

Following the identification of these density peaks, SUBFIND applies a rigorous unbinding procedure. This iterative process removes particles whose kinetic energy exceeds their potential energy relative to the subhalo centre, ensuring the final object is self-bound. This step effectively mitigates the limitations of the initial FoF grouping by retaining only gravitationally bound particles. However, SUBFIND is known for a conservative approach to mass assignment. Near the dense centres of host haloes, it can struggle to distinguish subhalo material from the background. This occasionally leads to artificial mass loss or the temporary disappearance of subhaloes during their pericentric passage, which is their closest approach to the host centre [170, 171].

Alternative identification strategies, such as Spherical Overdensity (SO) criteria, offer a different perspective. Codes such as the AMIGA Halo Finder (AHF) use mesh refinement to locate density peaks and iteratively identify nested haloes and subhaloes through spherical overdensity definitions [172]. These methods are built upon spherical collapse arguments, though they face challenges near host centres where steep background density gradients can contaminate subhalo measurements.

Comparative studies show that FoF-based methods and SO finders usually agree on basic properties such as position and bulk velocity to within 1%. However, they differ by about 10% in mass and up to 20% in spin parameters because they use different methods to collect and assign particles at the halo edges [166].

Recent advancements have introduced phase space and temporal tracking methods to overcome the limitations of 3D configuration space finders. Phase space algorithms such as ROCKSTAR employ the full six-dimensional information of position and velocity to identify structures [173]. By searching for particles that move coherently against the host background, these finders can recover subhaloes that have been heavily stripped of their spatial density but remain dynamically distinct. Similarly, the VELOCIRAPTOR code identifies structures by comparing local velocity distributions to the background mean [174]. These 6D approaches significantly reduce the scatter

in measurements of the maximum circular velocity, making it a robust parameter for comparing results across different simulation codes [171].

In this thesis, we follow the standard FoF and SUBFIND methodology [6, 84, 162]. The FoF algorithm provides a rapid and computationally efficient tool for identifying parent structures in large volumes [165], while SUBFIND refines these groups to extract gravitationally self-bound substructures [165, 166, 171]. In all analyses presented in this thesis, we use only first-level subhaloes, defined as gravitationally self-bound structures identified directly within the host halo, excluding higher-order nested structures returned by SUBFIND. This convention is applied consistently across Chapters 3-5. In Chapter 4, the semi-analytical boost-factor model implements a two-level substructure hierarchy: first-level subhaloes are drawn directly from the simulation catalogue, while a second-level nested contribution is computed analytically for each first-level subhalo acting as a secondary host, without further recursion.

Although alternative finders offer different strengths, this approach provides a well-characterised framework that facilitates comparison with major simulation suites. Haloes and subhaloes are identified in the simulation output during the primary data reduction stage. A minimum resolution threshold of 100 bound particles per subhalo is adopted following convergence tests in the original COCO ΛCDM DM simulation analysis [162], which demonstrated stable results for subhalo abundance statistics and for structural quantities such as density profiles, $V_{\rm max}$, $R_{\rm max}$, and concentration estimates. This threshold is applied uniformly to all subhalo-based measurements in this thesis, including merger-tree derived quantities.

The analysis sample is defined as follows. Host haloes are characterised by their mass M_{200}, defined as the mass enclosed within R_{200}, where the mean interior density equals 200 times the critical density of the Universe at the corresponding redshift, $\rho_{\rm c}(z) = 3H(z)^2/8\pi G$. This definition is used consistently throughout the thesis. The host haloes are divided into three mass bins with median masses $\langle M_{200}\rangle = 10^{10}$, 10^{11}, and $10^{12}h^{-1}{\rm M}_\odot$. Subhaloes are selected as all gravitationally self-bound structures identified by SUBFIND within R_{200} of their host halo, subject to the 100-particle limit. Subhaloes are therefore analysed only if they satisfy the resolution criterion and lie within the host halo boundary. The cosmic web environment is assigned using the position of each halo at $z = 0$, by mapping it onto a precomputed density-field classification grid described in Section 2.2.1. The environment is defined by the voxel containing the halo centre, which is labelled as void, wall, filament, or node.

To track the time evolution of haloes and subhaloes between simulation snapshots, we used merger tree catalogues constructed from the SUBFIND catalogues. These trees provide a temporally ordered representation of the hierarchical assembly of the structure, enabling consistent tracking across discrete snapshots. The merger trees are

built using the algorithm of Jiang et al. [175], an updated version of Merson et al. [176], originally developed for the GALFORM semi-analytic model [177]. The method relies on unique particle-based linking of subhaloes between consecutive snapshots, where descendants are identified by maximal sharing of bound particles [178].

The progenitor-descendant links are defined snapshot by snapshot, forming a directed graph in which each subhalo has a unique descendant and may have multiple progenitors. The main progenitor branch is defined as the branch that contains the most massive progenitor at each step when tracing the tree backward in time [159]. This provides a consistent description of the history of dominant mass assembly.

These merger trees allow reconstruction of subhalo accretion histories, including infall events and peak mass. The infall event is defined as the snapshot at which a halo first becomes a gravitationally bound substructure within a more massive host halo, marking the transition from a central halo to a satellite system. The peak mass is defined as the maximum bound mass attained by the subhalo over its resolved history prior to infall, or prior to its last reliable detection in cases where the subhalo becomes temporarily disrupted or falls below the SUBFIND resolution limit [179, 180]. These quantities are used throughout Chapter 5.

2.2 Identifying components of the cosmic web

The properties of large-scale structures, such as their spatial distribution, characteristic size, and density, are deeply linked to fundamental cosmological parameters, including the matter density and dark energy [181]. Because these structures span both linear and non-linear regimes, their geometry and topology encode the dynamical history of gravitational collapse, while also providing a framework for investigating the environmental physics of galaxy evolution. However, objectively detecting web elements remains a significant numerical challenge due to the multi-scale nature of the network and the lack of discrete physical boundaries. Current methodologies for classifying the cosmic web can be broadly organised into several distinct methodological frameworks.

Topological and Watershed Techniques: Drawing from algebraic topology and Morse theory, these finders focus on the connectivity and persistence of structures. Watershed-based algorithms, such as VIDE [182] or SpineWeb [53], treat the density field as a topographic landscape, segmenting space into catchment basins to define voids and their surrounding boundaries. VIDE is primarily designed for the identification of voids, while SpineWeb reconstructs the filamentary and wall-like morphology surrounding these underdense regions. A complementary approach, the DISPERSE algorithm [183], uses discrete Morse theory and persistence concepts to identify

the filamentary skeleton and its associated critical points in noisy datasets. More mathematically abstract descriptions involve Persistent Betti Numbers [184], which characterise the connectivity of the web through multi-scale counting of topological features.

Stochastic and Graphical Frameworks: These techniques operate directly on discrete distributions of tracers such as galaxies or haloes, without requiring an explicit reconstruction of a continuous density field. Graphical methods employ graph theory, such as the Minimal Spanning Tree (MST) or modern derivatives like T-ReX [185], to trace the spine of the filamentary network. Stochastic models, such as the Bisous model [186, 187], analyse point processes by fitting aligned cylindrical structures to the distribution to statistically identify filaments. Recent advancements include ASTRA [188], which introduces a probabilistic ranking framework to quantify uncertainties in the reconstruction of the cosmic web from sparse and noisy observational data, allowing for a more robust classification of filamentary structures based on statistical likelihood rather than deterministic assignment.

Phase-Space Dynamics and Machine Learning: A physically motivated family of classifiers relies on the fact that the primordial mass distribution behaves as a 3D sheet folding within 6D phase space. Methods such as ORIGAMI [167] and Multi-Stream Web Analysis (MSWA) identify structures by counting stream-crossings or sheet-folds, where caustics trace the formation history of filaments and walls. Complementing these are data-driven approaches, including convolutional neural networks (CNNs) trained on simulated density fields, as well as graph-based spatial clustering methods that construct reduced backbone representations of galaxy distributions, such as the ABACUS algorithm [189]. In this approach, ABACUS is used primarily as a preprocessing and structure-reduction step, identifying representative backbone points through local neighbourhood merging before any subsequent analysis. While these methods offer significant computational efficiency, they require calibration against physical formalisms to ensure that spurious numerical features are not misclassified as real structures.

Geometric and Scale-Space Hessian Methods: This final class represents the most frequently employed approach to characterising large-scale structure, relying on the local curvature of fields such as density, tidal potential, or velocity shear. By evaluating the eigenvalues of the Hessian matrix, these finders identify the dimensionality of collapse, characterising regions as nodes, filaments, walls, or voids. While early implementations like the T-web [8] and V-web employed fixed smoothing scales, modern frameworks employ a scale-space formalism to capture the hierarchical nature of the web. In this study, we use the `CaCTus` framework [190], which is a new implementation of the NEXUS+ algorithm [191]. `CaCTus` overcomes traditional scale-dependence by

identifying the strongest morphological signature across multiple smoothing lengths and employs logarithmic density smoothing to enhance tenuous filaments. Additionally, post-processing tools like COWS [192] can be applied to these Hessian-based fields to extract the skeletal spine of filaments, determining their precise endpoints and lengths.

2.2.1 CaCTus

The CaCTus framework is a software implementation of the NEXUS+ methodology for cosmic web identification [41, 191]. The source code and accompanying documentation will be made publicly available in Naidoo et al. (in prep.).[1] It belongs to a class of scale-space Hessian-based structure finders designed to characterise the multi-scale geometry of the cosmic web. In contrast to single-scale classifiers such as the T-web and V-web [8, 193], which apply a direct threshold $\lambda_{\rm th}$ to eigenvalues of the tidal or velocity shear tensor evaluated at a single smoothing scale, CaCTus evaluates morphological information across multiple smoothing lengths.

The NEXUS+ algorithm extends the standard NEXUS approach by modifying the filtering stage used to construct the scale-space representation. In particular, for filamentary and wall-like structures, the environmental signatures are computed from a log-density field, whereas for node-like structures the standard density field is used. This log-Gaussian transformation reduces the dominance of high-density peaks and enhances the contrast of diffuse filamentary and wall-like features [41]. Nodes, being compact and approximately isotropic structures, do not require this transformation for reliable identification.

The input to the CaCTus pipeline is the dimensionless density field obtained from simulation data using a Cloud-in-Cell interpolation onto a regular Cartesian grid. The density field is defined as

$$f(\mathbf{x}) = \frac{\rho(\mathbf{x})}{\bar{\rho}}, \tag{2.2}$$

where $\rho(\mathbf{x})$ is the density and $\bar{\rho}$ is the mean density of the volume.

To capture the multi-scale structure of the cosmic web, the field is smoothed over a hierarchy of scales using a kernel W_{R_n}, typically Gaussian. The smoothed field at scale R_n is given by

$$f_{R_n}(\mathbf{x}) = \int f(\mathbf{x}')\, W_{R_n}(\mathbf{x} - \mathbf{x}') d\mathbf{x}'. \tag{2.3}$$

By varying the smoothing scale in discrete logarithmic steps, a scale-space representation of the density field is constructed, allowing structures of different characteristic sizes to be identified.

[1] At the time of writing, the CaCTus implementation is being prepared for public release.

The local geometry at each scale is quantified using the Hessian matrix,

$$H_{ij,R_n}(\mathbf{x}) = R_n^2 \frac{\partial^2 f_{R_n}(\mathbf{x})}{\partial x_i \partial x_j}, \tag{2.4}$$

where the factor R_n^2 ensures scale-independent normalisation. The eigenvalues $\lambda_1 \leq \lambda_2 \leq \lambda_3$ of the Hessian describe the local curvature of the density field and provide a geometric basis for identifying anisotropic structures. In the `CaCTus` implementation used in this work, the Hessian is evaluated on the standard density field for node identification, and on the logarithmically smoothed density field for filamentary and wall-like structures, improving sensitivity to low-density anisotropic features.

This procedure yields a hierarchical map of the cosmic web, which can be compared conceptually with standard single-scale classification schemes. For reference, Table 2.2 summarises the intuitive eigenvalue-counting logic often used in tidal- or velocity-shear classifiers. These rules should not be read as the operational definition of the `CaCTus`/NEXUS+ environments used in this thesis, because the latter relies on multi-scale Hessian signatures of the density or log-density field, followed by scale-space maximisation and segmentation thresholds.

Table 2.2: Eigenvalue-threshold criteria commonly used in cosmic web classifiers based on the tidal or velocity shear tensor. Environments are assigned according to the number of eigenvalues $\lambda_1 \leq \lambda_2 \leq \lambda_3$ that exceed a threshold $\lambda_{\rm th}$, typically taken as $\lambda_{\rm th} = 0$ [7, 8]. The precise sign convention may vary depending on the tensor definition adopted.

Environment	Condition
Void	$\lambda_1, \lambda_2, \lambda_3 < \lambda_{\rm th}$
Wall	$\lambda_1, \lambda_2 < \lambda_{\rm th}, \lambda_3 > \lambda_{\rm th}$
Filament	$\lambda_1 < \lambda_{\rm th}, \lambda_2, \lambda_3 > \lambda_{\rm th}$
Node	$\lambda_1, \lambda_2, \lambda_3 > \lambda_{\rm th}$

The environmental response is combined through a scale-space maximisation,

$$S(\mathbf{x}) = \max_{R_n} \left[S_{R_n}(\mathbf{x}) \right], \tag{2.5}$$

ensuring that each spatial position is associated with the scale at which its morphological response is strongest. The `CaCTus` implementation adopted in this work

follows the general NEXUS+ framework and applies a consistent set of segmentation and thresholding criteria for the identification of cosmic web environments.

The final environmental assignment is performed in a staged sequence following Cautun et al. [191]. Nodes are identified first using combined constraints on signature strength, density, and enclosed mass, ensuring that only highly collapsed regions are selected, corresponding to systems with $\lambda_1 \approx \lambda_2 \approx \lambda_3 < 0$, with enclosed mass exceeding $5 \times 10^{14} h^{-1} M_\odot$ and mean interior density above $300\rho_c(z)$. Filaments are subsequently extracted from the remaining regions using the filament signature together with thresholds calibrated from the variation of enclosed mass as a function of signature strength. Wall regions are then assigned from cells with significant wall signatures that are not already classified as nodes or filaments, while all remaining regions are classified as voids. This staged procedure produces a consistent segmentation of the density field while preserving the multi-scale information encoded in the environmental signatures.

The configuration of the `CaCTus` implementation used in this work is summarised in Table 2.3.

Table 2.3: Configuration of the `CaCTus` cosmic web classification algorithm used in this work.

Parameter	Value
Grid	256^3 cells, spacing 0.275 h^{-1}Mpc
Smoothing scales	$R_0 = 0.5$ h^{-1}Mpc to 4 h^{-1}Mpc, 7 scales, $R_n = 2^{n/2} R_0$
Density smoothing	Gaussian for nodes; log-Gaussian for filaments/walls
Thresholding	Calibrated from variation of enclosed mass vs. signature strength

Chapter 3

Paper I: Caught in the cosmic web: Environmental effects on subhalo abundance and internal density profiles

"If I can see farther, it is only because I stand on the shoulders of giants"– Isaac Newton

This chapter consists of a reproduced version of an open-access article published in Astronomy & Astrophysics.[2]

Hunde, F. M., Newton, O., Hellwing, W. A., Bilicki, M., & Naidoo, K. 2025, "Caught in the cosmic web: Environmental effects on subhalo abundance and internal density profiles," *Astronomy & Astrophysics*, 700, A65.
DOI: https://doi.org/10.1051/0004-6361/202452246
arXiv: https://arxiv.org/abs/2409.09226

3.1 Introduction

In this chapter, we investigate how the cosmic web influences the abundance and internal properties of DM subhaloes. Previous studies have largely focused on the dependence of subhalo populations on host halo mass and assembly history, while the additional role of the surrounding large-scale environment has received comparatively less attention. Understanding these environmental effects is important for accurately modelling satellite galaxy populations, interpreting the clustering of low-mass systems, and assessing how classical small-scale ΛCDM tensions, such as too-big-to-fail, may depend on host environment in addition to baryonic physics, selection effects, and host-halo mass.

[2] In accordance with the journal's copyright policy (https://www.aanda.org/for-authors/author-information/copyright), ESO grants authors the non-exclusive right to reproduce published material in dissertations, provided appropriate bibliographic credit is given.

To explore these effects, we analyse the DM-only COLOR N-body simulation, which resolves substructure across a wide dynamical range. The cosmic web morphology is identified using the multi-scale `CaCTus` algorithm, an implementation based on the `NEXUS+` framework, which classifies host haloes into nodes, filaments, walls, and voids. This environmental segmentation enables the influence of the cosmic web to be separated from the dependence on host halo mass alone. The analysis focuses on subhaloes hosted by low- and intermediate mass haloes grouped into three mass bins with median values of $\langle M_{200} \rangle = 10^{10}$, 10^{11}, and $10^{12}\,h^{-1}\,\mathrm{M}_{\odot}$. We excluded node environments from our study because they are dominated by cluster mass hosts and heavily tidally-disrupted "backsplash" haloes [110].

We first quantify the abundance of subhaloes across different environments. At fixed host mass, filament and wall haloes host systematically richer subhalo populations than void haloes. For host haloes with $\langle M_{200} \rangle = 10^{10}\,h^{-1}\,\mathrm{M}_{\odot}$, wall environments contain subhaloes that can be up to a factor of two more massive than those found in voids at the high mass end, while at lower subhalo masses the abundance excess is typically $\sim$ 25%. These environmental differences decrease progressively toward higher host halo masses. We then examine the substructure mass fraction, f_{sub}, which measures the fraction of host mass bound in subhaloes. Filament hosts are found to contain approximately 2–15% more mass in substructure than void hosts, whereas void haloes exhibit systematically smoother density distributions with correspondingly lower subhalo mass fractions.

The analysis is extended to the internal structure of subhaloes through the V_{max}–R_{max} relation, which acts as a proxy for concentration. Subhaloes hosted by haloes in filamentary environments are systematically more concentrated than those in lower-density regions, while subhaloes in voids show an approximately 5–9% suppression in concentration relative to filament populations across most host mass bins. Similar environmental trends are observed in the subhalo velocity function. Relative to the cosmic mean, filament environments exhibit approximately 5–15% enhancements in subhalo abundance, whereas void environments show deficits ranging from 5–25%, with the strongest effects occurring for low-mass hosts.

The results indicate that environmental effects can alter the expected internal structure of Milky Way-like subhalo populations. At fixed Milky Way-like host mass, the comparison between filament and wall environments shows that wall hosts contain fewer highly concentrated subhaloes than filament hosts, an effect that may reduce the severity of too-big-to-fail-like interpretations in environment-dependent satellite models. Collectively, these findings demonstrate that subhalo populations retain a measurable imprint of the cosmic web environment of their hosts and that neglecting

these environmental dependencies may introduce systematic biases into studies of satellite populations and indirect DM observables.

3.2 Author's contribution

In the process of this article preparation, I led:

- The analysis of the simulated DM halo and subhalo catalogues from the COLOR simulation, including the computation of all subhalo population statistics.
- Adapting and running the code to map haloes onto the cosmic web using the density field classified by the `CaCTus` algorithm, and processing the resulting catalogues for environment assignment.
- Processing the halo and subhalo catalogues for web-type assignment for the analysis.
- The creation of all figures in the paper, with the exception of Figure 1.
- The physical interpretation of the patterns of halo and subhalo populations across different cosmic web environments.
- Writing the majority of the manuscript, including the initial draft and subsequent revisions.

A&A, 700, A65 (2025)
https://doi.org/10.1051/0004-6361/202452246

Astronomy & Astrophysics

Caught in the cosmic web: Environmental effects on subhalo abundance and internal density profiles

Feven Markos Hunde[1,⋆], Oliver Newton[1,⋆], Wojciech A. Hellwing[1,⋆], Maciej Bilicki[1], and Krishna Naidoo[2]

[1] Center for Theoretical Physics, Polish Academy of Sciences, Al. Lotników 32/46, 02-668 Warsaw, Poland
[2] University College London, Gower Street, London, WC1E 6BT, United Kingdom

Received 13 September 2024 / Accepted 19 June 2025

ABSTRACT

Using the high-resolution N-body cosmological simulation COLOR, we explored the cosmic web (CW) environmental effects on subhalo populations and their internal properties. We used `CaCTus`, which incorporates an implementation of the state-of-the-art segmentation method NEXUS+, to delineate the simulation volume into nodes, filaments, walls, and voids. We grouped host haloes by virial mass, and segmented each mass bin into consecutive CW elements. This reveals that subhalo populations in hosts within specific environments differ on average from the cosmic mean. The subhalo mass function is affected strongly, where hosts in filaments typically contain more subhaloes (5–20%), while hosts in voids are subhalo-poor, with 25% fewer subhaloes. We find that the abundance of the most massive subhaloes, with reduced masses of $\mu \equiv M_{\rm sub}/M_{200}$ is most sensitive to the CW environment. A corresponding picture emerges when looking at subhalo mass fractions, $f_{\rm sub}$, where the filament hosts are significantly more granular (having higher $f_{\rm sub}$) than the cosmic mean, while the void hosts have much smoother density distributions (with $f_{\rm sub}$ lower by 2 – 20% than the mean). Finally, when we look at the subhalo internal kinematic $V_{\rm max}$–$R_{\rm max}$ relations, we find that subhaloes located in the void and wall hosts exhibit density profiles with lower concentrations than the mean, while the filament hosts demonstrate much more concentrated mass profiles. Across all our samples, the effect of the CW environment generally strengthens with decreasing host halo virial mass. Our results show that host location in the large-scale CW introduces significant systematic effects on internal subhalo properties and population statistics. Understanding and accounting for them is crucial for the unbiased interpretation of observations related to small scales and to satellite galaxies.

Key words. dark matter – large-scale structure of Universe

1. Introduction

Observational efforts to map the large-scale spatial distribution of galaxies show that they are arranged in an interconnected filamentary network (e.g. de Lapparent et al. 1986; Colless et al. 2003; Tegmark et al. 2004). This vast, complex, and multi-scale structure spans spatial scales from a few to several hundred megaparsecs, and is now known as the cosmic web (Bond et al. 1996). Numerical simulations within the framework of the Λ+cold dark matter (ΛCDM) paradigm show that the cosmic web originates from the gravitational amplification of the small Gaussian density fluctuations present within the primordial plasma (Doroshkevich 1970; Zel'dovich 1970; Shandarin & Zeldovich 1989). Therefore, the cosmic web is one of the most significant outcomes of the anisotropic gravitational collapse governing the evolution of structure throughout the Universe (Peebles 1980; Adler 1981; Bardeen et al. 1986).

Classically, the cosmic web is delineated into four distinct components: high-density nodes inhabited primarily by galaxy clusters, groups, and extremely massive galaxies; elongated filaments of galaxies and intergalactic gas; flattened walls spanning the nearly empty space between the filaments; and very underdense voids (Aragón-Calvo et al. 2007a; van de Weygaert & Platen 2011; Cautun et al. 2013, 2014a). To first order, this structure emerges in a well-ordered sequence as matter is evacuated from voids through walls and onto filaments, through which it is channelled towards the highest-density nodes (Doroshkevich 1970; Cautun et al. 2014a).

The anisotropic gravitational collapse driving the emergence of the cosmic web is also responsible for the hierarchical assembly of dark matter (DM) haloes on smaller scales. These gravitationally bound systems grow via the merger and coalescence of smaller haloes and the smooth accretion of mass (White & Rees 1978; Blumenthal et al. 1984; White & Frenk 1991; Frenk & White 2012). They are an essential ingredient of contemporary galaxy formation models, which posit that baryons accumulate deep within the potential wells of DM haloes and seed the growth of galaxies (e.g. White & Rees 1978; White & Frenk 1991). Thus, the properties of galaxies are sensitive to those of their host, and understanding how they are influenced by their environment is critically important.

The first attempts to connect DM halo properties with the cosmic web were carried out using gravity-only numerical simulations (Gao et al. 2005; Wang et al. 2007). They show that the most massive DM haloes are typically found only in the highest-density cosmic web environments (Alonso et al. 2015; Hellwing et al. 2021), and their abundance (Metuki et al. 2015, 2016), concentrations (Avila-Reese et al. 2005), and assembly histories are similarly correlated with environmental density (Hahn et al. 2007b; Rey et al. 2019). Other works have shown that halo spins and shapes typically align with the principal axes of the filaments they are embedded within (Aragón-Calvo et al. 2007b; Hahn et al.

⋆ Corresponding authors: `fevenm@cft.edu.pl`, `onewton@cft.edu.pl`, `hellwing@cft.edu.pl`

2007a,b; Libeskind et al. 2012; Forero-Romero et al. 2014; Ganeshaiah Veena et al. 2018, 2019, 2021), or are aligned towards the centres of the nearest void (Patiri et al. 2006). Hydrodynamic simulations show that galaxy properties such as star formation rates (Aragon Calvo et al. 2019; Malavasi et al. 2022), metallicity (Xu et al. 2020), and angular momentum (Danovich et al. 2015) exhibit a similar dependence on the large-scale environment. Observational studies of galaxies have also shown that their mass and luminosity (Wang et al. 2017), formation times (Zhang et al. 2021), morphological properties (Dressler 1980), as well as the activity of the active galactic nucleus (Miraghaei 2020) are influenced by the nature of their environment.

On even smaller scales, the correlation between the internal properties of low-mass haloes and their cosmic web environment appears to be even stronger (Benítez-Llambay et al. 2013). Hellwing et al. (2021), hereafter H21, showed that haloes with masses below $M = 6 \times 10^{10}\, h^{-1}\,\mathrm{M}_\odot$ residing in higher-density environments, such as filaments, are more concentrated compared to those found in voids, for example. They also showed that low-mass haloes in dense environments form earlier than their counterparts with similar masses in low-density cosmic web environments. Most of the haloes in this mass regime reside within the orbit of a more massive host and were accreted during its hierarchical assembly.

The subset of low-mass haloes that survive the tidal interactions with their hosts persist for long periods as subhaloes, some of which may host satellite galaxies (Klypin et al. 1999; Stoehr et al. 2002; Han et al. 2012). Satellite galaxies form in the highly non-linear regime of structure formation, characterised by short timescales, high densities, and chaotic orbits. They are therefore sensitive probes of the underlying cosmological model and the faint end of galaxy formation (e.g. Enzi et al. 2021; Lovell et al. 2021; Newton et al. 2021; Deason et al. 2022; Dome et al. 2023; Wang et al. 2023; Newton et al. 2024), and efforts to understand how the cosmic environment influences their properties is a subject of growing interest (Libeskind et al. 2015; Tempel et al. 2015). Some of the best-characterised systems of low-mass galaxies currently available are the satellite populations of the Milky Way, M31, and Centaurus A, and they show evidence of the influence of the large-scale cosmic web environment. For example, the flattened, planar configuration of the satellites around their hosts (Pawlowski et al. 2012b; Hammer et al. 2013; Müller et al. 2018) may be connected to their correlated directions of accretion via filaments (Libeskind et al. 2005; Ibata et al. 2013; Cautun et al. 2015; Gillet et al. 2015; Libeskind et al. 2015; González & Padilla 2016; Wang et al. 2020; Dupuy et al. 2022; Gámez-Marín et al. 2024, though see Pawlowski et al. 2012a). The abundance of satellites may also be enhanced, and their specific star formation rates suppressed, compared to other similar systems if they reside in filaments (Guo et al. 2015; Darvish et al. 2017).

Over the last two decades, cosmological simulations have finally been able to reliably resolve the substructure within haloes, inciting interest in the abundance and internal properties of subhaloes in DM haloes. To characterise this information, studies have employed metrics such as the subhalo mass and velocity functions, radial distribution, and internal density profile (Gao et al. 2004b; Van Den Bosch et al. 2005; Springel et al. 2008; Gao et al. 2011, 2012; Cautun et al. 2014c; Han et al. 2016; Hellwing et al. 2016; Moliné et al. 2023). While previous authors have examined how these properties depend on those of their host, here we expand these analyses to consider the influence of the cosmic web environments surrounding their hosts. To date, the effect of the cosmic web on the properties of subhalo populations has not been fully explored. The goal of this paper is to address this gap in understanding and, using gravity-only numerical simulations, to connect the present-day properties of subhalo populations with the cosmic web environments of their hosts. Establishing the influence of the cosmic web environment on these properties will allow the proper incorporation of these environmental effects into the modelling of both DM haloes and galaxy-based observables.

Using a high-resolution N-body simulation (Hellwing et al. 2016) with a new implementation of the state-of-the-art multi-scale cosmic web identifier, NEXUS+ (Cautun et al. 2013), we performed a systematic study of the correlations between the cosmic web environment and the properties of subhalo populations. We investigated how the environment of the host haloes affects the subhalo mass and velocity functions, substructure mass fractions, and concentrations. We find significant and robust evidence for the impact of the cosmic web environment on several subhalo population statistics.

This paper is structured as follows. In Sect. 2 we introduce the details of the COpernicus complexio LOw Resolution (COLOR) simulations and the methods that we used to find and characterise the DM halo and subhalo populations. In Sect. 3 we present the cosmic web segmentation algorithm used for this study. In Sect. 4 we compare different properties of DM subhaloes as a function of their locations within the cosmic web environment. In Sect. 5 we discuss and summarise our findings and their implications, and draw our conclusion.

2. Simulations

For this work we used the COpernicus complexio LOw Resolution (COLOR) simulation, which is the parent box of COpernicus COmplexio (COCO), a DM-only zoom-in N-body simulation carried out at higher resolution (Bose et al. 2016; Hellwing et al. 2016). As our aim was to extend the analysis of H21 into a lower-mass regime, using the COCO CDM simulation was a natural choice given its superb resolution.

However, as COCO is a zoom-in simulation, its high-resolution volume is quite small. This restricts the size of the statistical sample that can be achieved in each cosmic web environment, especially so within void environments, which dominate the volume fraction of the cosmic web. To remedy this we chose an unusual trade-off, namely, we used the simulation with a larger volume to obtain better statistics, rather than the higher-resolution simulation that would provide better accuracy. The volume of the COLOR simulation is 14 times larger than COCO, which significantly improves our ability to study the subhalo populations.

COLOR follows the evolution of ~4.25 billion particles $\left(1620^3\right)$, each with mass, $m_\mathrm{p} = 6.19 \times 10^6\, h^{-1}\,\mathrm{M}_\odot$, in a periodic box with a side length of $L = 70.4\,\mathrm{Mpc}$, encompassing a total volume of $3.5 \times 10^5\, h^{-3}\,\mathrm{Mpc}^3$. COLOR assumes cosmological parameters obtained from the 7-year Wilkinson Microwave Anisotropy Probe (WMAP-7) data (Komatsu et al. 2011): $\Omega_\mathrm{m} = 0.272, \Omega_\Lambda = 0.728$, $\Omega_\mathrm{b} = 0.04455$, $h = 0.704$, $\sigma_8 = 0.81$ and $n_\mathrm{s} = 0.967$.

Dark matter haloes were identified using the friends-of-friends (FOF) algorithm with a linking length of $b = 0.2$ times the mean inter-particle separation (Davis et al. 1985). For the purposes of this paper, only haloes massive enough to host a resolved subhalo population are useful. Therefore, for our initial analysis, we consider only the FOF groups with at least 10^3

particles, which imposes an effective mass threshold of $M_{\rm FOF} \gtrsim 10^9\,h^{-1}\,{\rm M}_\odot$.

For each FOF group we also compute its mass, M_{200}. This is the mass contained within the radius, R_{200}, which encloses an average density of 200 times the critical density of the Universe, $\rho_{\rm c}(z) \equiv 3H(z)^2/8\pi{\rm G}$, at the redshift at which the halo is identified. In this analysis, we use M_{200} as the host halo mass definition unless stated otherwise. We found gravitationally bound substructures in each FOF group using the SubFind algorithm (Springel et al. 2001), which identifies candidate subhaloes by searching for overdense regions within the FOF groups and selecting only gravitationally self-bound subhaloes. SubFind defines the mass of a subhalo to be the total mass of all particles gravitationally bound to the overdensity. This identification process is sensitive to the resolution of the simulation. Better particle resolution improves the ability to resolve subhaloes and reduces numerical artefacts, thereby enhancing the accuracy of subhalo abundance estimates and internal density profiles (e.g. Springel et al. 2008; Reed et al. 2005). To minimise the effect of numerical artefacts, we require all the subhaloes we study to be composed of at least 100 particles. We focus our analysis on the subhaloes located within the virial radius, R_{200}, of their parent host halo.

Beyond resolution effects, the choice of halo and subhalo finder, as well as the method used to segment the cosmic web, can introduce systematic variations in how structures are identified and assigned to cosmic web environments. Although we do not explore alternative methods directly in this work, previous studies (e.g. Forero-Romero et al. 2009; Cautun et al. 2013; Libeskind et al. 2018) show that major cosmic web features are recovered robustly across different cosmic web classifiers, and that commonly used halo-finding algorithms typically produce consistent halo catalogues above the resolution threshold. Nevertheless, discrepancies remain in details such as subhalo boundaries and membership, particularly for low-mass or satellite systems. Based on these studies, we estimate that such methodological differences may induce shifts in the subhalo statistics by 10−20% (see more in Knebe et al. 2013; Onions et al. 2012). We acknowledge this limitation and expect that our main conclusions, which are based on relative comparisons between environments and using conservative selection cuts (i.e. requiring at least 100 particles per subhalo), remain robust.

3. Cosmic web segmentation

Choosing a useful physical definition to differentiate between the four cosmic web environments is not straightforward. Unlike the assignment of halo boundaries, where common choices often relate to the physical process of virialization, there is currently no simple physical criterion that allows one to formulate a single, clear definition of the cosmic web components. Due to the intrinsic multi-scale and multi-dimensional nature of the cosmic web, one must use somewhat arbitrary technical descriptions that may be less physically motivated. Popular choices include methods based on the eigenvalues of the Hessian of: the cosmic density field (Aragón-Calvo et al. 2007a; Nurmi et al. 2007; Bond et al. 2010); the velocity shear tensor (Hoffman et al. 2012; Pomarède et al. 2017); a combination of both density field and velocity shear tensor information (Cautun et al. 2013); and the tidal or deformation tensor (Forero-Romero et al. 2009). Other methods use watershed segmentations of the density field (Aragón-Calvo et al. 2010), the cosmic web skeleton construction using Morse theory (Sousbie 2011), and the identification of caustics (Feldbrugge et al. 2018), among others. We refer to Libeskind et al. (2018) for the most recent comprehensive presentation and comparison of the most commonly used methods.

In this work, we follow the methodology adopted by H21 and use the NEXUS+ approach for the cosmic web segmentation (first developed by Cautun et al. 2013). In contrast to H21, we employ a new implementation of an adapted version of the NEXUS+ algorithm, which will be provided in the code package CaCTus and described in detail in Naidoo et al. (in prep.)[1]. The main features of NEXUS+ relevant to our study are its ability to segment the cosmic web in a multi-scale fashion, and its parametric approach that is mostly user-free and enables a self-consistent identification of the cosmic web across all scales resolved in the simulation. As the starting point we use high-resolution density fields calculated for the COLOR simulations using a simple Cloud-In-Cell (CIC) technique. The DM density field is computed on a cubic lattice with dimensions of 256^3, with a one-dimensional grid spacing of 0.275 Mpc.

The classification of haloes into cosmic web environments can vary depending on the segmentation method, particularly for haloes near environmental boundaries. However, the NEXUS+ method (implemented here via the CaCTus code) offers a significant advantage over traditional Hessian-based classifiers. Unlike single-scale approaches that rely on fixed eigenvalue thresholds, NEXUS+ uses a multi-scale filtering strategy and self-adaptive thresholds to extract the dominant environmental signal at each location. This produces highly stable and physically motivated classifications that are less sensitive to noise or resolution effects (Cautun et al. 2013, 2014a).

Below we summarise the basic set-up and all essential components of the CaCTus implementation of the NEXUS+ algorithm, which consists of five steps.

1. First, we smooth the DM density field,

$$f(\boldsymbol{x}) \equiv \frac{\rho(\boldsymbol{x})}{\langle\rho\rangle}\,, \tag{1}$$

with a Gaussian filter and adopt several smoothing scales, R_n, resulting in a smoothed field, $f_{R_n}(\boldsymbol{x})$. The smoothing scales are chosen in increments of $R_n = 2^{n/2}R_0$, where $R_0 = 0.5$ Mpc represents the smallest scale where structures are expected to be detected. For the COLOR simulation, we use seven filter scales ranging from 0.5 to 4 Mpc. For filament and wall environments, the signatures are computed from smoothed log-density fields, while for the nodes, the signatures are computed with usual density smoothing. This is because logarithmic smoothing helps to enhance the asymmetric web-like features of filaments and walls, but is not necessary for nodes, which are roughly spherical structures (see more in Cautun et al. 2014a, 2015).

2. Second, for each filtering scale, the Hessian matrix, $\mathrm{H}_{ij,R_n}(\boldsymbol{x})$, is calculated via

$$\mathrm{H}_{ij,R_n}(\boldsymbol{x}) = R_n^2\,\left(\partial^2 f_{R_n(\boldsymbol{x})}/\partial x_i \partial x_j\right)\,, \tag{2}$$

where H_{ij} is the Hessian of the smoothed density field, and R_n^2 is a factor to normalise the Hessian across different smoothing scales. Then, the eigenvalues of the smoothed density field corresponding to each smoothing scale are computed, and are given by $\det\left(\mathrm{H}_{ij} - \lambda_a \mathrm{I}\right) = 0$, where $\lambda_1 \le \lambda_2 \le \lambda_3$.

[1] CaCTus is being prepared for public release. At the time of writing it is not yet publicly available.

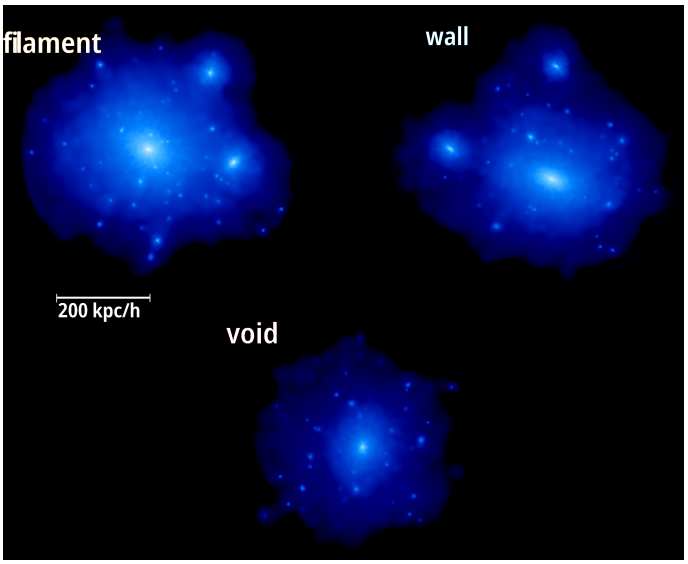

Fig. 1. Renderings of the projected density of DM in three similarly massive haloes selected from different cosmic web environments identified by CaCTus. Moving clockwise from the upper left, the haloes are selected from a filament, wall, and void environment, and have masses of $M_{200} = 8.3 \times 10^{11}$, 7.0×10^{11}, and $3.5 \times 10^{11}\, h^{-1}\,\mathrm{M}_\odot$, respectively. The void halo presented here is one of the most massive found in that environment in the COLOR volume. After adjusting for the factor of two in halo mass, the most striking difference is the relative lack of massive subhaloes in the void host when compared to the other two.

3. Third, the computed eigenvalues and their associated signs are used to determine the environmental signature at each grid element, which is labelled as a node, filament, or wall. This process requires the determination of a threshold value for the environmental signature, $S_{R_n}(x)$. The precise calculations can be found in Equations (6) and (7) of Cautun et al. (2013). Qualitatively, node environments correspond to regions with $\lambda_1 \approx \lambda_2 \approx \lambda_3 < 0$ with a minimum average density greater than $300\rho_c(z)$, and a minimum mass greater than $5 \times 10^{14}\, h^{-1}\,\mathrm{M}_\odot$. Filament environments have $\lambda_1 \approx \lambda_2 < 0$ and $|\lambda_3| \ll |\lambda_2| \backsimeq |\lambda_1|$, and walls have $\lambda_1 < 0$ and $|\lambda_1| \gg |\lambda_2| \backsimeq |\lambda_3|$. The regions that are not classified as nodes, filaments, or walls are defined as voids.
4. Fourth, steps one to three are repeated for each smoothing scale, and the resulting environmental signatures are combined into one parameter-free, multi-scale signature, $S(x) = \max[S_{R_n}(x)]$. This environmental signature traces the morphology of particular points independently of the smoothing scale, R_n.
5. Finally, cosmic web environments are then assigned to voxels in sequence, starting with clusters, then filaments, and finally walls, following Cautun et al. (2013). Cluster environments are obtained by finding the cluster signature threshold, S_c^{thresh}, where half of the cluster environments with a mass greater than $5 \times 10^{14}\, h^{-1}\,\mathrm{M}_\odot$ have a mean density greater than $300\rho_c(z)$. The regions satisfying all of the following criteria are classified as clusters:
   - The cluster signature, $S_c > S_c^{\mathrm{thresh}}$.
   - The mass is greater than $5 \times 10^{14}\, h^{-1}\,\mathrm{M}_\odot$.
   - The mean density is greater than $300\rho_c(z)$.

   For filaments, we first compute the mass, $M(S_f)$, contained in regions of the simulations which are not classified as clusters with a filament signature value that is greater than or equal to S_f. As S_f decreases, $M(S_f)$ increases. To determine a reasonable filament signature threshold, we fit a polynomial to $\partial M(S_f)^2/\partial S_f$. The peak of this curve determines the filament signature threshold, such that

$$S_f^{\mathrm{thresh}} \equiv \max\left|\frac{\partial M(S_f)^2}{\partial S_f}\right|. \tag{3}$$

   All regions that are not already classified as clusters for which $S_f > S_f^{\mathrm{thresh}}$ are then classified as filaments. We discard spurious filament classifications by removing filament structures with a volume greater than $10\, h^{-3}\mathrm{Mpc}^3$. The threshold signature value for wall environments, S_w^{thresh}, is determined in the same way as filaments substituting the wall environment signature, S_w, in place of S_f. Any regions not already classified as clusters or filaments for which $S_w > S_w^{\mathrm{thresh}}$ are classified as walls. All remaining unclassified regions are assigned as voids.

We have compared the environmental maps for the COLOR density field at $z = 0$ obtained using CaCTus with the maps used in H21, which were produced using the original NEXUS+ algorithm, and found very good agreement between the two.

4. The dependence of subhalo population properties on the cosmic web

In this section, we study several properties of the subhalo populations within the context of the cosmic web environment in which the parent halo is located. First, we bin all host haloes in three ranges of virial mass corresponding to the median values of $\langle M_{200}\rangle = 10^{10}$, 10^{11}, and $10^{12}\, h^{-1}\,\mathrm{M}_\odot$. Within each bin, we divide the host haloes into filaments, walls, and voids. H21 showed that most haloes found in node environments are either central clusters, group-mass haloes, or have been strongly processed by the tidal forces in the node (e.g. the known as backsplash haloes). For the former, a separate environmental analysis is not warranted because this category of hosts can be treated as clusters and galaxy group hosts. For the latter, the comparison with the rest of our sample is problematic. Most haloes in filaments, walls, and voids are field haloes, which facilitates the creation of samples of unperturbed host haloes in each environment. In contrast, the low-mass host haloes in samples constructed from node environments are often strongly processed and may be tidally disrupted. For example, the concentration–mass relation established for node haloes in H21 deviates by many sigma from expectations. For these reasons, in our analysis, we ignore the node environment and focus only on the host halo samples in filaments, walls, and voids. As a basic illustration of how subhalo systems compare between hosts located in different cosmic web elements, we show Fig. 1.

Additionally, we introduce a synthetic sample called the equally weighted sample, constructed by reweighting the full population of host haloes in each cosmic web environment so that the effective contribution from each environment matches that of the environment with the smallest number of host haloes within each mass bin. This approach mitigates the sensitivity of our results to cosmic variance, which depends on the specific simulation volume we use. It also allows us to control for the bias introduced by using the cosmic mean sample, which consists of the combined set of all host haloes from walls, filaments, and voids in each mass bin. This tends to favour the richest environment, which across all mass bins is the filament environment. Throughout this paper, we characterise environmental trends by expressing subhalo properties as ratios relative to two distinct reference samples: (i) the cosmic mean, and (ii) the equally

Table 1. Number density of host haloes in each host mass bin in each cosmic web environment.

$\langle M_{200}\rangle$	Host halo number density $\left(\mathrm{Mpc}^{-3}\,h^3\right)$			
$\left(h^{-1}\,\mathrm{M}_\odot\right)$	Cosmic mean	Filaments	Walls	Voids
10^{12}	1.29×10^{-4} (2149)	1.23×10^{-4} (2047)	6.75×10^{-6} (130)	–
10^{11}	1.01×10^{-3} (16 711)	5.68×10^{-4} (8640)	4.14×10^{-4} (7438)	2.50×10^{-5} (483)
10^{10}	7.72×10^{-3} (127 972)	2.87×10^{-3} (45 885)	3.71×10^{-3} (62 250)	1.13×10^{-3} (18 736)

Notes. The numbers in brackets are the total counts of host haloes. We note that we only consider haloes that have at least 1000 particles. As the void environment contains only one halo in the $\langle M_{200}\rangle = 10^{12}\,h^{-1}\,\mathrm{M}_\odot$ mass bin, we do not provide any value there.

Table 2. Host halo mass ranges of each mass bin, $\langle M_{200}\rangle$, for the halo sample in each cosmic web environment.

Sample	Mass bin $\langle\log M_{200}\,/\,h^{-1}\,\mathrm{M}_\odot\rangle$		
	12	11	10
Cosmic mean	11.72–12.72	10.72–11.72	9.72–10.72
Filaments	11.68–12.77	10.67–11.68	9.73–10.67
Walls	11.87–12.71	10.75–11.87	9.71–10.75
Voids	–	10.85–11.95	9.77–10.85

weighted sample. We denote the fractional deviation with respect to the cosmic mean as $\mathscr{D} \equiv X/X_{\rm cm} - 1$, where X denotes a given subhalo statistic or property of interest. The deviation relative to the equally weighted sample is denoted as $D \equiv X/X_{\rm eq} - 1$. These two measures, $\mathscr{D}$ and D, allow us to probe global environmental effects while reducing sensitivity to the specific cosmic web makeup of the simulation box.

For the range of masses of our hosts, the halo mass function is a steep power-law. Thus, constructing host mass bins in decades of fixed width would skew the halo mass distribution towards the lower-mass end of the bin. To alleviate this problem, we group the host haloes into three bins in such a way that the resulting median masses in each bin are: $\langle M_{200}\rangle = \left[10^{10}, 10^{11}, 10^{12}\right]\,h^{-1}\,\mathrm{M}_\odot$. Table 1 shows the number density of the host haloes (the number of haloes in a given cosmic web environment divided by the volume occupied by that specific environment) in each mass bin across different environments. We provide the range of host halo masses spanned by each bin in each cosmic web environment in Table 2.

4.1. The subhalo mass function

Other works have established that the normalised abundance of haloes, or the halo mass function, may depend on environment (Cautun et al. 2014a; Alonso et al. 2015; Libeskind et al. 2018, H21). Specifically, H21 showed that within NEXUS+ environments, the fraction of haloes distributed among different cosmic web elements strongly depends on the halo virial mass. Cluster and group-mass haloes with $M_{200} \gtrsim 10^{13}\,h^{-1}\,\mathrm{M}_\odot$ almost exclusively inhabit the densest parts of the cosmic web (i.e. the nodes). However, as the host mass decreases, less massive host haloes gradually dominate the host halo abundance in the other three environments (i.e. filaments, walls, and voids). The NEXUS+ segmentation hints at a trend towards an equipartition into those three environments at the smallest masses probed in H21, i.e. $M_{200} \approx 10^{10}\,h^{-1}\,\mathrm{M}_\odot$. The variation of halo abundance across the different cosmic web environments suggests that the averaged abundance of subhaloes should also be a function of the cosmic web environment. If the trends observed in halo abundance directly translate to subhalo abundance, then the abundance of the most massive subhaloes will be a strong function of the cosmic web environment of the host. If the most massive haloes (i.e. proto-subhaloes) live in filaments, hosts residing in voids and walls will have fewer large subhaloes. To quantify and check this, we first look at the subhalo mass function (SHMF).

In hierarchical structure formation models like CDM, it is convenient to express the subhalo mass in relation to the mass of its host. Thus, for each subhalo, we define the reduced subhalo mass, $\mu \equiv M_{\rm sub}/M_{200}$, and study the cumulative SHMF (cSHMF), $N(\geq\mu)$, which is less susceptible to random Poissonian fluctuations than a differential SHMF. This will become useful, especially for low-mass hosts from the void and wall environments, where, as we show below, the hosts have few subhaloes.

In Fig. 2 we show the mean cSHMF, $\overline{N}(\geq\,\mu)$, across each environment. Each panel corresponds to hosts binned by $\langle M_{200}\rangle$, and we differentiate the cSHMF into the following samples: hosts from the entire simulation volume (green triangles), those found in filaments (orange diamonds), walls (light blue circles), and voids (dark red squares). In addition, as mentioned earlier, as our unbiased reference point we plot the equally weighted sample (dark blue stars), drawn uniformly from all of those environments. In the middle subpanels, we show the fractional deviation, $D(\geq\mu)$, of the cSHMFs for each environmental sample with respect to the equally weighted sample. By construction, an environmental sample with $D = 0.2$ contains 20% more subhaloes than the equally weighted sample, while $D = -0.2$ indicates a 20% deficit. To provide additional context, the lower subpanels in each figure show the fractional deviation of each environment relative to the cosmic mean, denoted $D(\geq\mu)$. This serves as a cosmologically representative baseline and illustrates how the cSHMF in each environment differs from that of the entire halo population within the corresponding host mass bin. For the $\langle M_{200}\rangle = 10^{12}\,h^{-1}\,\mathrm{M}_\odot$ mass bin, we only find one host in the voids, thus, we ignore the void sample in that bin and focus only on the comparison between hosts in filament and wall environments. The error bars represent the standard error on the mean, estimated from 1000 bootstrap resamples. Finally, the two dashed lines illustrate a simple single power-law model for the cSHMF of the form $\overline{N}(\geq\,\mu) \propto \mu^{-s}$, with the scale-free case of $s = 1$ shown by the black dashed line, and the COCO simulation best-fitting cases of $s = 0.94, 0.93$, and 0.92 for each respective host mass bin (Hellwing et al. 2016) with magenta lines. Comparing our data with the dashed lines, we find that a single power-law provides a good description of the cSHMF only up to a transition point $\mu \lesssim \mu_{\rm t}$. Beyond this scale, the cSHMF exhibits a significant exponential suppression relative to the power-law fit. For our three host halo mass bins, we estimate

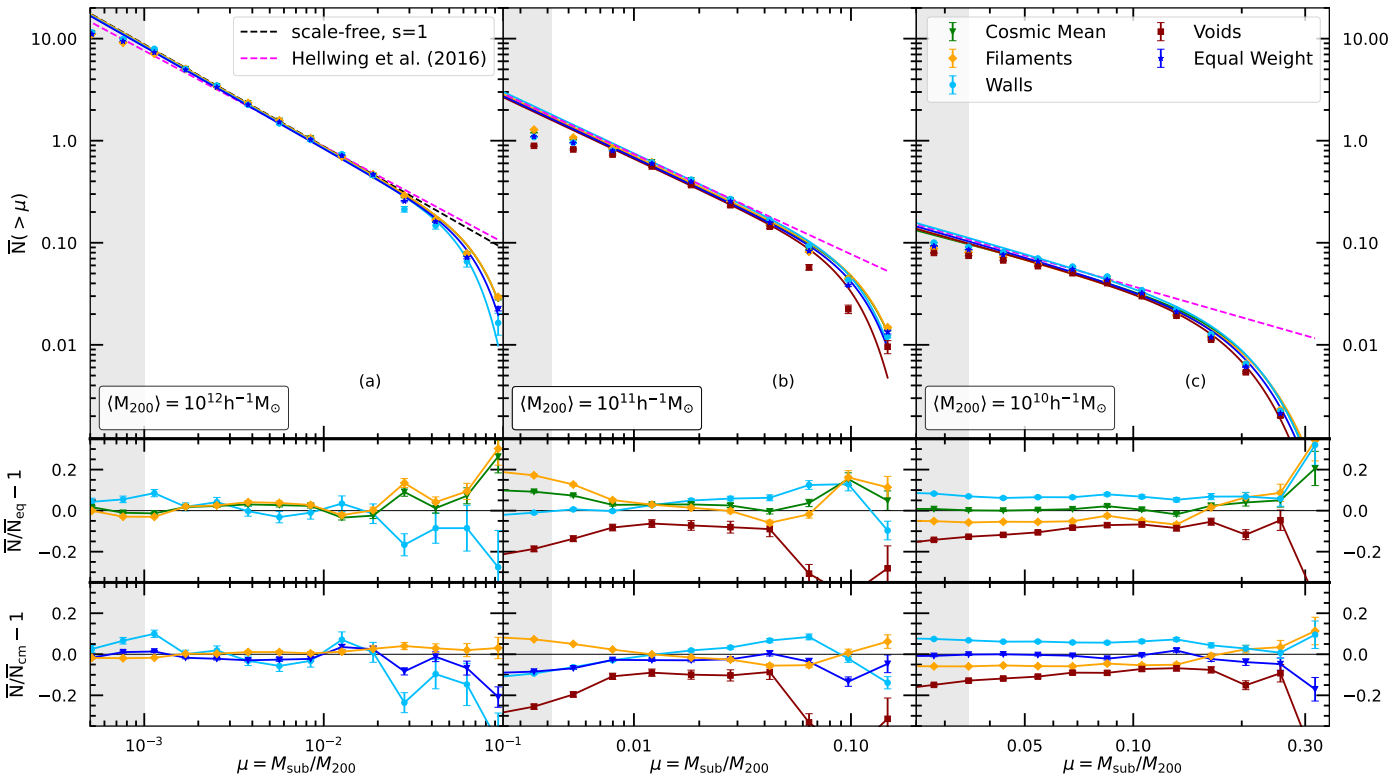

Fig. 2. Upper panels: mean cumulative subhalo mass functions for host haloes in three different mass bins, $\langle M_{200}\rangle$, shown as data points, sampled from different environments: cosmic mean (green triangles), filaments (yellow diamonds), walls (light blue circles), voids (dark red squares), and our synthetic equally weighted sample (dark blue stars). The error bars represent bootstrapped 1σ uncertainties. The solid lines with matching colours indicate the best fits to the exponential power-law model from Eq. (4). The grey shaded regions on the left of each panel indicate the subhalo resolution limit, $\mu_{\rm min}$. The two dashed lines illustrate the single power-law models for the scale-free case (black) and the best fit from the COCO simulations (magenta) of Hellwing et al. (2016). Middle panels: fractional deviation of each subhalo mass function with respect to the equally weighted sample, D. Lower panels: Fractional deviation with respect to the cosmic mean, $\mathscr{D}$. The error bars in the ratio panels show uncertainties calculated through standard error propagation. We note the different ranges of the x-axes among the panels.

Table 3. Best-fitting β values and power-law slope s for cumulative subhalo mass functions.

$\langle M_{200}\rangle \left[h^{-1}\,\mathrm{M}_\odot\right]$	Cosmic mean	Filaments	Walls	Voids	Equally weighted	Power-law slope, s
10^{12}	129 ± 4	100 ± 9	124 ± 8	–	94 ± 2	0.93 ± 0.02
10^{11}	89 ± 6	79 ± 5	95 ± 4	89 ± 2	97 ± 3	0.92 ± 0.02
10^{10}	67 ± 2	48 ± 1	54 ± 2	60 ± 2	57 ± 1	0.91 ± 0.01

Notes. The best-fitting β values are obtained from fits of Eq. (4) to the cSHMF, shown as a function of the host halo mass, in the cosmic mean, filament, wall, void, and the equally weighted samples. The final column shows the best-fitting power-law slope, s, which is independent of the host halo environment.

$\mu_{\rm t} \sim 0.03, 0.04$, and 0.1, with the transition occurring at larger subhalo-to-host mass ratios for lower-mass hosts. This trend partially reflects the effects of simulation mass resolution: lower-mass host haloes can only reliably resolve relatively massive subhaloes, effectively shifting the onset of the cutoff to higher μ. In all cases, the deviation from the power-law exceeds 10% and lies beyond the 1σ bootstrap uncertainty, indicating a statistically robust departure from scale-free behaviour. This observation primarily applies to the cosmic mean and equally weighted sample. In all cases, the void cSHMFs appear to have a noticeably steeper slope than for the hosts in COCO and the COLOR equally weighted samples. The slope for the wall sample in the most massive bin is similarly steep. Across all environmental samples in all mass bins, the shape of the cSHMF in the regime of the most massive subhaloes, $\mu \geq \mu_{\rm t}$, significantly deviates from a uniform power-law.

The exponential decay of the subhalo abundance at large μ is not surprising. Major mergers, i.e. events that correspond to the accretion of a massive subhalo, are quite rare. This makes the capture of such subhaloes intrinsically stochastic and Poissonian (Fakhouri et al. 2010). Thus, a more realistic model for the cSHMF should take the form of an exponential power-law. To illustrate this, we consider the relationship proposed by Giocoli et al. (2010):

$$\overline{N}(>\mu) = a\mu^{-s}\exp(-\beta\mu^3)\,. \tag{4}$$

Here a denotes the normalisation, s is a power-law exponent, and β is an exponential slope that determines the strength of the drop-off at high μ values. To determine the best-fitting values listed in Table 3, we fit the data only down to a specific $\mu_{\rm min}$ value. For each host mass sample, $\mu_{\rm min}$ represents the minimum converged subhalo mass, which we take to be equal to

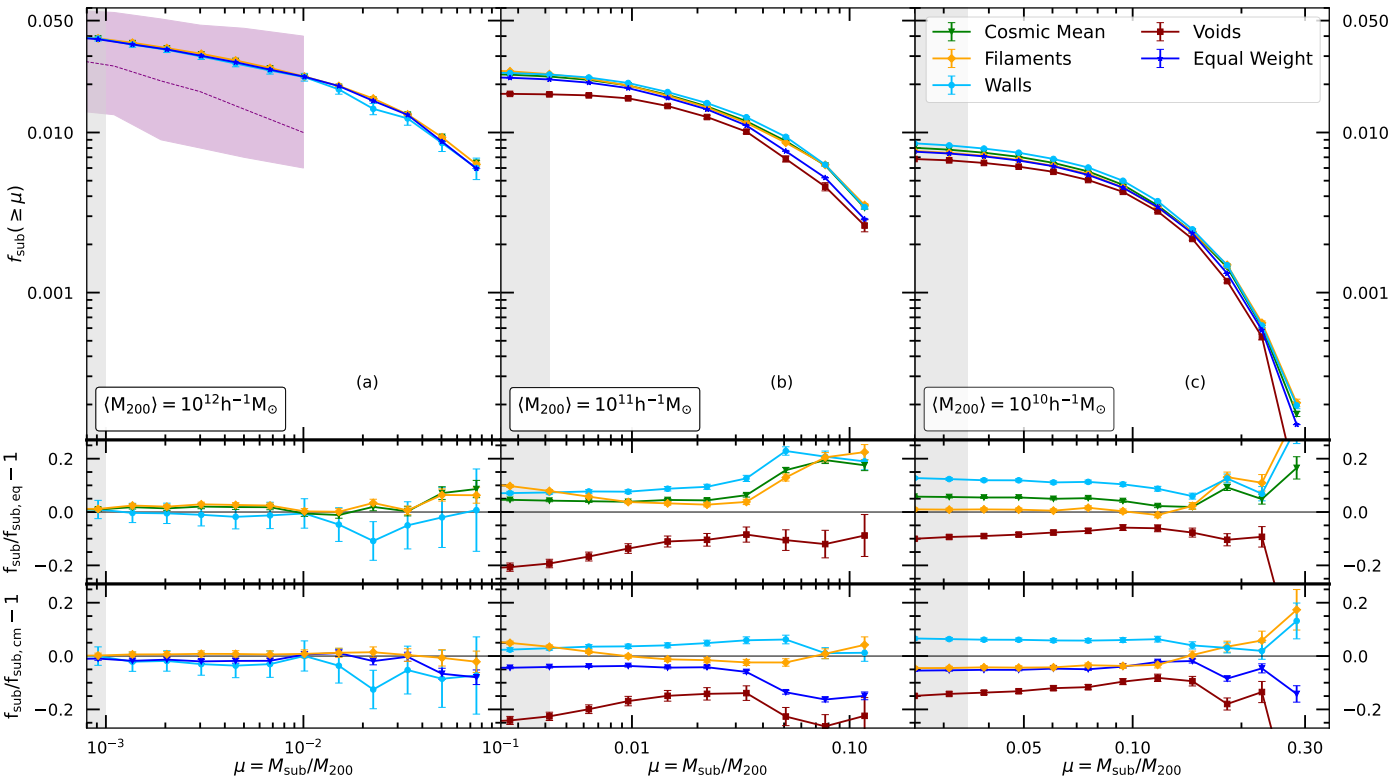

Fig. 3. Upper panels: fraction of the host halo mass in substructures. We show the same environmental samples as in Fig. 2 for the two mass bins where the μ ranges are above the resolution limits. As before, the error bars correspond to the bootstrapped 1σ errors. The grey shaded regions at the left of each panel show the subhalo resolution limit of the simulation. Middle panels: ratios of the substructure mass fraction in each environment with respect to the equally weighted sample, D. Lower panels: Ratios of the substructure mass fraction in each environment relative to the cosmic mean, $\mathscr{D}$. The error bars in the ratio panel are estimated using standard error propagation. For comparison, we show the median and 60% scatter (dashed line and shaded region) from the MILLENNIUM II simulation (Gao et al. 2011).

$100 \times m_{\rm p}$. For COLOR, this sets our limiting subhalo mass to $M_{\rm sub} = 6.19 \times 10^8\, h^{-1}\,{\rm M}_\odot$. The grey shaded region represents values below the $\mu_{\rm min}$ value for each mass bin.

Using the model from Eq. (4), we can now analyse our cSHMF in a more systematic way. In each cosmic web environment, the cSHMF is approximately universal within the μ regime where the SHMF closely follows a power-law, with only a weak dependence on the parent halo mass. This is in agreement with previous work (Diemand et al. 2004; Gao et al. 2004b; Van Den Bosch et al. 2005; Giocoli et al. 2008; Angulo et al. 2009; Chua et al. 2017; Gao et al. 2011; Jiang & Bosch 2016, H21). However, for $\mu \geq \mu_{\rm t}$ the abundance of subhaloes decreases significantly and is described by a transition from a power-law to an exponential decay. The reduction of the cSHMF amplitude is especially prominent among subhaloes found in, on average, less massive haloes, which agrees with the previous results (Van Den Bosch et al. 2005; Reed et al. 2005).

Our results from Fig. 2 show that the cSHMF can differ substantially between hosts with the same mass located in different cosmic web environments. We find that haloes located in filaments contain, on average, the highest number of subhaloes, with $0.1 \leq D(\mu \geq \mu_{\rm t}) < 0.2$ as shown in the middle subpanels. In the most massive host bin, filament subhaloes contribute the largest share of subhaloes across this μ range. For the two lower-mass host bins, subhaloes in walls outnumber those in filaments just above $\mu_{\rm t}$. Filament subhaloes regain the largest contribution at the high-μ end. In comparison, perhaps unsurprisingly, hosts found in voids typically have the fewest subhaloes, with $-0.05 \leq D(\mu \geq \mu_{\rm t}) < -0.25$. In all cases, the biggest differences between environments materialise for the large μ-values, i.e. in the regime of massive and rare subhaloes. Here, at $\mu \gtrsim \mu_{\rm t}$, the relative differences between the mean cSHMF of the environmental samples and the equally weighted samples, D can be as large as 0.25. Thus, the abundance of massive subhaloes exhibits a strong dependence on the cosmic web environment of their host. This variation is captured by the best-fit values of the β-parameter, which we provide in Table 3.

In the low subhalo mass regime ($\mu \lesssim \mu_{\rm t}$), the differences between environments are more subtle but remain consistent with the trends discussed above. For the two most massive host halo bins, the cSHMF amplitude in filaments is elevated by approximately 5–20% relative to other environments. In the lowest host mass bin, however, walls exhibit the highest subhalo abundance, exceeding other environments by 5–12%. In contrast, voids consistently show a suppressed cSHMF that is lower by 5–25% across all mass bins. The cSHMFs also show that environmental effects typically become stronger with decreasing host mass. The lower subpanels illustrate how the cSHMF in each cosmic web environment deviates from the cosmic mean, as measured by $\mathscr{D}(\geq \mu)$. In the most massive host bin, filament subhaloes closely follow the cosmic mean, with $\mathscr{D} \approx 1$. As the host mass decreases, the cSHMF in filaments is suppressed more strongly, with $\mathscr{D}$ declining from -0.02 to -0.05. In contrast, the cSHMF in walls is enhanced as the host mass increases, with $\mathscr{D}$ rising from 0.03 to 0.08. The abundance of subhaloes in void hosts remains consistently suppressed across all host mass bins, and we find the largest deficit, $\mathscr{D} = -0.15$, in massive subhaloes in the lowest-mass hosts.

Table 4. Subhalo richness: Mean total number of subhaloes with $\mu \geq 0.04$ for all our host halo mass and environment samples.

Host mass	Subhalo richness				
$\langle M_{200} \rangle \left[h^{-1}\,\mathrm{M}_\odot\right]$	Cosmic mean	Filaments	Walls	Voids	Equally weighted
10^{12}	0.147 ± 0.009	0.147 ± 0.009	0.146 ± 0.011	–	0.146 ± 0.008
10^{11}	0.138 ± 0.003	0.129 ± 0.004	0.123 ± 0.005	0.113 ± 0.019	0.124 ± 0.013
10^{10}	0.075 ± 0.001	0.074 ± 0.001	0.079 ± 0.001	0.071 ± 0.001	0.075 ± 0.001

Our results for the cSHMF show that the variation in subhalo abundance is both a function of the host mass and the cosmic web environment of the host. To reduce this complexity and obtain a more direct measure of the environmental effects, we look at the average expected total number of subhaloes above some mass threshold computed for hosts of different masses and cosmic web environments. We choose to count all subhaloes with $\mu \geq 0.04$ for a given host and compute the average per host mass bin and environment. We call this the subhalo richness because it corresponds to the mean expected number of subhaloes for a given host sample. We have collected the subhalo richness computed for all our host samples in Table 4. Subhalo richness exhibits a consistent host mass-dependent decline across environments. In the equally weighted sample, richness decreases by ∼14% from the 10^{12} to $10^{11}\,h^{-1}\,\mathrm{M}_\odot$ bin, followed by a steeper 40% drop to the $10^{10}\,h^{-1}\,\mathrm{M}_\odot$ bin. Filament and wall environments show similar trends, with initial reductions of 12% and 16%, respectively, between the two higher-mass bins, followed by more substantial decreases of 43% and 44% to the lowest-mass bin. In contrast to other environments, the void sample shows a more moderate reduction in subhalo richness, decreasing by 37% from the 10^{11} to $10^{10}\,h^{-1}\,\mathrm{M}_\odot$ bin.

The higher subhalo richness of hosts in filaments can be attributed to the dynamic environment that filaments provide for halo interactions and mergers. Haloes within filaments are situated in regions of higher matter density and experience stronger tidal forces, increasing the likelihood of substructure accretion through frequent gravitational encounters and mergers (Hahn et al. 2007b; Ganeshaiah Veena et al. 2018). In contrast, more underdense regions such as voids are characterised by slower structure formation, weaker tidal fields, and reduced merger activity. Consequently, haloes in voids tend to form later and accrete much less external material compared to their counterparts in denser environments (Gao et al. 2004a; Hahn et al. 2007b; Hellwing et al. 2021).

Another interesting quantity to investigate in the context of cosmic web effects is the fraction of the total mass of haloes contained in subhaloes,

$$f_{\mathrm{sub}}(\geq \mu_0) = \int_{\mu_0}^{1} \mu \frac{\mathrm{d}N}{\mathrm{d}\mu}. \tag{5}$$

We can understand this as an effective measure of the halo granularity. Haloes with low fractions of mass locked in subhaloes should exhibit smoother density profiles, while in contrast large f_{sub} might indicate violent virialisation in progress and/or a significant number of recent mergers. Previous studies of high-resolution N-body simulations have established that typically the mass fraction locked in subhaloes (for $\mu \gtrsim 10^{-4}$–10^{-2}) ranges from 5 to 20% of the host mass (Ghigna et al. 1998, 2000; de Lucia et al. 2004; Gao et al. 2004b, 2011; Contini et al. 2012).

In Fig. 3 we show the cumulative mass fraction in subhaloes as a function of the normalised subhalo mass, μ, for our five standard samples. The middle panels display the fractional deviation of the cumulative subhalo mass fraction, $D(\geq \mu)$, for each environmental sample relative to the equally weighted baseline. The lower subpanels show the corresponding fractional deviation, $\mathscr{D}(\geq \mu)$, measured with respect to the cosmic mean sample. The variation across different cosmic web environments is not dramatic, with f_{sub} typically deviating by 2–20% from the equally weighted sample. For the majority of the samples, this observed effect is weak but statistically distinguishable within the 1σ bootstrap errors. There are a couple of interesting points of attention concerning the results shown in Fig. 3. First, we note that for the $\langle M_{200} \rangle = 10^{12}\,h^{-1}\,\mathrm{M}_\odot$ sample, our results agree well with what Gao et al. (2011) obtained for comparable host masses in the MILLENNIUM-II Simulation (shown with the dashed line and corresponding purple shaded region). For this host mass bin, the filament sample has higher mass fractions and the wall population exhibits lower values than the equally weighted sample. For the $\langle M_{200} \rangle = 10^{11}\,h^{-1}\,\mathrm{M}_\odot$ bin, we also see a bimodal effect on f_{sub}, but now where both filament and wall hosts have, on average, higher subhalo mass fractions, while only the void population displays lower values. The variation of f_{sub} with cosmic web environment is a sizeable effect which can potentially be important for strong lensing mass modelling studies. We leave a more thorough investigation into this matter for future studies.

4.2. The subhalo velocity function

So far, we have used the total subhalo mass, as identified by SUBFIND, to characterise the subhalo size. It is well known that, once subhaloes start orbiting within their hosts, they are subject to a strong and non-linear tidal mass stripping process. This makes the subhalo mass a less stable and sometimes even poorly defined quantity. Another way to characterise the size of a subhalo is to use the maximum of its circular orbit velocity, V_{max}. This quantity is less affected by the strong tidal processing of the subhalo because it depends on the total enclosed mass of the subhalo. Several studies have demonstrated that for many applications V_{max} is a robust halo size description (Ghigna et al. 1998, 2000; Muldrew et al. 2011; Knebe et al. 2011; Onions et al. 2012; Knebe et al. 2013; Cautun et al. 2014c).

Here, we use the subhalo velocity functions as another measure of subhalo size and abundance. The circular velocity, denoted as V_{circ}, is conventionally expressed as

$$V_{\mathrm{circ}} \equiv \sqrt{\frac{GM(<r)}{r}}, \tag{6}$$

where $M(<r)$ is the mass enclosed inside a sphere of radius, r, centred at the (sub)halo centre. Each subhalo has the maximum circular velocity, V_{max}, which represents the peak value of the circular velocity profile that is attained at a radius R_{max}. We use

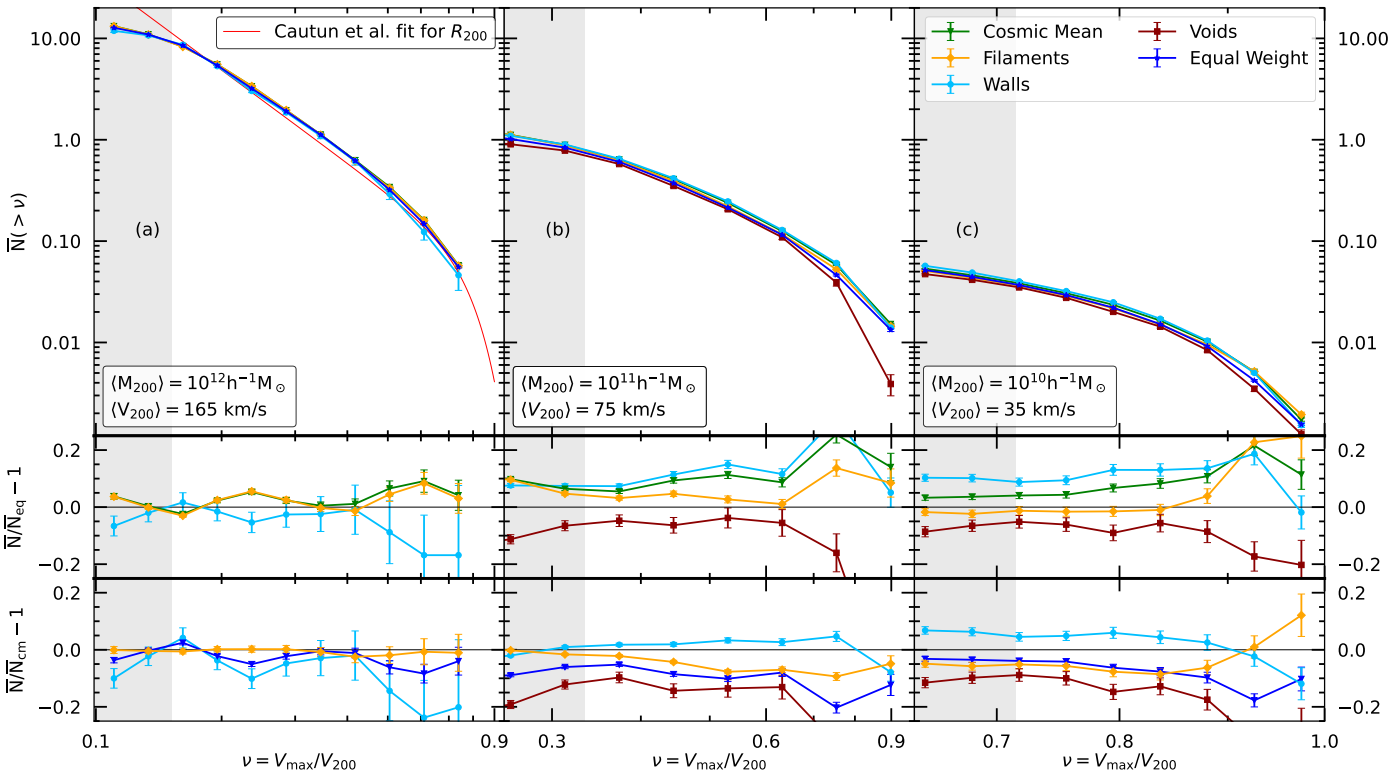

Fig. 4. Upper panels: mean cumulative distribution of subhaloes within R_{200} as a function of $\nu = V_{max}/V_{200}$ in the cosmic mean sample (green triangles), filaments (yellow diamonds), walls (light blue circles), voids (dark red squares), and the equally weighted sample (dark blue stars) for different host masses. The solid lines simply connect the data points, in contrast to Fig. 2 in which they represent fits to the data. In the legend, we provide the median V_{200} for the given host halo mass bin. The solid red line in the figure depicts the best-fit function from Cautun et al. (2014c) for subhaloes within the radius R_{200}. The error bars represent the standard error on the mean, estimated from 1000 bootstrap resamples. Middle panels: Fractional deviation of $\overline{N}(>\nu)$ for each environment compared to the cumulative velocity function of an equally weighted sample, D. Lower panels: Deviation of $\overline{N}(>\nu)$ with respect to cosmic mean sample, $\mathscr{D}$. The uncertainties shown in the ratio panels were computed through standard error propagation.

V_{max} as a stable measure of the abundance of the subhalo population.

In Fig. 4, we show the cumulative abundance of subhaloes (SHVF), $\overline{N}(>\nu)$, as a function of $\nu = V_{max}/V_{200}$, where V_{200} is the circular velocity of the host halo at R_{200}. The subhaloes in bins of host masses (now with the corresponding $\langle V_{200}\rangle$ values) across different environments are presented in the same manner as described in Fig. 2. The solid red line presents the best-fit to the mean subhalo count in Milky Way-mass haloes within R_{200} of the host from Cautun et al. (2014c). The middle subpanels show the fractional deviation of the SHVF, $D(>\nu)$, of each environmental sample with respect to the equally weighted sample. The lower subpanels present the fractional deviation compared to the cosmic mean sample, $\mathscr{D}(>\nu)$. The qualitative behaviour with host samples and environments is similar to what we have seen in Fig. 2, albeit with some slight differences. As the host halo mass decreases, the dependence on the cosmic web environment increases. The environmental dependence of the abundance of subhaloes observed in Fig. 2 is confirmed in Fig. 4. However, while the SHMF shows a strong dependence on host halo mass, the SHVF exhibits a weaker but still noticeable dependence on host mass, consistent with findings from previous studies (Hellwing et al. 2016; Moliné et al. 2023). The fact that the environmental trends depicted both in SHMF and SHVF are in large qualitative agreement reassures us that the trends and effects we see here are real and robust down to the simulation resolution limit.

4.3. The V_{max}–R_{max} relation

In cosmologies that describe hierarchical structure formation, such as the CDM model, halo (and thus also subhalo) density profile concentrations correlate with specific formation times. This relationship arises because, during the hierarchical assembly of (sub)haloes, the innermost regions are the first to form. Material accreted later tends to have higher angular momentum, preventing it from settling in the central parts of the (sub)halo mass distribution. Consequently, the inner regions of (sub)halo density profiles are dynamically old, and the density achieved during assembly determines the (sub)halo concentration. As the Universe's average background density decreases over time, older (sub)haloes typically exhibit higher central densities and concentrations (Wechsler et al. 2002; Gao et al. 2004b; Springel et al. 2008; Mao et al. 2015; Ludlow et al. 2016). Previous works (Bullock et al. 2001; Macció et al. 2007; Alonso et al. 2015, H21) have shown that halo concentration is dependent on the cosmic web environment. We want to check if this correlation is also exhibited by the host's subhalo population. This corresponds to a picture where sub(haloes) forming in dense environments are likely to be more concentrated and form earlier (Bullock et al. 2001; Sheth & Tormen 2004; Avila-Reese et al. 2005; Harker et al. 2006; Wechsler et al. 2006; Maulbetsch et al. 2007; Ludlow et al. 2016; Chen et al. 2020).

To study the subhalo density profiles, we exploit the V_{max}–R_{max} relation. This can be readily used to study the internal kinematics and the associated density profiles of (sub)haloes

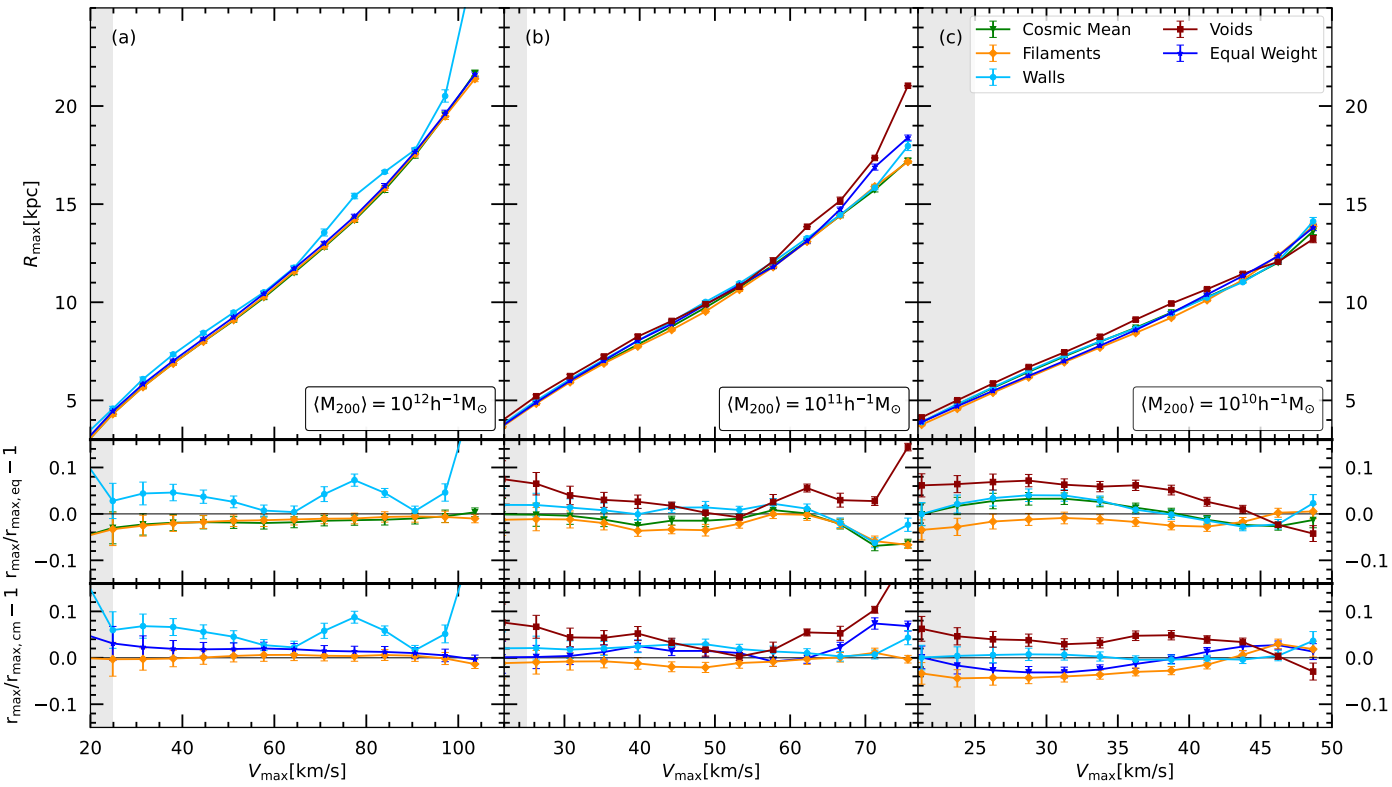

Fig. 5. The mean V_{max}–R_{max} relation of the subhaloes within R_{200} for different host masses across different cosmic web environments. The error bars show the bootstrap errors on the mean. The grey shaded regions at the left of each panel show the subhalo resolution limit of the simulation. Upper panels: Solid lines with error bars represent subhaloes in voids (squares), walls (circles), filaments (diamonds), the cosmic mean sample (triangles), and the equally weighted sample (stars). Middle panels: Fractional deviation of the R_{max} values of each environment from that of the equally weighted sample, D. Lower panels: Relative divergence of R_{max} values compared to the full-volume sample, $\mathscr{D}$. In the ratio panels, the error bars represent the uncertainty obtained via standard error propagation.

(Springel et al. 2008; Hellwing et al. 2016). The relation stems from a strong correlation of (sub)halo internal kinematics with the internal mass distribution, allowing a reliable estimation of the steepness of the (sub)halo mass profile. Extra care should be taken here since the V_{max} can be affected by the gravitational softening length (ϵ). The general effect can lead to a reduction in the maximum circular velocities of subhaloes, particularly when the value of R_{max} is not significantly greater than ϵ. To address this, following Hellwing et al. (2016), we have applied the adequate correction proposed by Eq. (10) in Springel et al. (2008). This correction compensates approximately for the gravitational softening effect on V_{max}.

In Fig. 5, we show the mean V_{max}–R_{max} relation for our subhalo populations in various host and environmental samples. The error bars indicate the bootstrapped uncertainty on the means. To better highlight the trends, the middle subpanels show the fractional deviation, D, of the different samples taken with respect to the equally weighted one, while the lower subpanels display the same quantity but computed relative to the cosmic mean sample, $\mathscr{D}$. The grey shaded region represents the area below the resolution limit of the COLOR box, $V_{max} = 25\,\mathrm{km\,s^{-1}}$ (see Hellwing et al. 2016 for more detailed analysis).

From Fig. 5 we draw three important findings. First, the mean R_{max} values for filament samples are lower than for other environments at fixed V_{max}. The middle subpanels in Fig. 5 show the fractional deviation of subhaloes in filaments with respect to the equally weighted sample, showing 1–8% suppression. This implies that, compared to walls and voids, subhaloes found in hosts in filaments have, on average, more concentrated density profiles. Conversely, the subhalo populations residing in haloes within voids have the highest mean R_{max} values, with showing a 1–8% enhancement. This suggests that subhaloes living in systems found in voids have, on average, less concentrated density profiles than the cosmic mean predicted for the whole CDM population.

Secondly, we find that the V_{max}–R_{max} relationship is affected more strongly by the environment as the host mass decreases. When examining the residuals in the $10^{11}\,h^{-1}\,\mathrm{M}_\odot$ bin (middle column of Fig. 5, middle subpanel), the largest differences between subhaloes in any given environment and the equally weighted sample ranges from 2 to 8%. However, this increases to approximately 3–9% in the $10^{10}\,h^{-1}\,\mathrm{M}_\odot$ bin (middle subpanel of the right-hand column of Fig. 5).

The lower subpanels of Fig. 5 highlight how the R_{max}–V_{max} relation varies with environment relative to the average across all hosts within the same mass bin. In the highest-mass bin, filament subhaloes show mean R_{max} values that closely follow the cosmic mean. However, towards lower host masses, their R_{max} values fall increasingly further below the cosmic mean, with $\mathscr{D}$ increasing in magnitude from about 2% to 5% below the mean. Wall subhaloes, by contrast, start ∼10% above the cosmic mean, then gradually approach the mean as host mass decreases. Subhaloes in voids remain consistently above the cosmic mean across all bins, with their largest deviation ($\mathscr{D} \sim 0.08$) appearing at the low-mass end.

One of the small-scale ΛCDM discrepancies, which was underscored by Boylan-Kolchin et al. (2011), is known as the too big to fail (TBTF) problem. It arises from a difference

between the distribution of internal properties inferred for the most massive satellites of Milky Way mass hosts in the AQUARIUS simulation suite and the internal properties of the observed dwarf Milky Way satellites (Boylan-Kolchin et al. 2012). A similar assertion was made for the field dwarf galaxies discovered in the Local Group (Garrison-Kimmel et al. 2014). Many possible reasons have been proposed for the discrepancy, with some suggesting that processes connected to baryonic physics can lower the $V_{\rm max}$ values of subhaloes hosting dwarf galaxies, while others claim that assuming a lower virial mass of the Galactic DM halo (Sawala et al. 2013) could significantly alleviate the problem, given the strong correlation between the abundance of high $V_{\rm max}$ satellites and the host virial mass (Cautun et al. 2014b). The second feature we observe in Fig. 5 carries significant implications for the TBTF problem. Moving the Milky Way halo from a cosmic filament to a cosmic wall alleviates the TBTF problem by decreasing the number of high $V_{\rm max}$ satellites while increasing their $R_{\rm max}$ values. Our results also signify the importance of control over the cosmic environment when constructing theoretical predictions for subhalo kinematic and density distributions.

The third important observation concerns a trend associated with the mass of the parent halo. Specifically, at fixed $V_{\rm max}$, subhaloes exhibit systematically lower mean $R_{\rm max}$ values when they are hosted by lower-mass haloes. To provide further detail, the environmental effects above $V_{\rm max} = 80\,{\rm km\,s^{-1}}$ become noticeable within the $10^{12}\,h^{-1}\,{\rm M}_\odot$ mass bin. The difference becomes progressively pronounced, approximately ranging from 3 to 8% across all $V_{\rm max}$ values for bins within the range 10^{10}–$10^{11}\,h^{-1}\,{\rm M}_\odot$.

5. Summary and discussion

In this paper we analysed the impact of the cosmic web environment on the subhalo populations of host haloes at $z = 0$. To do this, we employed the CaCTus implementation of the NEXUS+ algorithm to segment the COLOR Gravity-only N-body simulation into four cosmic web environments (see Sections 2 and 3). We disentangled the competing effects of the host halo on the subhalo properties from those of the environment by dividing the subhalo populations into bins according to the masses of their hosts. We focused on host haloes with masses in the range $\langle M_{200}\rangle = 10^{10}$ to $10^{12}\,h^{-1}\,{\rm M}_\odot$. Our results extend previous studies that had already identified a strong relationship between DM halo properties and their respective locations within the cosmic web to smaller intrahalo scales.

Our main findings can be summarised as follows:

- At fixed host mass, the abundance of subhaloes depends on the cosmic web environment of their hosts (Fig. 2). Host haloes with $\langle M_{200}\rangle = 10^{10}\,h^{-1}\,{\rm M}_\odot$ in walls have subhaloes that are as much as two times more massive than hosts with the same mass in voids. At subhalo masses below $\mu_{\rm t}$ the abundance of subhaloes in wall haloes is only 25% greater than in void haloes. The size of these differences decreases as the host halo mass is increased.
- The measure of the halo granularity, the mass fraction in subhaloes, $f_{\rm sub}$, shows a sizeable variation with the cosmic web (Fig. 3). Here, typically filament hosts tend to be more granular, with 2–15% more mass in subhaloes than void hosts. Void hosts, on the other hand, have 5–15% less mass in subhaloes and are characterised by a smoother density distribution. Generally, lower-mass hosts show a stronger dependence on the cosmic web.
- The absolute difference in velocity functions between different environments is smaller than the difference in mass functions (Fig. 4). Subhaloes in filaments have 5–15% higher subhalo abundance in the velocity function, while subhaloes in voids have 5–25% lower abundance relative to the cosmic mean. This is because subhaloes with similar masses can have very different $V_{\rm max}$.
- The relative differences between the velocity functions in various environments are generally smaller than what we observe for mass functions. Generally, we start to observe a greater than 10% environmental difference in the velocity function above $0.5\,V_{200}$ for the most massive host bin. For lower-mass hosts, the differences are seen for a larger range of subhalo ν values.
- Subhaloes in filaments are most concentrated, and those in voids are least concentrated (Fig. 5). This corresponds to an approximate 5 to 9% suppression in concentration for void subhaloes relative to filament subhaloes across all host mass bins, although in the $10^{12}\,h^{-1}\,{\rm M}_\odot$ bin it is largely absent below $V_{\rm max} = 80\,{\rm km\,s^{-1}}$.
- The characteristic density profile also displays a dependence on the parent halo mass by showing a reduction of $R_{\rm max}$ value as the host halo mass decreases.

Our results indicate that the abundance and internal properties of subhalo populations depend on the cosmic web environment of their host. The influence of this environment becomes stronger as the host halo mass decreases below the Milky Way mass scale. Studies that do not account for this intrinsic link between the properties of subhalo populations and the large-scale environment may be affected by systematic uncertainties that bias their results.

In this paper we analysed the SHMF as a function of $\mu = M_{\rm sub}/M_{200}$ in different cosmic web environments. The SHMF exhibits a dependence on the cosmic web environment in which they are located. The environmental effect on the mass function becomes more noticeable with decreasing host halo mass. This is consistent with the same trend observed in the host halo mass function, as previously demonstrated in H21. Our results specifically revealed the relative differences in the SHMFs across different environments exceeding 10% at lower host mass ranges. Subhaloes in voids exhibited consistently lower numbers compared to those in filaments and walls. Interestingly, the normalisation and the power-law slope of the mass functions displayed a similar pattern across all environments and with a slight dependence on host masses. However, the exponential slope, β, influencing the drop-off at the higher-mass end, shows a dependence on the cosmic web environment and the parent halo mass. Furthermore, in agreement with previous studies (Gao et al. 2004a; Giocoli et al. 2008; Ishiyama et al. 2013), our findings demonstrate a dependency of the SHMF on the host halo mass.

The fraction of the host mass contained in subhaloes, $f_{\rm sub}$, is highest in filament environments, indicating that filament hosts are more substructure-rich, or more granular, than their counterparts in other cosmic web environments. This supports the idea that filaments promote subhalo accretion and survival through enhanced merger activity (Bond et al. 1996; Colberg et al. 2005; Ma et al. 2025). By contrast, haloes in voids tend to exhibit smoother density profiles, reflecting their more isolated and quiescent environments and assembly histories. These findings are consistent with the results of Hellwing et al. (2021), who showed that halo accretion histories are affected strongly by their cosmic web environment, with filament haloes undergoing more frequent mergers.

In addition, we analysed the subhalo velocity function to investigate an alternative perspective on the abundance of subhaloes within the cosmic web. It shows a similar dependence

on the cosmic web environment such as the mass function. The environmental effect on the velocity functions becomes more pronounced with decreasing parent halo mass. In a manner similar to the mass function, subhaloes hosted by haloes within filaments exhibit a higher population count compared to those in walls and voids in massive host haloes. However, a shift occurs in the case of low-mass hosts, where subhaloes hosted by haloes located in walls show a larger population than those in other environments, and the relative difference is 5–10% higher than in the mass function.

Furthermore, we investigated the $V_{\rm max}-R_{\rm max}$ relation of subhaloes, which characterises the concentration or characteristic density of subhaloes based on their maximum circular velocity and radius. This comprehensive analysis revealed different density profiles among subhaloes hosted by haloes residing within filaments, walls, and voids. Particularly, subhaloes within filaments and walls exhibited, on average, more concentrated density profiles compared to those inhabiting voids. Moreover, we found that this relation is affected by the mass of their host haloes. Interestingly, a discernible trend emerged: subhalo characteristics displayed lower dependence on cosmic web environments within higher-mass host haloes. However, a more substantial environmental impact became apparent with decreasing host halo mass. Notably, subhaloes hosted within filaments exhibited significantly more concentrated density profiles, particularly within lower-mass parent haloes, compared to those within massive hosts. Conversely, subhaloes in voids show on average less concentrated density profiles than in other environments. Another noteworthy feature of our results is that subhaloes tend to display lower $R_{\rm max}$ values when associated with low-mass hosts, especially in contrast to subhaloes hosted by massive haloes. This finding suggests that the characteristic density of subhaloes is not exclusively determined by their environmental location but is notably influenced by the mass of the parent halo.

It is well established that the overall properties of a subhalo, such as its mass measured at the virial radius, can be determined reliably with as few as 50−100 simulation particles (e.g. Springel et al. 2008; Onions et al. 2012; van den Bosch & Jiang 2016; Ludlow et al. 2019). However, such low particle counts are generally insufficient to accurately characterise the internal properties of subhaloes, such as their circular velocity profiles or concentrations. Studies have shown that subhaloes resolved with fewer than 3000 particles can exhibit significant deviations in their internal properties from converged results (Errani & Navarro 2021). Additionally, the choice of softening length and simulation time-step can further elevate the required resolution limit (van den Bosch & Ogiya 2018). The COLOR subhalo populations are not immune to numerical resolution effects, which can introduce both random and systematic biases. However, in our analysis, we mitigate these biases by studying the averaged internal properties of subhaloes within fixed mass and $V_{\rm max}$ bins. Importantly, we carefully compare subhalo populations using equally weighted samples constructed from hosts within the same bin. This approach largely eliminates systematic uncertainties arising from finite resolution effects when interpreting our results. While numerical instabilities can introduce additional random scatter in the properties of subhaloes, they do not strongly affect the intrinsic differences in the average properties caused by the cosmic web environment. As a result, our findings remain robust down to the resolution limits of the simulations in the mass ranges we consider.

An important consideration in our analysis is the relatively small volume of the COLOR simulation ($\sim 100^3$ Mpc^3), which may introduce some level of cosmic variance in the distribution of cosmic web environments. However, comparisons of volume and mass-filling fractions between COLOR and the larger Millennium simulation (Springel et al. 2005; Boylan-Kolchin et al. 2009), as reported by Hellwing et al. (2021), indicate that such effects are unlikely to significantly impact our results. Although some variation is expected due to the finite box size, our focus on relative differences across environments-rather than absolute values-helps preserve the robustness of our conclusions. Moreover, the use of an equally weighted sampling scheme, which enforces uniform representation across environments, further mitigates biases that could arise from the overabundance of structures like filaments in the full-volume distribution. A more detailed assessment of cosmic variance, particularly in underdense environments such as voids, is deferred to future work.

Addressing the 'small-scale challenges to the ΛCDM paradigm' requires a comprehensive approach that accounts for the influence of the cosmic environment. This research is the next step towards understanding the detailed influence of large-scale structures on the distribution and formation mechanisms of satellite galaxies. We will explore the dependence of the properties of subhaloes on the cosmic web environment in alternative DM scenarios and at higher redshifts in future work.

Acknowledgements. We thank the anonymous referee for insightful comments and questions that have helped improve the paper. We would like to thank Marius Cautun for constructive communication and comments on the implementation of NEXUS+ algorithm. Mariana Jaber, Rob Crain, Adi Nusser, Rien van de Weygaert, and Mike Hudson are acknowledged for enlightening discussions we had at various stages of this project. This work is supported via the research projects 'COLAB' and 'LUSTRE' funded by the National Science Center, Poland, under agreement number UMO-2020/39/B/ST9/03494 and UMO-2018/31/G/ST9/03388. MB is also supported by the Polish National Science Center through grants no. 2020/38/E/ST9/00395 and 2018/30/E/ST9/00698.

References

Adler, R. J. 1981, The Geometry of Random Fields (New York: Wiley)
Alonso, D., Eardley, E., & Peacock, J. A. 2015, MNRAS, 447, 2683
Angulo, R. E., Lacey, C. G., Baugh, C. M., & Frenk, C. S. 2009, MNRAS, 399, 983
Aragón-Calvo, M. A., Jones, B. J. T., van de Weygaert, R., & van der Hulst, J. M. 2007a, A&A, 474, 315
Aragón-Calvo, M. A., van de Weygaert, R., Jones, B. J. T., & van der Hulst, J. M. 2007b, ApJ, 655, L5
Aragón-Calvo, M. A., Platen, E., van de Weygaert, R., & Szalay, A. S. 2010, ApJ, 723, 364
Aragon Calvo, M. A., Neyrinck, M. C., & Silk, J. 2019, Open J. Astrophys., 2, 7
Avila-Reese, V., Colín, P., Gottlöber, S., Firmani, C., & Maulbetsch, C. 2005, ApJ, 634, 51
Bardeen, J. M., Bond, J. R., Kaiser, N., & Szalay, A. S. 1986, ApJ, 304, 15
Benítez-Llambay, A., Navarro, J. F., Abadi, M. G., et al. 2013, ApJ, 763, L41
Blumenthal, G. R., Faber, S. M., Primack, J. R., & Rees, M. J. 1984, Nature, 311, 517
Bond, J. R., Kofman, L., & Pogosyan, D. 1996, Nature, 380, 603
Bond, N. A., Strauss, M. A., & Cen, R. 2010, MNRAS, 409, 156
Bose, S., Hellwing, W. A., Frenk, C. S., et al. 2016, MNRAS, 455, 318
Boylan-Kolchin, M., Springel, V., White, S. D. M., Jenkins, A., & Lemson, G. 2009, MNRAS, 398, 1150
Boylan-Kolchin, M., Bullock, J. S., & Kaplinghat, M. 2011, MNRAS, 415, L40
Boylan-Kolchin, M., Bullock, J. S., & Kaplinghat, M. 2012, MNRAS, 422, 1203
Bullock, J. S., Kolatt, T. S., Sigad, Y., et al. 2001, MNRAS, 321, 559
Cautun, M., van de Weygaert, R., & Jones, B. J. T. 2013, MNRAS, 429, 1286
Cautun, M., van de Weygaert, R., Jones, B. J. T., & Frenk, C. S. 2014a, MNRAS, 441, 2923
Cautun, M., Frenk, C. S., van de Weygaert, R., Hellwing, W. A., & Jones, B. J. T. 2014b, MNRAS, 445, 2049
Cautun, M., Hellwing, W. A., van de Weygaert, R., et al. 2014c, MNRAS, 445, 1820
Cautun, M., Bose, S., Frenk, C. S., et al. 2015, MNRAS, 452, 3838
Chen, Y., Mo, H. J., Li, C., et al. 2020, ApJ, 899, 81

Chua, K. T. E., Pillepich, A., Rodriguez-Gomez, V., et al. 2017, MNRAS, 472, 4343
Colberg, J. M., Krughoff, K. S., & Connolly, A. J. 2005, MNRAS, 359, 272
Colless, M., Peterson, B. A., Jackson, C., et al. 2003, ArXiv e-prints [arXiv:astro-ph/0306581]
Contini, E., De Lucia, G., & Borgani, S. 2012, MNRAS, 420, 2978
Danovich, M., Dekel, A., Hahn, O., Ceverino, D., & Primack, J. 2015, MNRAS, 449, 2087
Darvish, B., Mobasher, B., Martin, D. C., et al. 2017, ApJ, 837, 16
Davis, M., Efstathiou, G., Frenk, C. S., & White, S. D. M. 1985, ApJ, 292, 371
de Lapparent, V., Geller, M. J., & Huchra, J. P. 1986, ApJ, 302, L1
de Lucia, G., Kauffmann, G., Springel, V., et al. 2004, MNRAS, 348, 333
Deason, A. J., Bose, S., Fattahi, A., et al. 2022, MNRAS, 511, 4044
Diemand, J., Moore, B., & Stadel, J. 2004, MNRAS, 353, 624
Dome, T., Fialkov, A., Sartorio, N., & Mocz, P. 2023, MNRAS, 525, 348
Doroshkevich, A. G. 1970, Astrophysics, 6, 320
Dressler, A. 1980, ApJ, 236, 351
Dupuy, A., Libeskind, N. I., Hoffman, Y., et al. 2022, MNRAS, 516, 4576
Enzi, W., Murgia, R., Newton, O., et al. 2021, MNRAS, 506, 5848
Errani, R., & Navarro, J. F. 2021, MNRAS, 505, 18
Fakhouri, O., Ma, C.-P., & Boylan-Kolchin, M. 2010, MNRAS, 406, 2267
Feldbrugge, J., van de Weygaert, R., Hidding, J., & Feldbrugge, J. 2018, JCAP, 2018, 027
Forero-Romero, J. E., Hoffman, Y., Gottlöber, S., Klypin, A., & Yepes, G. 2009, MNRAS, 396, 1815
Forero-Romero, J. E., Contreras, S., & Padilla, N. 2014, MNRAS, 443, 1090
Frenk, C. S., & White, S. D. M. 2012, Annalen der Physik, 524, 507
Gámez-Marín, M., Santos-Santos, I., Domínguez-Tenreiro, R., et al. 2024, ApJ, 965, 154
Ganeshaiah Veena, P., Cautun, M., van de Weygaert, R., et al. 2018, MNRAS, 481, 414
Ganeshaiah Veena, P., Cautun, M., Tempel, E., van de Weygaert, R., & Frenk, C. S. 2019, MNRAS, 487, 1607
Ganeshaiah Veena, P., Cautun, M., van de Weygaert, R., Tempel, E., & Frenk, C. S. 2021, MNRAS, 503, 2280
Gao, L., Lucia, G. D., White, S. D., & Jenkins, A. 2004a, MNRAS, 352, L1
Gao, L., White, S. D. M., Jenkins, A., Stoehr, F., & Springel, V. 2004b, MNRAS, 355, 819
Gao, L., Springel, V., & White, S. D. M. 2005, MNRAS, 363, L66
Gao, L., Frenk, C. S., Boylan-Kolchin, M., et al. 2011, MNRAS, 410, 2309
Gao, L., Navarro, J. F., Frenk, C. S., et al. 2012, MNRAS, 425, 2169
Garrison-Kimmel, S., Boylan-Kolchin, M., Bullock, J. S., & Kirby, E. N. 2014, MNRAS, 444, 222
Ghigna, S., Moore, B., Governato, F., et al. 1998, MNRAS, 300, 146
Ghigna, S., Moore, B., Governato, F., et al. 2000, ApJ, 544, 616
Gillet, N., Ocvirk, P., Aubert, D., et al. 2015, ApJ, 800, 34
Giocoli, C., Tormen, G., & Van Den Bosch, F. C. 2008, MNRAS, 386, 2135
Giocoli, C., Tormen, G., Sheth, R. K., & van den Bosch, F. C. 2010, MNRAS, 404, 502
González, R. E., & Padilla, N. D. 2016, ApJ, 829, 58
Guo, Q., Tempel, E., & Libeskind, N. I. 2015, ApJ, 800, 112
Hahn, O., Carollo, C. M., Porciani, C., & Dekel, A. 2007a, MNRAS, 381, 41
Hahn, O., Porciani, C., Carollo, C. M., & Dekel, A. 2007b, MNRAS, 375, 489
Hammer, F., Yang, Y., Fouquet, S., et al. 2013, MNRAS, 431, 3543
Han, J., Jing, Y. P., Wang, H., & Wang, W. 2012, MNRAS, 427, 2437
Han, J., Cole, S., Frenk, C. S., & Jing, Y. 2016, MNRAS, 457, 1208
Harker, G., Cole, S., Helly, J., Frenk, C., & Jenkins, A. 2006, MNRAS, 367, 1039
Hellwing, W. A., Frenk, C. S., Cautun, M., et al. 2016, MNRAS, 457, 3492
Hellwing, W. A., Cautun, M., van de Weygaert, R., & Jones, B. T. 2021, Phys. Rev. D, 103, 063517
Hoffman, Y., Metuki, O., Yepes, G., et al. 2012, MNRAS, 425, 2049
Ibata, R. A., Lewis, G. F., Conn, A. R., et al. 2013, Nature, 493, 62
Ishiyama, T., Rieder, S., Makino, J., et al. 2013, ApJ, 767, 146
Jiang, F., & Bosch, F. C. V. D. 2016, MNRAS, 458, 2848
Klypin, A., Kravtsov, A. V., Valenzuela, O., & Prada, F. 1999, ApJ, 522, 82
Knebe, A., Knollmann, S. R., Muldrew, S. I., et al. 2011, MNRAS, 415, 2293
Knebe, A., Pearce, F. R., Lux, H., et al. 2013, MNRAS, 435, 1618
Komatsu, E., Smith, K. M., Dunkley, J., et al. 2011, ApJS, 192, 18
Libeskind, N. I., Frenk, C. S., Cole, S., et al. 2005, MNRAS, 363, 146
Libeskind, N. I., Hoffman, Y., Knebe, A., et al. 2012, MNRAS, 421, L137
Libeskind, N. I., Hoffman, Y., Tully, R. B., et al. 2015, MNRAS, 452, 1052
Libeskind, N. I., van de Weygaert, R., Cautun, M., et al. 2018, MNRAS, 473, 1195
Lovell, M. R., Cautun, M., Frenk, C. S., Hellwing, W. A., & Newton, O. 2021, MNRAS, 507, 4826
Ludlow, A. D., Bose, S., Angulo, R. E., et al. 2016, MNRAS, 460, 1214
Ludlow, A. D., Schaye, J., & Bower, R. 2019, MNRAS, 488, 3663
Ma, W., Guo, H., & Jones, M. G. 2025, A&A, 695, A5
Macció, A. V., Dutton, A. A., Van Den Bosch, F. C., et al. 2007, MNRAS, 378, 55
Malavasi, N., Langer, M., Aghanim, N., Galárraga-Espinosa, D., & Gouin, C. 2022, A&A, 658, A113
Mao, Y.-Y., Williamson, M., & Wechsler, R. H. 2015, ApJ, 810, 21
Maulbetsch, C., Avila-Reese, V., Colín, P., et al. 2007, ApJ, 654, 53
Metuki, O., Libeskind, N. I., Hoffman, Y., Crain, R. A., & Theuns, T. 2015, MNRAS, 446, 1458
Metuki, O., Libeskind, N. I., & Hoffman, Y. 2016, MNRAS, 460
Miraghaei, H. 2020, AJ, 160, 227
Moliné, Á., Sánchez-Conde, M. A., Aguirre-Santaella, A., et al. 2023, MNRAS, 518, 157
Muldrew, S. I., Pearce, F. R., & Power, C. 2011, MNRAS, 410, 2617
Müller, O., Pawlowski, M. S., Jerjen, H., & Lelli, F. 2018, Science, 359, 534
Newton, O., Leo, M., Cautun, M., et al. 2021, JCAP, 2021, 062
Newton, O., Lovell, M. R., Frenk, C. S., et al. 2024, ArXiv e-prints [arXiv:2408.16042]
Nurmi, P., Heinämäki, P., Holopainen, J., et al. 2007, in Galaxy Evolution across the Hubble Time, eds. F. Combes, & J. Palouš, 235, 127
Onions, J., Knebe, A., Pearce, F. R., et al. 2012, MNRAS, 423, 1200
Patiri, S. G., Cuesta, A. J., Prada, F., Betancort-Rijo, J., & Klypin, A. 2006, ApJ, 652, L75
Pawlowski, M. S., Kroupa, P., Angus, G., et al. 2012a, MNRAS, 424, 80
Pawlowski, M. S., Pflamm-Altenburg, J., & Kroupa, P. 2012b, MNRAS, 423, 1109
Peebles, P. J. E. 1980, The Large-scale Structure of the Universe (Princeton: Princeton University Press)
Pomarède, D., Hoffman, Y., Courtois, H. M., & Tully, R. B. 2017, ApJ, 845, 55
Reed, D., Governato, F., Quinn, T., et al. 2005, MNRAS, 359, 237
Rey, M. P., Pontzen, A., & Saintonge, A. 2019, MNRAS, 485, 1906
Sawala, T., Frenk, C. S., Crain, R. A., et al. 2013, MNRAS, 431, 1366
Shandarin, S. F., & Zeldovich, Y. B. 1989, Rev. Mod. Phys., 61, 185
Sheth, R. K., & Tormen, G. 2004, MNRAS, 350, 1385
Sousbie, T. 2011, MNRAS, 414, 350
Springel, V., White, S. D. M., Tormen, G., & Kauffmann, G. 2001, MNRAS, 328, 726
Springel, V., White, S. D. M., Jenkins, A., et al. 2005, Nature, 435, 629
Springel, V., Wang, J., Vogelsberger, M., et al. 2008, MNRAS, 391, 1685
Stoehr, F., White, S. D. M., Tormen, G., & Springel, V. 2002, MNRAS, 335, L84
Tegmark, M., Blanton, M. R., Strauss, M. A., et al. 2004, ApJ, 606, 702
Tempel, E., Guo, Q., Kipper, R., & Libeskind, N. I. 2015, MNRAS, 450, 2727
van de Weygaert, R., & Platen, E. 2011, Int. J. Mod. Phys. Conf. Ser., 1, 41
van den Bosch, F. C., & Jiang, F. 2016, MNRAS, 458, 2870
van den Bosch, F. C., & Ogiya, G. 2018, MNRAS, 475, 4066
Van Den Bosch, F. C., Tormen, G., & Giocoli, C. 2005, MNRAS, 359, 1029
Wang, C.-W., Cooper, A. P., Bose, S., Frenk, C. S., & Hellwing, W. A. 2023, ApJ, 958, 166
Wang, H. Y., Mo, H. J., & Jing, Y. P. 2007, MNRAS, 375, 633
Wang, L., Gonzalez-Perez, V., Xie, L., et al. 2017, MNRAS, 468, 4579
Wang, P., Libeskind, N. I., Tempel, E., et al. 2020, ApJ, 900, 129
Wechsler, R. H., Bullock, J. S., Primack, J. R., Kravtsov, A. V., & Dekel, A. 2002, ApJ, 568, 52
Wechsler, R. H., Zentner, A. R., Bullock, J. S., Kravtsov, A. V., & Allgood, B. 2006, ApJ, 652, 71
White, S. D. M., & Frenk, C. S. 1991, ApJ, 379, 52
White, S. D. M., & Rees, M. J. 1978, MNRAS, 183, 341
Xu, W., Guo, Q., Zheng, H., et al. 2020, MNRAS, 498, 1839
Zel'dovich, Y. B. 1970, A&A, 5, 84
Zhang, Y., Yang, X., & Guo, H. 2021, MNRAS, 507, 5320

Chapter 4

Paper II: Caught in the Cosmic Web: Environmental Impacts on the Halo Substructure Boosts to Dark Matter Annihilation Signals

"Nothing in life is to be feared, it is only to be understood. Now is the time to understand more, so that we may fear less." – Marie Skłodowska-Curie

This paper is currently undergoing review in Physical Review D.

Hunde, F. M., Hellwing, W. A., and Bilicki, M., 2026, "Caught in the Cosmic Web: Environmental Impacts on the Halo Substructure Boosts to Dark Matter Annihilation Signals,"
arXiv: https://arxiv.org/abs/2604.26072

4.1 Introduction

In this chapter, we investigate how the large-scale cosmic web influences the halo substructure boost to DM annihilation signals. This work builds directly on the results presented in Chapter 3, where we showed that the cosmic web environment affects both the abundance of subhaloes and their internal density structure through the $V_{\rm max}--R_{\rm max}$ relation. Since DM annihilation rates scale with the square of the local density, unresolved substructure can substantially enhance the total predicted signal. Consequently, environmental variations in subhalo populations and concentrations are expected to propagate directly into the annihilation boost factor.

Most existing semi-analytic boost prescriptions assume that subhalo populations depend only on host halo mass and redshift. In this work, we extend two widely used semi-analytic formalisms, those of [85] and [86] models, by incorporating environment

dependent corrections calibrated from the COLOR gravity-only simulation. Our goal is to determine how the cosmic web modifies annihilation boosts relative to the standard environment averaged predictions commonly adopted in indirect detection studies.

To achieve this, we combine the COLOR N-body simulation with the `CaCTus` cosmic web classification framework to separate host haloes into filament, wall, and void environments. We then investigate how environment-dependent variations in host halo concentration, subhalo abundance, and subhalo internal structure affect the total annihilation luminosity. Rather than measuring annihilation signals directly from particle-level density maps, we construct deterministic semi-analytic boost predictions informed by the subhalo statistics extracted from the simulation.

We find a clear environmental dependence in the predicted annihilation boosts. Haloes residing in voids exhibit systematically suppressed boost factors of approximately 30–33% relative to the cosmic mean. The cosmic mean is a sample constructed by combining all host haloes from walls, filaments, and voids in each mass bin. In contrast, filament haloes display a strong mass-dependent transition, with low-mass hosts showing suppressions of roughly 15%, while high mass hosts exhibit enhancements of up to $\sim$ 12%. Wall environments generally produce intermediate behaviour between filaments and voids. These trends arise from the coupled environmental dependence of host halo concentrations and subhalo population properties.

Finally, we develop an empirical fitting prescription for the boost factor $B(M_{200}, z = 0)$ as a function of the cosmic web environment. This provides a practical framework for incorporating environmental effects into indirect detection forecasts and halo population modelling applications. Our results demonstrate that environment-blind boost models can introduce systematic biases into annihilation predictions and that the cosmic web should be accounted for when modelling the contribution of small-scale structure in applications where boost factor systematics are important.

4.2 Author's contribution

In the process of this article preparation, I led:

- The numerical analysis of the COLOR simulation data, computing all environment dependent subhalo proxies.
- The adaptation of semi-analytic boost frameworks to incorporate environment dependent parameters and propagate them into boost factor calculations.
- The assignment of haloes to cosmic web environments using the `CaCTus` algorithm, alongside constructing the environment-conditioned ingredient ratios used throughout the analysis.

- The production of all figures and data visualisations presented in the paper.
- The physical interpretation of the resulting cosmological trends.
- The writing of the majority of the manuscript.

Caught in the Cosmic Web: Environmental Impacts on the Halo Substructure Boosts to Dark Matter Annihilation Signals

Feven Markos Hunde,* Wojciech A. Hellwing,† and Maciej Bilicki
Center for Theoretical Physics, Polish Academy of Sciences, Al. Lotników 32/46, 02-668 Warsaw, Poland
(Dated: April 30, 2026)

The annihilation of dark matter (DM) particles is expected to produce Standard Model particles, providing a potential indirect signature of DM. The clumpy substructure of DM haloes amplifies the expected annihilation signal, an effect commonly quantified by the subhalo boost factor. Standard semi-analytic models usually treat this boost as a universal function of host-halo mass, neglecting systematic variations induced by the large-scale environment. In this work, we extend this framework by incorporating the influence of the cosmic web on subhalo populations. Using simulation-calibrated, environment-dependent ratios for host-halo concentrations, the subhalo mass function, and internal-structure proxies of subhalos based on the $V_{\rm max}$–$R_{\rm max}$ relation, we compute environment-conditioned boost predictions for haloes residing in filaments, walls, and voids. Our main result is the boost factor at fixed host-halo mass, expressed relative to the cosmic-mean prediction, $B(M, \mathrm{env})/B_{\rm CM}(M)$. We find a clear environmental modulation: in the fiducial distance-dependent model, filament haloes show a mass-dependent transition from a $\sim$ 15% suppression at the low-mass end to a modest enhancement of $\sim$ 12% for massive hosts, wall haloes remain intermediate, while void haloes stay suppressed by roughly 30–33% across the explored host-mass range. These results should be interpreted as deterministic model predictions obtained by propagating environment-dependent ingredient ratios through two standard semi-analytic boost frameworks. We provide an environment-aware prescription for subhalo boosts, together with modular environmental corrections that may also be useful in indirect-detection forecasts, strong-lensing mass modeling, and related halo-population applications.

I. INTRODUCTION

Cosmological and astrophysical observations indicate that dark matter (DM) constitutes over 80% of the total matter in the Universe [1, 2]. DM plays a crucial role in shaping the formation and evolution of cosmic structures, yet its fundamental particle nature remains unknown. Numerous theoretical candidates have been proposed, ranging from macroscopic objects such as primordial black holes [3] to particle candidates including Weakly Interacting Massive Particles (WIMPs) [4–7], axions [8, 9], sterile neutrinos [10, 11], and others.

Experimental searches span a wide mass range, from ultralight axions in the sub-eV regime to WIMPs at the GeV–TeV scale, but have so far yielded no conclusive detections [12, 13]. This lack of direct detection has motivated complementary approaches that seek to identify potential astrophysical signatures of DM interactions.

One such promising avenue is the indirect detection of DM. This approach searches for gamma rays, neutrinos, or other Standard Model particles produced by DM annihilation or decay in astrophysical environments. The expected flux depends on the underlying DM distribution, typically scaling with the square of the density [14–16]. Consequently, dense and clumpy regions, such as the galactic center, dwarf spheroidal galaxies, and galaxy clusters, are considered particularly promising targets for current and next-generation experiments [6, 17–19].

Within the cold dark matter (CDM) paradigm, cosmic structures grow hierarchically through gravitational instability, in a bottom-up scenario where the first objects to collapse correspond to the highest initial density fluctuations [20]. These small haloes merge and accrete to form progressively larger systems [21, 22]. This process naturally produces a population of subhalos within larger haloes. The most massive subhalos host luminous dwarf satellites, while many lower-mass subhalos remain dark, lacking baryonic matter [23, 24].

Gravitational instability also shapes the structure on larger scales, producing the intricate cosmic web [25–27]. This large-scale geometry forms a continuous network of dense clusters, elongated filaments, extended sheets, and vast under-dense voids [20, 28, 29]. The cosmic web is a striking manifestation of nonlinear gravitational evolution, influencing the growth, dynamics, and internal properties of individual haloes [30–36].

High-resolution cosmological simulations have shown that DM haloes are far from smooth, hosting a rich population of bound subhalos [37–39]. These subhalos are remnants of earlier mergers and accretion events that trace the same gravitational processes that built the cosmic web. The subhalo mass function (SHMF) follows an almost featureless power-law extending to masses far below current simulation resolutions [40, 41]. This extrapolation is supported by the redshift- and host-mass independence of the SHMF shape, with analytical models suggesting that substructure accounts for a substantial fraction of the total halo mass when extended down to the smallest scales [15, 42]. The smallest subhalos are eventually set by the microphysical properties of the DM

* fevenm@cft.edu.pl
† hellwing@cft.edu.pl

particle [43, 44]. Subhalos evolve under tidal interactions that strip their outskirts while often leaving intact dense cores [45, 46], making them powerful probes of both DM properties and hierarchical structure formation.

The clumpy substructure of DM haloes also plays a central role in indirect detection, if DM indeed decays or self-annihilates. Since the annihilation rate scales with the square of the density, the dense cores of subhalos can significantly boost the total annihilation luminosity relative to a smooth halo. The combined emission from an entire population of subhalos can therefore enhance the expected annihilation signal, an effect commonly quantified through the subhalo boost factor, i.e. the enhancement relative to the smooth host-halo contribution, [14–16, 47–50], making accurate modeling of the subhalo boost factor crucial for interpreting indirect detection data and constraining particle DM models.

The cosmic web environment strongly shapes halo and subhalo properties. The large-scale environment influences halo formation histories, concentrations, shapes, and spins, reflecting the anisotropic nature of the formation of cosmic structure [32, 35, 51, 52]. Subhalos within dense filaments tend to be more numerous, more concentrated, and exhibit modified radial distributions compared to those in walls or voids [53–56]. In [56, hereafter Paper I], we systematically studied how the cosmic web influences subhalo abundance and internal properties, demonstrating clear, mass-dependent variations in subhalo abundance and internal structure across filaments, walls, and voids, precisely the ingredients that enter the boost-factor modeling developed here.

Despite these advances, most of the existing models for subhalo boost factors are calibrated on simulations of isolated host haloes. These models often assume that the properties of the subhalo depend solely on the mass of the host halo and the radial distance from the halo centre [14, 15, 57], without explicitly accounting for the influence of the large-scale cosmic web environment. This omission may introduce systematic biases into boost-factor predictions, potentially misestimating the expected annihilation signals from haloes of similar mass but differing formation histories and environments.

In this paper, we investigate how the cosmic web influences subhalo populations and, in turn, DM annihilation signals, using high-resolution cosmological N–body simulations [58, 59]. We examine subhalos residing in different large-scale environments, including filaments, walls, and voids, and evaluate their contribution to the total annihilation luminosity. Our analysis employs a new implementation of the multi-scale cosmic web classifier NEXUS+[60] within the `CaCTus` framework, enabling robust identification of large-scale structures and a detailed characterization of environment-dependent subhalo properties. The ultimate goal is to develop a physically motivated description of the subhalo boost factor that explicitly accounts for the influence of the large-scale environment, thereby improving predictions for the spatial distribution and amplitude of DM annihilation signals in indirect-detection studies.

The framework of Sánchez-Conde and Prada [14], hereafter SCP14, provides an environment-independent description of substructure down to the smallest scales, while subsequent work has extended this picture by incorporating the subhalo position within the host and the effects of tidal evolution [e.g. 15, hereafter M17]. These approaches capture important internal and radial trends, but do not account for systematic variations driven by the large-scale cosmic web.

In this work, we build on existing semi-analytic descriptions by explicitly accounting for the role of the large-scale cosmic web. Our primary quantity of interest is the subhalo boost factor at fixed host-halo mass, expressed relative to the cosmic-mean prediction. Using environment-resolved measurements from simulations, we incorporate the environmental dependence of host-halo concentration, subhalo abundance, and subhalo internal structure into the SCP14 and M17 frameworks. The resulting annihilation luminosities and boost factors are therefore model predictions, rather than direct measurements of the full annihilation signal from the simulation. This allows us to quantify coherent, environment-conditioned variations in annihilation luminosities and boost factors that are not captured by models based on host mass and subhalo radius alone.

The paper is organized as follows: in Section II, we describe the simulation setup and the methods used to identify haloes and subhalos. Section III details our methodology for classifying the cosmic web. In Section IV, we present our main results on how subhalo properties and annihilation boost factors depend on the cosmic web environment. Finally, in Section V, we summarize our findings and discuss their implications for indirect detection of DM.

II. *N*–BODY SIMULATIONS

Our study uses the simulation of the COpernicus complexio LOw Resolution (COLOR) as the parent volume for the high-resolution COpernicus COmplexio (COCO) DM–only zoom-in N–body simulation [58, 59]. COLOR evolves $1620^3 \approx 4.25 \times 10^9$ particles from an initial redshift of $z_{\rm ini} = 127$ to the present day ($z = 0$) in a periodic cubic box of side 70.4 h^{-1} Mpc, corresponding to a comoving volume of 3.5×10^5 h^{-3} Mpc^3. Each DM particle has a mass of $m_{\rm p} = 6.19 \times 10^6$ $h^{-1}\,M_\odot$. The simulation assumes a flat ΛCDM cosmology consistent with the WMAP7 results [61], with parameters $\Omega_{\rm m} = 0.272$, $\Omega_{\rm b} = 0.04455$, $\Omega_\Lambda = 0.728$, $h = 0.704$, $n_{\rm s} = 0.967$ and $\sigma_8 = 0.81$.

Dark matter haloes are identified using a Friends-of-Friends (FOF) algorithm with a linking length equal to 0.2 times the mean inter-particle separation [62]. To ensure adequate resolution for substructure studies, we retain only FOF groups with at least 1000 particles ($M_{\rm FOF} \gtrsim 10^9$ $h^{-1}\,M_\odot$). The virial mass, M_{200}, is de-

fined as the mass enclosed within the virial radius, R_{200}, where the mean density is 200 times the critical density at the given redshift, $\rho_c(z) = 3H(z)^2/(8\pi G)$. Unless otherwise specified, M_{200} is used as the definition of the primary halo mass throughout this work.

Subhalos are identified within each FOF halo using the SubFind algorithm [63], which locates over-dense gravitationally bound regions. The subhalo mass corresponds to the total mass of the bound particles. To reduce spurious detections, we consider only subhalos containing at least 100 particles and located within the virial radius of their host halo.

In this work, we use the COLOR halo and subhalo catalog. The cosmic-web environment is assigned according to the web classification (see Section III) at the spatial position of the host-halo center. All subhalos associated with a given host therefore inherit the same large-scale environment label as their parent halo.

III. COSMIC WEB CLASSIFICATION

Defining the boundaries of the cosmic web, which consists of voids, walls, filaments, and nodes, is not straightforward. Unlike DM haloes, whose limits can be linked to virialisation, the cosmic web is hierarchical, anisotropic, and multi-scale, so its segmentation relies on algorithmic criteria. Various approaches have been proposed, including methods based on the eigenvalues of the Hessian of the density field [64–66], the velocity shear tensor [67, 68], combinations of density field and velocity shear information [60], the tidal or deformation tensor [69], watershed segmentation of the density field [70], cosmic web skeleton construction based on Morse theory [71], and the identification of caustics [72]. A thorough review of these methods is given in [29].

In this study, we adopt the approach of Hellwing et al. [35] and employ the NEXUS+ framework, implemented within our `CaCTus` algorithm introduced in Paper I. The `CaCTus` package provides an optimized implementation of the multi-scale NEXUS+ algorithm [60], enabling efficient segmentation of the cosmic web across a wide dynamic range. The code, along with detailed documentation, will be made publicly available in Naidoo et al. (in prep.)[73]

The density field is first computed from the COLOR simulation using a Cloud-In-Cell interpolation onto a 256^3 grid, yielding a spatial resolution of 0.275 h^{-1} Mpc. The dimensionless density field is defined as $f(\vec{x}) = \rho(\vec{x})/\langle\rho\rangle$ and smoothed over multiple scales with Gaussian filters defined as $R_n = 2^{n/2}R_0$, where $R_0 = 0.5\ h^{-1}$ Mpc, producing seven filter scales ranging from 0.5 to 4 h^{-1} Mpc. Filaments and walls are identified using the smoothed logarithmic density field, emphasizing their elongated and planar structures, while nodes are traced with the standard Gaussian-smoothed density to maintain their compact, nearly spherical shape [see also 28, 74].

For each smoothing scale, the normalized Hessian matrix of the smoothed density field is computed as

$$H_{ij,R_n}(\vec{x}) = R_n^2 \frac{\partial^2 f_{R_n}(\vec{x})}{\partial x_i\, \partial x_j}, \tag{1}$$

where the factor R_n^2 ensures scale-invariant normalization. The eigenvalues $\lambda_1 \le \lambda_2 \le \lambda_3$ are obtained by solving the characteristic equation $\det(H_{ij,R_n} - \lambda I) = 0$, and their relative values and signs are used to determine the morphological signature of each environment. In general, node-like regions correspond to $\lambda_1 \approx \lambda_2 \approx \lambda_3 < 0$, filaments to $\lambda_1 \approx \lambda_2 < 0$ with $|\lambda_3| \ll |\lambda_1|$, and walls to $\lambda_1 < 0$ with $|\lambda_1| \gg |\lambda_2| \approx |\lambda_3|$. Regions not matching any of these criteria are classified as voids. The environmental signature strength $S_{R_n}(\vec{x})$ is computed at each grid cell following the formalism of Cautun et al. [60].

The results from all smoothing scales are then combined into a single, scale-independent morphological map by taking the maximum response at each location, $S(\vec{x}) = \max[S_{R_n}(\vec{x})]$, capturing the dominant structural signal independently of filter scale. A hierarchical classification is finally applied, starting with nodes followed by filaments, walls, and voids. Nodes are selected based on mass, density, and signature thresholds, filaments are identified using the corresponding signature threshold and volume criteria, and walls are assigned from the remaining unclassified regions. This approach produces a self-consistent, multi-scale segmentation of the cosmic web that is robust to resolution and noise, while capturing its hierarchical and anisotropic nature. Nodes are included in the classification for completeness, but are not used in our analysis because they occupy a very small volume fraction and are dominated by massive haloes, which have minimal impact on the environment-dependent subhalo ratios.

The specific configuration of the `CaCTus` algorithm used in this work is detailed in Table I. These parameters, including grid resolution and smoothing scales, are chosen to ensure a robust multi-scale extraction of the cosmic web components while maintaining consistency with established frameworks [e.g., 28, 60].

IV. RESULTS

In this section, we explore the influence of the large-scale cosmic web environment on DM haloes, their subhalo properties, and the resulting annihilation signals. In particular, we focus on host-halo concentrations, subhalo abundances, and subhalo internal structure and assess how these shape the environment-dependent DM annihilation boost factor. Rather than measuring boosts directly from particle-level ρ^2 in individual haloes, we compute them by propagating simulation-derived environmental corrections through the SCP14 and M17 semi-analytic frameworks. In practice, the host-halo concentration, the SHMF, and the internal structure of subhalos are modified according to the cosmic web environment

TABLE I. Numerical parameters and configuration for the `CaCTus` cosmic web classification.

Parameter	Value / Method
Grid Resolution	256^3 ($0.275\ h^{-1}$ Mpc cell size)
Interpolation Scheme	Cloud-In-Cell (CIC)
Smoothing Kernel	Gaussian, $R_n = 2^{n/2} R_0$
Filter Scales (R_n)	$\{0.5, 0.7, 1.0, 1.4, 2.0, 2.8, 4.0\}\ h^{-1}$ Mpc
Density Transform	Logarithmic (Filaments/Walls), Linear (Nodes)

and then propagated into the boost calculation. The resulting boost factors are therefore model predictions calibrated by simulation-based environmental trends, rather than direct measurements of the full annihilation signal from the simulation.

A. Subhalo Boost Factor

The DM annihilation signal is influenced by contributions from substructure within haloes. This effect is quantified by the boost factor $B(M)$, defined through the total luminosity of a halo including subhalos as $L_{\rm tot} = L_{\rm host}(1 + B(M))$, where $L_{\rm host}$ represents the luminosity of the smooth host component [14, 15, 75, 76]. Subhalos thus elevate the annihilation signal relative to a smooth DM distribution.

As a background of our analysis, we first examine the standard approach developed by SCP14. A key feature of their model is its physically motivated treatment of the concentration–mass relation, $c(M)$. Simple power-law extrapolations of the concentration–mass relation toward low masses, by contrast, can assign excessively high concentrations to the smallest halos. This leads to a significant overestimation of the boost factor, because the annihilation luminosity scales as $L \propto c^3$. The SCP14 model instead adopts the relation proposed by Prada et al. [77]. In that relation, halo concentrations flatten at low masses. Haloes below a certain mass acquire similar values of $c(M)$ that reflect their formation epochs rather than a continued steep power-law rise toward lower masses. This ensures that small haloes collapsing at similar epochs have comparable initial concentrations. As a result, the SCP14 approach provides a more realistic boost prediction than simple power-law extrapolations of $c(M)$ toward low masses.

The SCP14 model recursively accounts for the full hierarchy of substructure via the integral:

$$B(M) = \frac{1}{L(M)} \int_{M_{\rm min}}^{M} \frac{dN}{dm} \left[1 + B(m)\right] L(m)\, dm, \qquad (2)$$

where $L(M) = 4\pi M c^3 / f(c)^2$ (with $f(c) = \ln(1+c) - c/(1+c)$) is the annihilation luminosity of a smooth host halo of mass M and concentration c. The SHMF is parameterized as $dN/dm = (A/M)(m/M)^{-\alpha}$, with a slope $\alpha = 2$ and normalization $A = 0.012$ to match the $\sim 10\%$ mass fraction in substructure found in high-resolution simulations [14]. The term $B(m)$ represents the boost factor of a subhalo of mass m due to the next level of substructure, and the integration extends down to a minimum subhalo mass $M_{\rm min} = 10^{-6}\ M_\odot$, which is set by particle physics considerations. We adopt Eq. 2 as the basis for computing the boost factor in our analysis. We then extend this framework by replacing the universal host-halo concentration–mass relation, SHMF, and subhalo structural parameters with environment-dependent values derived from our simulation, enabling the computation of $B(M, \mathrm{env})$ for haloes in different cosmic web environments.

In addition to the SCP14 framework, we also consider the distance-dependent subhalo concentration model of M17, which explicitly accounts for both subhalo mass and radial position within the host halo. In this model, the boost factor is computed as

$$B(M) = \frac{3}{L_{\rm smooth}(M)} \int_{M_{\rm min}}^{M} \frac{dN(m)}{dm}\, dm \int_0^1 dx_{\rm sub} \times \left[1 + B(m)\right] L(m, x_{\rm sub})\, x_{\rm sub}^2, \qquad (3)$$

where $L(m, x_{\rm sub})$ is the annihilation luminosity of a subhalo of mass m at a normalized radial coordinate $x_{\rm sub} = R_{\rm sub}/R_{200}$. The integral over $x_{\rm sub}$ accounts for contributions from both inner, high-density and outer, lower-density regions, with $x_{\rm sub}^2$ representing the spherical volume element. $L_{\rm smooth}(M)$ is the luminosity of the smooth host halo. This formulation captures the effects of tidal evolution on subhalo concentrations without yet including explicit environment-dependent modifications.

B. Host halo concentration

The concentration of a DM halo quantifies how tightly mass is packed toward its center. It is commonly defined as $c \equiv R_{\rm vir}/r_s$, where $R_{\rm vir}$ is the virial radius and r_s is the scale radius of the halo's density profile. Higher concentrations correspond to haloes that assembled earlier and accumulated mass more efficiently in their central regions. Concentration, therefore, traces both halo assembly history and the larger-scale environment in which

a halo evolves. Haloes in dense regions of the cosmic web, such as filaments, generally assemble earlier and develop higher central densities than those in under-dense regions, consistent with the accelerated growth expected in such environments [35]. This environmental dependence is captured in the concentration–mass relation, which exhibits a systematic variation across the cosmic web [35, 78]. Although the global relation is well described by a smoothly broken power law with a characteristic transition mass, the slope steepens in over-dense regions and flattens at low masses [14, 59]. In practice, filament haloes tend to be more concentrated than the cosmic mean, while void haloes consistently display the lowest concentrations across the relevant mass range.

In our analysis, we adopt the concentration–mass relation from the SCP14 model as our baseline, based on the physically motivated parametrization of Prada et al. [77] for the median halo concentration, $c(M)$, which naturally captures the flattening of concentrations at low masses. We adopt the specific $z = 0$ fitting function provided by SCP14, using the fitting parameters from Hellwing et al. [59], derived for the combined COCO+COLOR simulation suite employed in this work. As noted by Ref. [59], the original SCP14 parametrization systematically over-predicts the concentrations of haloes with $M_{200} \lesssim 10^{11}\,h^{-1}\,M_\odot$, due to a mismatch in the low-mass slope. To remedy this, Hellwing et al. [59] refitted the same functional form using the combined COCO+COLOR simulation suite. The resulting parametrization accurately reproduces the median concentration to better than 1% through the entire halo mass range 10^{-6} to $10^{15}\,h^{-1}\,M_\odot$.

To account for environmental effects, we apply multiplicative ratios from Hellwing et al. [35], hereafter H21, to the baseline SCP14 concentration–mass relation,

$$c(M_{200}, \mathrm{env}) = c_{\mathrm{SCP14}}(M_{200}) \times \mathcal{R}_c(\mathrm{env}, M_{200}), \qquad (4)$$

Here, $\mathcal{R}_c(\mathrm{env}, M_{200})$ denotes the ratio of the median halo concentration in a given environment to the cosmic mean at the same mass, as illustrated in the left panel of Fig. 1. These environment-dependent concentration ratios are taken directly from the measurements of H21, and were derived using the combined COCO+COLOR simulation suite. Filament haloes are more concentrated than the cosmic mean at low masses, void haloes are less concentrated, and wall haloes remain closer to the cosmic mean. This multiplicative scaling preserves the mass-dependent shape of the SCP14 relation while explicitly embedding the empirically observed environmental variation. The ratios for filaments start above unity at low masses and decrease toward the cosmic mean, leveling off beyond $10^{11}\,h^{-1}\,M_\odot$. The ratios for voids begin below unity and increase toward the cosmic mean, also remaining nearly constant past $10^{11}\,h^{-1}\,M_\odot$. For walls, the ratios start near the cosmic mean, decrease slightly, and then rise at higher masses. These environment-dependent concentrations, $c(M_{200}, \mathrm{env})$, are subsequently used in the calculation of the boost factor, entering Eq. 2 as the host halo concentration to account for environmental modulation of the host density profile.

C. Subhalo mass function

The subhalo mass function characterizes the abundance of subhalos within a host halo as a function of subhalo mass, m. It provides a statistical description of the hierarchical substructure across a wide mass range. The abundance and mass distribution of subhalos are closely linked to the host halo's formation history and dynamical evolution, which are influenced by the large-scale cosmic web environment.

Analysis of the high-resolution COLOR simulations in Paper I showed that subhalo populations depend systematically on environment. Halos in filaments host a larger number of bound substructures than those in walls or voids, reflecting earlier formation times and higher survival rates of substructures in dense regions. Conversely, haloes in under-dense regions form later and retain fewer subhalos, whereas haloes in walls exhibit abundances close to the cosmic mean.

In Paper I, we quantified the environmental dependence through cumulative SHMF ratios. These cumulative measurements provide the baseline environmental trends that we adopt here. For the boost-factor calculation, however, we require differential SHMF ratios, which we compute directly from the simulation data and use in Eq. 2:

$$\mathcal{R}_{\mathrm{SHMF}}(m) = \frac{dN/dm_{\mathrm{env}}}{dN/dm_{\mathrm{CM}}}, \qquad (5)$$

where dN/dm_{env} and dN/dm_{CM} are the differential number of subhalos per unit mass in a given environment and in the cosmic mean, respectively.

To describe the mass dependence of these differential ratios, we fit a power-law transition function of the form

$$\mathcal{R}_{\mathrm{SHMF}}(m) = p + \frac{q - p}{1 + (m_b/m)^{\nu}}\,. \qquad (6)$$

where p and q are the low- and high-mass plateaus, respectively, m_b sets the transition mass, and ν controls the steepness of the transition. Fits are performed over environment-specific mass ranges to ensure robust parameter estimation and avoid high-mass regions with limited statistics. The lower bound is set to $6.2 \times 10^8\,h^{-1}\,M_\odot$, corresponding to 100 times the particle mass, while the upper bound is given by the maximum halo mass, m_{max}, in each environment, as listed in Table II.

The best-fit parameters for the subhalos hosted by the haloes in the filaments, walls, and voids are reported in Table II. Each environment exhibits a distinct plateau and transition mass, reflecting the influence of large-scale structure on subhalo abundances. For the filament

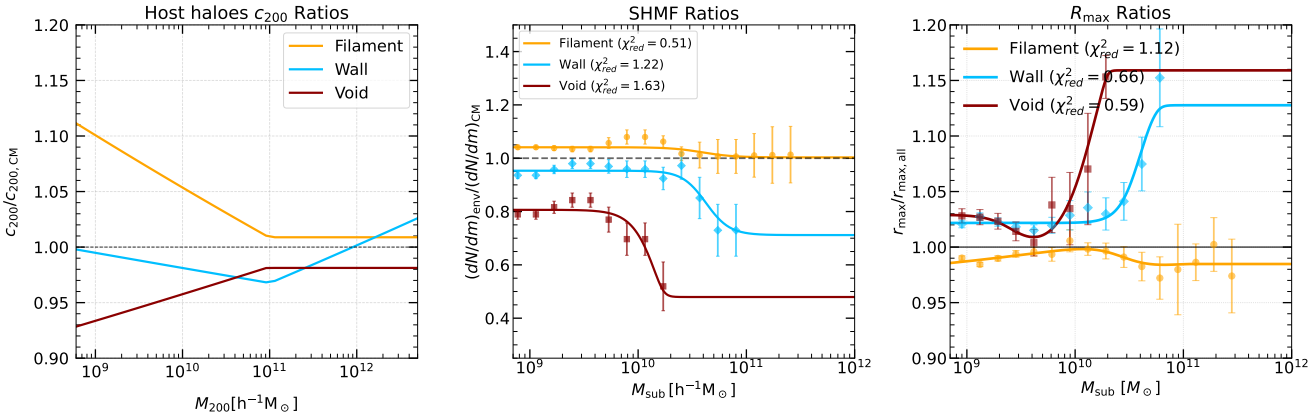

FIG. 1. *Left Panel:* Host halo concentration relative to the cosmic mean as a function of halo mass. The curves show median concentration ratios for different cosmic web environments, taken from H21 using the COCO+COLOR simulations (Table I, therein). Together with the middle and right panels, this panel summarizes the three environment-dependent ingredients propagated into the boost calculation. *Middle Panel:* Differential SHMF ratios, $(dN/dm)_{\mathrm{env}}/(dN/dm)_{\mathrm{CM}}$, where the data points are calculated from simulation data for each environment. Solid lines show the corresponding single power-law transition fits to these differential ratios (Eq. 6). These fitted differential curves are used in Eq. 7 for all subsequent calculations. *Right Panel:* Subhalo R_{max} ratio relative to the cosmic mean as a function of subhalo mass m. Solid curves show the best-fit power-law transition models: a single power-law transition form is used for the wall environment, while a double power-law transition model with a controlled high-mass plateau is adopted for filaments and voids (Eqs. 6 and 11).

and void fits, the inferred transition mass lies close to the upper edge of the fitted interval, so it should be interpreted mainly as an effective scale governing the smooth turnover of the interpolation, rather than as a sharply resolved physical break within the sampled mass range. The middle panel of Fig. 1 shows the measured $\mathcal{R}_{\mathrm{SHMF}}(m)$ with error bars representing bootstrap errors on the mean. The corresponding reduced χ^2 values are also shown as a compact indicator of fit quality. Typical residuals remain at the few-percent level, staying within about 5% over most of the fitted mass range; larger deviations occur only in the more weakly populated bins, where the statistical uncertainties are also largest.

To incorporate these results in calculations that require the differential SHMF, we employ:

$$\frac{dN}{dm}(m, M_{200}, \mathrm{env}) = \frac{dN_{\mathrm{SCP14}}}{dm}(m, M_{200}) \times \mathcal{R}_{\mathrm{SHMF}}(\mathrm{env}, m), \tag{7}$$

where we use the fitted differential ratios $\mathcal{R}_{\mathrm{SHMF}}(m)$. These fitted ratios provide a smooth working representation of the environmental correction and remain consistent with the finite-difference estimates from the simulation data. This ensures that the differential SHMF applied in Eq. (7) accurately reflects the environmental trends measured in Paper I.

By applying $\mathcal{R}_{\mathrm{SHMF}}(\mathrm{env}, m)$ in the computation of the boost factor (Eq. 2), the subhalo abundance at each mass is rescaled to include these environmental variations. This ensures that the recursive evaluation of the annihilation luminosity captures both the hierarchical structure of the host halo and the modulation imposed by the large-scale cosmic web, which can substantially affect the predicted DM annihilation signal.

D. Subhalo concentration

The internal density structure of subhalos strongly influences their contribution to the DM annihilation signal. We characterize subhalo compactness using the characteristic concentration, c_v, defined as [39, 40, 79]:

$$c_v = 2\left(\frac{V_{\mathrm{max}}}{H_0 R_{\mathrm{max}}}\right)^2, \tag{8}$$

where V_{max} is the maximum circular velocity, R_{max} the radius at which it occurs, and H_0 the Hubble constant, included so that c_v remains a dimensionless concentration proxy. This definition is particularly suitable for subhalos, whose outer regions are often stripped tidally and lack well-defined virial radii. Unlike traditional mass-dependent c_{200}, which depends on virial mass and radius, c_v relies on V_{max} and R_{max}, which remain well-resolved in simulations even for stripped subhalos. Therefore, c_v provides a robust, model-independent measure of subhalo inner densities across different environments and host masses.

The environmental dependence of c_v is derived from the ratio of the mean values of R_{max} at fixed V_{max}, using the environment-resolved relations V_{max}–R_{max} of Paper I. For a given V_{max}, a smaller R_{max} corresponds to a more compact subhalo of higher density, while a larger R_{max} indicates a more extended subhalo of lower density. The subhalos in the filaments exhibit a smaller R_{max} at fixed V_{max}, reflecting earlier formation, while those in the voids have a larger R_{max}, indicative of lower densities.

At fixed V_{max}, Eq. 8 implies $c_v \propto (V_{\mathrm{max}}/R_{\mathrm{max}})^2$, and therefore $c_v \propto R_{\mathrm{max}}^{-2}$ at fixed V_{max}, Let $R_{\mathrm{max,env}}$ and

TABLE II. Best-fit parameters of the power-law transition model for the environment-dependent SHMF ratios (Eq. 6). The maximum halo mass, $m_{\rm max}$, indicates the upper limit of the mass range used for fitting each environment.

Environment	p	q	$\log_{10} m_b\ [h^{-1}\,M_\odot]$	ν	$\log_{10} m_{\rm max}[h^{-1}\,M_\odot]$
Filament	1.04 ± 0.01	1.00 ± 0.05	10.59 ± 0.79	2.97 ± 1.04	11.00
Wall	0.95 ± 0.01	0.71 ± 0.11	10.63 ± 0.18	4.01 ± 1.93	10.78
Void	0.81 ± 0.01	0.37 ± 0.28	10.10 ± 0.16	3.49 ± 1.63	10.23

$R_{\rm max,CM}$ denote the environment-specific and cosmic-mean values of $R_{\rm max}$, respectively. The concentration ratio can then be written as

$$\frac{c_{\rm sub,env}}{c_{\rm sub,CM}} = \frac{c_{v,\rm env}}{c_{v,\rm CM}} = \left(\frac{R_{\rm max,CM}}{R_{\rm max,env}}\right)^2 = \mathcal{R}^{-2}_{\rm max,sub}({\rm env}, m). \tag{9}$$

This derivation assumes that $V_{\rm max}$ remains fixed and that variations in subhalo density are entirely captured by changes in $R_{\rm max}$. It naturally explains why the concentration correction scales as the inverse square of the $R_{\rm max}$ ratio, as implemented in the following equation.

In the SCP14 framework, subhalo concentrations, $c_{\rm SCP14,sub}$, are assumed to follow the concentrations of field haloes of the same mass. Low-mass haloes collapse nearly simultaneously in the early Universe, producing similar natal concentrations, which results in a flattening of $c(M)$ at small masses. Field-halo concentrations thus provide a reasonable approximation for subhalos.

To account for environmental modulation, we scale the SCP14 subhalo concentrations using the inverse-square of the $R_{\rm max}$ ratio:

$$c_{\rm sub}(m, {\rm env}) = c_{\rm SCP14,sub}(m) \times \mathcal{R}^{-2}_{\rm max,sub}({\rm env}, m), \tag{10}$$

The inverse-square scaling ensures that subhalos with smaller $R_{\rm max}$, indicating higher central densities, receive larger concentrations, while those with larger $R_{\rm max}$ have reduced $c_{\rm sub}$. This preserves physical consistency while capturing the systematic variations in the internal structure of subhalos across different cosmic web environments.

For walls, the mass dependence of $\mathcal{R}_{\rm max,sub}$ is modelled using the power-law transition function (Eq. 6), with environment-specific parameters listed in Table III. For voids and filaments, where the trend of the $R_{\rm max}$ ratios is more complex, we adopt a power-law function of two transitions with a controlled high-mass plateau:

$$\mathcal{R}_{\rm max,sub}(m) = \begin{cases} b + \dfrac{c-b}{1+(m_{t1}/m)^{s_1}} \\ \quad + \frac{d-c}{1+(m_{t2}/m)^{s_2}}, & m \le m_{\rm pl} \\ \mathcal{R}_{\rm max,sub}(m_{\rm pl}), & m > m_{\rm pl} \end{cases} \tag{11}$$

where b, c, and d are the low-mass, intermediate, and high-mass plateaus, respectively. Parameters m_{t1} and m_{t2} are the transition masses, and s_1 and s_2 control the steepness of the respective transitions. The plateau mass $m_{\rm pl}$ above which the fit is kept constant is determined by the last data value, denoted as $m_{\rm max}$ in Table III, to prevent the high-mass tail from diverging due to limited statistics. This controlled plateau ensures that the two-transition power-law function accurately captures the valley and overall trend of the $R_{\rm max}$ ratios in voids and filaments.

Table III lists the best-fit parameters for the environment-dependent $R_{\rm max}$ ratios. The fit reproduces the measured $\mathcal{R}_{\rm max,sub}$ ratios to within about 1–2% over most of the fitted range, with somewhat larger deviations appearing only in the highest-mass bins where the uncertainties increase substantially. These ratios indicate that the subhalos in filaments have a smaller $R_{\rm max}$ relative to the cosmic mean, corresponding to higher characteristic densities, while the subhalos in walls display intermediate values, and those in the voids exhibit the largest $R_{\rm max}$, reflecting lower internal densities. Across the subhalo mass range, these differences illustrate that the internal structure of subhalos is modulated by their location within the cosmic web.

The mass-dependent behavior of the $R_{\rm max}$ ratio captures the systematic variation in subhalo compactness. Subhalos in denser environments are more centrally concentrated, whereas those in under-dense regions are comparatively less concentrated. This modulation affects the expected DM annihilation signal, since subhalos with smaller $R_{\rm max}$ produce stronger contributions to the luminosity. The right panel of Fig. 1 illustrates these trends, showing the differences in characteristic subhalo density across filaments, walls, and voids. Consequently, the $R_{\rm max}$ ratios provide a quantitative measure of how environmental conditions influence subhalo structure.

This environment-dependent characterization of subhalo internal structure provides the necessary input for computing the annihilation boost factor in host haloes, which we describe in the following subsection.

E. Environment-dependent luminosity and boost predictions

To assess the impact of the environment on halo properties and their potential DM annihilation signals, we compute the total annihilation luminosity of host haloes, including their substructure. Here, following standard usage in the boost-factor literature, "annihilation luminosity" denotes the volume integral of ρ^2 up to particle-

TABLE III. Best-fit parameters for environment-dependent subhalo $r_{\rm max}$ ratios using fitted transition models.

Environment	b	c	$\log_{10} m_{t1}[h^{-1}\,M_\odot]$	s_1	d	$\log_{10} m_{t2}[h^{-1}\,M_\odot]$	s_2	$\log_{10} m_{\rm max}[h^{-1}\,M_\odot]$
Filament	0.97 ± 0.20	1.03 ± 0.85	10.00 ± 0.78	0.42 ± 0.22	1.00 ± 0.68	10.43 ± 0.69	3.02 ± 1.35	11.00
Wall	1.02 ± 0.01	1.14 ± 0.12	10.60 ± 0.29	3.78 ± 1.03	–	–	–	10.78
Void	1.03 ± 0.01	0.99 ± 0.18	9.44 ± 0.70	3.50 ± 0.95	1.25 ± 1.06	10.20 ± 1.27	2.61 ± 0.45	10.23

physics prefactors, rather than radiative power in watts. Fig. 2 shows the total halo luminosity, $L_{\rm tot}$, as a function of host mass M_{200} for filaments, walls, and voids, alongside the cosmic mean. Haloes residing in filaments exhibit the highest total luminosities at fixed mass, reflecting both a higher number of subhalos and increased subhalo densities, whereas haloes in voids are the least luminous. Wall haloes follow the cosmic mean trend closely, with minor deviations at intermediate masses. It is important to note that the environmental trend in the total annihilation luminosity need not mirror that of the boost factor. Because the boost is defined relative to the smooth host contribution, environment-dependent changes in host-halo concentration also modify the denominator, so a population with a higher total luminosity can still exhibit a suppressed boost relative to the cosmic mean.

Having quantified how host halo concentration, the SHMF, and subhalo internal density structure vary systematically across the cosmic web, we now incorporate these environmental effects into the computation of the DM annihilation boost factor. Our approach extends the standard SCP14 framework, originally expressed in Eq. 2, by replacing the universal concentration–mass relation, SHMF, and subhalo structural parameters with their environment-dependent counterparts:

$$B(M,\mathrm{env}) = \frac{1}{L(M,\mathrm{env})}\int_{M_{\rm min}}^{M}\frac{dN}{dm}(m,M,\mathrm{env}) \times \left[1+B(m,\mathrm{env})\right] L(m,\mathrm{env})\,dm, \quad (12)$$

where $L(M,\mathrm{env})$ denotes the annihilation luminosity of the smooth host halo, calculated using the environment-dependent concentration $c(M,\mathrm{env})$ (H21, Fig. 5 and Table 2 therein). The term $L(m,\mathrm{env})$ accounts for the internal structure of subhalos through their environment-dependent $R_{\rm max}$ ratios (Eq. 10). By explicitly incorporating variations in both subhalo abundance and internal density, Eq. 12 generalizes the recursive formulation of SCP14, capturing the influence of the cosmic web on the DM distribution within host haloes and their substructure. For computational efficiency, we limit the calculation to two hierarchical levels of substructure (subhalos and sub-subhalos). This approximation is standard and captures the dominant contribution to the annihilation signal, with deeper levels typically contributing only subdominant corrections in comparable semi-analytic treatments [e.g. 14, 15].

Fig. 3 presents the resulting environment-dependent

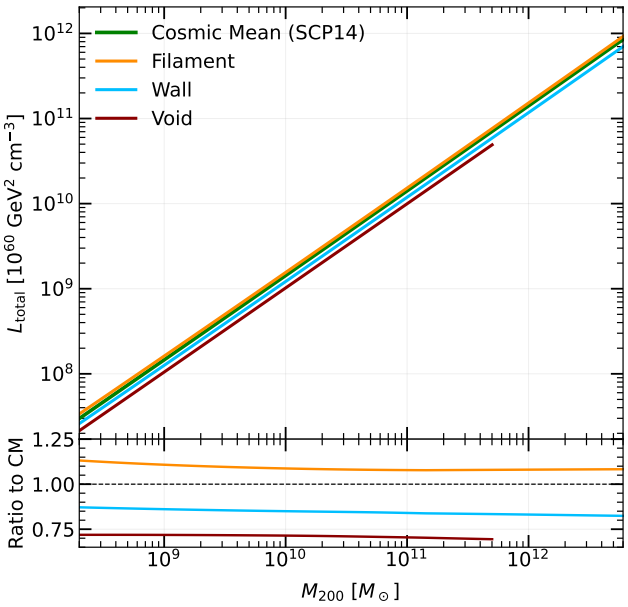

FIG. 2. Total halo luminosity as a function of host halo mass M_{200} for different cosmic environments, including filaments, walls, and voids. The green line shows the cosmic mean prediction from the original SCP14 model without environmental modifications. These curves are not direct ρ^2 measurements from simulations but are model predictions obtained by propagating environment-dependent ingredient ratios into the SCP14 framework. The vertical scale is shown in the conventional annihilation-luminosity units of $10^{60}\,\mathrm{GeV^2\,cm^{-3}}$. The bottom panel shows the ratio of environment-dependent halo luminosities to the cosmic mean. The curves are deterministic from the fits and do not include halo-to-halo scatter.

subhalo boost factors as a function of host halo mass. At the high-mass end ($M \gtrsim 10^{11}\,h^{-1}\,M_\odot$), the haloes embedded in the filaments exhibit the biggest boosts, driven by enhanced subhalo abundances and higher characteristic internal densities. This combination significantly increases the total annihilation luminosity in dense cosmic web regions. In contrast, haloes residing in voids display the lowest boost factors across all masses, reflecting their systematically lower subhalo abundances and reduced internal densities. At lower host halo masses, ($M \lesssim 10^{11}\,h^{-1}M_\odot$), all three environments remain below or close to the cosmic-mean prediction, with filament haloes still providing the largest boost, wall haloes remaining intermediate, and void haloes the most sup-

pressed.

Combining the physical interpretation of subhalo abundance, internal density, and host halo concentration with the quantitative power-law transition fits, Fig. 3 summarises the baseline SCP14-based environment-dependent boost prediction obtained by propagating the fitted concentration, SHMF, and subhalo-structure corrections into Eq. 2. The lower panel of Fig. 3 shows the ratio of these environment-dependent boosts to the cosmic-mean prediction. Filament haloes display a smooth increase with host mass, starting at a suppression of ~ 0.85 at low masses, crossing unity near $M \sim 10^{11}\,h^{-1}\,M_\odot$, and reaching an enhancement of ~ 1.07 at the high-mass end. Wall haloes reach a peak ratio of approximately 0.90 at intermediate masses, before decreasing to ~ 0.76 at the high-mass end. Void haloes remain suppressed across the entire mass range, with ratios as low as ~ 0.7, reflecting their lower subhalo abundance and reduced internal densities. It is worth stressing that the cosmic-mean reference here is the global boost factor prediction, not the average of the three explicitly shown environments. At low host masses, all three displayed environments can therefore lie below the cosmic mean simultaneously. This reflects both the fact that the reference includes the full halo population used to define the cosmic mean, and that the boost is normalised by the smooth host contribution, so environment-dependent changes in host concentration can suppress the boost ratio even when the total annihilation luminosity is not correspondingly reduced.

The results presented here should be interpreted as deterministic model predictions based on best-fit environment-dependent corrections to the adopted semi-analytic framework. In the present implementation, we do not propagate halo-to-halo scatter, uncertainties in the fitted environmental ratios, or classification uncertainties associated with the Cosmic Web assignment. We therefore regard the trends reported here as a first characterization of the systematic impact of large-scale environment on boost-factor modeling, with a full uncertainty propagation left for future work.

Extending the standard distance-dependent subhalo concentration model of M17 (Eq. 3), we now include the effects of the cosmic web environment, moving from the baseline SCP14-based calculation of Fig. 3 to a fiducial model that also incorporates the radial dependence of subhalo structure within the host halo. In this framework, the subhalo concentration depends on both its mass and radial position within the host halo. The normalized radius is defined as $x_{\rm sub} = R_{\rm sub}/R_{200}$, representing the subhalo's distance from the host center in units of the host virial radius. The full parametrization of the concentration is provided in Appendix A. In this fiducial variant, tidal stripping is not introduced as an additional environment-dependent correction, but is incorporated implicitly through the distance-dependent subhalo concentration prescription adopted from M17. Using these distance- and environment-dependent concentrations, the subhalo boost factor can be expressed as

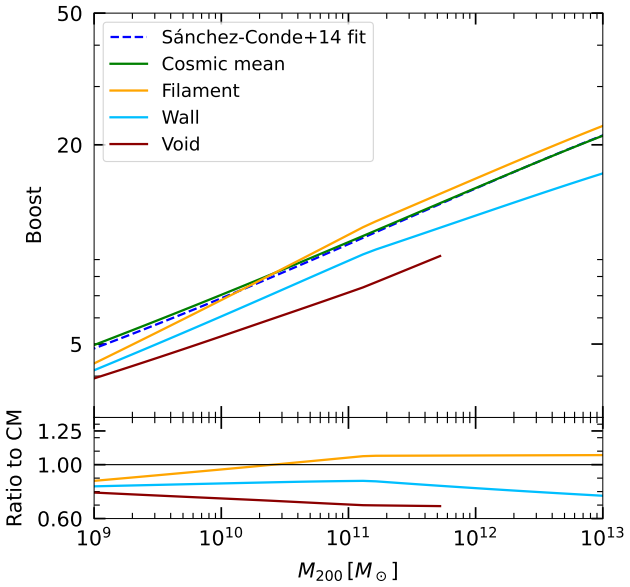

FIG. 3. *Upper panel:* Baseline SCP14-based environment-dependent subhalo boost factors as a function of host halo mass for each cosmic-web environment. The solid green line shows the cosmic-mean boost, while the black dashed line represents the fit from SCP14. The curves shown here are direct model predictions obtained from the fitted environmental ingredients and do not include halo-to-halo scatter. *Lower panel:* Ratio of the environment-specific boost factors to the cosmic mean. The curves are deterministic from the fits and do not include uncertainties from halo-to-halo scatter.

$$B(M,\mathrm{env}) = \frac{3}{L_{\rm sm}(M,\mathrm{env})}\int_{M_{\rm min}}^{M}\frac{dN(m,\mathrm{env})}{dm}\,dm \times \int_0^1 dx_{\rm sub}\left[1+B(m,\mathrm{env})\right]L(m,x_{\rm sub},env)\,x_{\rm sub}^2, \tag{13}$$

where $L(m, x_{\rm sub}, \mathrm{env})$ denotes the annihilation luminosity of a subhalo of mass m at radius $x_{\rm sub}$, incorporating both distance-dependent concentrations and environmental modulation. The factor $x_{\rm sub}^2$ accounts for the spherical volume element, while $L_{\rm sm}(M, \mathrm{env})$ is the luminosity of the smooth host halo including environmental effects. This formulation generalizes the original model (Eq. 3) by explicitly including cosmic web variations in subhalo abundance and internal structure. Relative to the SCP14-based result of Fig. 3, it therefore adds the radial dependence of subhalo concentrations within the host halo while preserving the same environment-dependent ingredient corrections.

Fig. 4 shows the resulting environment-dependent subhalo boost factors obtained in the fiducial M17-based model, which differs from Fig. 3 by explicitly including the radial dependence of subhalo concentrations and

TABLE IV. Best-fitting values of the polynomial coefficients given in Eq. 14 for the fit to the subhalo boost factor in the cosmic-mean and environment-dependent cases shown in Fig. 4.

Environment	b_0	b_1	b_2	b_3
Cosmic mean	0.468 ± 0.094	-0.058 ± 0.030	$1.666 \times 10^{-2} \pm 3.079 \times 10^{-3}$	$-4.232 \times 10^{-4} \pm 1.024 \times 10^{-4}$
Filament	1.385 ± 0.095	-0.423 ± 0.030	$5.769 \times 10^{-2} \pm 3.106 \times 10^{-3}$	$-1.811 \times 10^{-3} \pm 1.033 \times 10^{-4}$
Wall	1.068 ± 0.134	-0.320 ± 0.044	$4.867 \times 10^{-2} \pm 4.727 \times 10^{-3}$	$-1.684 \times 10^{-3} \pm 1.643 \times 10^{-4}$
Void	-0.430 ± 0.125	0.215 ± 0.043	$-1.138 \times 10^{-2} \pm 4.958 \times 10^{-3}$	$3.915 \times 10^{-4} \pm 1.848 \times 10^{-4}$

the associated tidal-evolution effects encoded in that prescription. The upper panel presents the boost as a function of host M_{200} mass for each cosmic web environment. The green solid line indicates the cosmic-mean prediction from M17 without environment modifications, the blue dotted line shows the SCP14 fit, and the black dashed lines correspond to polynomial fits introduced below in Eq. 14 for each environment. The lower panel displays the ratio to the cosmic-mean prediction, highlighting the relative impact of the cosmic web.

Tidal stripping, as encoded in the adopted distance-dependent M17 concentration prescription, primarily removes outer subhalo material while leaving the dense inner regions largely intact. High-resolution simulations have shown that this process reduces subhalo mass and size relative to field haloes [39, 46, 79–85], but the inner density cusp of a subhalo remains largely intact, which is crucial for DM annihilation studies because the luminosity is dominated by the dense central regions. This effect typically reduces the boost by 20–30% and is modulated by the environment, with filament haloes generally dominating at high masses, walls intermediate, and voids the most suppressed.

With the distance- and environment-dependent subhalo concentrations and tidal stripping included, the resulting boosts in Fig. 4 follow the same qualitative trends as Fig. 3. Filament haloes are slightly more enhanced at high host M_{200} masses, reaching ~ 1.12 times the cosmic mean compared to ~ 1.07 in the SCP14-based environment-dependent model, while walls and voids retain similar intermediate and suppressed behavior, respectively. This illustrates that incorporating distance-dependent concentrations amplifies the boost in dense cosmic web environments without altering the overall pattern set by the SCP14-based environment-dependent model.

For convenient implementation in future semi-analytical models or N-body analyses, we provide an analytical representation of the environment-specific boost factors shown in Fig. 4. Following the general functional form of M17, we parametrize these values using a logarithmic polynomial expansion:

$$\log_{10} B(M_{200}, z=0) = \sum_{i=0}^{3} b_i \left[\log_{10}\left(\frac{M_{200}}{M_\odot}\right)\right]^i, \quad (14)$$

where the environment-dependent coefficients b_i are listed in Table IV. The uncertainties are derived from the fit covariance matrix. This environment-dependent extension of the M17 framework is intended as a practical fitting prescription for downstream applications, including annihilation forecast calculations, halo-population modeling, and environment-aware semi-analytic studies of dark-matter targets.

The fit reported above is calibrated for $z = 0$ host haloes in the mass range $10^9 \lesssim M_{200}/(M_\odot/h) \lesssim 10^{13}$, and for the three large-scale environments considered in this work, namely filaments, walls, and voids. It should therefore be used as an interpolation formula within this calibrated domain. Its validity outside this mass range, at higher redshift, or for alternative cosmological calibrations remains to be tested. Across the calibrated mass range, the polynomial representation reproduces the boost curves very closely, with absolute residuals typically of order 10^{-2} and nowhere exceeding about 2×10^{-2}.

V. SUMMARY AND CONCLUSIONS

In this work, we have explored how the cosmic web environment influences DM haloes and their substructure, and the potential implications for annihilation signals. Using the high-resolution COLOR simulation [59], together with the SCP14 semi-analytic framework and the environment-dependent trends calibrated in Hellwing et al. [35], Markos Hunde et al. [56], we examined how host-halo concentration, subhalo abundance, and subhalo internal structure vary systematically across filaments, walls, and voids. These environment-dependent corrections were incorporated into the computation of subhalo boost factors, and we also considered the distance- and environment-dependent concentration model of M17 to explore the impact of tidal stripping and subhalo radial positions on the boosts.

The main findings of this study are:

- Host halo concentrations show a dependence on the cosmic web environment, with haloes in filaments generally more concentrated, walls intermediate, and void haloes less concentrated relative to the cosmic mean.
- The subhalo mass function varies systematically with environment. Filament haloes host the largest number of subhalos at higher host masses, whereas

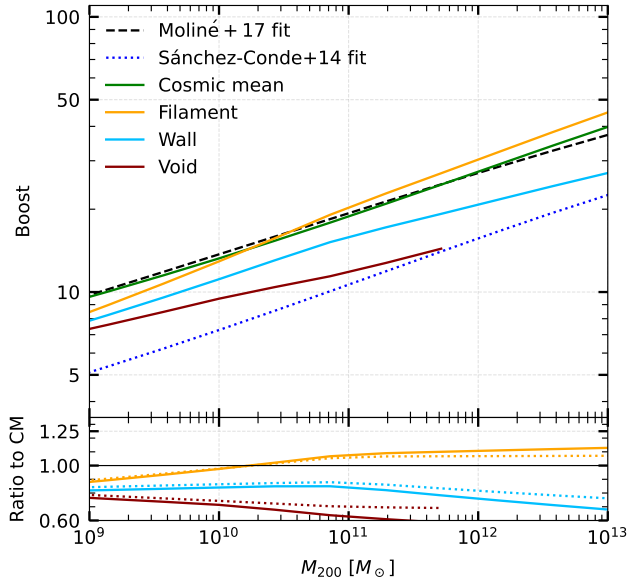

FIG. 4. Environment-dependent subhalo boost factor as a function of M_{200} mass of the host. *Upper panel:* Boost factors for haloes in different cosmic web environments. The green solid line shows the cosmic-mean prediction from M17 without environment modification, the blue dotted line shows the SCP14 fit, and the black dashed lines indicate the polynomial fits for each environment. Tidal stripping is included in the calculations. *Lower panel:* Ratio of each environment to the cosmic-mean prediction, showing the relative effect of the cosmic web. Compared to Fig. 3, these curves are computed in the M17-based distance-dependent framework, in which subhalo concentrations depend explicitly on both subhalo mass and radial position within the host halo.

wall haloes can have slightly higher subhalo numbers at lower host masses. Void haloes consistently contain the fewest subhalos.

- Subhalo internal densities, quantified via $R_{\rm max}$ ratios or characteristic concentrations, also vary with environment. Subhalos in filaments tend to have higher densities, those in walls are intermediate, and void subhalos are lower in density, reflecting differences in formation times and tidal influences.

- Environment-modulated subhalo boost factors reflect the combined effects of host-halo concentration, subhalo abundance, and subhalo internal structure. Filament haloes consistently exhibit the largest boosts, wall haloes remain intermediate, and void haloes are the most suppressed. Relative to the cosmic mean, filament boosts rise from about 0.85 at low host masses to 1.07 near $10^{11}\ h^{-1}\,M_\odot$, wall boosts remain below unity and decline to ~ 0.76 at the high-mass end, while void boosts stay suppressed across the full mass range and can drop to approximately 0.70.

- Incorporating the distance-dependent concentration model of M17 preserves the same environmental ordering, but increases the high-mass filament boost from $\sim$ 1.07 in the baseline SCP14-based model to $\sim$ 1.12. At low host masses, filament boosts remain below unity, while wall and void boosts stay intermediate and suppressed, respectively.

These results suggest that the predicted DM annihilation signal is influenced not only by the number of subhalos but also by their internal densities, which vary with environment. The observed modulation implies that different cosmic web locations can lead to subtle but meaningful variations in expected signals. Including environmental effects alongside structural variations provides a framework that allows for more nuanced predictions of annihilation boosts.

Although this study is limited to two hierarchical levels of subhalos, it illustrates how variations in halo and subhalo properties may influence DM annihilation signals. The trends identified here remain consistent across the different subhalo and concentration models explored. Future work could consider additional complexities, such as tidal interactions, halo assembly histories, and other local environmental factors, to further assess their potential impact on predicted signals.

Overall, incorporating variations in host halo concentration, subhalo abundance, and internal density structure associated with the cosmic web provides a more detailed understanding of how environmental factors might shape the DM annihilation signal. These findings demonstrate the potential importance of considering environmental context when interpreting indirect detection signals or constructing theoretical predictions.

A. Implications for Indirect Detection Signals

In our model, the cosmic web environment modulates boost factors by tens of percent: the ratio $B(M, \mathrm{env})/B_{\rm CM}(M)$ ranges from approximately 70% in voids to 112% in filaments across the host-mass range explored (see Fig. 4). This level of variation is comparable to other key theoretical uncertainties, such as halo-to-halo scatter in concentration and uncertainties in the normalization and slope of the SHMF, demonstrating that environmental effects are a significant source of variation rather than a minor higher-order correction.

The sensitivity arises from the coordinated variation of host halo concentration, subhalo abundance, and internal density structure. Because annihilation rates scale as ρ^2, even modest shifts in these properties across the cosmic web can produce discernible differences in the expected DM signal. Consequently, haloes residing in denser, more massive regions, such as filaments, are predicted to generate stronger annihilation signatures than their counterparts in underdense environments. This is consistent with foundational substructure studies [e.g., 16, 39, 75], while adding an explicit spatial context:

the increased subhalo mass fraction and elevated central densities in filaments imply that annihilation luminosities can be systematically enhanced relative to an environment-agnostic, cosmic-mean population.

For observational strategies, these results suggest that targets located in different large-scale environments may exhibit modest variations in expected annihilation flux depending on their position within the cosmic web. Selecting haloes in filamentary regions could yield slightly higher expected annihilation signals, whereas searches in under-dense voids may be subject to lower expected fluxes. Similarly, for studies of the Milky Way or nearby galaxies, acknowledging that the local environment shapes the subhalo population could lead to more nuanced foreground or background estimates. Including information on the spatial distribution and structural variation of subhalos allows for a refinement of predictions without requiring drastic changes to existing detection paradigms.

Comparisons with alternative subhalo concentration models, such as distance-dependent prescriptions, indicate that variations in subhalo internal density can further alter the boost factor, particularly for specific host halo mass ranges. While the trends observed here are consistent with general substructure expectations, they suggest that environmental modulation introduces an additional layer of variation that is highly relevant for interpreting indirect detection signals. In practice, accounting for the cosmic web environment provides a more nuanced view of potential annihilation luminosities, helping to quantify relative differences between haloes rather than producing absolute predictions. This approach assists in refining theoretical models and observational strategies while maintaining consistency with existing expectations.

Beyond the final boost-factor predictions, this work also provides a set of intermediate, environment-dependent ingredients that may be useful more broadly: corrections to the host-halo concentration, the differential SHMF, and the subhalo internal-structure proxy based on the $V_{\rm max}$–$R_{\rm max}$ relation. Because these components are fitted separately and expressed in modular form, they can in principle be propagated into other semi-analytic or forward-model frameworks that are sensitive to subhalo abundance and internal structure. This includes strong-lensing mass modelling, where forward modelling of lensed images is increasingly used to constrain the inner mass distribution of lenses and the presence of low-mass dark subhaloes [86]. While such an application is beyond the scope of the present paper, the fitted ingredients derived here provide a natural starting point for incorporating cosmic-web environmental information into lensing-oriented subhalo models.

ACKNOWLEDGMENTS

The authors thank Oliver Newton for discussion and comments at the early stage of this project and Krishna Naidoo for running the `CaCTus` cosmic web classification for us on the COLOR data. This work was supported via the research project "COLAB" funded by the National Science Centre, Poland, under agreement number UMO-2020/39/B/ST9/03494.

Appendix A: Subhalo Concentration Model

The subhalo concentration model described here is introduced in Section IV, where its application to computing the subhalo boost factor is presented. This section provides the full parametrization of the model, including the dependence on subhalo mass and radial position within the host halo.

We adopt the distance-dependent concentration model of M17, calibrated against high-resolution numerical simulations. In this framework, the concentration depends explicitly on both the subhalo mass and its radial distance from the host center. This formulation incorporates the combined effects of hierarchical structure formation and tidal evolution inside the host halo.

The concentration is parametrized as Eq. (7) in M17:

$$c_{200}(m_{200}, x_{\rm sub}) = c_0 \left[1 + \sum_{i=1}^{3} a_i \left(\log_{10} \frac{m_{200}}{10^8\, h^{-1}\, M_\odot}\right)^i\right] \times \Big[1 + b\, \log_{10}(x_{\rm sub})\Big], \tag{A1}$$

where $c_0 = 19.9$, $a_i = \{-0.195, 0.089, 0.089\}$, and $b = -0.54$. The radial coordinate is defined as $x_{\rm sub} = R_{\rm sub}/R_{\rm vir}$. The first bracket captures the mass dependence, reflecting the earlier formation times of lower-mass haloes in a hierarchical scenario. The second bracket introduces a radial modulation that decreases c_{200} with increasing distance from the host center, accounting for tidal stripping and dynamical processing. As a result, subhalos located closer to the host center are predicted to be more concentrated than those in the outskirts.

The environmental dependence of subhalo concentrations is illustrated in Fig. 5. Each panel corresponds to a different radial bin, with the upper subpanel showing the median c_{200} as a function of m_{200} in distinct large-scale environments. The lower sub-panel shows the concentration in each environment relative to the cosmic mean, indicating the effect of the cosmic web on subhalo internal structure.

The influence of the cosmic web on subhalo concentration is secondary to radial position, with a negligible impact for subhalos in the inner host regions ($x_{\rm sub} < 0.1$). However, a distinct environmental hierarchy emerges in the outer radial bins ($0.3 < x_{\rm sub} < 1.0$). In these outskirts, subhalos in filaments closely track the cosmic mean, effectively defining the average concentration. In contrast, subhalos in voids exhibit the most significant deviation, with concentrations approximately 12–15% lower than the cosmic mean. Subhalos residing in walls represent an intermediate population, showing a

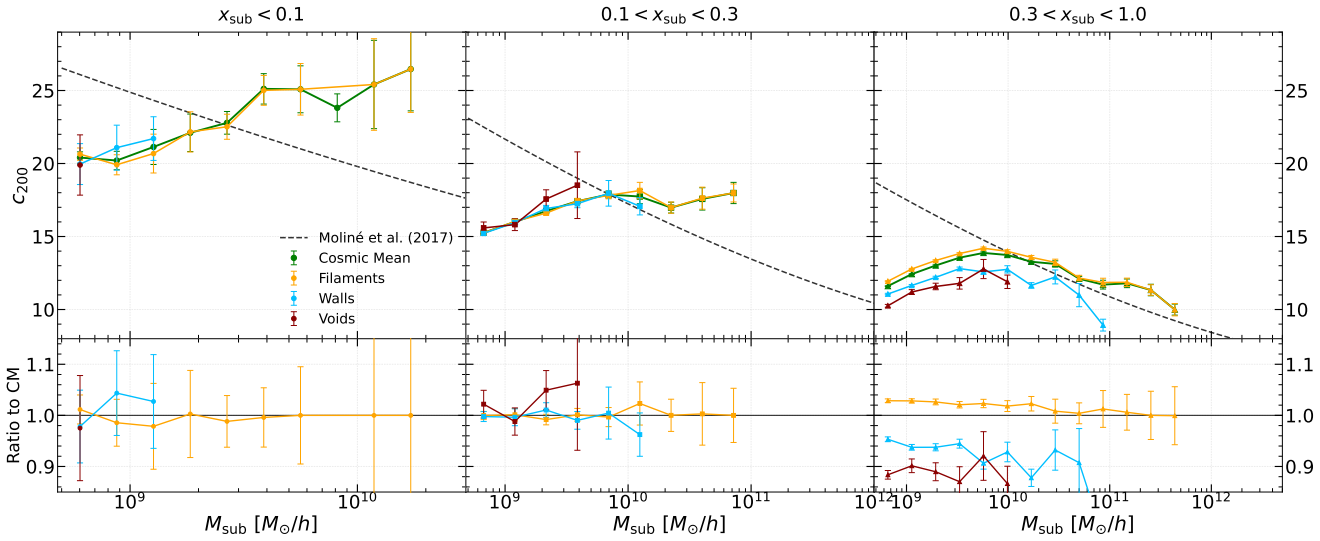

FIG. 5. Median subhalo concentration c_{200} as a function of subhalo mass $m_{\rm sub}$ in three radial bins. In each panel, the upper sub-panel displays the median concentration for different large-scale environments, with error bars indicating the 1σ bootstrap uncertainties, while the black dashed line represents the concentration-mass relation from M17 evaluated at the median $x_{\rm sub}$ of each bin. The lower subpanel shows the concentration in each environment relative to the cosmic mean.

modest deficit of roughly 5% compared to the mean. This suggests that less dense cosmic environments correlate with lower subhalo concentrations as one moves toward the host outskirts.

This behavior is consistent with tidal evolution within the host potential. Subhalos in the inner regions experience stronger tidal stripping and repeated dynamical interactions, which effectively homogenize their structural properties and erase differences inherited from the large-scale environment. In contrast, subhalos in the outskirts are less dynamically processed and therefore retain a residual dependence on the cosmic web, with the observed trends reflecting the local density conditions and assembly histories of their respective environments before accretion.

[1] G. Bertone and D. Hooper, Reviews of Modern Physics **90**, 045002 (2018), arXiv:1605.04909 [astro-ph.CO].

[2] Planck Collaboration, N. Aghanim, Y. Akrami, M. Ashdown, J. Aumont, C. Baccigalupi, M. Ballardini, A. J. Banday, R. B. Barreiro, N. Bartolo, S. Basak, R. Battye, K. Benabed, J.-P. Bernard, M. Bersanelli, P. Bielewicz, J. J. Bock, J. R. Bond, J. Borrill, F. R. Bouchet, F. Boulanger, M. Bucher, C. Burigana, R. C. Butler, E. Calabrese, J.-F. Cardoso, J. Carron, A. Challinor, H. C. Chiang, J. Chluba, L. P. L. Colombo, C. Combet, D. Contreras, B. P. Crill, F. Cuttaia, P. de Bernardis, G. de Zotti, J. Delabrouille, J.-M. Delouis, E. Di Valentino, J. M. Diego, O. Doré, M. Douspis, A. Ducout, X. Dupac, S. Dusini, G. Efstathiou, F. Elsner, T. A. Enßlin, H. K. Eriksen, Y. Fantaye, M. Farhang, J. Fergusson, R. Fernandez-Cobos, F. Finelli, F. Forastieri, M. Frailis, A. A. Fraisse, E. Franceschi, A. Frolov, S. Galeotta, S. Galli, K. Ganga, R. T. Génova-Santos, M. Gerbino, T. Ghosh, J. González-Nuevo, K. M. Górski, S. Gratton, A. Gruppuso, J. E. Gudmundsson, J. Hamann, W. Handley, F. K. Hansen, D. Herranz, S. R. Hildebrandt, E. Hivon, Z. Huang, A. H. Jaffe, W. C. Jones, A. Karakci, E. Keihänen, R. Keskitalo, K. Kiiveri, J. Kim, T. S. Kisner, L. Knox, N. Krachmalnicoff, M. Kunz, H. Kurki-Suonio, G. Lagache, J.-M. Lamarre, A. Lasenby, M. Lattanzi, C. R. Lawrence, M. Le Jeune, P. Lemos, J. Lesgourgues, F. Levrier, A. Lewis, M. Liguori, P. B. Lilje, M. Lilley, V. Lindholm, M. López-Caniego, P. M. Lubin, Y.-Z. Ma, J. F. Macías-Pérez, G. Maggio, D. Maino, N. Mandolesi, A. Mangilli, A. Marcos-Caballero, M. Maris, P. G. Martin, M. Martinelli, E. Martínez-González, S. Matarrese, N. Mauri, J. D. McEwen, P. R. Meinhold, A. Melchiorri, A. Mennella, M. Migliaccio, M. Millea, S. Mitra, M.-A. Miville-Deschênes, D. Molinari, L. Montier, G. Morgante, A. Moss, P. Natoli, H. U. Nørgaard-Nielsen, L. Pagano, D. Paoletti, B. Partridge, G. Patanchon, H. V. Peiris, F. Perrotta, V. Pettorino, F. Piacentini, L. Polastri, G. Polenta, J.-L. Puget, J. P. Rachen, M. Reinecke, M. Remazeilles, A. Renzi, G. Rocha, C. Rosset, G. Roudier, J. A. Rubiño-Martín, B. Ruiz-Granados, L. Salvati, M. Sandri, M. Savelainen, D. Scott, E. P. S. Shellard, C. Sirignano, G. Sirri, L. D. Spencer, R. Sunyaev, A.-S. Suur-Uski, J. A. Tauber, D. Tavagnacco, M. Tenti, L. Toffolatti, M. Tomasi, T. Trombetti, L. Valenziano, J. Valiviita, B. Van Tent, L. Vibert, P. Vielva, F. Villa, N. Vittorio, B. D. Wandelt, I. K. Wehus, M. White, S. D. M. White, A. Zacchei, and A. Zonca,

A&A **641**, A6 (2020), arXiv:1807.06209 [astro-ph.CO].
[3] B. Carr and F. Kuhnel, arXiv e-prints , arXiv:2110.02821 (2021), arXiv:2110.02821 [astro-ph.CO].
[4] G. Jungman, M. Kamionkowski, and K. Griest, Phys. Rep. **267**, 195 (1996), arXiv:hep-ph/9506380 [hep-ph].
[5] G. Bertone, D. Hooper, and J. Silk, Phys. Rep. **405**, 279 (2005), arXiv:hep-ph/0404175 [hep-ph].
[6] T. Bringmann and C. Weniger, Physics of the Dark Universe **1**, 194 (2012), arXiv:1208.5481 [hep-ph].
[7] L. Roszkowski, E. M. Sessolo, and S. Trojanowski, Reports on Progress in Physics **81**, 066201 (2018).
[8] S. J. Asztalos, L. J. Rosenberg, K. van Bibber, P. Sikivie, and K. Zioutas, Annual Review of Nuclear and Particle Science **56**, 293 (2006).
[9] D. J. E. Marsh, Phys. Rep. **643**, 1 (2016).
[10] J. L. Feng, ARA&A **48**, 495 (2010), arXiv:1003.0904 [astro-ph.CO].
[11] J. Kopp, arXiv e-prints , arXiv:2109.00767 (2021), arXiv:2109.00767 [hep-ph].
[12] T. Marrodán Undagoitia and L. Rauch, Journal of Physics G Nuclear Physics **43**, 013001 (2016), arXiv:1509.08767 [physics.ins-det].
[13] M. Battaglieri, A. Belloni, A. Chou, P. Cushman, B. Echenard, R. Essig, J. Estrada, J. L. Feng, B. Flaugher, P. J. Fox, P. Graham, C. Hall, R. Harnik, J. Hewett, J. Incandela, E. Izaguirre, D. McKinsey, M. Pyle, N. Roe, G. Rybka, P. Sikivie, T. M. P. Tait, N. Toro, R. Van De Water, N. Weiner, K. Zurek, E. Adelberger, A. Afanasev, D. Alexander, J. Alexander, V. Cristian Antochi, D. M. Asner, H. Baer, D. Banerjee, E. Baracchini, P. Barbeau, J. Barrow, N. Bastidon, J. Battat, S. Benson, A. Berlin, M. Bird, N. Blinov, K. K. Boddy, M. Bondi, W. M. Bonivento, M. Boulay, J. Boyce, M. Brodeur, L. Broussard, R. Budnik, P. Bunting, M. Caffee, S. S. Caiazza, S. Campbell, T. Cao, G. Carosi, M. Carpinelli, G. Cavoto, A. Celentano, J. Hyeok Chang, S. Chattopadhyay, A. Chavarria, C.-Y. Chen, K. Clark, J. Clarke, O. Colegrove, J. Coleman, D. Cooke, R. Cooper, M. Crisler, P. Crivelli, F. D'Eramo, D. D'Urso, E. Dahl, W. Dawson, M. De Napoli, R. De Vita, P. DeNiverville, S. Derenzo, A. Di Crescenzo, E. Di Marco, K. R. Dienes, M. Diwan, D. Handiipondola Dongwi, A. Drlica-Wagner, S. Ellis, A. Chigbo Ezeribe, G. Farrar, F. Ferrer, E. Figueroa-Feliciano, A. Filippi, G. Fiorillo, B. Fornal, A. Freyberger, C. Frugiuele, C. Galbiati, I. Galon, S. Gardner, A. Geraci, G. Gerbier, M. Graham, E. Gschwendtner, C. Hearty, J. Heise, R. Henning, R. J. Hill, D. Hitlin, Y. Hochberg, J. Hogan, M. Holtrop, Z. Hong, T. Hossbach, T. B. Humensky, P. Ilten, K. Irwin, J. Jaros, R. Johnson, M. Jones, Y. Kahn, N. Kalantarians, M. Kaplinghat, R. Khatiwada, S. Knapen, M. Kohl, C. Kouvaris, J. Kozaczuk, G. Krnjaic, V. Kubarovsky, E. Kuflik, A. Kusenko, R. Lang, K. Leach, T. Lin, M. Lisanti, J. Liu, K. Liu, M. Liu, D. Loomba, J. Lykken, K. Mack, J. Mans, H. Maris, T. Markiewicz, L. Marsicano, C. J. Martoff, G. Mazzitelli, C. McCabe, S. D. McDermott, A. McDonald, B. McKinnon, D. Mei, T. Melia, G. A. Miller, K. Miuchi, S. M. P. Nazeer, O. Moreno, V. Morozov, F. Mouton, H. Mueller, A. Murphy, R. Neilson, T. Nelson, C. Neu, Y. Nosochkov, C. O'Hare, N. Oblath, J. Orrell, J. Ouellet, S. Pastore, S. Paul, M. Perelstein, A. Peter, N. Phan, N. Phinney, M. Pivovaroff, A. Pocar, M. Pospelov, J. Pradler, P. Privitera, S. Profumo, M. Raggi, S. Rajendran, N. Randazzo, T. Raubenheimer, C. Regenfus, A. Renshaw, A. Ritz, T. Rizzo, L. Rosenberg, A. Rubbia, B. Rybolt, T. Saab, B. R. Safdi, E. Santopinto, A. Scarff, M. Schneider, P. Schuster, G. Seidel, and H. Sekiya, arXiv e-prints , arXiv:1707.04591 (2017), arXiv:1707.04591 [hep-ph].
[14] M. A. Sánchez-Conde and F. Prada, MNRAS **442**, 2271 (2014), arXiv:1312.1729 [astro-ph.CO].
[15] Á. Moliné, M. A. Sánchez-Conde, S. Palomares-Ruiz, and F. Prada, MNRAS **466**, 4974 (2017), arXiv:1603.04057 [astro-ph.CO].
[16] S. Ando, T. Ishiyama, and N. Hiroshima, Galaxies **7**, 68 (2019), arXiv:1903.11427 [astro-ph.CO].
[17] S. Colafrancesco, S. Profumo, and P. Ullio, A&A **455**, 21 (2006), arXiv:astro-ph/0507575 [astro-ph].
[18] M. Kamionkowski, S. M. Koushiappas, and M. Kuhlen, Phys. Rev. D **81**, 043532 (2010), arXiv:1001.3144 [astro-ph.GA].
[19] J. Pearson, H. Dickinson, S. Sinha, and S. Serjeant, arXiv e-prints , arXiv:2509.22609 (2025), arXiv:2509.22609 [astro-ph.CO].
[20] J. R. Bond, L. Kofman, and D. Pogosyan, Nature **380**, 10.1038/380603a0 (1996).
[21] S. D. M. White and M. J. Rees, MNRAS **183**, 10.1093/mnras/183.3.341 (1978).
[22] V. Springel, MNRAS **364**, 1105 (2005), arXiv:astro-ph/0505010 [astro-ph].
[23] V. Springel, Monthly notices of the royal astronomical society **364**, 1105 (2005).
[24] J. Zavala and C. S. Frenk, Galaxies **7**, 81 (2019), arXiv:1907.11775 [astro-ph.CO].
[25] A. G. Doroshkevich, Astrophysics **6**, 320 (1970).
[26] Y. B. Zel'dovich, A&A **5**, 84 (1970).
[27] S. F. Shandarin and Y. B. Zeldovich, Reviews of Modern Physics **61**, 185 (1989).
[28] M. Cautun, R. van de Weygaert, B. J. T. Jones, and C. S. Frenk, MNRAS **441**, 2923 (2014), arXiv:1401.7866 [astro-ph.CO].
[29] N. I. Libeskind, R. van de Weygaert, M. Cautun, B. Falck, E. Tempel, T. Abel, M. Alpaslan, M. A. Aragón-Calvo, J. E. Forero-Romero, R. Gonzalez, S. Gottlöber, O. Hahn, W. A. Hellwing, Y. Hoffman, B. J. Jones, F. Kitaura, A. Knebe, S. Manti, M. Neyrinck, S. E. Nuza, N. Padilla, E. Platen, N. Ramachandra, A. Robotham, E. Saar, S. Shandarin, M. Steinmetz, R. S. Stoica, T. Sousbie, and G. Yepes, MNRAS **473**, 1195 (2018).
[30] M. A. Aragón-Calvo, R. van de Weygaert, B. J. T. Jones, and J. M. van der Hulst, ApJ **655**, L5 (2007), arXiv:astro-ph/0610249 [astro-ph].
[31] O. Hahn, C. M. Carollo, C. Porciani, and A. Dekel, MNRAS **381**, 41 (2007), arXiv:0704.2595 [astro-ph].
[32] O. Metuki, N. I. Libeskind, Y. Hoffman, R. A. Crain, and T. Theuns, MNRAS **446**, 10.1093/mnras/stu2166 (2015).
[33] D. Alonso, E. Eardley, and J. A. Peacock, MNRAS **447**, 2683 (2015), arXiv:1406.4159 [astro-ph.CO].
[34] P. Ganeshaiah Veena, M. Cautun, R. van de Weygaert, E. Tempel, B. J. T. Jones, S. Rieder, and C. S. Frenk, MNRAS **481**, 414 (2018), arXiv:1805.00033 [astro-ph.CO].
[35] W. A. Hellwing, M. Cautun, R. van de Weygaert, and B. T. Jones, Phys. Rev. D **103**, 063517 (2021),

arXiv:2011.08840 [astro-ph.CO].
[36] P. Ganeshaiah Veena, M. Cautun, R. van de Weygaert, E. Tempel, and C. S. Frenk, MNRAS **503**, 2280 (2021), arXiv:2007.10365 [astro-ph.CO].
[37] B. Moore, S. Ghigna, F. Governato, G. Lake, T. Quinn, J. Stadel, and P. Tozzi, ApJ **524**, L19 (1999), arXiv:astro-ph/9907411 [astro-ph].
[38] A. Klypin, A. V. Kravtsov, O. Valenzuela, and F. Prada, ApJ **522**, 82 (1999), arXiv:astro-ph/9901240 [astro-ph].
[39] J. Diemand, M. Kuhlen, P. Madau, M. Zemp, B. Moore, D. Potter, and J. Stadel, Nature **454**, 735 (2008), arXiv:0805.1244 [astro-ph].
[40] V. Springel, J. Wang, M. Vogelsberger, A. Ludlow, A. Jenkins, A. Helmi, J. F. Navarro, C. S. Frenk, and S. D. M. White, MNRAS **391**, 1685 (2008), arXiv:0809.0898 [astro-ph].
[41] T. Ishiyama, F. Prada, A. A. Klypin, M. Sinha, R. B. Metcalf, E. Jullo, B. Altieri, S. A. Cora, D. Croton, S. de la Torre, D. E. Millán-Calero, T. Oogi, J. Ruedas, and C. A. Vega-Martínez, MNRAS **506**, 4210 (2021), arXiv:2007.14720 [astro-ph.CO].
[42] N. Hiroshima, S. Ando, and T. Ishiyama, Phys. Rev. D **97**, 123002 (2018), arXiv:1803.07691 [astro-ph.CO].
[43] M. Boylan-Kolchin, J. S. Bullock, and M. Kaplinghat, MNRAS **415**, L40 (2011), https://academic.oup.com/mnrasl/article-pdf/415/1/L40/54669362/mnrasl_415_1_l40.pdf.
[44] L. E. Strigari and R. H. Wechsler, ApJ **749**, 75 (2012), arXiv:1111.2611 [astro-ph.CO].
[45] F. C. van den Bosch and G. Ogiya, MNRAS **475**, 4066 (2018), arXiv:1801.05427 [astro-ph.GA].
[46] S. B. Green, F. C. van den Bosch, and F. Jiang, MNRAS **503**, 4075 (2021), arXiv:2103.01227 [astro-ph.GA].
[47] L. E. Strigari, S. M. Koushiappas, J. S. Bullock, and M. Kaplinghat, Phys. Rev. D **75**, 083526 (2007), arXiv:astro-ph/0611925 [astro-ph].
[48] L. Bergström, New Journal of Physics **11**, 105006 (2009), arXiv:0903.4849 [hep-ph].
[49] M. Cirelli, Pramana **79**, 1021 (2012), arXiv:1202.1454 [hep-ph].
[50] T. Ishiyama and S. Ando, MNRAS **492**, 3662 (2020), arXiv:1907.03642 [astro-ph.CO].
[51] O. Hahn, C. Porciani, C. M. Carollo, and A. Dekel, MNRAS **375**, 489 (2007), arXiv:astro-ph/0610280 [astro-ph].
[52] O. Metuki, N. I. Libeskind, and Y. Hoffman, MNRAS **460**, 10.1093/mnras/stw979 (2016).
[53] F. Jiang and F. C. V. D. Bosch, MNRAS **458**, 10.1093/mnras/stw439 (2016).
[54] G. Ogiya, O. Hahn, and A. B. Hirschmann, Monthly Notices of the Royal Astronomical Society **503**, 1233 (2021).
[55] R. Errani and J. F. Navarro, Monthly Notices of the Royal Astronomical Society **505**, 18 (2021).
[56] F. Markos Hunde, O. Newton, W. A. Hellwing, M. Bilicki, and K. Naidoo, A&A **700**, A65 (2025), arXiv:2409.09226 [astro-ph.CO].
[57] Á. Moliné, M. A. Sánchez-Conde, A. Aguirre-Santaella, T. Ishiyama, F. Prada, S. A. Cora, D. Croton, E. Jullo, R. B. Metcalf, T. Oogi, and J. Ruedas, MNRAS **518**, 157 (2022).
[58] S. Bose, W. A. Hellwing, C. S. Frenk, A. Jenkins, M. R. Lovell, J. C. Helly, and B. Li, MNRAS **455**, 318 (2016).
[59] W. A. Hellwing, C. S. Frenk, M. Cautun, S. Bose, J. Helly, A. Jenkins, T. Sawala, and M. Cytowski, MNRAS **457**, 3492 (2016), arXiv:1505.06436 [astro-ph.CO].
[60] M. Cautun, R. van de Weygaert, and B. J. T. Jones, MNRAS **429**, 1286 (2013), arXiv:1209.2043 [astro-ph.CO].
[61] E. Komatsu, K. M. Smith, J. Dunkley, C. L. Bennett, B. Gold, G. Hinshaw, N. Jarosik, D. Larson, M. R. Nolta, L. Page, D. N. Spergel, M. Halpern, R. S. Hill, A. Kogut, M. Limon, S. S. Meyer, N. Odegard, G. S. Tucker, J. L. Weiland, E. Wollack, and E. L. Wright, ApJS **192**, 18 (2011), arXiv:1001.4538 [astro-ph.CO].
[62] M. Davis, G. Efstathiou, C. S. Frenk, and S. D. M. White, ApJ **292**, 10.1086/163168 (1985).
[63] V. Springel, S. D. M. White, G. Tormen, and G. Kauffmann, MNRAS **328**, 726 (2001), arXiv:astro-ph/0012055 [astro-ph].
[64] M. A. Aragón-Calvo, B. J. T. Jones, R. van de Weygaert, and J. M. van der Hulst, A&A **474**, 315 (2007), arXiv:0705.2072 [astro-ph].
[65] P. Nurmi, P. Heinämäki, J. Holopainen, P. Pihajoki, E. Saar, M. Einasto, and J. Einasto, in Galaxy Evolution across the Hubble Time, Vol. 235, edited by F. Combes and J. Palouš (2007) pp. 127–127.
[66] N. A. Bond, M. A. Strauss, and R. Cen, MNRAS **409**, 156 (2010), https://academic.oup.com/mnras/article-pdf/409/1/156/6221724/mnras0409-0156.pdf.
[67] Y. Hoffman, O. Metuki, G. Yepes, S. Gottlöber, J. E. Forero-Romero, N. I. Libeskind, and A. Knebe, MNRAS **425**, 2049 (2012), https://academic.oup.com/mnras/article-pdf/425/3/2049/3052482/425-3-2049.pdf.
[68] D. Pomarède, Y. Hoffman, H. M. Courtois, and R. B. Tully, ApJ **845**, 55 (2017), arXiv:1706.03413 [astro-ph.CO].
[69] J. E. Forero–Romero, Y. Hoffman, S. Gottlöber, A. Klypin, and G. Yepes, MNRAS **396**, 1815 (2009), https://academic.oup.com/mnras/article-pdf/396/3/1815/5804803/mnras0396-1815.pdf.
[70] M. A. Aragón-Calvo, E. Platen, R. van de Weygaert, and A. S. Szalay, ApJ **723**, 364 (2010), arXiv:0809.5104 [astro-ph].
[71] T. Sousbie, MNRAS **414**, 350 (2011), https://academic.oup.com/mnras/article-pdf/414/1/350/3809858/mnras0414-0350.pdf.
[72] J. Feldbrugge, R. van de Weygaert, J. Hidding, and J. Feldbrugge, J. Cosmology Astropart. Phys. **2018**, 027 (2018), arXiv:1703.09598 [astro-ph.CO].
[73] `CaCTus`is currently being prepared for public release and is not yet available at the time of writing.
[74] M. Cautun, S. Bose, C. S. Frenk, Q. Guo, J. Han, W. A. Hellwing, T. Sawala, and W. Wang, MNRAS **452**, 3838 (2015), arXiv:1506.04151 [astro-ph.GA].
[75] M. Kuhlen, J. Diemand, and P. Madau, ApJ **686**, 262 (2008), arXiv:0805.4416 [astro-ph].
[76] M. Stref, T. Lacroix, and J. Lavalle, Galaxies **7**, 65 (2019), arXiv:1905.02008 [astro-ph.CO].
[77] F. Prada, A. A. Klypin, A. J. Cuesta, J. E. Betancort-Rijo, and J. Primack, MNRAS **423**, 3018 (2012), arXiv:1104.5130 [astro-ph.CO].
[78] V. Avila-Reese, P. Colín, S. Gottlöber, C. Firmani, and C. Maulbetsch, ApJ **634**, 51 (2005), arXiv:astro-ph/0508053 [astro-ph].
[79] J. Diemand, M. Kuhlen, and P. Madau, ApJ **667**, 859 (2007), arXiv:astro-ph/0703337 [astro-ph].
[80] J. E. Taylor and A. Babul, ApJ **559**, 716 (2001), arXiv:astro-ph/0012305 [astro-ph].
[81] A. V. Kravtsov, O. Y. Gnedin, and A. A. Klypin, ApJ

609, 482 (2004), arXiv:astro-ph/0401088 [astro-ph].
[82] G. Ogiya, F. C. van den Bosch, O. Hahn, S. B. Green, T. B. Miller, and A. Burkert, MNRAS **485**, 189 (2019), arXiv:1901.08601 [astro-ph.GA].
[83] R. Errani and J. Peñarrubia, MNRAS **491**, 4591 (2020), arXiv:1906.01642 [astro-ph.GA].
[84] R. Errani and J. F. Navarro, MNRAS **505**, 18 (2021), arXiv:2011.07077 [astro-ph.GA].
[85] A. J. Benson and X. Du, MNRAS **517**, 1398 (2022), arXiv:2206.01842 [astro-ph.GA].
[86] N. B. Hogg, J. W. Nightingale, Q. He, J. McCleary, G. Mahler, A. Amvrosiadis, G. Gozaliasl, E. Berman, R. J. Massey, D. Scognamiglio, M. Franco, D. Liu, M. Shuntov, L. Paquereau, O. Ilbert, N. Allen, S. Toft, H. B. Akins, C. M. Casey, J. S. Kartaltepe, A. M. Koekemoer, H. J. McCracken, J. D. Rhodes, B. E. Robertson, N. E. Drakos, A. L. Faisst, H. Hatamnia, and S. L. Newman, MNRAS **544**, 782 (2025), arXiv:2503.08785 [astro-ph.GA].

Chapter 5

Caught in the Cosmic Web: Environmental Effects on the Evolution of Subhalo Properties

"The sun does not forget a village just because it is small."
— Senegalese Proverb

5.1 Introduction

In the hierarchical framework of cosmic structure formation, DM haloes do not evolve in isolation. Their growth, internal kinematics, and the evolution of the subhaloes they contain are closely connected to the surrounding large-scale structure of the cosmic web [14, 110, 181]. As matter collapses gravitationally, haloes form within an anisotropic network of filaments, walls, and voids that continuously channels mass and shapes the local gravitational environment [41, 53]. In this sense, the cosmic web provides more than a geometric description of the matter distribution, acting instead as a dynamical framework that shapes the geometry of accretion, maps tidal fields, and influences the long-term evolution of substructure [111].

Previous chapters established that subhalo populations exhibit a measurable dependence on the cosmic web environment. In particular, Chapter 3 demonstrated that host haloes residing in filamentary regions contain systematically different subhalo populations compared to those in walls and voids. However, analyses based solely on present-day subhalo properties cannot easily distinguish whether these environmental differences are already imprinted on the infalling population before accretion or whether they arise primarily through tidal evolution inside the host halo potential [156, 194]. Disentangling these possibilities is necessary for understanding how the large-scale environment influences the non-linear evolution of structure.

Subhaloes are particularly sensitive probes of environmental evolution because they undergo significant gravitational processing after crossing the virial boundary of a host halo. Once accreted, subhaloes experience tidal stripping, dynamical friction, and impulsive tidal heating during pericentric passages through the host potential [195]. These processes progressively remove loosely bound outer material, reduce the total bound mass of the subhalo, and may eventually lead to complete disruption [115, 196]. The efficiency of this evolution depends strongly on host halo mass, orbital trajectory, and time since infall, all of which are correlated with the surrounding large-scale environment [197, 198]. Consequently, the subhalo population observed at $z = 0$ reflects a combination of its initial conditions at accretion and the cumulative effects of subsequent tidal evolution.

To disentangle these effects, this chapter focuses on quantities measured at the epoch when subhaloes attain their maximum mass and maximum circular velocity, denoted $M_{\rm peak}$ and $V_{\rm peak}$, respectively. Because these peak quantities are reached before substantial host driven tidal stripping becomes dominant, they provide a more stable description of the subhalo population near the time of accretion [194, 199]. In contrast, present-day masses and velocities may differ significantly from their pre-infall configurations due to long term dynamical evolution within the host environment [200]. Comparing these peak quantities with their present-day counterparts therefore allows the cumulative effects of environmental processing to be quantified directly.

This comparison also provides additional clarity regarding the physical origin of the environmental trends identified in Chapter 3. If systematic variations are already present at the peak state, this suggests that part of the observed $z = 0$ signal arises from biased accretion histories or pre-infall environmental conditioning before subhaloes enter their final host halo [111, 201]. Conversely, if these environmental differences emerge mainly between the peak and present time populations, then post-accretion tidal evolution likely plays the dominant role in shaping the signal observed at $z = 0$. Tracing individual subhalo lineages through merger trees therefore enables these two contributions to be separated in a consistent framework.

Understanding this environmental modulation is important beyond the study of subhalo dynamics alone. The abundance, spatial distribution, and internal density profiles of subhaloes influence predictions for DM annihilation signals [85, 86, 202], gravitational lensing observables [203], and the satellite galaxy populations associated with DM haloes [84, 121]. Therefore, environmental variations in tidal stripping efficiency may propagate into observable signatures that are relevant to constrain both the nature of DM and the models of galaxy formation.

The aim of this chapter is to investigate how the cosmic web environment influences both the peak properties and subsequent structural evolution of DM subhaloes.

By employing merger trees constructed from the COLOR simulation, the analysis compares subhalo mass functions, velocity functions, and mass accretion histories across filament, wall, and void environments for a range of host halo masses. Through this comparison, the chapter examines the extent to which the environmental trends observed at $z = 0$ are inherited from the infalling population versus amplified through post-accretion tidal evolution.

The chapter is organised as follows. Section 5.2 summarises the subhalo selection criteria and merger tree methodology. Section 5.3 examines the environmental dependence of subhalo populations at peak mass and peak circular velocity. Section 5.5 investigates the subsequent tidal evolution of these populations through cumulative mass and velocity function evolution together with subhalo mass accretion histories. Finally, Section 5.6 summarises the main conclusions and discusses possible extensions of this work.

5.2 Methods

Our analysis is based on the COLOR simulation and the associated halo and subhalo catalogues introduced in Chapter 2. As detailed there, these catalogues are constructed using the FoF algorithm and the SUBFIND halo finder [169]. Merger trees are constructed from the SUBFIND subhalo catalogues by linking progenitor and descendant subhaloes across consecutive simulation snapshots. From these trees, we trace the main progenitor branch of each subhalo, defined as the unique evolutionary path obtained by recursively selecting the progenitor that contributes the largest fraction of bound mass.

To characterise the mass scale of the host haloes, we use the virial mass M_{200}. Alongside mass, we track the internal structure of subhaloes via the maximum circular velocity, $V_{\rm max}$, which represents the maximum value of the rotational velocity profile, $V_{\rm max} = \max\left(\sqrt{GM_{\rm sub}(< r)/r}\right)$. For each subhalo, we define the peak mass, $M_{\rm peak}$ and peak circular velocity, $V_{\rm peak}$ as the maximum values that $M_{\rm sub}$ and $V_{\rm max}$ attain over its entire merger history. Peak quantities are independent of any specific accretion timeline by definition. Tracking these peak quantities allows us to mitigate the systematic effects of post accretion tidal stripping. This approach provides a cleaner tracer of the subhalo properties at its stage of maximum growth over its entire lifetime.

In other studies, alternative tracking metrics are frequently used to define subhalo properties. These include the mass and maximum circular velocity recorded precisely at the snapshot of first infall, $M_{\rm infall}$, $V_{\rm infall}$, or equivalently $M_{\rm acc}$, $V_{\rm acc}$, as well as the maximum velocity at their history, $V_{\rm peak}$ [e.g., 204, 205]. While systematic variations between these definitions generally remain at the few-to-ten percent level,

the distinctions carry specific physical implications. For example, absolute lifetime peak values ($M_{\rm peak}$, $V_{\rm peak}$) naturally capture subsequent subhalo-subhalo mergers that occur after a system enters a larger host, which fixed accretion metrics omit [206].

We classified host haloes using the `CaCTus` framework, which segments the cosmic density field into filaments, walls, and voids, as described in Chapter 2. We assign each host halo to the cosmic web environment of the grid cell containing its centre of mass. We group host haloes into three distinct mass bins with median masses $\langle M_{200} \rangle = 10^{10}$, 10^{11}, and $10^{12}\,h^{-1}\mathrm{M}_{\odot}$. Finally, we apply a resolution cut requiring a minimum of 100 bound particles per subhalo throughout our analysis to avoid numerical artefacts.

5.3 Environmental Effect on Subhalo Peak Properties

5.3.1 Subhalo Mass Function at Peak Mass

The cumulative subhalo mass function (CSHMF) quantifies the mean number of subhaloes per host halo. It provides a fundamental statistical description of halo substructure in hierarchical structure formation models [84, 114]. The abundance and mass spectrum of subhaloes encode information about the assembly history of the host halo. These quantities also reflect the efficiency of tidal processing and the surrounding large-scale environment. For these reasons, the CSHMF is a widely used probe for connecting DM structure to galaxy formation and satellite populations.

When constructed using the present-day bound mass $M_{\rm sub}$, the CSHMF reflects the combined effects of subhalo accretion and subsequent dynamical evolution within the host halo potential. After infalling, subhaloes experience tidal stripping, tidal heating, and dynamical friction. All of these processes progressively reduce their bound mass. They may eventually lead to complete disruption [207]. As a result, the present-day subhalo mass function represents both the original accreted population and the cumulative impact of environmental processing over cosmic time.

To disentangle these effects, we additionally construct the CSHMF using the peak mass $M_{\rm peak}$. We define this quantity as the maximum bound mass attained by each subhalo along its entire main progenitor history. Since $M_{\rm peak}$ is typically reached before significant tidal stripping begins, it provides a robust tracer of the original subhalo population. It preserves information about the accretion history of the host halo [194]. Peak mass quantities are also closely related to empirical galaxy halo connection models. In those frameworks, stellar mass correlates more strongly with the maximum historical halo mass than with the stripped present-day mass [208, 209]. Comparing the CSHMF constructed from $M_{\rm peak}$ with the present-day distribution

allows the cumulative effects of tidal evolution to be isolated and quantified across different environments.

Figure 5.1 presents the CSHMFs measured at peak mass and at $z = 0$ for three host mass bins and different cosmic web environments. In all cases, the peak mass distributions lie systematically above the present-day distributions. This difference demonstrates that subhaloes lose a substantial fraction of their bound mass after accretion into the host halo [194]. The lower panels quantify this suppression through the ratio $\bar{N}_{z=0}/\bar{N}_{\rm peak}$. Values below unity directly measure the degree to which tidal evolution has reduced the surviving subhalo population relative to its original accreted state.

The magnitude of this suppression increases strongly with host halo mass. For our lowest mass bin, the ratio $\bar{N}_{z=0}/\bar{N}_{\rm peak}$ lies in the range 0.05 to 0.15 at the low-mass end of the CSHMF. This value indicates that only 5 to 15 percent of the original subhalo population survives to $z = 0$. For the intermediate mass bin, where $\langle M_{200}\rangle = 10^{11}\,h^{-1}\mathrm{M}_\odot$, the ratio rises to approximately 0.25 to 0.30 at the low-$M_{\rm sub}$ end. It then declines toward 0.05 at the high mass end. In the most massive hosts, where $\langle M_{200}\rangle = 10^{12}\,h^{-1}\mathrm{M}_\odot$, the ratio at low subhalo masses is approximately 0.30 to 0.35. It declines steeply toward zero at the high-$M_{\rm sub}$ end where massive subhaloes are rare and stochastic.

This systematic increase of the survival fraction with host mass indicates that subhaloes in lower-mass hosts have experienced more complete tidal processing by $z = 0$ relative to their peak state. This trend is consistent with the expectation that lower-mass hosts completed their assembly at earlier epochs when the mean cosmic density was higher. Earlier assembly resulted in longer effective stripping timescales relative to the subhalo orbital period [120].

The environmental dependence of this suppression varies significantly across the three host mass bins. In the lowest-mass bin, the ratio curves for all environments are tightly clustered. Void hosts lie marginally below the filament and wall populations by approximately 1–3% over most of the plotted mass range. The environmental signal at this mass scale is therefore weak. In the intermediate mass bin, a clear environmental hierarchy emerges. Void hosts show a noticeably suppressed survival fraction. Their ratio $\bar{N}_{z=0}/\bar{N}_{\rm peak}$ is approximately 0.05 to 0.10 lower than the filament and cosmic mean samples at low subhalo masses. Their peak to $z = 0$ ratio is lower. This behaviour could reflect later infall times, less concentrated host potentials, or fewer pericentric passages accumulated over the available time [97, 120]. The filament and cosmic mean samples trace one another closely throughout this mass bin. This agreement suggests that the cosmic mean is dominated by filament hosts at this mass scale, which is consistent with the number density statistics of Chapter 3.

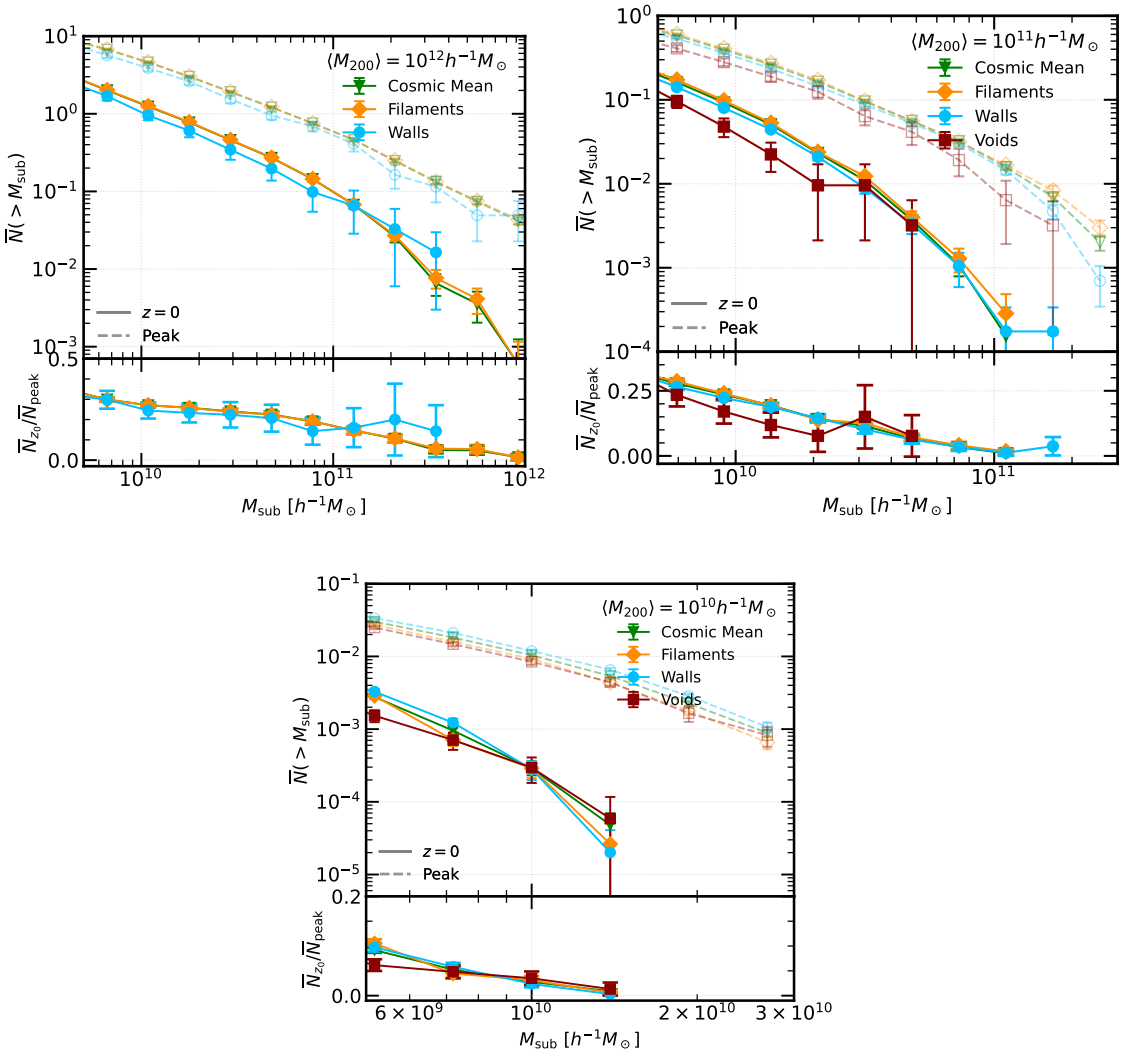

Figure 5.1: The cumulative subhalo mass function measured using peak mass $M_{\rm peak}$ (dashed lines) and present-day mass at $z = 0$ (solid lines). Results are split across three host mass bins and by the cosmic web environment: cosmic mean (green), filaments (yellow), walls (light blue), and voids (dark red). The corresponding lower panels display the ratio of the present-day to peak mass CSHMF, $\bar{N}_{z=0}/\bar{N}_{\rm peak}$ to quantify the degree of environmental suppression. Error bars denote bootstrap uncertainties on the mean.

For the most massive hosts, only filament, wall, and cosmic mean samples are shown. The void environment contains too few hosts at this mass. Here, wall hosts exhibit a bit lower survival fraction than filament hosts across intermediate subhalo masses. The separation is approximately 0.05 to 0.10 in the ratio panel. This difference may reflect a systematic variation in assembly history between massive wall and filament haloes at this mass scale [7, 110].

The suppression of CSHMF from peak to $z = 0$ is most pronounced at the low-mass end of the CSHMF across all host mass bins and environments. This behaviour is consistent with previous work showing that low-mass subhaloes are particularly vulnerable to tidal disruption. Their vulnerability stems from their shallower potential wells and lower binding energies [97, 196].

5.3.2 Subhalo Velocity Function at Peak Velocity

The maximum circular velocity, $V_{\rm max}$, traces the inner structure of subhaloes. It is less sensitive to tidal stripping than the total bound mass because the central regions of subhaloes remain more tightly bound during tidal evolution [170]. Because of this property, velocity based statistics provide a complementary description of the subhalo population to mass based quantities. This approach separates changes in the outer structure from changes in the central potential.

The $V_{\rm peak}$ widely adopted in galaxy halo connection models where galaxy properties correlate more closely with $V_{\rm peak}$ than with the present-day $V_{\rm max}$ [209]. The cumulative subhalo velocity function (CSHVF) is calculated from $V_{\rm peak}$ describes the subhalo population before tidal evolution becomes significant. This statistics is directly analogous to the CSHMF examined at $M_{\rm peak}$ in the previous section.

Figure 5.2 shows the CSHVF at peak velocity and at $z = 0$ for the same three host mass bins and different cosmic web environments. In all cases, the peak velocity distributions lie above the present-day distributions. This offset confirms that subhaloes experience a measurable reduction through time. This reduction arises because tidal stripping and dynamical heating progressively alter the mass profile at all radii at late stages of evolution. These processes eventually lower the peak of the circular velocity curve [104, 129]. The ratio panels quantify this suppression through $\bar{N}_{z=0}/\bar{N}_{\rm peak}$. Values below unity indicate the degree to which the velocity function has evolved since its peak state.

The velocity function survives substantially better than the mass function. This is the primary qualitative result from this comparison. Across all three mass bins of the host, the ratio $\bar{N}_{z=0}/\bar{N}_{\rm peak}$ for CSHVF lies in the range of 0.70 to 0.80 at the low end $V_{\rm max}$. It then declines to 0.10 to 0.20 at high $V_{\rm max}$. Comparing these values

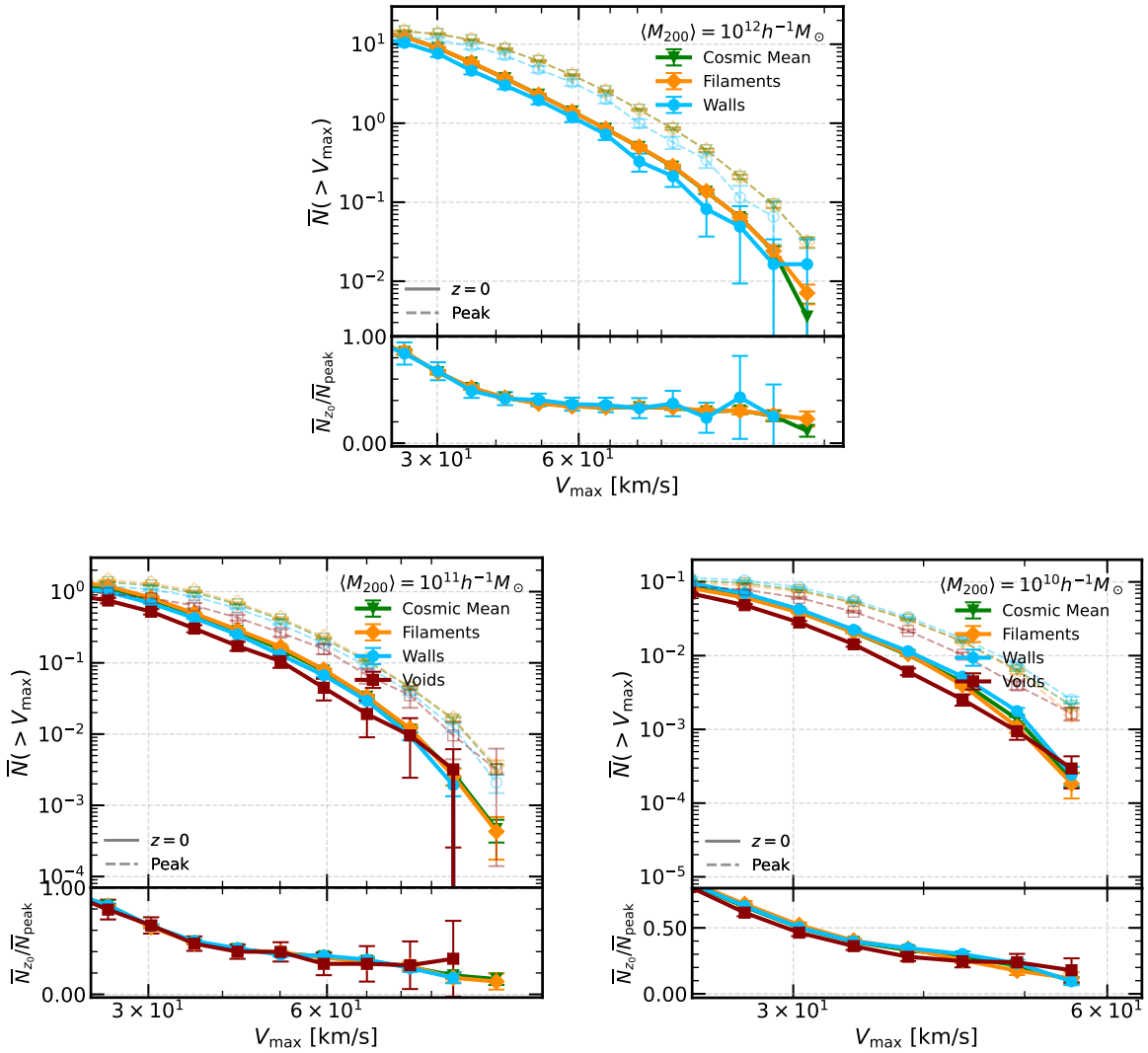

Figure 5.2: The cumulative subhalo velocity function measured using peak circular velocity $V_{\rm peak}$ (dashed lines) and present-day velocity at $z = 0$ (solid lines). Results are shown across three host mass bins for the different cosmic web environments, with color-coding identical to Figure 5.1. The corresponding lower panels display the ratio of the present-day to peak-velocity CSHVF, $\bar{N}_{z=0}/\bar{N}_{\rm peak}$ to quantify the structural evolution. Error bars denote bootstrap uncertainties on the mean.

directly with the corresponding CSHMF ratios from the previous section reveals a clear hierarchy. In the lowest-mass hosts, where $\langle M_{200} \rangle = 10^{10}\, h^{-1}\mathrm{M}_{\odot}$, the CSHVF ratio at low velocity is approximately 0.75. By contrast, the corresponding CSHMF ratio at low subhalo mass was only 0.05 to 0.15. Even in our most massive host bin, where, the CSHMF ratio reached only 0.30 to 0.35 at the low-mass end. The CSHVF ratio at the same host mass scale is approximately 0.85 to 0.90. This substantial difference between the two tracers quantifies the outside-in nature of tidal stripping. Loosely bound outer material is removed efficiently, driving more changes in total mass. Meanwhile, the dense central regions traced by V_{max} remain comparatively intact [100, 170].

Environmental differences in the velocity function are so weak. The peak and present-day CSHMFs show an environmental ordering across host mass bins. In marked contrast, the CSHVF ratio panels reveal no statistically significant separation between cosmic web environments at any of the three host masses. In the lowest-mass bin, void hosts show marginally suppressed ratios at intermediate velocities where $V_{\mathrm{max}} \sim 30\,\mathrm{km\,s^{-1}}$. The values are approximately 0.45 to 0.50 compared to 0.55 to 0.60 for filaments and walls. This difference is small and lies near the bootstrap uncertainties. In the intermediate and high-mass bins, the ratio curves for all environments are essentially coincident throughout the full velocity range. No systematic separation is visible between filaments, walls, and voids. The environmental spread in the CSHVF ratios is therefore substantially smaller than the corresponding spread in the CSHMF ratios found in Section 5.3.1.

The host-mass dependence of the CSHVF ratios mirrors that found for the CSHMF. The absolute suppression of the CSHVF is slightly larger in more massive hosts at high V_{max}. In those regions, the ratio declines to 0.10 to 0.15 compared to approximately 0.20 in the lowest-mass bin. This modest trend is consistent with longer effective stripping timescales and more pericentric passages accumulated by subhaloes in more massive hosts. These environments remove enough outer material to eventually affect the inner circular velocity profile. However, this host-mass dependence is considerably weaker in the CSHVF than in the CSHMF.

5.3.3 Environmental Dependence of Subhalo Mass and Velocity Loss

The post-infall evolution of subhaloes is directly quantified by comparing their present-day properties to their historical peak values. We evaluate this tidal processing using two complementary diagnostics: the mass ratio $M_{\mathrm{sub,z=0}}/M_{\mathrm{peak}}$ and the velocity ratio $V_{\mathrm{max,z=0}}/V_{\mathrm{peak}}$.

Figure 5.3 shows the ratio $M_{\mathrm{sub,z=0}}/M_{\mathrm{peak}}$ as a function of normalized subhalo mass $\mu = M_{\mathrm{sub}}/M_{200}$. Across all environments, the ratio decreases toward lower subhalo

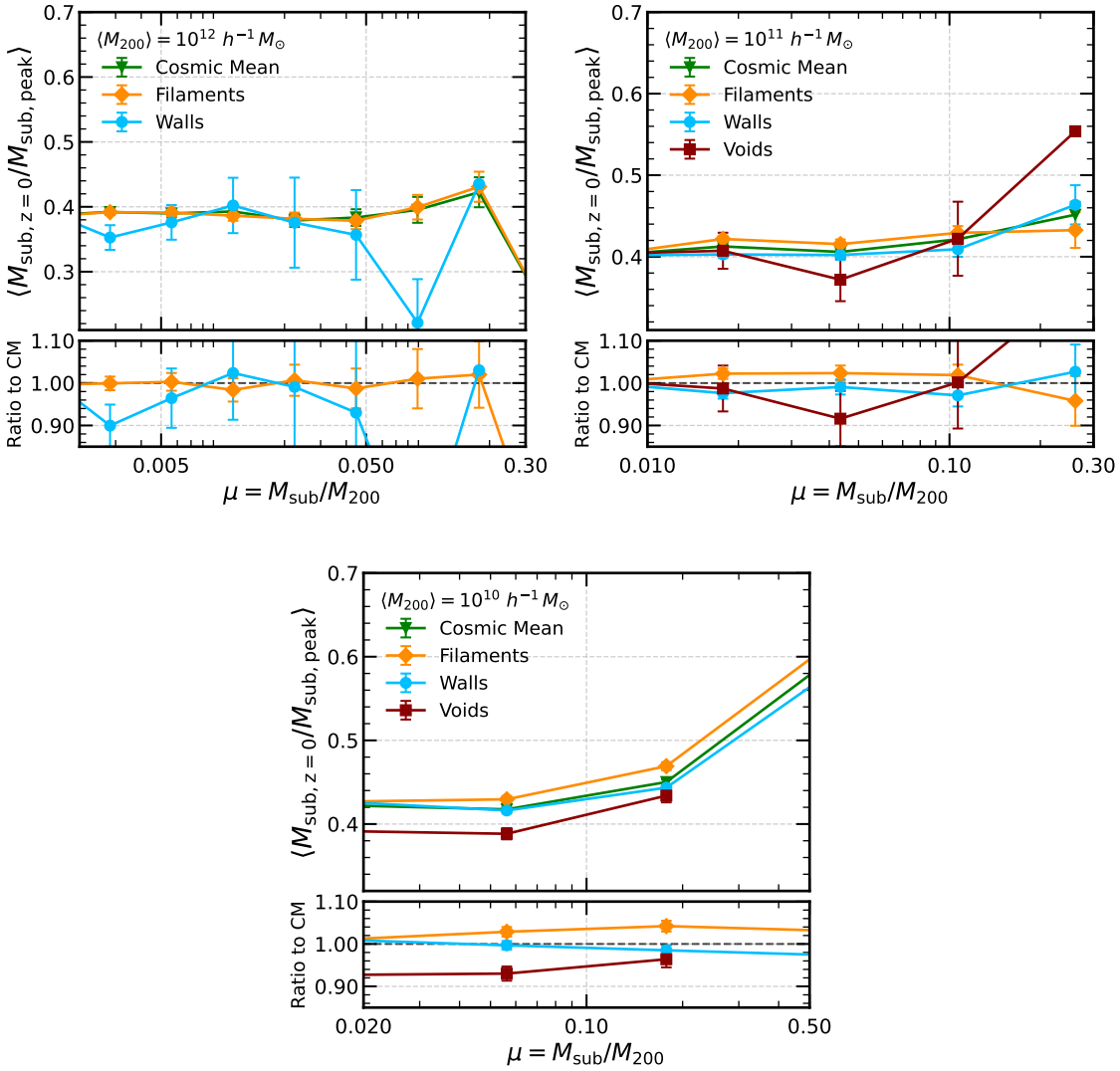

Figure 5.3: The ratio of subhalo mass at $z = 0$ to peak mass, $M_{\rm sub,z=0}/M_{\rm peak}$, binned by host mass in different cosmic web environments. The lower panels show the ratio of each environment to the cosmic mean. Error bars indicate bootstrap uncertainties on the mean.

masses, reflecting the high efficiency of tidal stripping for less bound systems [196]. The median $M_{\mathrm{sub,z=0}}/M_{\mathrm{peak}}$ ratios range from approximately 0.30 to 0.60, meaning subhaloes lose 40% to 70% of their peak mass. A clear environmental dependency is present. At fixed host mass, subhaloes in filaments show the lowest ratios, while those in voids and walls retain a larger fraction of their peak mass. This separation indicates that tidal mass loss is more efficient in dense regions of the cosmic web. The lower panels show that this environmental suppression is strongest in the most massive host bin.

Figure 5.4 presents the corresponding velocity ratio $V_{\mathrm{max,z=0}}/V_{\mathrm{peak}}$ as a function of normalized velocity $\nu = V_{\mathrm{max}}/V_{200}$. The velocity ratios remain significantly higher than the mass ratios, spanning from about 0.70 to 0.90. This indicates that 70% to 90% of their peak maximum circular velocity survives. This higher retention occurs because V_{max} traces the inner potential of subhaloes, which evolves more slowly and is less sensitive to stripping than the outer mass distribution [170].

Despite this central resilience, a subtle environmental trend remains visible. Subhaloes in filaments exhibit slightly lower $V_{\mathrm{max,z=0}}/V_{\mathrm{peak}}$ ratios compared to low-density regions, particularly in the highest host mass bin. The lower panels confirm that deviations from the cosmic mean are smaller than in the mass case. This behavior indicates that post-accretion factors preferentially strip outer material while leaving central regions comparatively intact [209].

Conversely, the mass accretion histories of host haloes show only a weak dependence on the large-scale cosmic web environment. The differences between environments remain at the level of a few percent and largely fall within the intrinsic scatter. This result is consistent with previous findings [111, 210, 211]. It suggests that the cosmic web influences halo substructure primarily through slight variations in tidal processing efficiency and accretion geometry, rather than through major differences in the bulk mass growth of the host haloes themselves.

5.4 Mass Accretion History

The mass accretion history (MAH) describes the growth of the main progenitor of a halo over cosmic time. It traces how DM haloes assemble through smooth accretion and mergers [3]. Merger trees are used to reconstruct this evolution from early times to the present-day [2, 168, 210]. To construct this path, tracking begins with a halo identified today. The algorithm steps backward in time to the previous data snapshot and selects the largest contributing progenitor known as the main progenitor. This selection repeats step by step into the past until the progenitor mass drops below the simulation

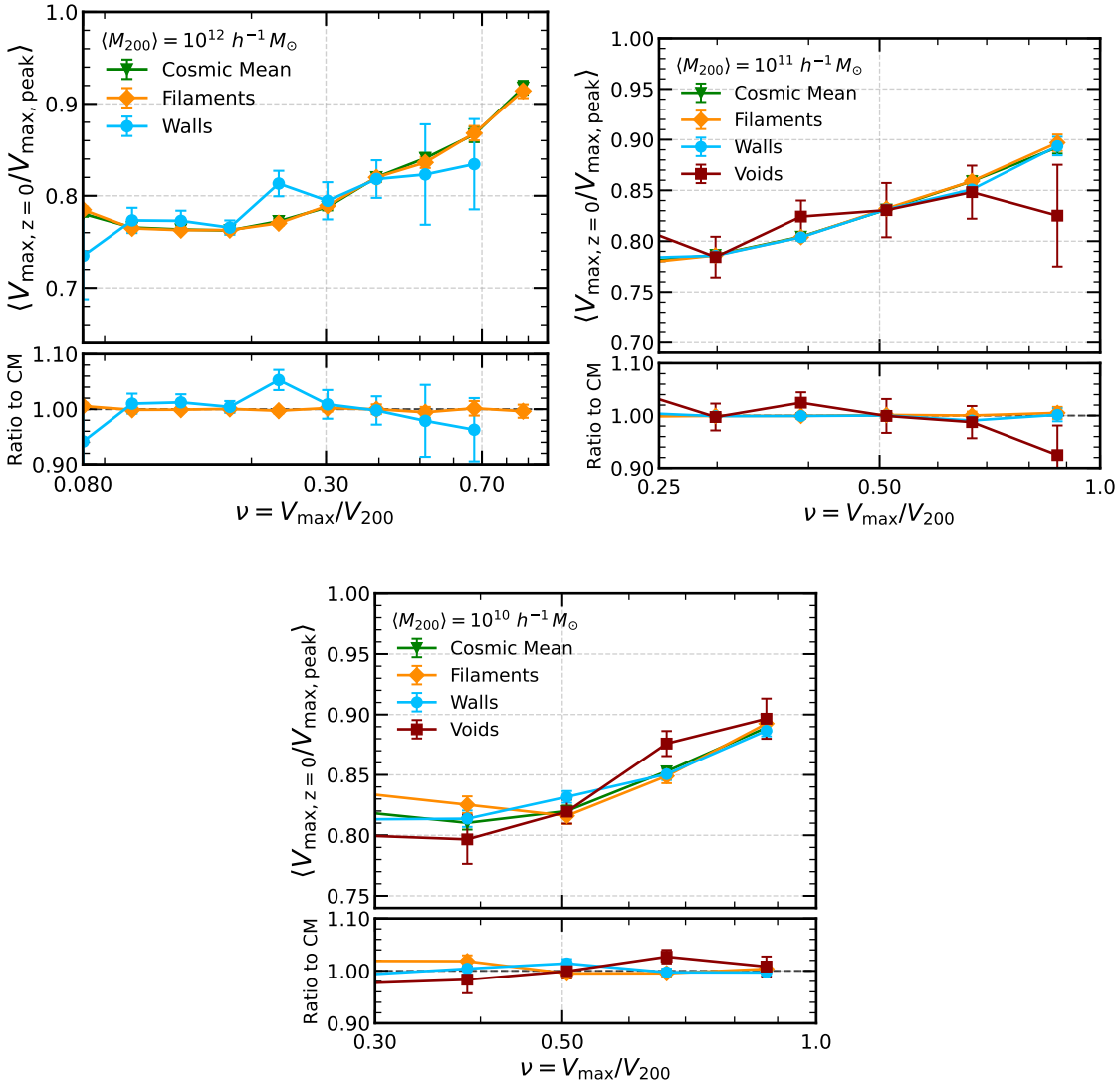

Figure 5.4: The ratio of subhalo maximum circular velocity at $z = 0$ to peak value, $V_{\mathrm{max,z=0}}/V_{\mathrm{peak}}$, binned by host mass in different cosmic web environments. The lower panels show the ratio of each environment to the cosmic mean. Error bars indicate bootstrap uncertainties on the mean.

resolution limit. Tracking the changing mass along this primary evolutionary sequence yields the accretion history of the halo [212].

In this work, the MAH refers specifically to this main progenitor branch and is defined as $M(z)/M_{z=0}$, where $M(z)$ is the mass of the main progenitor at redshift z and $M(z=0)$ is the present-day host halo mass. The assembly history of a host halo is closely connected to the evolution of its subhalo population. This growth history determines when subhaloes are accreted and how long they remain inside the host halo potential [213, 214]. Haloes that exhibit early formation contain subhaloes that have experienced tidal stripping and dynamical friction for a longer period of time. This reduces the masses and structural properties of the subhaloes that survive at $z = 0$. In contrast, haloes that exhibit late formation retain a larger fraction of recently accreted subhaloes that have undergone less tidal evolution [215, 216]. Given that past works have shown that these host assembly histories are often linked with the large-scale environmental density [7, 217], understanding the host MAH is an important step. It serves as a helpful baseline for isolating these broader environmental associations from the internal, post-infall evolution of subhaloes within their host potentials.

Figure 5.5 shows the median MAH of the main progenitor for three host median mass bins centred on 10^{10}, 10^{11}, and 10^{12} $h^{-1}\mathrm{M}_{\odot}$. The upper panels show the evolution of $M(z)/M_{z=0}$ with redshift. Overall, the differences between individual halo curves within each sample remain small compared to the intrinsic scatter in the growth histories of the main progenitor. The evolution of the median main progenitor MAH can be described using the exponential fit introduced by Wechsler et al. [3],

$$M(z) = M_{z=0}e^{-\alpha z}, \tag{5.1}$$

where α sets the rate of mass growth with redshift. This parametrisation provides a compact description of the average assembly history. In Figure 5.5, this fitting function is applied to the median main progenitor MAH of the $10^{12}\,h^{-1}\,\mathrm{M}_{\odot}$ sample.

In the lowest mass bin of $10^{10}\,h^{-1}\,\mathrm{M}_{\odot}$, the main progenitor masses remain closely aligned across the full redshift range, indicating weak variation in the assembly of low mass main progenitors. As shown in Table 5.1, this sample displays early formation, holding 90.9% of its final mass at $z = 2.5$ and peaking at 101.8% near $z = 1.0$ before settling at $z = 0$. The intermediate mass bin of $10^{11}\,h^{-1}\,\mathrm{M}_{\odot}$ shows slightly larger variation in its growth history. The differences remain small compared to the intrinsic scatter, with the main progenitor mass accounting for 57.6% of $M_{z=0}$ at $z = 2.5$ and increasing to 86.9% by $z = 1.0$. This evolutionary path is not strictly monotonic with redshift when compared to the normalized trends of the other bins, which is consistent with previous studies of main progenitor growth near the nonlinear mass

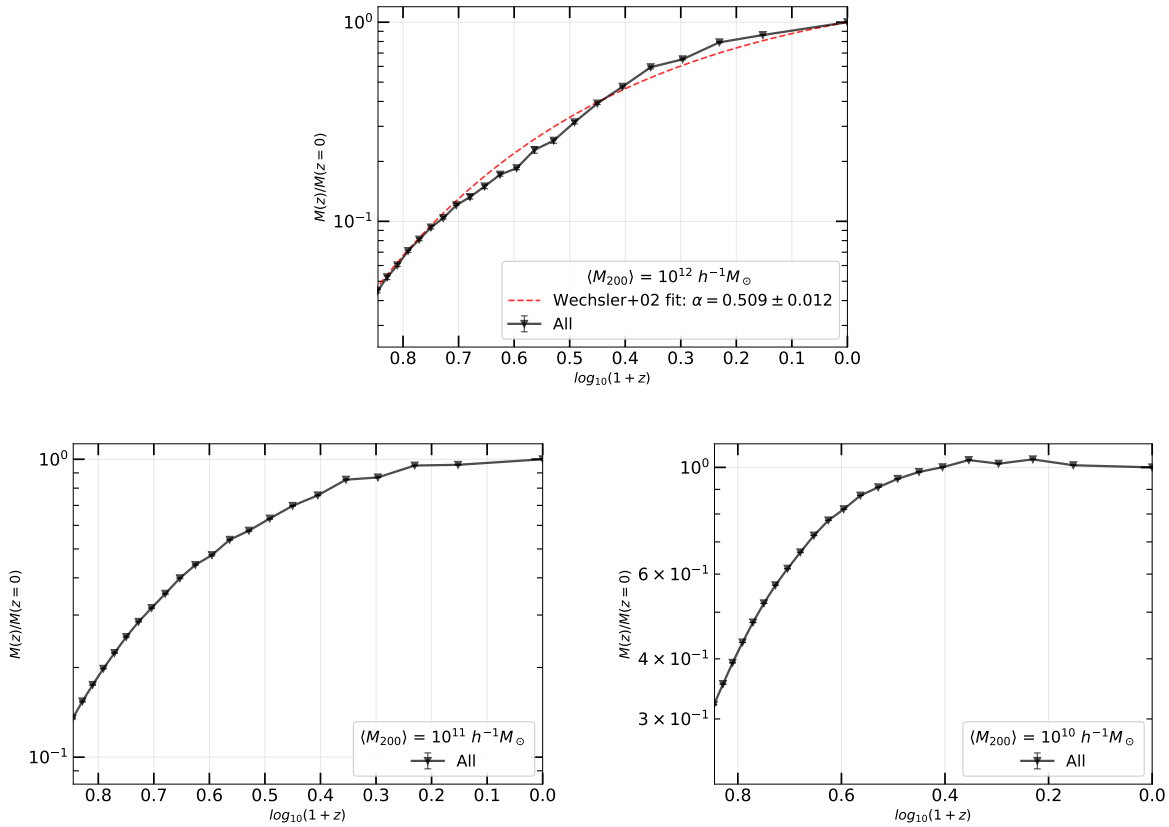

Figure 5.5: Mass accretion history of the main progenitor of haloes, shown in bins of present-day host halo mass. The evolution is expressed as the median $M(z)/M_{z=0}$. The dashed red line in the top panel represents the fit given by Eq. 5.1 following the Wechsler et al. [3]. Error bars correspond to 1σ bootstrap uncertainties on the median.

scale [111, 211]. In our highest mass bin of $10^{12}\,h^{-1}\,\mathrm{M}_\odot$, the normalized median main progenitor curve closely tracks the shapes of the lower mass bins, confirming a consistent underlying profile across the full redshift range. Table 5.1 summarizes this absolute mass evolution across redshift and captures how assembly rates differ across mass scales. When evaluating the normalized mass fractions $M(z)/M_0$, the results indicate a clear hierarchical signature where the $10^{12}\,h^{-1}\,\mathrm{M}_\odot$ sample displays late formation, holding only 25.4% of its final mass at $z = 2.5$.

However, tracking the absolute mass numbers reveals a complete trend reversal. The $10^{12}\,h^{-1}\,\mathrm{M}_\odot$ host had already established a massive progenitor core of $2.54{\times}10^{11}\,h^{-1}\,\mathrm{M}_\odot$ at $z = 2.5$, a scale the lowest mass bin never achieves. This dual behavior agrees with the framework established by [218] and [219], demonstrating that while normalized fractions map out classical hierarchical growth, absolute mass scaling captures an early core assembly that operates in an inverse direction.

Table 5.1: Median main progenitor mass $M_{200}(z)$ as a function of redshift for three present-day host halo mass bins. The values correspond to the main progenitor branch traced through merger trees. The table complements the MAH curves shown in Figure 5.5 by providing the corresponding absolute masses at each redshift.

	Median main progenitor $M_{200}(z)$ $[h^{-1}M_\odot]$					
$\langle M_{200}(z{=}0)\rangle$	$z = 0$	$z = 0.5$	$z = 1$	$z = 1.5$	$z = 2$	$z = 2.5$
$10^{10}h^{-1}M_\odot$	1.00×10^{10}	1.01×10^{10}	1.02×10^{10}	1.00×10^{10}	9.47×10^{9}	9.09×10^{9}
$10^{11}h^{-1}M_\odot$	1.00×10^{11}	9.58×10^{10}	8.69×10^{10}	7.57×10^{10}	6.32×10^{10}	5.76×10^{10}
$10^{12}h^{-1}M_\odot$	1.00×10^{12}	8.62×10^{11}	6.51×10^{11}	4.74×10^{11}	3.14×10^{11}	2.54×10^{11}

5.5 Environmental Impact on Subhalo Evolution

5.5.1 Evolution of Subhalo Mass Function

The peak mass analysis of Section 5.3.1 established that environmental differences in subhalo abundance are already present when evaluating subhaloes at their historical peak states. This section extends that framework by examining how the CSHMF, expressed as a function of the normalised subhalo mass $\mu = M_{\rm sub}/M_{200}$, evolves across redshift in distinct cosmic web environments. Tracking this evolution evaluates whether the environmental signal grows, remains constant, or diminishes over time, isolating the epochs at which the large-scale environment exerts the strongest influence on substructure content.

Regarding the methodology, a relevant detail concerns the cosmic web classification, that we assign at $z = 0$ and hold fixed across all high redshifts. This setup builds on the fact that the large-scale network architecture is already well-established at high redshift. Consequently, the cosmic web does not undergo a major structural reorganisation between $z \sim 2$ and $z = 0$ [41]. However, this background framework is not completely rigid. As shown by Cautun et al. [41], the cosmic web experiences a continuous internal mass consolidation over time. During this process, filamentary volume fractions decrease by roughly a factor of two.

Figure 5.6 presents the CSHMF as a function of the normalised subhalo mass, $\mu \equiv M_{\rm sub}/M_{200}$, for three cosmic web environments, filaments, walls, and voids, across four redshifts: $z = 0$, 0.5, 1.0, and 2.0. These results are shown separately for three present-day host mass regimes with median masses $\langle M_{200}\rangle = 10^{10}$, 10^{11}, and $10^{12}\,h^{-1}{\rm M}_\odot$. Because we trace the main progenitor branch of each host halo backward over cosmic time, the median host mass at each earlier snapshot is systematically

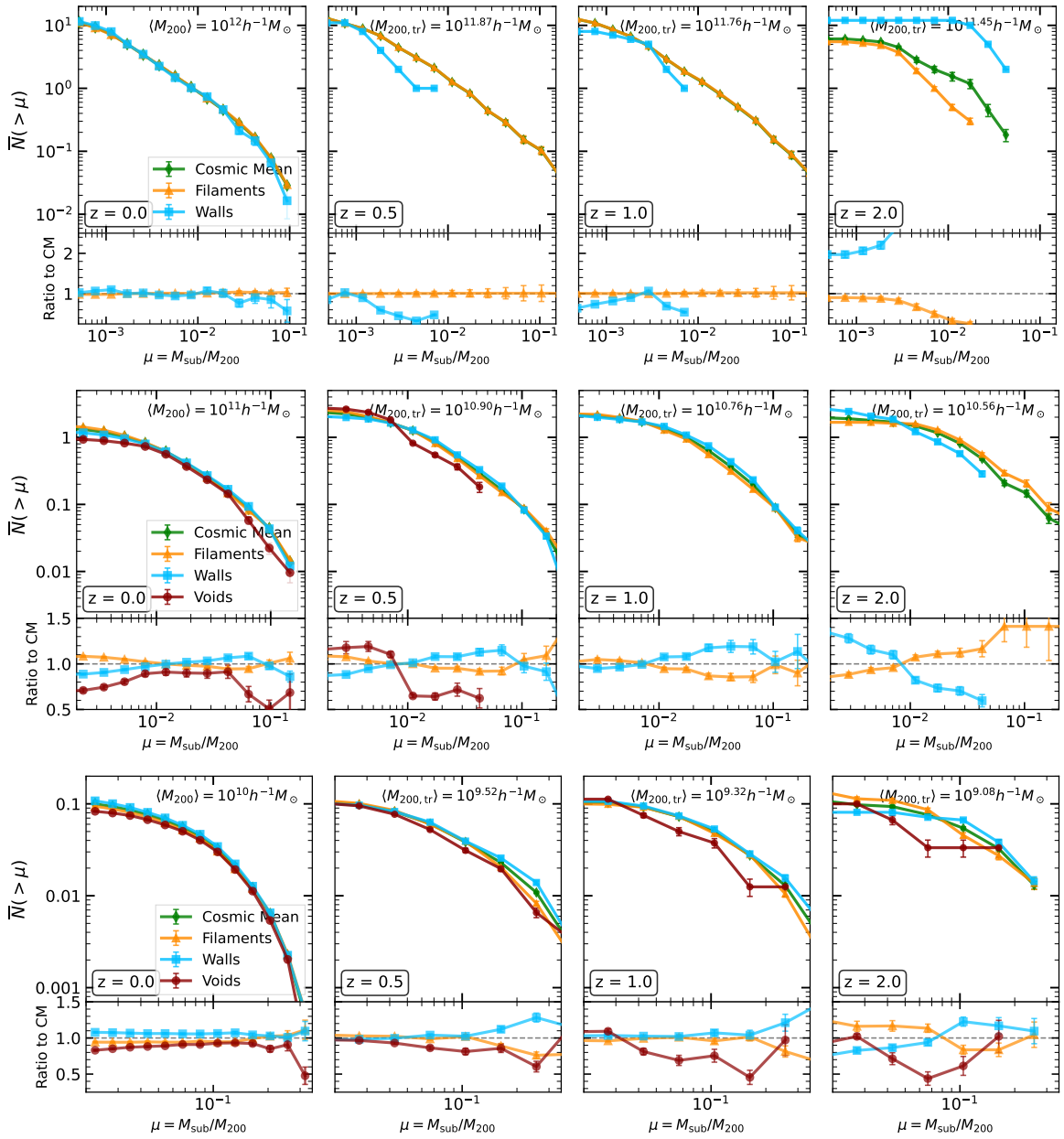

Figure 5.6: The cumulative subhalo mass function expressed as a function of the normalised subhalo mass, $\mu \equiv M_{\mathrm{sub}}/M_{200}$, across different cosmic web environments for three present-day median host halo mass bins. Panels from left to right track the evolution across four redshifts between $z = 0$ and $z = 2.0$ along the main progenitor branch of the host haloes, with the corresponding median traced progenitor masses, $\langle M_{200,\mathrm{tr}}\rangle$. The lower subpanels show the ratio of the environmental CSHMF to the redshift-matched cosmic mean within the same mass bin. Error bars denote 1σ bootstrap uncertainties on the mean CSHMF.

smaller than its present-day counterpart, as indicated in the legends. The traced median progenitor masses, denoted as $\langle M_{200,\mathrm{tr}} \rangle$, decrease systematically with redshift, reflecting the fact that these host systems had only assembled a fraction of their final virial mass at earlier epochs. Across the entire sample, the tracked progenitor hosts contain approximately 25% to 40% of their final $z = 0$ mass when evaluated at $z = 2.0$. The lower panels display the ratio of the environmental CSHMF to the cosmic mean computed within the same host mass bin and at the same snapshot, providing a redshift-matched reference frame for isolating differential environmental signals.

For $10^{12}\,h^{-1}\mathrm{M}_{\odot}$ host bin, the environmental tracking exhibits a distinct transition between early assembly phases and late-time structural stability, with environmental effects becoming visibly more pronounced at earlier epochs. At low redshift, the subhalo abundance in filament environments closely traces the cosmic average throughout the full μ range, while wall hosts display a minor deficit at the high-μ end. Moving to intermediate redshifts, a pronounced suppression emerges for host systems residing within cosmic walls, where ratios drop to approximately 0.5 near $\mu \sim 10^{-2}$ while filaments remain close to unity. However, a qualitative structural reversal appears at $z = 2.0$: the abundance in filament progenitors drops below the cosmic mean (to ratios of approximately 0.7-0.8), while wall progenitors conversely exhibit an elevated subhalo ratio. This high-redshift reversal highlights the active, early assembly phase of filamentary structures relative to the delayed formation of cosmic walls. Because massive haloes in dense filaments form early and undergo rapid, merger-driven growth at these epochs, their main progenitor branches experience rapid virial mass inflation that temporarily drives down their normalised subhalo ratios relative to the field average [41].

For our $10^{11}\,h^{-1}\mathrm{M}_{\odot}$ mass bin, the data show a prominent and dynamically evolving environmental signature that intensifies at higher redshifts. At $z = 0$, the dominant feature is the clear suppression of substructure within void hosts, where ratios sit at approximately 0.80-0.85 across most of the μ range, whereas filament and wall profiles remain closely clustered near unity. Tracking this population to higher redshifts reveals that the void deficit becomes substantially more severe at $z = 0.5$, dropping to approximately 0.5 at high μ, before gradually flattening at $z = 1.0$. By $z = 2.0$, the environmental modulation strengthens and the hierarchy reverses completely: filament systems rise significantly above the cosmic average, ratios of 1.2-1.3, while wall populations fall well below it, 0.7-0.8, and void hosts return toward the mean. This systematic shift provides direct evidence of the delayed, late formation history characterising underdense environments. At high redshifts, the ambient density perturbations within voids grow slowly, meaning their progenitor systems have not yet

entered the active growth stages that drive the strong environmental differentiation and severe tidal stripping observed at later epochs [190, 210].

For the low-mass hosts, a clear environmental dependency is present across all examined epochs, showing notable amplification at the highest redshifts. While the low and intermediate redshift regimes remain relatively bound within approximately $\pm 10\%$ of the cosmic average across the lower-to-intermediate μ range, a substantial environmental divergence of 15% to 50% manifests at the high-μ end. At $z = 2.0$, this separation increases further as filaments and walls diverge sharply by up to 25%-50% near the resolution limit. This pronounced variation confirms that the strong environmental signature identified in the absolute subhalo populations of low-mass systems at $z = 0$, as detailed in Chapter 3 is carried over directly from high redshift. Because low-mass haloes collapse and finish their primary assembly exceptionally early in cosmic history, their subhalo configurations are highly sensitive to their primordial background environments, embedding a strong structural signature that is maintained throughout their subsequent cosmic evolution [111, 217].

Several overarching trends emerge from this analysis. The environmental signal in the CSHMF is present across all redshifts examined, confirming that the influence of the large-scale cosmic web on subhalo abundance is not a purely late-time phenomenon; rather, it grows increasingly dynamic and pronounced at high redshift. The signal is systematically modulated by host mass, which aligns with the assembly bias framework where the properties of haloes depend on their large-scale environmental configuration [111, 211]. However, the character of the environmental signal changes with redshift in a mass-dependent manner. At low redshift, the dominant trend is the suppression of void hosts relative to the mean, while at high redshift the environmental ordering shifts as progenitor systems navigate distinct phases of their early assembly histories. This demonstrates that the present-day environmental differences observed in Chapter 3 are built up gradually over time through a combination of environmentally biased accretion histories and differential tidal processing, rather than being established instantaneously at a single epoch.

5.5.2 Evolution of the $V_{\rm max}$–$R_{\rm max}$ Relation

The $V_{\rm max}$–$R_{\rm max}$ relation provides a direct probe of the internal density structure of subhaloes, since at fixed $V_{\rm max}$ a smaller $R_{\rm max}$ corresponds to a more centrally concentrated mass profile [6, 84]. In Chapter 3, we showed that this relation carries a clear environmental imprint at $z = 0$: subhaloes hosted by filament haloes are systematically more concentrated, while those in void hosts are less concentrated by a comparable amount. This environmental ordering gets stronger toward lower host

masses, where the influence of the large-scale structure on subhalo internal structure is most pronounced.

The peak velocity analysis of Section 5.3.2 established that V_{max} is a more resilient tracer than total mass, with the CSHVF surviving substantially better from peak to $z = 0$ and showing only weak environmental separation. This raises a natural question if the environmental signal in the V_{max}–R_{max} relation observed at $z = 0$ originates from differences already present at the epoch of peak circular velocity, or if it emerges and grows through subsequent tidal evolution within the host. Examining the V_{max}–R_{max} relation at earlier epochs and comparing it to the $z = 0$ result allows this question to be addressed directly. Tracking this relation across redshift therefore bridges the two earlier analyses: it tests whether the environmental effect differences found in Chapter 3 are a late-time product of differential tidal processing or a reflection of pre-existing structural differences in the infalling population, and quantifies how the signal builds up over cosmic time.

The evolution of the V_{max}–R_{max} relation across redshift reveals a clear competition between host mass effects and large-scale environmental forces. At $z = 0$, a visible cosmic web effect exists across both massive and low-mass host haloes as discussed in Chapter 3. However, this present-day environmental variation remains small and changes the subhalo radius by less than 10 %. According to [220], subhaloes experience continuous outer mass loss from tidal forces until their internal density balances the surrounding background density. Host haloes in dense filaments are expected to experience stronger ambient tidal fields and higher background densities than comparable systems in underdense regions. The observed offsets in the V_{max}–R_{max} relation are therefore consistent with stronger environmental processing and different accretion histories in filamentary environments. However, because this analysis does not directly measure individual stripping histories or orbital parameters, the result should be interpreted as evidence for environment-dependent structural evolution rather than as a direct measurement of the stripping mechanism itself.

When we track this relation back to high redshift, the cosmic web effect grows noticeably stronger. The structural separation between filaments and voids increases significantly at $z = 1.0$ and $z = 2.0$ because the host progenitors are in their early assembly phases. At our highest redshift of $z = 2.0$, the environmental effect reaches 30 to 40 %. This high-redshift environmental effect is particularly pronounced in the intermediate and low-mass host haloes. At these early epochs, the unique accretion geometry and strong background tidal forces of the cosmic web shape the infalling subhalo populations directly. As time passes toward $z = 0$, the mass of the host halo grows significantly. This growing host gravity begins to dominate the inner subhalo dynamics over the large-scale web environment. The continuous localized tidal

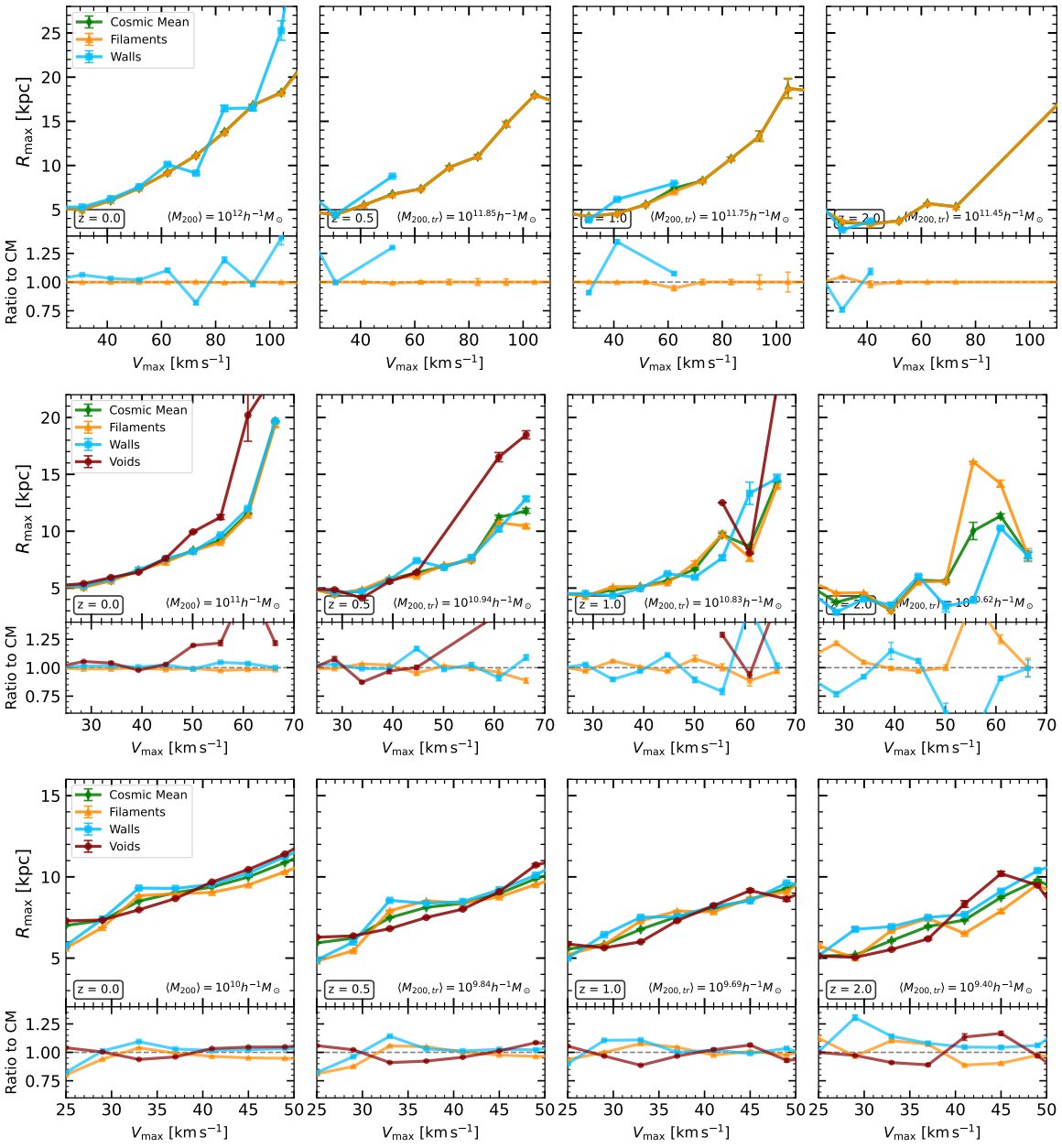

Figure 5.7: The median $V_{\max}$–$R_{\max}$ relation of subhaloes hosted by haloes across different cosmic web environments for three present-day median host halo mass bins. Panels from left to right track the evolution across four redshifts between $z = 0$ and $z = 2.0$ along the main progenitor branch of the host haloes, with the corresponding median traced progenitor masses, $\langle M_{200,\mathrm{tr}}\rangle$. The lower subpanels show the ratio of the environmental median relation to the redshift-matched cosmic mean within the same mass bin. Error bars denote 1σ bootstrap uncertainties on the median relation.

processing inside the host potential drives the profiles of all surviving subhaloes toward a more universal mean. This internal host evolution explains why the environmental signal is most pronounced at high redshift and becomes more subtle at later times.

5.6 Summary and Discussion

In this chapter, we have extended the $z = 0$ analysis of Chapter 3 by introducing a comprehensive temporal tracking framework using merger trees constructed from the COLOR simulation. Our primary objective was to investigate how the large-scale cosmic web environment shapes the initial conditions of DM subhaloes at their accretion epoch and drives their subsequent post-infall structural processing. By contrasting lifetime peak attributes against highly stripped $z = 0$ configurations, and tracing the evolutionary snapshots of the cumulative subhalo mass and velocity functions from $z = 2.0$ down to the present day, we isolated the distinct channels through which the cosmic web modulates non-linear substructure evolution.

We find that a clear environmental ordering is already present at peak mass and peak velocity. Filament hosts carry the richest subhalo populations, followed by walls, while voids remain the most subhalo poor. This hierarchy directly mirrors the $z = 0$ trends, supporting the interpretation that a significant fraction of the environmental signal is already present before accretion through pre-infall environmental conditioning [111]. However, this initial bias is substantially amplified over time by post-accretion tidal stripping, which operates more efficiently within the deeper gravitational potentials of dense environments [120, 213].

Our analysis also highlights a major structural decoupling between subhalo mass and velocity tracking. The velocity function survives substantially better than the mass function from peak to $z = 0$ across all regimes. Subhaloes retain 70% to 90% of their peak circular velocity while losing 40% to 70% of their peak mass. This result directly quantifies the outside-in geometry of tidal stripping, where loosely bound outer material is removed efficiently while dense central cores remain comparatively intact [220]. Strikingly, environmental variations are nearly absent in the velocity tracking, indicating that the environmental dependence of tidal processing is carried almost entirely by the outer mass distribution.

Furthermore, we show that the environmental signal is dynamic and changes character with redshift in a mass-dependent manner. For intermediate and massive host bins, filament progenitors drop below the cosmic mean at $z = 2.0$ while wall progenitors rise above it. This high-redshift reversal reflects the active, rapid assembly phase of early filamentary structures [41]. In contrast, the environmental signal in

low-mass hosts remains present at high redshift and persists consistently to $z = 0$, showing a 15%–50% divergence at the high-μ end.

The evolution of the $V_{\rm max}$–$R_{\rm max}$ relation shows that large-scale environmental forces compete directly with internal host mass effects over cosmic time. At $z = 0$, the cosmic web effect is present but small, changing the subhalo radius by less than 10%because dense filaments systematically strip outer subhalo mass into compact cores compared to underdense voids [220]. However, when tracking this relation back to high redshift, $z = 2.0$, the environmental effect becomes much more pronounced, reaching a 30–40% variation, particularly within intermediate and low-mass host haloes. This strong high-redshift separation occurs because young host progenitors are highly sensitive to the unique accretion geometries and strong background tidal fields of the early cosmic web. As time moves toward the present day, the rapid mass growth of the host haloes generates dominant local gravitational forces that continuously process all surviving subhaloes toward a universal structural profile, making the environmental signature increasingly subtle at later epochs.

These results provide a coherent framework for interpreting environmental trends in substructure. The relative resilience of velocity-based quantities supports the use of $V_{\rm peak}$ as a robust proxy in semi-empirical galaxy–halo connection models [209], while still allowing for modest environmental dependence. Additionally, the similarity of the host MAHs supports the interpretation that the environment-conditioned inputs used in Chapter 4 capture substructure-level environmental signatures rather than being driven only by simple offsets in host assembly time.

Chapter 6

Conclusions and Future Work

"Somewhere, something incredible is waiting to be known." — Carl Sagan

"If you can't fly, run. If you can't run, walk. If you can't walk, crawl, but by all means keep moving." — Martin Luther King Jr.

6.1 Conclusions

In this dissertation, we studied how the large-scale cosmic web environment systematically affects the properties and evolution of DM halo substructure. We also examined how these environmental mechanisms propagate into predictions for DM annihilation signals. Our analysis is grounded in the high-resolution collisionless N-body framework of the COLOR simulation [6]. We employed the multi-scale `CaCTus` cosmic web classifier [190] to segment the simulation volume into nodes, filaments, walls, and voids. Together, I addressed the three central questions posed in the introduction. First, we determined whether the cosmic web environment systematically affects subhalo abundance and internal structure at fixed host mass. Second, I evaluated whether these environmental dependencies alter DM annihilation boost predictions. Third, my thesis provides evidence for the relative roles of pre-infall differences and subsequent tidal evolution within the host in shaping the observed environmental trends.

We find that the cosmic web environment imprints measurable and systematic signals on the subhalo populations of host haloes at $z = 0$. This effect remains clear even when we consider host haloes of comparable mass. For this analysis, we divided

host haloes at $z = 0$ into three discrete mass bins with median masses $\langle M_{200} \rangle = 10^{10}$, 10^{11}, and $10^{12}\, h^{-1}\mathrm{M}_{\odot}$. We then compared their subhalo populations across filament, wall, and void environments. Our analysis of the CSHMF at $z = 0$ revealed that haloes residing in filaments and walls host systematically richer subhalo populations than their counterparts in voids at a fixed host mass. For the lowest host mass bin, we find that wall environments contained subhaloes that were up to a factor of two more massive at the high mass end. These same environments showed a typical abundance excess of approximately 25% at lower subhalo masses. We note that these environmental differences at $z = 0$ diminished progressively with increasing host halo mass. This trend demonstrates that the relative influence of the large-scale environment weakens as halo mass grows. Such behavior matches the assembly bias framework, where the large-scale tidal field most strongly conditions the growth of low mass systems [107, 111, 211]. Correspondingly, our measurements of the subhalo mass fraction f_{sub} at $z = 0$ showed that filament haloes retain approximately 2% to 20% more of their virial mass in bound substructure compared to void haloes. Conversely, we find that void environments exhibit systematically smoother density distributions.

We examined the internal structure of subhaloes through the V_{max}–R_{max} relation at $z = 0$. This relation serves as a proxy for subhalo concentration [6, 41]. We find that subhaloes in filamentary environments are systematically more concentrated than those in lower density regions. Conversely, void subhaloes showed an approximately 5% to 9% suppression in concentration relative to filament populations across most host mass bins. Our measurements of the subhalo velocity function at $z = 0$ aligned these structural trends. Filament environments showed 5% to 15% enhancements in subhalo abundance relative to the cosmic mean. Meanwhile, void environments displayed deficits of 5% to 25%. We observed the strongest signatures at low host masses. These present-day results established that subhalo populations carry a distinct imprint of the large-scale environment of their host haloes. Consequently, we demonstrate that neglecting environmental dependencies introduces systematic biases into studies of satellite galaxy populations [108, 221, 222]. It also biases statistics of substructures [223]. Such omissions impact any observational signal that depends on the internal density profiles of DM subhaloes.

We extended these results directly to quantify the consequences for DM indirect detection. We achieved this by examining how the cosmic web modulates the substructure boost to annihilation signals. The DM annihilation rate scales with the square of the local density. Consequently, unresolved substructure substantially enhances the total predicted annihilation luminosity relative to a smooth host halo baseline [84, 85]. We extended two widely used semi analytic frameworks by incorporating environment dependent corrections for host halo concentration,

subhalo mass function normalisation, and internal subhalo structure [85, 86]. We calibrated all of these corrections directly from the COLOR simulation. Our results demonstrated a clear and mass dependent environmental signature in the predicted boost factors. Haloes residing in void environments showed systematically suppressed boost factors of approximately 30% to 33% relative to the cosmic mean across the full host halo mass range considered. In contrast, filament haloes displayed a strong mass dependent transition. Low mass hosts exhibited suppressions of roughly 15%. Meanwhile, high mass hosts showed enhancements of up to approximately 12%. Wall environments produced intermediate behavior between filaments and voids. These trends arise directly from the coupled environmental dependence of host halo concentrations, subhalo abundance, and subhalo internal density profiles. We developed an empirical fitting prescription for the boost factor $B(M_{200}, z = 0)$ as a function of cosmic web environment. This prescription provides a practical framework for incorporating environmental effects into indirect detection forecasts [90] and halo population modelling applications. Our results show that environment blind boost models introduce systematic biases into annihilation predictions. We conclude that the cosmic web is an essential component when modelling the contribution of small scale structure in applications where boost factor systematics are significant [87].

We investigated the evolutionary changes associated with these environmental trends by tracking subhalo histories through merger trees constructed from the COLOR simulation. For this analysis, we tracked the subhaloes across cosmic time relative to the static cosmic web environment defined at $z = 0$. This framework evaluated whether the environmental differences observed at $z = 0$ are already emerging in the subhalo population at their peak state, defined as the maximum value a property reaches over the entire history of the subhalo [156, 194]. We compared cumulative subhalo mass and velocity functions constructed from these peak quantities ($M_{\rm peak}$, $V_{\rm peak}$) with their present-day counterparts. The peak distributions lie systematically above the $z = 0$ distributions across all environments and host mass bins, supporting substantial post-peak mass and velocity loss [97, 196]. Crucially, this vertical offset depends strongly on the chosen structural tracer. While the velocity function exhibits remarkable resilience, retaining 70% to 90% of its peak amplitude across all environments, the mass function shows severe depletion, with surviving fractions dropping as low as 5% to 15% in lower-mass hosts. This difference supports an outside-in interpretation of environmental processing. Furthermore, while the mass loss ratio displays a weak environmental ordering where filament subhaloes are stripped more, this environmental signal is strikingly less in the velocity ratios. Together, these peak to present comparisons demonstrate that the environmental signatures observed at $z = 0$ arise from a combination of a pre-existing environmental hierarchy at accretion

and a spatially varying stripping efficiency that alters the outer mass profiles while leaving the central subhalo structure intact.

Our measurements of the mass loss ratios $M_{\mathrm{sub,z=0}}/M_{\mathrm{peak}}$ and $V_{\mathrm{max,z=0}}/V_{\mathrm{peak}}$ showed that mass is more strongly affected by tidal evolution than the maximum circular velocity. Across the examined population, the median $M_{\mathrm{sub,z=0}}/M_{\mathrm{peak}}$ ratios ranged from approximately 0.25 to 0.60, meaning subhaloes lost 40% to 75% of their peak mass. In contrast, the $V_{\mathrm{max,z=0}}/V_{\mathrm{peak}}$ ratios remained significantly higher, spanning from about 0.70 to 0.90, indicating that 70% to 90% of their peak maximum circular velocity survived. The maximum circular velocity traces the inner potential of subhaloes and generally evolves more slowly [170]. This behavior indicates that post accretion factors preferentially strip outer material while leaving central regions comparatively intact. Thus, the inner structure of subhaloes appears to remain largely resilient across these environments [41]. While the differences between environments are subtle, a mild environmental imprint remains visible in these structural ratios. Conversely, we find that the mass accretion histories of host haloes showed only a weak dependence on the static cosmic web environment. The differences between environments remained at the level of a few percent and largely fell within the intrinsic scatter. This result is consistent with previous findings [111, 210, 211]. It suggests that the large-scale environment influences halo substructure primarily through slight variations in tidal processing efficiency and accretion geometry rather than through major differences in the bulk mass growth of host haloes.

By tracking the evolutionary history of both the CSHMF and the V_{max}–R_{max} relation, this thesis demonstrates that the cosmic web shapes the abundance and internal density profiles of subhaloes through an early, time-dependent environmental signature that becomes increasingly regulated by host halo growth toward $z = 0$. While the CSHMF shows a dynamic high-redshift reversal due to active, merger-driven progenitor growth within filaments [224], the V_{max}–R_{max} relation displays a pronounced 30 to 40% environmental variation at $z = 2.0$ where dense filamentary tidal fields systematically strip outer subhalo envelopes into highly compact cores compared to underdense voids [220]. This structural divergence is highly relevant for observational galaxy studies because it supports the use of resilient velocity proxies like V_{peak} in semi-empirical galaxy-halo connection models while providing essential baselines for interpreting environmental satellite stripping, weak lensing signals, and galaxy assembly bias across diverse cosmic environments [138, 209]. As time moves toward the present day, the rapid mass assembly of the host haloes generates dominant local gravitational forces that continuously process all surviving subhaloes toward a universal profile, reducing the modern structural variation to less than 10%. However, these conclusions rest on analysis based on gravity-only simulation, a single cosmic web

classifier and finite subhalo resolution. Future work must leverage hydrodynamical simulations, larger volumes, and explicit convergence tests to refine the quantitative amplitudes of structural parameters like $V_{\max}$ and $R_{\max}$.

6.2 Future Work

The results established in this dissertation suggest several possible avenues for further investigation. These avenues include extensions within the current N-body framework, improvements to physical modelling choices, and possible connections to observational data products.

A primary limitation of our current analysis is its reliance on gravity-only simulations, which omit the effects of baryonic physics. Processes such as gas cooling, stellar feedback, AGN activity, and ram pressure stripping can alter the inner structure of subhaloes, modifying their concentration-mass relations and survival rates [225, 226]. These changes are expected to affect the DM annihilation boost factor, as central baryonic contraction may deepen potentials while tidal shocks from stellar discs can enhance the disruption of low-mass systems. A valuable extension would be to apply the `CaCTus` environmental framework to matched hydrodynamical simulation suites, such as EAGLE [227], IllustrisTNG [228], MillenniumTNG [229] or FLAMINGO [230]. Comparing the estimated boost factors and $V_{\max}$–$R_{\max}$ relations between DM-only and hydrodynamical runs across identical environments would help evaluate the scope of baryonic corrections to the annihilation luminosity within different cosmic web types [124].

Additionally, expanding this framework to larger cosmological volumes and alternative cosmic web segmentation frameworks would help test the generalizability of the observed trends. Replicating this analysis in larger boxes, such as MillenniumTNG [229], could reduce statistical sample variance and improve the statistics for rare, high-mass hosts. Furthermore, evaluating these trends against different cosmic web segmentation schemes would be beneficial. Comparing with a velocity shear based approach or topological methods like `DisPerSE` [183] would clarify whether the relative resilience of the inner subhalo potential remains stable across different geometric definitions of the cosmic web environment.

Finally, these environment-conditioned statistics offer a baseline that could be integrated into empirical galaxy-halo connection models and linked to future surveys. Incorporating environment-dependent subhalo mass functions into subhalo abundance matching techniques may refine mock satellite galaxy populations within voids and filaments [231, 232]. These models could then be compared with upcoming satellite counts and luminosity functions from Stage IV surveys like Euclid, DESI, and LSST.

Importantly, the potential environmental variations in subhalo concentrations and internal structures discussed here could have implications for strong gravitational lensing sensitivities. The frequency and properties of substructure-induced perturbations in extended arcs are known to be sensitive to the small-scale mass profiles of intervening subhaloes. Comparing these environment-dependent structural trends with subhalo detection thresholds modelled for upcoming imaging surveys, such as the strong lenses expected from Euclid, may help clarify whether environmental modulation could influence expected subhalo discovery rates or affect parameters derived from lens substructure statistics [233].

For indirect DM detection, an environment-aware boost model could provide inputs for alternative templates for the isotropic diffuse gamma-ray background and its angular power spectrum. Comparing these models with Fermi-LAT data and future observations from the Cherenkov Telescope Array Observatory may offer a way to explore environmental variations in DM annihilation signatures observationally [89, 90].

References

[1] V. Springel, S. D. M. White, A. Jenkins, C. S. Frenk, N. Yoshida, L. Gao, J. Navarro, R. Thacker, D. Croton, J. Helly, J. A. Peacock, S. Cole, P. Thomas, H. Couchman, A. Evrard, J. Colberg, and F. Pearce, "Simulations of the formation, evolution and clustering of galaxies and quasars", Nature **435**, 629 (2005), arXiv:astro-ph/0504097 [astro-ph] .

[2] C. Lacey and S. Cole, "Merger rates in hierarchical models of galaxy formation", MNRAS **262**, 627 (1993).

[3] R. H. Wechsler, J. S. Bullock, J. R. Primack, A. V. Kravtsov, and A. Dekel, "Concentrations of Dark Halos from Their Assembly Histories", ApJL **568**, 52 (2002), arXiv:astro-ph/0108151 [astro-ph] .

[4] Planck Collaboration, N. Aghanim, Y. Akrami, M. Ashdown, J. Aumont, C. Baccigalupi, M. Ballardini, A. J. Banday, R. B. Barreiro, N. Bartolo, S. Basak, R. Battye, K. Benabed, J. P. Bernard, M. Bersanelli, P. Bielewicz, J. J. Bock, J. R. Bond, J. Borrill, F. R. Bouchet, F. Boulanger, M. Bucher, C. Burigana, R. C. Butler, E. Calabrese, J. F. Cardoso, J. Carron, A. Challinor, H. C. Chiang, J. Chluba, L. P. L. Colombo, C. Combet, D. Contreras, B. P. Crill, F. Cuttaia, P. de Bernardis, G. de Zotti et al., "Planck 2018 results. VI. Cosmological parameters", A&A **641**, A6 (2020), arXiv:1807.06209 [astro-ph.CO] .

[5] E. Komatsu, K. M. Smith, J. Dunkley, C. L. Bennett, B. Gold, G. Hinshaw, N. Jarosik, D. Larson, M. R. Nolta, L. Page, D. N. Spergel, M. Halpern, R. S. Hill, A. Kogut, M. Limon, S. S. Meyer, N. Odegard, G. S. Tucker, J. L. Weiland, E. Wollack, and E. L. Wright, "Seven-year Wilkinson Microwave Anisotropy Probe (WMAP) Observations: Cosmological Interpretation", ApJS **192**, 18 (2011), arXiv:1001.4538 [astro-ph.CO] .

[6] W. A. Hellwing, C. S. Frenk, M. Cautun, S. Bose, J. Helly, A. Jenkins, T. Sawala, and M. Cytowski, "The Copernicus Complexio: a high-resolution view of the small-scale Universe", MNRAS **457**, 3492 (2016), arXiv:1505.06436 [astro-ph.CO] .

[7] O. Hahn, C. Porciani, C. M. Carollo, and A. Dekel, "Properties of dark matter haloes in clusters, filaments, sheets and voids", MNRAS **375**, 489 (2007), arXiv:astro-ph/0610280 [astro-ph] .

[8] J. E. Forero-Romero, Y. Hoffman, S. Gottlöber, A. Klypin, and G. Yepes, "A dynamical classification of the cosmic web", MNRAS **396**, 1815 (2009), arXiv:0809.4135 [astro-ph] .

[9] E. Hubble, "A Relation between Distance and Radial Velocity among Extra-Galactic Nebulae", Proceedings of the National Academy of Science **15**, 168 (1929).

[10] A. A. Penzias and R. W. Wilson, "Measurement of the Flux Density of CAS a at 4080 Mc/s.", ApJL **142**, 1149 (1965).

[11] A. G. Riess, A. V. Filippenko, P. Challis, A. Clocchiatti, A. Diercks, P. M. Garnavich, R. L. Gilliland, C. J. Hogan, S. Jha, R. P. Kirshner, B. Leibundgut, M. M. Phillips, D. Reiss, B. P. Schmidt, R. A. Schommer, R. C. Smith, J. Spyromilio, C. Stubbs, N. B. Suntzeff, and J. Tonry, "Observational Evidence from Supernovae for an Accelerating Universe and a Cosmological Constant", AJ **116**, 1009 (1998), arXiv:astro-ph/9805201 [astro-ph] .

[12] S. Perlmutter, G. Aldering, G. Goldhaber, R. A. Knop, P. Nugent, P. G. Castro, S. Deustua, S. Fabbro, A. Goobar, D. E. Groom, I. M. Hook, A. G. Kim, M. Y. Kim, J. C. Lee, N. J. Nunes, R. Pain, C. R. Pennypacker, R. Quimby, C. Lidman, R. S. Ellis, M. Irwin, R. G. McMahon, P. Ruiz-Lapuente, N. Walton, B. Schaefer, B. J. Boyle, A. V. Filippenko, T. Matheson, A. S. Fruchter, N. Panagia, H. J. M. Newberg, W. J. Couch, and T. S. C. Project, "Measurements of Ω and Λ from 42 High-Redshift Supernovae", ApJL **517**, 565 (1999), arXiv:astro-ph/9812133 [astro-ph] .

[13] G. R. Blumenthal, S. M. Faber, J. R. Primack, and M. J. Rees, "Formation of galaxies and large-scale structure with cold dark matter.", Nature **311**, 517 (1984).

[14] J. R. Bond, L. Kofman, and D. Pogosyan, "How filaments of galaxies are woven into the cosmic web", Nature **380**, 603 (1996), arXiv:astro-ph/9512141 [astro-ph] .

[15] J. F. Navarro, C. S. Frenk, and S. D. M. White, "The Structure of Cold Dark Matter Halos", ApJL **462**, 563 (1996), arXiv:astro-ph/9508025 [astro-ph] .

[16] A. Friedmann, "Über die Krümmung des Raumes", Zeitschrift fur Physik **10**, 377 (1922).

[17] D. W. Hogg, "Distance measures in cosmology", arXiv e-prints , astro-ph/9905116 (1999), arXiv:astro-ph/9905116 [astro-ph] .

[18] S. Weinberg, Cosmology (Oxford University Press, Oxford, 2008).

[19] A. H. Guth, "The Inflationary Universe: A Possible Solution to the Horizon and Flatness Problems", Phys. Rev. D **23**, 347 (1981).

[20] P. J. E. Peebles, Principles of Physical Cosmology (Princeton university press, 1993).

[21] H. Mo, F. C. van den Bosch, and S. White, Galaxy Formation and Evolution (Cambridge University Press, 2010).

[22] G. F. Smoot, C. L. Bennett, A. Kogut, E. L. Wright, J. Aymon, N. W. Boggess, E. S. Cheng, G. de Amici, S. Gulkis, M. G. Hauser, G. Hinshaw, P. D. Jackson, M. Janssen, E. Kaita, T. Kelsall, P. Keegstra, C. Lineweaver, K. Loewenstein, P. Lubin, J. Mather, S. S. Meyer, S. H. Moseley, T. Murdock, L. Rokke, R. F. Silverberg, L. Tenorio, R. Weiss, and D. T. Wilkinson, "Structure in the COBE Differential Microwave Radiometer First-Year Maps", ApJ **396**, L1 (1992).

[23] C. L. Bennett, D. Larson, J. L. Weiland, N. Jarosik, G. Hinshaw, N. Odegard, K. M. Smith, R. S. Hill, B. Gold, M. Halpern, E. Komatsu, M. R. Nolta, L. Page, D. N. Spergel, E. Wollack, J. Dunkley, A. Kogut, M. Limon, S. S. Meyer, G. S. Tucker, and E. L. Wright, "Nine-year Wilkinson Microwave Anisotropy Probe (WMAP) Observations: Final Maps and Results", ApJS **208**, 20 (2013), arXiv:1212.5225 [astro-ph.CO] .

[24] P. J. E. Peebles, The large-scale structure of the universe (Princeton University Press, 1980).

[25] J. H. Jeans, "The Stability of a Spherical Nebula", Philosophical Transactions of the Royal Society of London Series A **199**, 1 (1902).

[26] Y. B. Zel'dovich, "Gravitational instability: An approximate theory for large density perturbations.", A&A **5**, 84 (1970).

[27] T. Padmanabhan, Structure Formation in the Universe (Cambridge University Press, 1993).

[28] G. Efstathiou, M. Davis, S. D. M. White, and C. S. Frenk, "Numerical techniques for large cosmological N-body simulations", ApJS **57**, 241 (1985).

[29] J. E. Gunn and J. R. Gott, III, "On the Infall of Matter Into Clusters of Galaxies and Some Effects on Their Evolution", ApJL **176**, 1 (1972).

[30] S. D. M. White and M. J. Rees, "Core condensation in heavy halos: a two-stage theory for galaxy formation and clustering", MNRAS **183**, 10.1093/mnras/183.3.341 (1978).

[31] W. H. Press and P. Schechter, "Formation of Galaxies and Clusters of Galaxies by Self-Similar Gravitational Condensation", ApJL **187**, 425 (1974).

[32] J. R. Bond, S. Cole, G. Efstathiou, and N. Kaiser, "Excursion Set Mass Functions for Hierarchical Gaussian Fluctuations", ApJL **379**, 440 (1991).

[33] R. van de Weygaert and J. R. Bond, "Observations and Morphology of the Cosmic Web", in A Pan-Chromatic View of Clusters of Galaxies and the Large-Scale Structure, Lecture Notes in Physics, Vol. 740, edited by M. Plionis, O. López-Cruz, and D. Hughes (Springer, Dordrecht, The Netherlands, 2008) p. 409.

[34] R. van de Weygaert and W. Schaap, The cosmic web: Geometric analysis, in Data Analysis in Cosmology, edited by V. J. Martinez, E. Saar, E. M. Gonzales, and M. J. Pons-Borderia (Springer Berlin Heidelberg, Berlin, Heidelberg, 2009) pp. 291–413.

[35] V. de Lapparent, M. J. Geller, and J. P. Huchra, "A Slice of the Universe", ApJ **302**, L1 (1986).

[36] G. M. Voit, "Tracing cosmic evolution with clusters of galaxies", Reviews of Modern Physics **77**, 207 (2005), arXiv:astro-ph/0410173 [astro-ph] .

[37] Y.-j. Peng, S. J. Lilly, K. Kovač, M. Bolzonella, L. Pozzetti, A. Renzini, G. Zamorani, O. Ilbert, C. Knobel, A. Iovino, C. Maier, O. Cucciati, L. Tasca, C. M. Carollo, J. Silverman, P. Kampczyk, L. de Ravel, D. Sanders, N. Scoville, T. Contini, V. Mainieri, M. Scodeggio, J.-P. Kneib, O. Le Fèvre, S. Bardelli, A. Bongiorno, K. Caputi, G. Coppa, S. de la Torre, P. Franzetti, B. Garilli, F. Lamareille, J.-F. Le Borgne, V. Le Brun, M. Mignoli, E. Perez Montero, R. Pello et al., "Mass and Environment as Drivers of Galaxy Evolution in SDSS and zCOSMOS and the Origin of the Schechter Function", ApJL **721**, 193 (2010), arXiv:1003.4747 [astro-ph.CO] .

[38] D. Zakharova, S. McGee, B. Vulcani, and G. De Lucia, "The impact of large-scale structure on the anisotropic quenching of satellites", A&A **693**, A113 (2025), arXiv:2412.06640 [astro-ph.GA] .

[39] A. Dressler, "Galaxy morphology in rich clusters: implications for the formation and evolution of galaxies.", ApJL **236**, 351 (1980).

[40] A. V. Kravtsov and S. Borgani, "Formation of Galaxy Clusters", ARA&A **50**, 353 (2012), arXiv:1205.5556 [astro-ph.CO] .

[41] M. Cautun, R. van de Weygaert, B. J. T. Jones, and C. S. Frenk, "Evolution of the cosmic web", MNRAS **441**, 2923 (2014), arXiv:1401.7866 [astro-ph.CO] .

[42] R. Cen and J. P. Ostriker, "Where Are the Baryons?", ApJL **514**, 1 (1999), arXiv:astro-ph/9806281 [astro-ph] .

[43] T. Tuominen, J. Nevalainen, E. Tempel, T. Kuutma, N. Wijers, J. Schaye, P. Heinämäki, M. Bonamente, and P. Ganeshaiah Veena, "An EAGLE view of the missing baryons", A&A **646**, A156 (2021), arXiv:2012.09203 [astro-ph.CO] .

[44] C. Pichon, D. Pogosyan, T. Kimm, A. Slyz, J. Devriendt, and Y. Dubois, "Rigging dark haloes: why is hierarchical galaxy formation consistent with the inside-out build-up of thin discs?", MNRAS **418**, 2493 (2011), arXiv:1105.0210 [astro-ph.CO] .

[45] S. Codis, C. Pichon, and D. Pogosyan, "Spin alignments within the cosmic web: a theory of constrained tidal torques near filaments", MNRAS **452**, 3369 (2015), arXiv:1504.06073 [astro-ph.CO] .

[46] K. Kraljic, S. Arnouts, C. Pichon, C. Laigle, S. de la Torre, D. Vibert, C. Cadiou, Y. Dubois, M. Treyer, C. Schimd, S. Codis, V. de Lapparent, J. Devriendt, H. S. Hwang, D. Le Borgne, N. Malavasi, B. Milliard, M. Musso, D. Pogosyan, M. Alpaslan, J. Bland-Hawthorn, and A. H. Wright, "Galaxy evolution in the metric of the cosmic web", MNRAS **474**, 547 (2018), arXiv:1710.02676 [astro-ph.GA] .

[47] H. J. Martínez, H. Muriel, and V. Coenda, "Galaxies infalling into groups: filaments versus isotropic infall", MNRAS **455**, 127 (2016), arXiv:1510.00390 [astro-ph.GA] .

[48] D. Kleiner, K. A. Pimbblet, D. H. Jones, B. S. Koribalski, and P. Serra, "Evidence for H I replenishment in massive galaxies through gas accretion from the cosmic web", MNRAS **466**, 4692 (2017), arXiv:1701.03467 [astro-ph.GA] .

[49] T. Kuutma, A. Tamm, and E. Tempel, "From voids to filaments: environmental transformations of galaxies in the SDSS", A&A **600**, L6 (2017), arXiv:1703.04338 [astro-ph.GA] .

[50] M. J. Geller and J. P. Huchra, "Mapping the Universe", Science **246**, 897 (1989).

[51] J. R. Gott, III, M. Jurić, D. Schlegel, F. Hoyle, M. Vogeley, M. Tegmark, N. Bahcall, and J. Brinkmann, "A Map of the Universe", ApJL **624**, 463 (2005), arXiv:astro-ph/0310571 [astro-ph] .

[52] H. Lietzen, E. Tempel, L. J. Liivamägi, A. Montero-Dorta, M. Einasto, A. Streblyanska, C. Maraston, J. A. Rubiño-Martín, and E. Saar, "Discovery of a massive supercluster system at z ∼0.47", A&A **588**, L4 (2016), arXiv:1602.08498 [astro-ph.CO] .

[53] M. A. Aragón-Calvo, R. van de Weygaert, and B. J. T. Jones, "Multiscale phenomenology of the cosmic web", MNRAS **408**, 2163 (2010), arXiv:1007.0742 [astro-ph.CO] .

[54] Y. Dubois, C. Pichon, C. Welker, D. Le Borgne, J. Devriendt, C. Laigle, S. Codis, D. Pogosyan, S. Arnouts, K. Benabed, E. Bertin, J. Blaizot, F. Bouchet, J.-F. Cardoso, S. Colombi, V. de Lapparent, V. Desjacques, R. Gavazzi, S. Kassin, T. Kimm, H. McCracken, B. Milliard, S. Peirani, S. Prunet, S. Rouberol, J. Silk, A. Slyz, T. Sousbie, R. Teyssier, L. Tresse, M. Treyer, D. Vibert, and M. Volonteri, "Dancing in the dark: galactic properties trace spin swings along the cosmic web", MNRAS **444**, 1453 (2014), arXiv:1402.1165 [astro-ph.CO] .

[55] V. Icke, "Voids and filaments", MNRAS **206**, 1P (1984).

[56] R. K. Sheth and R. van de Weygaert, "A hierarchy of voids: much ado about nothing", MNRAS **350**, 517 (2004), arXiv:astro-ph/0311260 [astro-ph] .

[57] K. Kreckel, E. Platen, M. A. Aragón-Calvo, J. H. van Gorkom, R. van de Weygaert, J. M. van der Hulst, and B. Beygu, "The Void Galaxy Survey: Optical Properties and H I Morphology and Kinematics", AJ **144**, 16 (2012), arXiv:1204.5185 [astro-ph.CO] .

[58] B. Beygu, K. Kreckel, J. M. van der Hulst, T. H. Jarrett, R. Peletier, R. van de Weygaert, J. H. van Gorkom, and M. A. Aragon-Calvo, "The void galaxy survey: Star formation properties", MNRAS **458**, 394 (2016), arXiv:1601.08228 [astro-ph.GA] .

[59] P. J. E. Peebles, "The Void Phenomenon", ApJL **557**, 495 (2001), arXiv:astro-ph/0101127 [astro-ph] .

[60] E. G. P. Bos, R. van de Weygaert, K. Dolag, and V. Pettorino, "The darkness that shaped the void: dark energy and cosmic voids", MNRAS **426**, 440 (2012), arXiv:1205.4238 [astro-ph.CO] .

[61] F. Zwicky, "On the masses of nebulae and of clusters of nebulae", ApJL **86**, 217 (1937).

[62] V. C. Rubin, J. Ford, W. Kent, and N. Thonnard, "Rotational properties of 21 Sc galaxies with extended rotation curves", ApJL **238**, 471 (1980).

[63] M. Bartelmann and M. Maturi, "Weak gravitational lensing", Scholarpedia **12**, 32440 (2017), arXiv:1612.06535 [astro-ph.CO] .

[64] D. Clowe, M. Bradač, A. H. Gonzalez, and et al., "A Direct Empirical Proof of the Existence of Dark Matter", ApJ **648**, L109 (2006).

[65] R. V. Wagoner, W. A. Fowler, and F. Hoyle, "On the Synthesis of Elements at Very High Temperatures", ApJL **148**, 3 (1967).

[66] G. Jungman, M. Kamionkowski, and K. Griest, "Supersymmetric dark matter", Phys. Rep. **267**, 195 (1996), arXiv:hep-ph/9506380 [hep-ph] .

[67] G. Arcadi, M. Dutra, P. Ghosh, M. Lindner, Y. Mambrini, M. Pierre, S. Profumo, and F. S. Queiroz, "The waning of the WIMP? A review of models, searches, and constraints", European Physical Journal C **78**, 203 (2018), arXiv:1703.07364 [hep-ph] .

[68] G. Arcadi, D. Cabo-Almeida, M. Dutra, P. Ghosh, M. Lindner, Y. Mambrini, J. P. Neto, M. Pierre, S. Profumo, and F. S. Queiroz, "The waning of the WIMP: endgame?", European Physical Journal C **85**, 152 (2025), arXiv:2403.15860 [hep-ph] .

[69] M. W. Goodman and E. Witten, "Detectability of certain dark-matter candidates", Phys. Rev. D **31**, 3059 (1985).

[70] J. Liu, X. Chen, and X. Ji, "Current status of direct dark matter detection experiments", Nature Physics **13**, 212 (2017), arXiv:1709.00688 [astro-ph.CO] .

[71] P. Salucci, F. Nesti, G. Gentile, and C. Frigerio Martins, "The dark matter density at the Sun's location", A&A **523**, A83 (2010), arXiv:1003.3101 [astro-ph.GA] .

[72] J. Bovy and S. Tremaine, "On the Local Dark Matter Density", ApJL **756**, 89 (2012), arXiv:1205.4033 [astro-ph.GA] .

[73] J. I. Read, "The local dark matter density", Journal of Physics G Nuclear Physics **41**, 063101 (2014), arXiv:1404.1938 [astro-ph.GA] .

[74] P. F. de Salas and A. Widmark, "Dark matter local density determination: recent observations and future prospects", Reports on Progress in Physics **84**, 104901 (2021), arXiv:2012.11477 [astro-ph.GA] .

[75] A. K. Drukier, K. Freese, and D. N. Spergel, "Detecting cold dark-matter candidates", Phys. Rev. D **33**, 3495 (1986).

[76] R. Bernabei, P. Belli, F. Cappella, R. Cerulli, C. J. Dai, A. D'Angelo, H. L. He, A. Incicchitti, H. H. Kuang, J. M. Ma, F. Montecchia, F. Nozzoli, D. Prosperi, X. D. Sheng, and Z. P. Ye, "First results from DAMA/LIBRA and the combined results with DAMA/NaI", European Physical Journal C **56**, 333 (2008), arXiv:0804.2741 [astro-ph] .

[77] J. Aalbers, D. S. Akerib, C. W. Akerlof, A. K. Al Musalhi, F. Alder, A. Alqahtani, S. K. Alsum, C. S. Amarasinghe, A. Ames, T. J. Anderson, N. Angelides, H. M. Araújo, J. E. Armstrong, M. Arthurs, S. Azadi, A. J. Bailey, A. Baker, J. Balajthy, S. Balashov, J. Bang, J. W. Bargemann, M. J. Barry, J. Barthel, D. Bauer, A. Baxter, K. Beattie, J. Belle, P. Beltrame, J. Bensinger, T. Benson, E. P. Bernard, A. Bhatti, A. Biekert, T. P. Biesiadzinski, H. J. Birch, B. Birrittella, G. M. Blockinger et al., "First Dark Matter Search Results from the LUX-ZEPLIN (LZ) Experiment", Phys. Rev. Lett. **131**, 041002 (2023), arXiv:2207.03764 [hep-ex] .

[78] J. E. Gunn, B. W. Lee, I. Lerche, D. N. Schramm, and G. Steigman, "Some astrophysical consequences of the existence of a heavy stable neutral lepton.", ApJL **223**, 1015 (1978).

[79] L. Bergström, P. Ullio, and J. H. Buckley, "Observability of γ rays from dark matter neutralino annihilations in the Milky Way halo", Astroparticle Physics **9**, 137 (1998), arXiv:astro-ph/9712318 [astro-ph] .

[80] F. Halzen and D. Hooper, "The indirect search for dark matter with IceCube", New Journal of Physics **11**, 105019 (2009), arXiv:0910.4513 [astro-ph.HE] .

[81] G. Bertone, "The moment of truth for WIMP dark matter", Nature **468**, 389 (2010), arXiv:1011.3532 [astro-ph.CO] .

[82] K. Morå, "Dark Matter Searches with H.E.S.S", arXiv e-prints , arXiv:1512.00698 (2015), arXiv:1512.00698 [astro-ph.HE] .

[83] M. Doro, "A review of the past and present MAGIC dark matter search program and a glimpse at the future", arXiv e-prints , arXiv:1701.05702 (2017), arXiv:1701.05702 [astro-ph.HE] .

[84] V. Springel, J. Wang, M. Vogelsberger, A. Ludlow, A. Jenkins, A. Helmi, J. F. Navarro, C. S. Frenk, and S. D. M. White, "The Aquarius Project: the subhaloes of galactic haloes", MNRAS **391**, 1685 (2008), arXiv:0809.0898 [astro-ph] .

[85] M. A. Sánchez-Conde and F. Prada, "The flattening of the concentration-mass relation towards low halo masses and its implications for the annihilation signal boost", MNRAS **442**, 2271 (2014), arXiv:1312.1729 [astro-ph.CO] .

[86] Á. Moliné, M. A. Sánchez-Conde, S. Palomares-Ruiz, and F. Prada, "Characterization of subhalo structural properties and implications for dark matter annihilation signals", MNRAS **466**, 4974 (2017), arXiv:1603.04057 [astro-ph.CO] .

[87] D. Hooper and S. J. Witte, "Gamma rays from dark matter subhalos revisited: refining the predictions and constraints", J. Cosmology Astropart. Phys. **2017**, 018 (2017), arXiv:1610.07587 [astro-ph.HE] .

[88] J. Zavala and C. S. Frenk, "Dark Matter Haloes and Subhaloes", Galaxies **7**, 81 (2019), arXiv:1907.11775 [astro-ph.CO] .

[89] M. Ackermann, A. Albert, B. Anderson, W. B. Atwood, L. Baldini, G. Barbiellini, D. Bastieri, K. Bechtol, R. Bellazzini, E. Bissaldi, R. D. Blandford, E. D. Bloom, R. Bonino, E. Bottacini, T. J. Brandt, J. Bregeon, P. Bruel, R. Buehler, G. A. Caliandro, R. A. Cameron, R. Caputo, M. Caragiulo, P. A. Caraveo, C. Cecchi, E. Charles, A. Chekhtman, J. Chiang, G. Chiaro, S. Ciprini, R. Claus, J. Cohen-Tanugi, J. Conrad, A. Cuoco, S. Cutini, F. D'Ammando, A. de Angelis, F. de Palma et al., "Searching for Dark Matter Annihilation from Milky Way Dwarf Spheroidal Galaxies with Six Years of Fermi Large Area Telescope Data", Phys. Rev. Lett. **115**, 231301 (2015), arXiv:1503.02641 [astro-ph.HE] .

[90] M. Di Mauro, X. Hou, C. Eckner, G. Zaharijas, and E. Charles, "Search for γ -ray emission from dark matter particle interactions from the Andromeda and Triangulum galaxies with the Fermi Large Area Telescope", Phys. Rev. D **99**, 123027 (2019), arXiv:1904.10977 [astro-ph.HE] .

[91] O. Buchmueller, C. Doglioni, and L.-T. Wang, "Search for dark matter at colliders", Nature Physics **13**, 217 (2017), arXiv:1912.12739 [hep-ex] .

[92] D. Abercrombie, N. Akchurin, E. Akilli, J. Alcaraz Maestre, B. Allen, B. Alvarez Gonzalez, J. Andrea, A. Arbey, G. Azuelos, P. Azzi, M. Backović, Y. Bai, S. Banerjee, J. Beacham, A. Belyaev, A. Boveia, A. J. Brennan, O. Buchmueller, M. R. Buckley, G. Busoni, M. Buttignol, G. Cacciapaglia, R. Caputo, L. Carpenter, N. Filipe Castro, G. Gomez Ceballos, Y. Cheng, J. P. Chou, A. Cortes Gonzalez, C. Cowden, F. D'Eramo, A. De Cosa, M. De Gruttola, A. De Roeck, A. De Simone, A. Deandrea, Z. Demiragli et al., "Dark Matter Benchmark Models for Early LHC Run-2 Searches: Report of the ATLAS/CMS Dark Matter Forum", arXiv e-prints , arXiv:1507.00966 (2015), arXiv:1507.00966 [hep-ex] .

[93] J. Abdallah, H. Araujo, A. Arbey, A. Ashkenazi, A. Belyaev, J. Berger, C. Boehm, A. Boveia, A. Brennan, J. Brooke, O. Buchmueller, M. Buckley, G. Busoni, L. Calibbi, S. Chauhan, N. Daci, G. Davies, I. De Bruyn, P. De Jong, A. De Roeck, K. de Vries, D. Del Re, A. De Simone, A. Di Simone, C. Doglioni, M. Dolan, H. K. Dreiner, J. Ellis, S. Eno, E. Etzion, M. Fairbairn, B. Feldstein, H. Flaecher, E. Feng, P. Fox, M.-H. Genest, L. Gouskos et al., "Simplified models for dark matter searches at the LHC", Physics of the Dark Universe **9**, 8 (2015), arXiv:1506.03116 [hep-ph] .

[94] A. Boveia and C. Doglioni, "Dark Matter Searches at Colliders", Annual Review of Nuclear and Particle Science **68**, 429 (2018), arXiv:1810.12238 [hep-ex] .

[95] J. Einasto, "A method for the determination of the galactic rotation parameters", Trudy Astrofizicheskogo Instituta Alma-Ata **5**, 87 (1965).

[96] J. F. Navarro, E. Hayashi, C. Power, A. R. Jenkins, C. S. Frenk, S. D. M. White, V. Springel, J. Stadel, and T. R. Quinn, "The inner structure of ΛCDM haloes - III. Universality and asymptotic slopes", MNRAS **349**, 1039 (2004), arXiv:astro-ph/0311231 [astro-ph] .

[97] L. Gao, J. F. Navarro, S. Cole, C. S. Frenk, S. D. M. White, V. Springel, A. Jenkins, and A. F. Neto, "The redshift dependence of the structure of massive Λ cold dark matter haloes", MNRAS **387**, 536 (2008), arXiv:0711.0746 [astro-ph] .

[98] A. Klypin, G. Yepes, S. Gottlöber, F. Prada, and S. Heß, "MultiDark simulations: the story of dark matter halo concentrations and density profiles", MNRAS **457**, 4340 (2016), arXiv:1411.4001 [astro-ph.CO] .

[99] D. Lynden-Bell, "Statistical mechanics of violent relaxation in stellar systems", MNRAS **136**, 101 (1967).

[100] M. Boylan-Kolchin, C.-P. Ma, and E. Quataert, "Dynamical friction and galaxy merging time-scales", MNRAS **383**, 93 (2008), arXiv:0707.2960 [astro-ph] .

[101] S. Chandrasekhar, "Dynamical Friction. I. General Considerations: the Coefficient of Dynamical Friction.", ApJL **97**, 255 (1943).

[102] G. Tormen, A. Diaferio, and D. Syer, "Survival of substructure within dark matter haloes", MNRAS **299**, 728 (1998), arXiv:astro-ph/9712222 [astro-ph] .

[103] J. Binney and S. Tremaine, Galactic Dynamics: Second Edition (Princeton University Press, Princeton, NJ, 2008).

[104] J. E. Taylor and A. Babul, "The evolution of substructure in galaxy, group and cluster haloes - I. Basic dynamics", MNRAS **348**, 811 (2004), arXiv:astro-ph/0301612 [astro-ph] .

[105] J. E. Barnes and L. Hernquist, "Dynamics of interacting galaxies.", ARA&A **30**, 705 (1992).

[106] B. Allgood, R. A. Flores, J. R. Primack, A. V. Kravtsov, R. H. Wechsler, A. Faltenbacher, and J. S. Bullock, "The shape of dark matter haloes: dependence on mass, redshift, radius and formation", MNRAS **367**, 1781 (2006), arXiv:astro-ph/0508497 [astro-ph] .

[107] H. Y. Wang, H. J. Mo, and Y. P. Jing, "Environmental dependence of cold dark matter halo formation", MNRAS **375**, 633 (2007), arXiv:astro-ph/0608690 [astro-ph] .

[108] O. Metuki, N. I. Libeskind, Y. Hoffman, R. A. Crain, and T. Theuns, "Galaxy properties and the cosmic web in simulations", MNRAS **446**, 10.1093/mnras/stu2166 (2015).

[109] D. Alonso, E. Eardley, and J. A. Peacock, "Halo abundances within the cosmic web", MNRAS **447**, 2683 (2015), arXiv:1406.4159 [astro-ph.CO] .

[110] W. A. Hellwing, M. Cautun, R. van de Weygaert, and B. T. Jones, "Caught in the cosmic web: Environmental effect on halo concentrations, shape, and spin", Phys. Rev. D **103**, 063517 (2021), arXiv:2011.08840 [astro-ph.CO] .

[111] O. Hahn, C. M. Carollo, C. Porciani, and A. Dekel, "The evolution of dark matter halo properties in clusters, filaments, sheets and voids", MNRAS **381**, 41 (2007), arXiv:0704.2595 [astro-ph] .

[112] P. Ganeshaiah Veena, M. Cautun, R. van de Weygaert, E. Tempel, B. J. T. Jones, S. Rieder, and C. S. Frenk, "The Cosmic Ballet: spin and shape alignments of haloes in the cosmic web", MNRAS **481**, 414 (2018), arXiv:1805.00033 [astro-ph.CO] .

[113] M. Davis, G. Efstathiou, C. S. Frenk, and S. D. M. White, "The evolution of large-scale structure in a universe dominated by cold dark matter", ApJL **292**, 371 (1985).

[114] L. Gao, S. D. M. White, A. Jenkins, F. Stoehr, and V. Springel, "The subhalo populations of ΛCDM dark haloes", MNRAS **355**, 819 (2004), arXiv:astro-ph/0404589 [astro-ph] .

[115] J. Diemand, M. Kuhlen, P. Madau, M. Zemp, B. Moore, D. Potter, and J. Stadel, "Clumps and streams in the local dark matter distribution", Nature **454**, 735 (2008), arXiv:0805.1244 [astro-ph] .

[116] P. Madau, J. Diemand, and M. Kuhlen, "Dark Matter Subhalos and the Dwarf Satellites of the Milky Way", ApJL **679**, 1260 (2008), arXiv:0802.2265 [astro-ph] .

[117] T. Ishiyama, S. Rieder, J. Makino, S. Portegies Zwart, D. Groen, K. Nitadori, C. de Laat, S. McMillan, K. Hiraki, and S. Harfst, "The Cosmogrid Simulation: Statistical Properties of Small Dark Matter Halos", ApJL **767**, 146 (2013), arXiv:1101.2020 [astro-ph.CO] .

[118] S. Garrison-Kimmel, M. Boylan-Kolchin, J. S. Bullock, and K. Lee, "ELVIS: Exploring the Local Volume in Simulations", MNRAS **438**, 2578 (2014), arXiv:1310.6746 [astro-ph.CO] .

[119] S. Profumo, K. Sigurdson, and M. Kamionkowski, "What Mass Are the Smallest Protohalos?", Phys. Rev. Lett. **97**, 031301 (2006), arXiv:astro-ph/0603373 [astro-ph] .

[120] A. R. Zentner, A. A. Berlind, J. S. Bullock, A. V. Kravtsov, and R. H. Wechsler, "The Physics of Galaxy Clustering. I. A Model for Subhalo Populations", ApJL **624**, 505 (2005), arXiv:astro-ph/0411586 [astro-ph] .

[121] L. Gao, J. F. Navarro, C. S. Frenk, A. Jenkins, V. Springel, and S. D. White, "The phoenix project: The dark side of rich galaxy clusters", MNRAS **425**, 10.1111/j.1365-2966.2012.21564.x (2012).

[122] K. Belotsky, A. Kirillov, and M. Y. Khlopov, "Astrophysical manifestations of clumps of cold dark matter", Physics of Atomic Nuclei **76**, 469 (2013).

[123] K. Belotsky, A. Kirillov, and M. Khlopov, "Gamma-ray evidence for dark matter clumps", Gravitation and Cosmology **20**, 47 (2014), arXiv:1212.6087 [astro-ph.HE] .

[124] L. J. Chang, M. Lisanti, and S. Mishra-Sharma, "Search for dark matter annihilation in the Milky Way halo", Phys. Rev. D **98**, 123004 (2018), arXiv:1804.04132 [astro-ph.CO] .

[125] A. Del Popolo and M. Le Delliou, "Small Scale Problems of the ΛCDM Model: A Short Review", Galaxies **5**, 17 (2017), arXiv:1606.07790 [astro-ph.CO] .

[126] J. S. Bullock and M. Boylan-Kolchin, "Small-Scale Challenges to the ΛCDM Paradigm", ARA&A **55**, 343 (2017), arXiv:1707.04256 [astro-ph.CO] .

[127] G. Kauffmann and S. D. White, MNRAS **261**, 921 (1993).

[128] B. Moore, "Evidence against dissipation-less dark matter from observations of galaxy haloes", Nature **370**, 629 (1994).

[129] A. Klypin, A. V. Kravtsov, O. Valenzuela, and F. Prada, "Where Are the Missing Galactic Satellites?", ApJL **522**, 82 (1999), arXiv:astro-ph/9901240 [astro-ph] .

[130] R. A. Flores and J. R. Primack, "Observational and Theoretical Constraints on Singular Dark Matter Halos", ApJ **427**, L1 (1994), arXiv:astro-ph/9402004 [astro-ph] .

[131] S.-H. Oh, D. A. Hunter, E. Brinks, B. G. Elmegreen, A. Schruba, F. Walter, M. P. Rupen, L. M. Young, C. E. Simpson, M. C. Johnson, K. A. Herrmann, D. Ficut-Vicas, P. Cigan, V. Heesen, T. Ashley, and H.-X. Zhang, "High-resolution Mass Models of Dwarf Galaxies from LITTLE THINGS", AJ **149**, 180 (2015), arXiv:1502.01281 [astro-ph.GA] .

[132] M. Boylan-Kolchin, J. S. Bullock, and M. Kaplinghat, "Too big to fail? The puzzling darkness of massive Milky Way subhaloes", MNRAS **415**, L40 (2011), https://academic.oup.com/mnrasl/article-pdf/415/1/L40/54669362/mnrasl_415_1_l40.pdf .

[133] B. Moore, S. Ghigna, F. Governato, G. Lake, T. Quinn, J. Stadel, and P. Tozzi, "Dark Matter Substructure within Galactic Halos", ApJ **524**, L19 (1999), arXiv:astro-ph/9907411 [astro-ph] .

[134] M. Kuhlen, P. Madau, and J. Silk, "Exploring Dark Matter with Milky Way Substructure", Science **325**, 970 (2009), arXiv:0907.0005 [astro-ph.GA] .

[135] A. Drlica-Wagner, K. Bechtol, E. S. Rykoff, E. Luque, A. Queiroz, Y.-Y. Mao, R. H. Wechsler, J. D. Simon, B. Santiago, B. Yanny, E. Balbinot, S. Dodelson, A. Fausti Neto, D. J. James, T. S. Li, M. A. G. Maia, J. L. Marshall, A. Pieres, K. Stringer, A. R. Walker, T. M. C. Abbott, F. B. Abdalla, S. Allam, A. Benoit-Lévy, G. M. Bernstein, E. Bertin, D. Brooks, E. Buckley-Geer, D. L. Burke, A. Carnero Rosell, M. Carrasco Kind, J. Carretero, M. Crocce, L. N. da Costa, S. Desai, H. T. Diehl, J. P. Dietrich et al., "Eight Ultra-faint Galaxy Candidates Discovered in Year Two of the Dark Energy Survey", ApJL **813**, 109 (2015), arXiv:1508.03622 [astro-ph.GA] .

[136] J. S. Bullock, A. V. Kravtsov, and D. H. Weinberg, "Reionization and the Abundance of Galactic Satellites", ApJL **539**, 517 (2000), arXiv:astro-ph/0002214 [astro-ph] .

[137] M. Boylan-Kolchin, J. S. Bullock, and M. Kaplinghat, "The Milky Way's bright satellites as an apparent failure of ΛCDM", MNRAS **422**, 1203 (2012), https://academic.oup.com/mnras/article-pdf/422/2/1203/3464467/mnras0422-1203.pdf .

[138] E. J. Tollerud, M. Boylan-Kolchin, and J. S. Bullock, "M31 satellite masses compared to ΛCDM subhaloes", MNRAS **440**, 3511 (2014), arXiv:1403.6469 [astro-ph.GA] .

[139] M. Cautun, C. S. Frenk, R. van de Weygaert, W. A. Hellwing, and B. J. T. Jones, "Milky Way mass constraints from the Galactic satellite gap", MNRAS **445**, 2049 (2014), arXiv:1405.7697 [astro-ph.CO] .

[140] J. F. Navarro, A. Ludlow, V. Springel, J. Wang, M. Vogelsberger, S. D. M. White, A. Jenkins, C. S. Frenk, and A. Helmi, "The diversity and similarity of simulated cold dark matter haloes", MNRAS **402**, 21 (2010), arXiv:0810.1522 [astro-ph] .

[141] J. D. Simon, A. D. Bolatto, A. Leroy, L. Blitz, and E. L. Gates, "High-Resolution Measurements of the Halos of Four Dark Matter-Dominated Galaxies: Deviations from a Universal Density Profile", ApJL **621**, 757 (2005), arXiv:astro-ph/0412035 [astro-ph] .

[142] K. A. Oman, J. F. Navarro, A. Fattahi, C. S. Frenk, T. Sawala, S. D. M. White, R. Bower, R. A. Crain, M. Furlong, M. Schaller, J. Schaye, and T. Theuns, "The unexpected diversity of dwarf galaxy rotation curves", MNRAS **452**, 3650 (2015), arXiv:1504.01437 [astro-ph.GA] .

[143] P. Boldrini, "The Cusp-Core Problem in Gas-Poor Dwarf Spheroidal Galaxies", Galaxies **10**, 5 (2021), arXiv:2201.01056 [astro-ph.GA] .

[144] V. Iršič, M. Viel, M. G. Haehnelt, J. S. Bolton, S. Cristiani, G. D. Becker, V. D'Odorico, G. Cupani, T.-S. Kim, T. A. M. Berg, S. López, S. Ellison, L. Christensen, K. D. Denney, and G. Worseck, "New constraints on the free-streaming of warm dark matter from intermediate and small scale Lyman-α forest data", Phys. Rev. D **96**, 023522 (2017), arXiv:1702.01764 [astro-ph.CO] .

[145] E. O. Nadler, A. Drlica-Wagner, K. Bechtol, S. Mau, R. H. Wechsler, V. Gluscevic, K. Boddy, A. B. Pace, T. S. Li, M. McNanna, A. H. Riley, J. García-Bellido, Y.-Y. Mao, G. Green, D. L. Burke, A. Peter, B. Jain, T. M. C. Abbott, M. Aguena, S. Allam, J. Annis, S. Avila, D. Brooks, M. Carrasco Kind, J. Carretero, M. Costanzi, L. N. da Costa, J. De Vicente, S. Desai, H. T. Diehl, P. Doel, S. Everett, A. E. Evrard, B. Flaugher, J. Frieman, D. W. Gerdes, D. Gruen et al., "Constraints on Dark Matter Properties from Observations of Milky Way Satellite Galaxies", Phys. Rev. Lett. **126**, 091101 (2021), arXiv:2008.00022 [astro-ph.CO] .

[146] S. Tulin and H.-B. Yu, "Dark matter self-interactions and small scale structure", Phys. Rep. **730**, 1 (2018), arXiv:1705.02358 [hep-ph] .

[147] F. Kahlhoefer, M. Kaplinghat, T. R. Slatyer, and C.-L. Wu, "Diversity in density profiles of self-interacting dark matter satellite halos", J. Cosmology Astropart. Phys. **2019**, 010 (2019), arXiv:1904.10539 [astro-ph.GA] .

[148] H.-Y. Schive, T. Chiueh, and T. Broadhurst, "Cosmic structure as the quantum interference of a coherent dark wave", Nature Physics **10**, 496 (2014), arXiv:1406.6586 [astro-ph.GA] .

[149] L. Hui, J. P. Ostriker, S. Tremaine, and E. Witten, "Ultralight scalars as cosmological dark matter", Phys. Rev. D **95**, 043541 (2017), arXiv:1610.08297 [astro-ph.CO] .

[150] A. D. Ludlow, J. F. Navarro, R. E. Angulo, M. Boylan-Kolchin, V. Springel, C. Frenk, and S. D. M. White, "The mass-concentration-redshift relation of cold dark matter haloes", MNRAS **441**, 378 (2014), arXiv:1312.0945 [astro-ph.CO] .

[151] R. W. Hockney and J. W. Eastwood, Computer Simulation Using Particles (McGraw-Hill, 1981).

[152] E. Bertschinger, "Simulations of Structure Formation in the Universe", ARA&A **36**, 599 (1998).

[153] J. S. Bagla, "Cosmological N-Body simulation: Techniques, Scope and Status", Current Science **88**, 1088 (2005), arXiv:astro-ph/0411043 [astro-ph] .

[154] M. Joyce, "Cosmological simulations of structure formation and the Vlasov equation", Communications in Nonlinear Science and Numerical Simulations **13**, 100 (2008), arXiv:0805.1453 [cond-mat.stat-mech] .

[155] R. E. Angulo and O. Hahn, "Large-scale dark matter simulations", Living Reviews in Computational Astrophysics **8**, 1 (2022), arXiv:2112.05165 [astro-ph.CO] .

[156] E. Hayashi, J. F. Navarro, J. E. Taylor, J. Stadel, and T. Quinn, "The Structural Evolution of Substructure", ApJL **584**, 541 (2003), arXiv:astro-ph/0203004 [astro-ph] .

[157] R. W. Hockney and J. W. Eastwood, Computer simulation using particles (Adam Hilger, 1988).

[158] J. S. Bagla and T. Padmanabhan, "Cosmological N-body simulations.", Pramana **49**, 161 (1997), arXiv:astro-ph/0411730 [astro-ph] .

[159] V. Springel, "The cosmological simulation code GADGET-2", MNRAS **364**, 1105 (2005), arXiv:astro-ph/0505010 [astro-ph] .

[160] R. Teyssier, "Cosmological hydrodynamics with adaptive mesh refinement. A new high resolution code called RAMSES", A&A **385**, 337 (2002), arXiv:astro-ph/0111367 [astro-ph] .

[161] A. Jenkins, "Second-order Lagrangian perturbation theory initial conditions for resimulations", MNRAS **403**, 1859 (2010), arXiv:0910.0258 [astro-ph.CO] .

[162] S. Bose, W. A. Hellwing, C. S. Frenk, A. Jenkins, M. R. Lovell, J. C. Helly, and B. Li, "The copernicus complexio: Statistical properties of warm dark matter haloes", MNRAS **455**, 318 (2016).

[163] V. Springel, N. Yoshida, and S. D. M. White, "GADGET: a code for collisionless and gasdynamical cosmological simulations", New A **6**, 79 (2001), arXiv:astro-ph/0003162 [astro-ph] .

[164] A. Jenkins, "A new way of setting the phases for cosmological multiscale Gaussian initial conditions", MNRAS **434**, 2094 (2013), arXiv:1306.5968 [astro-ph.CO] .

[165] A. Knebe, S. R. Knollmann, S. I. Muldrew, F. R. Pearce, M. A. Aragon-Calvo, Y. Ascasibar, P. S. Behroozi, D. Ceverino, S. Colombi, J. Diemand, K. Dolag, B. L. Falck, P. Fasel, J. Gardner, S. Gottlöber, C.-H. Hsu, F. Iannuzzi, A. Klypin, Z. Lukić, M. Maciejewski, C. McBride, M. C. Neyrinck, S. Planelles, D. Potter, V. Quilis, Y. Rasera, J. I. Read, P. M. Ricker, F. Roy, V. Springel, J. Stadel, G. Stinson, P. M. Sutter, V. Turchaninov, D. Tweed, G. Yepes, and M. Zemp, "Haloes gone MAD14: The Halo-Finder Comparison Project", MNRAS **415**, 2293 (2011), https://academic.oup.com/mnras/article-pdf/415/3/2293/5972749/mnras0415-2293.pdf .

[166] A. Knebe, F. R. Pearce, H. Lux, Y. Ascasibar, P. Behroozi, J. Casado, C. C. Moran, J. Diemand, K. Dolag, R. Dominguez-Tenreiro, P. Elahi, B. Falck, S. Gottlöber, J. Han, A. Klypin, Z. Lukić, M. Maciejewski, C. K. McBride, M. E. Merchán, S. I. Muldrew, M. Neyrinck, J. Onions, S. Planelles, D. Potter, V. Quilis, Y. Rasera, P. M. Ricker, F. Roy, A. N. Ruiz, M. A. Sgró, V. Springel, J. Stadel, P. M. Sutter, D. Tweed, and M. Zemp, "Structure finding in cosmological simulations: The state of affairs", MNRAS **435**, 10.1093/mnras/stt1403 (2013).

[167] B. Falck, "Origami: Structure-finding routine in n-body simulation", Astrophysics Source Code Library , ascl (2013).

[168] C. Lacey and S. Cole, "Merger rates in hierarchical models of galaxy formation – II. Comparison with N-body simulations", MNRAS **271**, 676 (1994), https://academic.oup.com/mnras/article-pdf/271/3/676/18539557/mnras271-0676.pdf .

[169] V. Springel, S. D. M. White, G. Tormen, and G. Kauffmann, "Populating a cluster of galaxies - I. Results at z=0", MNRAS **328**, 726 (2001), arXiv:astro-ph/0012055 [astro-ph] .

[170] S. I. Muldrew, F. R. Pearce, and C. Power, "The accuracy of subhalo detection", MNRAS **410**, 2617 (2011), arXiv:1008.2903 [astro-ph.CO] .

[171] J. Onions, A. Knebe, F. R. Pearce, S. I. Muldrew, H. Lux, S. R. Knollmann, Y. Ascasibar, P. Behroozi, P. Elahi, J. Han, M. Maciejewski, M. E. Merchán, M. Neyrinck, A. N. Ruiz, M. A. Sgró, V. Springel, and D. Tweed, "Subhaloes

going Notts: the subhalo-finder comparison project", MNRAS **423**, 1200 (2012), https://academic.oup.com/mnras/article-pdf/423/2/1200/2845306/mnras0423-1200.pdf .

[172] S. R. Knollmann and A. Knebe, "Ahf: Amiga's halo finder", The Astrophysical Journal Supplement Series **182**, 608–624 (2009).

[173] P. S. Behroozi, R. H. Wechsler, and H.-Y. Wu, "The ROCKSTAR Phase-space Temporal Halo Finder and the Velocity Offsets of Cluster Cores", ApJL **762**, 109 (2013), arXiv:1110.4372 [astro-ph.CO] .

[174] P. J. Elahi, R. J. Thacker, and L. M. Widrow, "Peaks above the Maxwellian Sea: a new approach to finding substructures in N-body haloes", MNRAS **418**, 320 (2011), arXiv:1107.4289 [astro-ph.CO] .

[175] L. Jiang, J. C. Helly, S. Cole, and C. S. Frenk, "N-body dark matter haloes with simple hierarchical histories", MNRAS **440**, 2115 (2014).

[176] A. I. Merson, C. M. Baugh, J. C. Helly, V. Gonzalez-Perez, S. Cole, R. Bielby, P. Norberg, C. S. Frenk, A. J. Benson, R. G. Bower, C. G. Lacey, and C. d. P. Lagos, "Lightcone mock catalogues from semi-analytic models of galaxy formation – I. Construction and application to the BzK colour selection", MNRAS **429**, 556 (2013).

[177] S. Cole, C. G. Lacey, C. M. Baugh, and C. S. Frenk, "Hierarchical galaxy formation", MNRAS **319**, 168 (2000), arXiv:astro-ph/0007281 [astro-ph] .

[178] J. C. Helly, S. Cole, C. S. Frenk, C. M. Baugh, A. Benson, and C. Lacey, "Galaxy formation using halo merger histories taken from N-body simulations", MNRAS **338**, 903 (2003).

[179] M. Boylan-Kolchin, V. Springel, S. D. M. White, and A. Jenkins, "There's no place like home? Statistics of Milky Way-mass dark matter haloes", MNRAS **406**, 896 (2010), https://academic.oup.com/mnras/article-pdf/406/2/896/18721116/mnr0406-0896.pdf .

[180] Q. Guo and S. White, "Numerical resolution limits on subhalo abundance matching", MNRAS **437**, 3228 (2014), arXiv:1303.3586 [astro-ph.CO] .

[181] N. I. Libeskind, R. van de Weygaert, M. Cautun, B. Falck, E. Tempel, T. Abel, M. Alpaslan, M. A. Aragón-Calvo, J. E. Forero-Romero, R. Gonzalez,

S. Gottlöber, O. Hahn, W. A. Hellwing, Y. Hoffman, B. J. Jones, F. Kitaura, A. Knebe, S. Manti, M. Neyrinck, S. E. Nuza, N. Padilla, E. Platen, N. Ramachandra, A. Robotham, E. Saar, S. Shandarin, M. Steinmetz, R. S. Stoica, T. Sousbie, and G. Yepes, "Tracing the cosmic web", MNRAS **473**, 1195 (2018).

[182] P. M. Sutter, G. Lavaux, N. Hamaus, A. Pisani, B. D. Wandelt, M. Warren, F. Villaescusa-Navarro, P. Zivick, Q. Mao, and B. B. Thompson, "VIDE: The Void IDentification and Examination toolkit", Astronomy and Computing **9**, 1 (2015), arXiv:1406.1191 [astro-ph.CO] .

[183] T. Sousbie, "The persistent cosmic web and its filamentary structure - I. Theory and implementation", MNRAS **414**, 350 (2011), arXiv:1009.4015 [astro-ph.CO] .

[184] P. Pranav, H. Edelsbrunner, R. van de Weygaert, G. Vegter, M. Kerber, B. J. T. Jones, and M. Wintraecken, "The topology of the cosmic web in terms of persistent Betti numbers", MNRAS **465**, 4281 (2017), arXiv:1608.04519 [astro-ph.CO] .

[185] T. Bonnaire, N. Aghanim, A. Decelle, and M. Douspis, "T-ReX: a graph-based filament detection method", A&A **637**, A18 (2020), arXiv:1912.00732 [astro-ph.CO] .

[186] R. S. Stoica, V. J. Martínez, J. Mateu, and E. Saar, "Detection of cosmic filaments using the Candy model", A&A **434**, 423 (2005), arXiv:astro-ph/0405370 [astro-ph] .

[187] E. Tempel, R. S. Stoica, V. J. Martínez, L. J. Liivamägi, G. Castellan, and E. Saar, "Detecting filamentary pattern in the cosmic web: a catalogue of filaments for the SDSS", MNRAS **438**, 3465 (2014), arXiv:1308.2533 [astro-ph.CO] .

[188] J. E. Forero-Romero, A. Palomino, F. L. Gómez-Cortés, and X.-D. Li, "Cosmic web classification through stochastic topological ranking", RAS Techniques and Instruments **4**, rzaf032 (2025), arXiv:2404.01124 [astro-ph.CO] .

[189] D. Kelesis, S. Basilakos, V. Papadopoulou Lesta, D. Fotakis, and A. Efstathiou, "Detecting and analysing the topology of the cosmic web with spatial clustering algorithms I: methods", MNRAS **516**, 5110 (2022), arXiv:2208.11393 [astro-ph.IM] .

[190] F. M. Hunde, O. Newton, W. A. Hellwing, M. Bilicki, and K. Naidoo, "Caught in the cosmic web: Environmental effects on subhalo abundance and internal density profiles", A&A **700**, A65 (2025), arXiv:2409.09226 [astro-ph.CO] .

[191] M. Cautun, R. van de Weygaert, and B. J. T. Jones, "NEXUS: tracing the cosmic web connection", MNRAS **429**, 1286 (2013), arXiv:1209.2043 [astro-ph.CO] .

[192] S. Pfeifer, N. I. Libeskind, Y. Hoffman, W. A. Hellwing, M. Bilicki, and K. Naidoo, "COWS: a filament finder for Hessian cosmic web identifiers", MNRAS **514**, 470 (2022), arXiv:2201.04624 [astro-ph.CO] .

[193] Y. Hoffman, O. Metuki, G. Yepes, S. Gottlöber, J. E. Forero-Romero, N. I. Libeskind, and A. Knebe, "A kinematic classification of the cosmic web", MNRAS **425**, 2049 (2012), https://academic.oup.com/mnras/article-pdf/425/3/2049/3052482/425-3-2049.pdf .

[194] G. A. Dooley, B. F. Griffen, P. Zukin, A. P. Ji, M. Vogelsberger, L. E. Hernquist, and A. Frebel, "The Effects of Varying Cosmological Parameters on Halo Substructure", ApJL **786**, 50 (2014), arXiv:1403.6828 [astro-ph.CO] .

[195] F. C. van den Bosch, G. Tormen, and C. Giocoli, "The mass function and average mass-loss rate of dark matter subhaloes", MNRAS **359**, 1029 (2005), arXiv:astro-ph/0409201 [astro-ph] .

[196] A. V. Kravtsov, A. A. Berlind, R. H. Wechsler, A. A. Klypin, S. Gottlöber, B. Allgood, and J. R. Primack, "The Dark Side of the Halo Occupation Distribution", ApJL **609**, 35 (2004), arXiv:astro-ph/0308519 [astro-ph] .

[197] J. Klimentowski, E. L. Łokas, A. Knebe, S. Gottlöber, L. A. Martinez-Vaquero, G. Yepes, and Y. Hoffman, "The grouping, merging and survival of subhaloes in the simulated Local Group", MNRAS **402**, 1899 (2010), arXiv:0909.1916 [astro-ph.CO] .

[198] A. Hou, L. C. Parker, and W. E. Harris, "The pre-processing of subhaloes in SDSS groups and clusters", MNRAS **442**, 406 (2014), arXiv:1404.7504 [astro-ph.GA] .

[199] A. Rodríguez-Puebla, P. Behroozi, J. Primack, A. Klypin, C. Lee, and D. Hellinger, "Halo and subhalo demographics with Planck cosmological parameters: Bolshoi-Planck and MultiDark-Planck simulations", MNRAS **462**, 893 (2016), arXiv:1602.04813 [astro-ph.CO] .

[200] F. C. van den Bosch, G. Ogiya, O. Hahn, and A. Burkert, "Disruption of dark matter substructure: fact or fiction?", MNRAS **474**, 3043 (2018), arXiv:1711.05276 [astro-ph.GA] .

[201] A. R. Wetzel, J. L. Tinker, C. Conroy, and F. C. van den Bosch, "Galaxy evolution in groups and clusters: satellite star formation histories and quenching time-scales in a hierarchical Universe", MNRAS **432**, 336 (2013), arXiv:1206.3571 [astro-ph.CO] .

[202] S. Ando, T. Ishiyama, and N. Hiroshima, "Halo substructure boosts to the signatures of dark matter annihilation", Galaxies **7**, 10.3390/galaxies7030068 (2019).

[203] N. Dalal and C. S. Kochanek, "Direct Detection of Cold Dark Matter Substructure", ApJL **572**, 25 (2002), arXiv:astro-ph/0111456 [astro-ph] .

[204] C. Conroy, R. H. Wechsler, and A. V. Kravtsov, "Modeling Luminosity-dependent Galaxy Clustering through Cosmic Time", ApJL **647**, 201 (2006), arXiv:astro-ph/0512234 [astro-ph] .

[205] P. S. Behroozi, R. H. Wechsler, and C. Conroy, "The Average Star Formation Histories of Galaxies in Dark Matter Halos from z = 0-8", ApJL **770**, 57 (2013), arXiv:1207.6105 [astro-ph.CO] .

[206] R. M. Reddick, R. H. Wechsler, J. L. Tinker, and P. S. Behroozi, "The Connection between Galaxies and Dark Matter Structures in the Local Universe", ApJL **771**, 30 (2013), arXiv:1207.2160 [astro-ph.CO] .

[207] G. Tormen, F. R. Bouchet, and S. D. M. White, "The structure and dynamical evolution of dark matter haloes", MNRAS **286**, 865 (1997), arXiv:astro-ph/9603132 [astro-ph] .

[208] S. Trujillo-Gomez, A. Klypin, J. Primack, and A. J. Romanowsky, "Galaxies in ΛCDM with Halo Abundance Matching: Luminosity-Velocity Relation, Baryonic Mass-Velocity Relation, Velocity Function, and Clustering", ApJL **742**, 16 (2011), arXiv:1005.1289 [astro-ph.CO] .

[209] J. Chaves-Montero, R. E. Angulo, J. Schaye, M. Schaller, R. A. Crain, M. Furlong, and T. Theuns, "Subhalo abundance matching and assembly bias in the EAGLE simulation", MNRAS **460**, 3100 (2016), arXiv:1507.01948 [astro-ph.GA] .

[210] O. Fakhouri, C.-P. Ma, and M. Boylan-Kolchin, "The merger rates and mass assembly histories of dark matter haloes in the two Millennium simulations", MNRAS **406**, 2267 (2010), arXiv:1001.2304 [astro-ph.CO] .

[211] M. C. Artale, I. Zehavi, S. Contreras, and P. Norberg, "The impact of assembly bias on the halo occupation in hydrodynamical simulations", MNRAS **480**, 3978 (2018), arXiv:1805.06938 [astro-ph.GA] .

[212] P. S. Behroozi, R. H. Wechsler, H.-Y. Wu, M. T. Busha, A. A. Klypin, and J. R. Primack, "Gravitationally Consistent Halo Catalogs and Merger Trees for Precision Cosmology", ApJL **763**, 18 (2013), arXiv:1110.4370 [astro-ph.CO] .

[213] C. Giocoli, G. Tormen, and F. C. van den Bosch, "The population of dark matter subhaloes: mass functions and average mass-loss rates", MNRAS **386**, 2135 (2008), arXiv:0712.1563 [astro-ph] .

[214] F. C. van den Bosch, "Dissecting the evolution of dark matter subhaloes in the Bolshoi simulation", MNRAS **468**, 885 (2017), arXiv:1611.02657 [astro-ph.GA] .

[215] F. Jiang and F. C. van den Bosch, "Statistics of Dark Matter Substructure: I. Model and Universal Fitting Functions", arXiv e-prints , arXiv:1403.6827 (2014), arXiv:1403.6827 [astro-ph.CO] .

[216] F. Jiang and F. C. van den Bosch, "Statistics of dark matter substructure - III. Halo-to-halo variance", MNRAS **472**, 657 (2017), arXiv:1610.02399 [astro-ph.CO] .

[217] R. Tojeiro, E. Eardley, J. A. Peacock, P. Norberg, M. Alpaslan, S. P. Driver, B. Henriques, A. M. Hopkins, P. R. Kafle, A. S. G. Robotham, P. Thomas, C. Tonini, and V. Wild, "Galaxy and Mass Assembly (GAMA): halo formation times and halo assembly bias on the cosmic web", MNRAS **470**, 3720 (2017), arXiv:1612.08595 [astro-ph.CO] .

[218] D. H. Zhao, H. J. Mo, Y. P. Jing, and G. Börner, "The growth and structure of dark matter haloes", MNRAS **339**, 12 (2003), arXiv:astro-ph/0204108 [astro-ph] .

[219] Y. Li, H. J. Mo, and L. Gao, "On halo formation times and assembly bias", MNRAS **389**, 1419 (2008), arXiv:0803.2250 [astro-ph] .

[220] J. D. Emberson, T. Kobayashi, and M. A. Alvarez, "Evolution of Low Mass Galactic Subhalos and Dependence on Concentration", ApJL **812**, 9 (2015), arXiv:1504.00667 [astro-ph.CO] .

[221] Y. Meng, H. Zheng, S. Liao, L. Xie, L. Wang, H. Chen, L. Gao, Q. Guo, Y. Jing, J. Wang, H. Yang, and G. Zeng, "The Impact of Cosmic Filaments on the Abundance of Satellite Galaxies", ApJL **998**, 251 (2026), arXiv:2509.22179 [astro-ph.GA] .

[222] B. Jego, K. Kraljic, M. Béthermin, and R. Davé, "Star-forming galaxies in the cosmic web in the last 11 Gyr", A&A **706**, A150 (2026), arXiv:2509.18077 [astro-ph.CO] .

[223] J.-S. Moon and J. Lee, "The Density Parity Model for the Evolution of the Subhalo Inner Spin Alignments with the Cosmic Web", ApJL **952**, 82 (2023), arXiv:2302.00679 [astro-ph.CO] .

[224] O. Fakhouri and C.-P. Ma, "The nearly universal merger rate of dark matter haloes in ΛCDM cosmology", MNRAS **386**, 577 (2008).

[225] K. T. E. Chua, A. Pillepich, V. Rodriguez-Gomez, M. Vogelsberger, S. Bird, and L. Hernquist, "Subhalo demographics in the Illustris simulation: effects of baryons and halo-to-halo variation", MNRAS **472**, 4343 (2017), https://academic.oup.com/mnras/article-pdf/472/4/4343/21074848/stx2238.pdf .

[226] G. Despali and S. Vegetti, "The impact of baryonic physics on the subhalo mass function and implications for gravitational lensing", MNRAS **469**, 1997 (2017), arXiv:1608.06938 [astro-ph.GA] .

[227] R. A. Crain, J. Schaye, R. G. Bower, M. Furlong, M. Schaller, T. Theuns, C. Dalla Vecchia, C. S. Frenk, I. G. McCarthy, J. C. Helly, A. Jenkins, Y. M. Rosas-Guevara, S. D. M. White, and J. W. Trayford, "The EAGLE simulations of galaxy formation: calibration of subgrid physics and model variations", MNRAS **450**, 1937 (2015), arXiv:1501.01311 [astro-ph.GA] .

[228] F. Marinacci, M. Vogelsberger, R. Pakmor, P. Torrey, V. Springel, L. Hernquist, D. Nelson, R. Weinberger, A. Pillepich, J. Naiman, and S. Genel, "First results from the IllustrisTNG simulations: radio haloes and magnetic fields", MNRAS **480**, 5113 (2018), arXiv:1707.03396 [astro-ph.CO] .

[229] R. Pakmor, V. Springel, J. P. Coles, T. Guillet, C. Pfrommer, S. Bose, M. Barrera, A. M. Delgado, F. Ferlito, C. Frenk, B. Hadzhiyska, C. Hernández-Aguayo, L. Hernquist, R. Kannan, and S. D. M. White, "The MillenniumTNG Project: the hydrodynamical full physics simulation and a first look at its galaxy clusters", MNRAS **524**, 2539 (2023), arXiv:2210.10060 [astro-ph.CO] .

[230] J. Schaye, R. Kugel, M. Schaller, J. C. Helly, J. Braspenning, W. Elbers, I. G. McCarthy, M. P. van Daalen, B. Vandenbroucke, C. S. Frenk, J. Kwan, J. Salcido, Y. M. Bahé, J. Borrow, E. Chaikin, O. Hahn, F. Huško, A. Jenkins, C. G. Lacey, and F. S. J. Nobels, "The FLAMINGO project: cosmological hydrodynamical simulations for large-scale structure and galaxy cluster surveys", MNRAS **526**, 4978 (2023), arXiv:2306.04024 [astro-ph.CO] .

[231] R. Dragomir, A. Rodríguez-Puebla, J. R. Primack, and C. T. Lee, "Does the galaxy-halo connection vary with environment?", MNRAS **476**, 741 (2018), arXiv:1710.09392 [astro-ph.GA] .

[232] D. Campbell, F. C. van den Bosch, N. Padmanabhan, Y.-Y. Mao, A. R. Zentner, J. U. Lange, F. Jiang, and A. S. Villarreal, "The galaxy clustering crisis in abundance matching", MNRAS **477**, 359 (2018), arXiv:1705.06347 [astro-ph.GA] .

[233] C. M. O'Riordan, G. Despali, S. Vegetti, M. R. Lovell, and Á. Moliné, "Sensitivity of strong lensing observations to dark matter substructure: a case study with Euclid", MNRAS **521**, 2342 (2023), arXiv:2211.15679 [astro-ph.CO] .